Andreev Reflection Spectroscopy:

Theory and Experiment

by

Jessica Anna Gifford

A Dissertation Presented in Partial Fulfillment
of the Requirements for the Degree
Doctor of Philosophy

Approved November 2015 by the
Graduate Supervisory Committee:

Tingyong Chen, Chair
Peter Bennett
Robert Nemanich
Kong-Thon Tsen

ARIZONA STATE UNIVERSITY

December 2015

ABSTRACT

A theoretical study of a three-dimensional (3D) N/S interface with arbitrary spin polarization and interface geometry is presented. The 3D model gives the same intrinsic spin polarization and superconducting gap dependence as the 1D model. This demonstrates that the 1D model can be use to fit 3D data.

Using this model, a Heusler alloy is investigated. Andreev reflection measurements show that the spin polarization is 80% in samples sputtered on unheated MgO(100) substrates and annealed at high temperatures. However, the spin polarization is considerably smaller in samples deposited on heated substrates.

Ferromagnetic Fe_xSi_{-x} alloys have been proposed as potential spin injectors into silicon with a substantial spin polarization. Andreev Reflection Spectroscopy (ARS) is utilized to determine the spin polarization of both amorphous and crystalline $Fe_{65}Si_{35}$ alloys. The amorphous phase has a significantly higher spin polarization than that of the crystalline phase.

In this thesis, (1111) Fe $SmO_{0.82}F_{0.18}FeAs$ and Pb superconductors are used to measure the spin polarization of a highly spin-polarized material, $La_{0.67}Sr_{0.33}MnO_3$. Both materials yield the same intrinsic spin polarization, therefore, Fe-superconductors can be used in ARS. Based on the behavior of the differential conductance for highly spin polarized LSMO and small polarization of Au, it can be concluded that the Fe-Sc is not a triplet superconductor.

Zero bias anomaly (ZBA), in point contact Andreev reflection (PCAR), has been utilized as a characteristic feature to reveal many novel physics. Complexities at a normal metal/superconducting interface often cause nonessential ZBA-like features, which may be mistaken as ZBA. In this work, it is shown that an extrinsic ZBA, which is due to the contact resistance, cannot be suppressed by a highly spin-polarized current while a nonessential ZBA cannot be affected the contact resistance.

Finally, Cu/Cu multilayer GMR structures were fabricated and the GMR% measured at 300 K and 4.5 K gave responses of 63% and 115% respectively. Not only do the GMR structures have a large enhancement of resistance, but by applying an external magnetic field it is shown that, unlike most materials, the spin polarization can be tuned to values of 0.386 to 0.415 from $H = 0$ kOe to $H = 15$ kOe.

DEDICATION

To my fiancé Daniel Gruss.

ACKNOWLEDGMENTS

I would like to thank my advisor, Dr. Tingyong Chen, for his guidance and mentor-ship throughout my graduate career. Dr. Chen has been instrumental in helping me learn new techniques and build the confidence that I needed to succeed in my work. He has always encouraged me to be the best researcher possible and has guided me through not only my research but other important aspects of my career such as presentations, networking, and professionalism. I have learned so much from his exceptional knowledge of physics and have admired his leadership abilities in the lab that I one day wish to emulate.

A special thanks to Dr. Bennett for mentoring me not only in research but coursework as well, advising me during my research, and allowing me to work in his lab in parallel with my thesis project. I would also like to thank Dr. Barry Wilkens for teaching me how to use his facilities and for helping me analyze and trouble shoot our data. I would also like to thank Dr. Robert Nemanich for giving me my first research project when joining Arizona State, and for advising me on my thesis. I am very grateful to also have Dr. Kong-Thon Tsen for being on my committee and for his comments suggestions during this process. If it were not for our collaborators Dr. Di Wu, Dr. Nate Newman, Dr. Jeffery Drucker, Mahmoud Vahidi, Bin Chen and many others, my research would have not been possible. I would like to thank my colleagues in our group including Gejian Zhao, Ji Zhang, Charles Snider, Dongrin Kim, Bochao Li, Miguel Bueno, Nathan Vargas, and Jonny Martinez for their instrumental help in helping me conduct my research and for supporting me throughout my graduate career. I would like to thank my fellow graduate students Sean Caudle, David Dotson, Amber Henry, Hank Lamm, and many others for their support and friendship, especially my first year in graduate school.

If it wa not for my colleague Joe Shammas, I wouldn't have had a bouncing board

for my ideas or a fellow graduate student to help me not only throughout my research but also the various other struggles of being in graduate school. I also extremely appreciated the help from my family, especially my sister, Nicole Allen, and parents, Robert and Julie Gifford, for supporting my decision to go to graduate school and believing in me.

I would like to thank Daniel Gruss most of all for supporting the hard decision to endure a five year, long distance relationship so that I could accomplish my dream of going to graduate school and earning my doctorate. Not only at times has he taken the time to put his research on hold to help me with mine, helping to edit and critique my thesis, and helping me financially, but he has been my emotional rock and has always been there when I needed him most. Thank you for your love, patience, endurance, and constant assurance that I made the right decision in continuing with my physics education.

TABLE OF CONTENTS

Page

CHAPTER Page

CHAPTER Page

CHAPTER Page

CHAPTER Page

LIST OF FIGURES

Figure Page

Figure Page

Figure Page

Figure Page

Chapter 1

INTRODUCTION

Unlike today's conventional electronics, which just utilize charge, the next generation of electronics will also take advantage of the conduction electrons' spin angular momentum, or spin. These electronics have the advantage of nonvolatilty, low power consumption, higher integration density, and higher processing speeds [1]. The main advantage of spintronics is its use in embedded memories and non-volatile memory devices such as the Magnetoresistive Random Access Memory (MRAM).

Spin was first realized in 1925 by physicist Ralph De Laer Dronig who was observing the anomalous Zeeman Effect and, in particular, the resulting orbital angular momentum. Dronig discovered that not only is there angular momentum but an electron can have additional angular momentum which is caused by the electron spinning about its axis with a fixed rotation of $\frac{1}{2}\hbar$. Just like angular momentum, the spin also has a magnetic moment. The interacting electrons can affect the magnetic and electrical properties of a material causing many types of magnetism including ferromagnetism [2]. Three years before Dronig's discovery, Stern and Gerlach unknowingly measured spin while trying to measure the quantum numbers m, l, and n. Using silver they believed their results showed a spin of $\hbar$ but it was later disproved by other groups who correctly found a spin of 0 [2].

The next major advancement in spintronics did not occur until the discovery of the giant magnetoresistive effect (GME) in 1988 by Albert Fert and Peter Gruenburg. Using Fe(001)/Cr(009) superlattices they discovered a reduction in resistivity of up to 2 in some samples. GMR describes a magnetoresistive effect in thin-film structures composed of alternating ferromagnetic and non-magnetic conductive layers. At zero

field there is an enhanced resistivity which can be as high as 120%. In 2007, both Fert and Gruenburg were awarded the Nobel Prize in Physics for this discovery [3].

IBM, in 1989, began to measure the GMR in various structures. In 1997, a group at IBM lead by Stuart Parkin created the first GMR hard disk head. It was based on the spin valve. The spin valve has been extensively used in magnetic recording read-heads and other magnetic field sensors. In conventional electronics, current carries no spin information. However, in spintronics, the current is spin-polarized and the spin polarization is used to describe the degree of polarization in a spin-polarized current. Tunneling magnetoresistance (TMR) or GMR values, for example, can be greatly enhanced if highly spin-polarized magnets are used as spin electrodes. This givesa critical current, used to manipulate nanomagnets , which can be prominently reduced if a current with high spin polarization is injected [4, 5].

Since the breakthrough of spin valve devices, many interesting discoveries have been made in the further development of GMR devices. Notable examples include the discovery, in 2001, of successful spin injection of a stream of electrons, with identical spins, into a semiconductor [6]. A device was developed, in 2003, which one could transfer spin electrons across molecular bridges between quantum dots [7]. Another example is the fabrication, in 2010, of thermo-spintronic chips that could run on heat [8]. However, one of the most notable breakthroughs is the fabrication of MRAM devices.

The first MRAM research was conducted in 1995 by Motorola. However, IBM was the key company in the early development of this device. Since then, MRAM has become the standard product and is used as the universal memory device [9]. Unlike random access memory (RAM), MRAM uses magnetic storage elements instead of storing memory as electric charge. To do this, two ferromagnetic plates separated by a dielectric insulator are used. The first plate is a permanent magnet and the

second can chance magnetic polarity with the external field. Therefore MRAM is just a specific type of spin valve. Some disadvantages to MRAM are that they need a substantial current to generate the magnetic field, and as you shrink the device, the induced fields can overlap and incorrectly store the memory [10]. One proposed solution is to use a GME device but progress has been slow due to other experimental factors that cause issues with this device.

Other proposed techniques include spin transfer torque (STT), which uses aligned spin electrons to torque domains in the device. These torques can be transferred to nearby layers and thus the torque, not current, will write the memory [11]. Another method is thermal assisted switching (TAS-MRAM), which quickly heats up the magnetic tunnel junctions (MTJs) while data is being written which then keeps the MTJs stable at colder temperatures. This helps with heating induced by high currents needed for MRAM [12]. Many groups are currently working on MRAM improvements which indicates that the development of spintronic devices will be crucial in future technologies.

In spintronics, the search for a circuit that perform logic operations, which is controlled by spin currents, is a crucial component. It can be faster and more efficient than charge-based semiconductor transistors currently in use today [13]. The physicist Alexander F. Andreev, in which Andreev Reflection Spectroscopy (ARS), is named was the first to experiment with ferromagnetic/superconducting interfaces in the 1960s. Before the discovery of ARS, the spin polarization of a metal and superconducting gap of a superconductor were very difficult to measure in an actual experiment. However, ARS allows one to measure both the spin polarization and superconducting gap rather easily. At the interface, it was thought that the opposing electrons destructively interfered, however, at temperatures below the critical temperature, which is the temperature where the superconductivity is killed, of the

superconductor the superconductivity and spin polarization can interact creating a sharp increase in the differential conductance about zero magnetic field [14]. ARS is described in greater detail in chapter 4. Using materials such as highly spin polarized materials or half metals, one can allow for spin polarizations to reach 100%. The spin polarization of many magnetic materials [15–27] including some half metals [22, 23] has been measured by ARS. Also, the gap of many superconductors, including the recently discovered Fe-superconductors [28, 29] have been measured.

This thesis will focus on ARS in three dimensions as well as determining the spin polarization and superconducting gap using this model. The thesis is organized as follows: Followed by this introduction is a brief description of spin polarization and a larger discussion of superconducting gap and the mechanisms of superconductivity on conventional and unconventional superconductors in chapter 2. Chapter 3 introduces magnetic nanostructures and their unusual properties and magnetoresistance regimes. Chapter 4 it aslo describes Andreev Reflection Spectroscopy (ARS) and the BTK theory that describes it. It also describes the ARS effects of both single and triplet superconductors in contact with polarized metals. Chapter 5 describes the point contact spectroscopy method and the experimental set ups for the various experiments that follow in later chapters. Chapter 6 introduces the theoretical model that is used to analyze the ARS result for the later chaptersl. The ARS results of a Heusler alloy, amorphous alloy, and Fe-Sc on LSMO will be investigates in chapters 7, 8, and 9 respectively. Chapter 11 will describe the giant magnetoresistive (GMR) effects on Co/Cu multilayer thin films as well as investigate the ARS properties associated with the material at low temperatures. Finally, the conclusions are summarized in chapter 12.

Chapter 2

SPIN POLARIZATION AND SUPERCONDUCTIVITY

At a normal metal/superconductor interface, it can often be difficult to measure the spin polarization of a metal and superconductive gap of a superconductor. Until the discovery of the Andreev Reflection (AR), to measure these values many complicated processes and data manipulations were needed. Now with the ability to perform AR measurements, the search for half metals with high spin polarizations has been a hot topic in spintronics. A half metal is a material that acts as a conductor to electrons with one spin orientation. This is important to spintronics because the ability to write data depends on the ability to pass electrons with specific spin orientations which act as the "1" and "0" bits of information. The higher the spin polarization, the easier it is to pass and manipulate the electron's spin using magnetic nanostructures, see chapter 3. The superconducting gap can yield important information about the critical field and critical magnetic field of the superconductor, as well as the energies need to create Cooper pairs and thus creating superconductivity. The BCS, see section 2.4, model describes the mechanisms of superconductivity, the superconducting gap, as well as their temperature dependence. This chapter will describe what spin polarization and superconducting gap are, and then will go into detail behind the mechanisms of superconductivity and the dependence of the gap on temperature.

2.1 Spin Polarization

Spin polarization is defined as the imbalance of density of states (DOS) of the number of spin up and spin down electrons at Fermi level normalized by the total

states,

$$P = \frac{N_{\uparrow}(E_F) - N_{\downarrow}(E_F)}{N_{\uparrow}(E_F) + N_{\downarrow}(E_F)} \ , \tag{2.1}$$

where E_F is the Fermi level, shown in equation 2.1. Figure 2.1 shows three examples of spin polarization as it relates to different types of metals. For non-magnetic metals, the spin up and spin down electrons at the Fermi level are equal, so the spin polarization is zero. In half metals, shown in figure 2.1, only one spin band is available at the Fermi level corresponding to a spin polarization of 1. For many ferromagnetic metals, the spin polarization is between 0 and 1, shown in figure 2.1.

For actual experiments, which are often not ideal or are clean interfaces, the spin polarization is often related to the specific measurement technique. If the contact size of the point contact is less than mean free path, then one has the diffusive spin polarization,

$$P_{ballistic} = \frac{N_{\uparrow}(E_F)v_{\uparrow F} - N_{\downarrow}(E_F)v_{\downarrow F}}{N_{\uparrow}(E_F)v_{\uparrow F} + N_{\downarrow}(E_F)v_{\downarrow F}} \ . \tag{2.2}$$

In the ballistic limit, the spin polarization is weighted by the Fermi velocities of the spin up and spin down electrons, while in the diffusive limit being weighted by the square of the Fermi velocities [30],

$$P_{diffusive} = \frac{N_{\uparrow}(E_F)v_{\uparrow F}^2 - N_{\downarrow}(E_F)v_{\downarrow F}^2}{N_{\uparrow}(E_F)v_{\uparrow F}^2 + N_{\downarrow}(E_F)v_{\downarrow F}^2} \ . \tag{2.3}$$

In a tunneling current, however, the spin polarization is weighted by the tunneling matrix. The spin polarization is more complicated, although the definition looks similar,

$$P_{tunnel} = \frac{N_{\uparrow}(E_F)|M_{\uparrow}|^2 - N_{\downarrow}(E_F)|M_{\downarrow}|^2}{N_{\uparrow}(E_F)|M_{\uparrow}|^2 + N_{\downarrow}(E_F)|M_{\downarrow}|^2} \ , \tag{2.4}$$

where $M_{\uparrow}$ and $M_{\downarrow}$ are the tunneling matrices [31].

When a magnetic material has full spin polarization ($P = 1$), it is called a half metal. Because the performance of a spintronic device (e. g. magnetoresistance

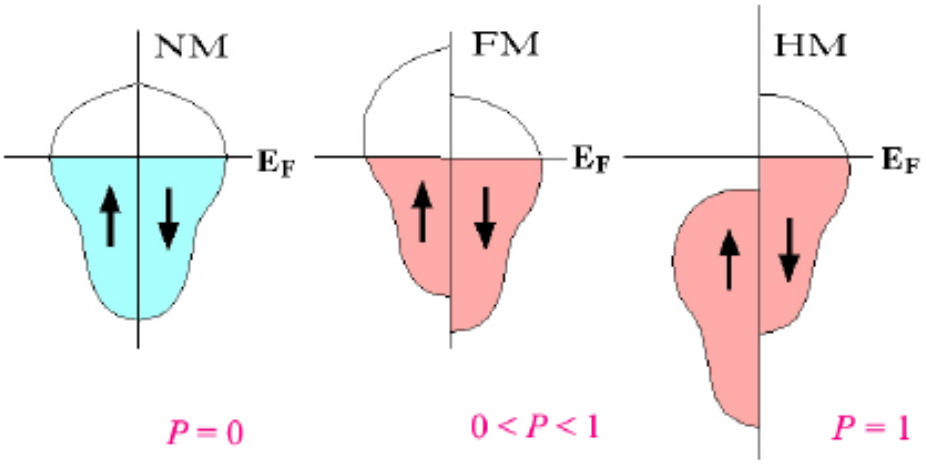

Figure 2.1: Definition of spin polarizations: (a) non-magnetic metals, polarization is zero, (b) magnetic metals, polarization is between zero and one, (c) half metallic metals, polarization is one.

percentages and sensitivity) relies critically on the polarization value of the magnetic materials used [22, 32–39], the hunt to find more half metals has been just as important as the search for a superconductor with a higher critical temperature (T_c). Many materials have been predicted to be half-metallic and some have been validated by experiments [22, 32–39]. However, CrO_2 is the only material thus far that has demonstrated half-metallic properties, which was measured using Andreev reflection spectroscopy (ARS), with a spin polarization of 98.6% [22].

Since its discovery in the 1950s, electron spin polarization has been extensively researched. Experimentally, photo-emission spectroscopy has become a standard method that measures the spin polarization based on Mott scattering [16]. However, this method is extremely dependent on the surface states and contamination. Widely different spin polarization values have been reported. For example, the polarization of Ni has been measured both to be 0% and 100% [16] by this method.

A second proposed method to measure the spin polarization is spin-dependent tunneling or tunneling magnetoresistance (TMR). In a ferromagnet/insulator/ ferromagnet (F1/I/F2) junctions, the tunneling probability depends on the orientation of the magnetization of the two electrodes as well as their density of states. From this, the spin polarization values can be extracted from the TMR value. In a ferromagnet/insulator/superconductor (F/I/S) junction, the conductance is proportional to the density of states of the superconductor's quasi-particles and the available states in the ferromagnetic layer. When a large external field is used to split the energy of up and down spins in this layer, the conductance spectra shift oppositely around zero bias voltage, creating four peaks. The spin polarization of the layer can be obtained by analyzing the conductance spectrum. However, the determined spin polarization value by the spin-dependent tunneling method is dependent on the quality of the tunneling layer as well as the type of the materials used. For example, the polarization

value of Fe obtained from the of F1/I/F2 tunnel junctions varies greatly according to the TMR value [40]. In MgO tunnel junctions, because of the unique coherent tunneling process in crystalline (001) MgO, the calculated polarization value is altogether different [41] for different tunneling junctions. Even the sign of the spin polarization of ferromagnetic Co can be different between junctions using Al_2O_3 and $SrTiO_3$ [16].

2.2 Superconducting Gap

Not only is the spin polarization difficult to experimentally measure, but the superconductor's gap, at a normal metal (NM)/(S) interface, is also experimentally difficult to measure. The superconducting gap is defined as the energy difference between the energy of ground state of the superconductor and the energy of the lowest quasi-particle excitation.

According to the Bardeen-Cooper-Schrieffer (BCS) theory (see section 2.4), the energy required to break a Cooper pair is,

$$E_g = 2\Delta(T) \ , \tag{2.5}$$

where Δ is the superconducting gap. For most conventional superconductors at the critical temperature T_c, with E_g, the energy can be written as,

$$E_g = 2\Delta(0) = 3.528 \ kT_c \ . \tag{2.6}$$

Equations 2.5 and 2.6 can be used to solve for the superconducting gap at temperatures $T \leq T_c$,

$$\Delta = 1.765 \ kT_c \ . \tag{2.7}$$

Figure 2.2 shows the energy verses temperature for these conventional superconductors [42].

In these experiments, the gap Δ closely relates to the mechanism of superconductivity but, as shown, there are very few techniques to measure it. There have

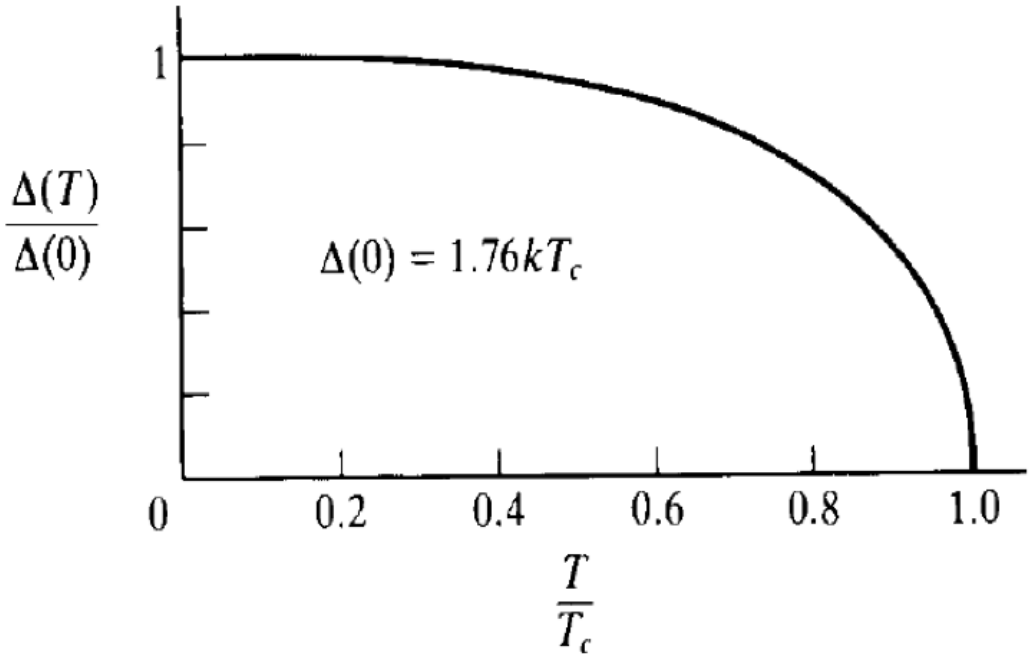

Figure 2.2: Temperature dependence of the energy gap in the BCS theory. Strictly speaking, this universal curve holds only in a weak-coupling limit, but it is a good approximation in most cases [42].

been a few methods developed as early as the 1960s to measure the superconducting gap. One such method proposed by the General Electric (GE) Research Laboratory uses electron tunneling to measure the superconducting gap [43]. The experimental device is made of two metals that are separated by a thin insulating film. A potential difference is created from electrons trying to penetrate the potential barrier. In low fields, the tunneling current is proportional to the applied voltage [44], which allows the information to be measured and the electronic structure of superconductors to be described. $Al/AlO_2/Pb$ samples were created by vapor-deposition of aluminum on glass slides. At temperatures of 4 K, a magnetic field is applied parallel to the film and the differential conductance $\frac{dI}{dV}$ is measured as a function of potential difference. Then by calculating the relative slope of this conductance, figure 2.3, one can solve for the superconducting gap [45]. This is done by finding the relative slope $\frac{dI}{dV} = 1$. This will yield half the energy gap and, in the case of the GE experiments for Pb, the measured gap is 4.2 kT_c [43].

A second common measurement technique is theAngle Resolved Photo-emission Spectroscopy (ARPES) [46]. Although ARPES is not sensitive to the phase of the order parameter, it does measure the absolute value of the momentum using the superconducting gap [47, 48]. $NdFeAs_(0.9)F_(0.1)$ single crystals were measured about the gamma pocket, which is fully gapped with no nodes. Using the momentum distribution curves (MDC), a plot of the ARPES, integrated over $\pm 20meV$ about the Fermi energy as a function of momentum[49, 50],is shown in figure 2.4 (e). The superconducting gap, along the high symmetry directions, is shown in figure 2.4 with directions (a) $\Gamma - X$ and (b) $\Gamma - M$. To measure this superconducting gap, the raw energy distribution curves (ECD) [51], which are reflected about the Fermi energy, are calculated shown in figure 2.4 (c) and (d). The superconducting gap is observed in both directs by two sharp peaks at the Fermi vector. Figure 2.4 (f) shows the

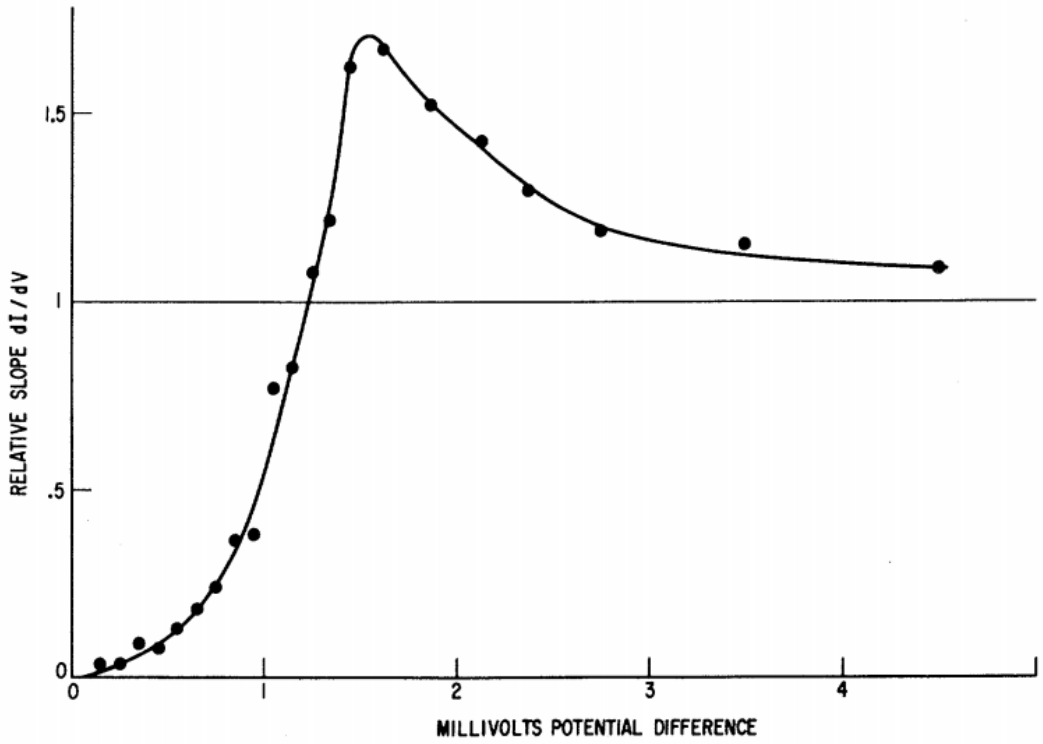

Figure 2.3: Slope $\frac{dI}{dV}$ of Pb superconductor at $T = 1.6K$ and $H = 0$ [43].

energy position of the coherent peaks as a function of momenta [52]. From this they plot the EDCS in figure 2.4 (g) and (h). From these coherence peaks one can find the superconducting gap by fitting this data with the BCS model [51] or by evaluating the energy position of the peaks verses the Fermi energy. For this example, the gap was found to be 15 meV [46].

Based on these two methods, it is apparent that trying to measure the superconducting gap is often quite difficult. Therefore Andreev Reflection Spectroscopy, see chapter 4, is a much easier technique to measure not only the superconducting gap but also the spin polarization of a metal.

2.3 Meissner Effect and Ginzburg-Landau Theory

There are two electrodynamical properties that govern superconductivity. In 1935, F. and H. London proposed the London equations [53]

$$\mathbf{E} = \frac{\partial}{\partial t}(\Lambda \mathbf{J}_s), \tag{2.8}$$

and

$$\mathbf{h} = -c\ \nabla \times (\Lambda \mathbf{J}_s)\ , \tag{2.9}$$

where

$$\Lambda = \frac{4\pi\lambda^2}{c^2} = \frac{m}{n_s e^2} \tag{2.10}$$

where Λ is a phenomenological parameter, $\mathbf{E}$ is the electric field applied, $\mathbf{J}_s$ is the total super-current, n_s is the number density of superconducting electrons, $\mathbf{h}$ is the flux density on a microscopic scale, m is the mass of the electrons, and e is the charge of the electron.

The equation 2.9 describes perfect conductivity since the superconducting electrons will be accelerated by any electric field as described by Ohm's law. The equation

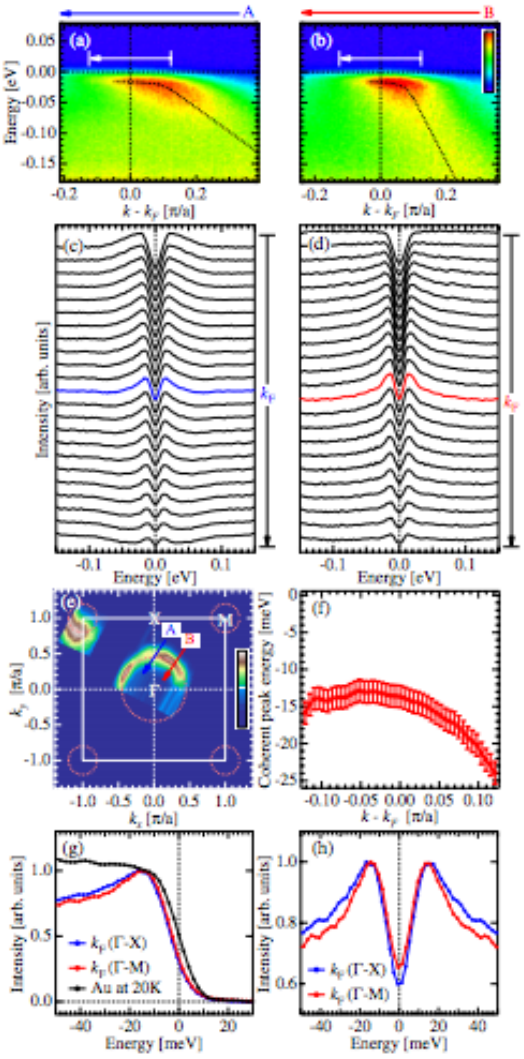

Figure 2.4: The superconducting gap along the high symmetry directions ($T = 20K$). (a),(b) ARPES intensity map along the $\Gamma - X$ and $\Gamma - M$ directions, respectively [directions shown in panel (e)]. Black dotted lines are a guide to the eye, outlining the dispersion of the band and the coherent peak. (c), (d) EDCs for panels (a) and (b), respectively. The momentum range is indicated by the white arrows in panels (a) and (b). The colored curves mark the EDC at k_F. (e) ARPES intensity map as a function of k_x and k_y momentum, integrated within 20 meV about the Fermi energy. Dotted circles are guides to the eye. (f) Dispersion of the coherent peak showing the back bending characteristic of the SC state obtained by EDC fits to data in panel (b). (g) Comparison of the EDCs in superconducting state at k_F points along $\Gamma - X$ and $\Gamma - M$ directions. (h) Symmetrized EDCs from the data in panel (g) [43].

2.10, when combined with Maxwell's equation $\nabla \times \mathbf{h} = \frac{4\pi \mathbf{J}}{c}$, yields the equation

$$\nabla^2 \mathbf{h} = \frac{\mathbf{h}}{\lambda^2} \ . \tag{2.11}$$

From equation 2.11, it can be shown that the magnetic field is screened from the interior of a sample with penetration depth λ. This is known as the Meissner effect [54]. The temperature dependence of this penetration depth is found to be

$$\lambda(T) \approx \lambda(0) \left[1 - (\frac{T}{T_c})^4\right]^{-\frac{1}{2}} \ . \tag{2.12}$$

Meissner later states that, not only is a magnetic field excluded from penetrating a superconductor, but a field is originally expelled as the temperature is cooled past T_c, for a normal metal. Figure 2.5 is a schematic diagram of this process. This implies that there is a reversible Meissner effect in which superconductivity can be destroyed by a critical magnetic field H_c described by

$$H_c(T) \approx H_c(0)[1 - (\frac{T}{T_c})^2]. \tag{2.13}$$

Next, the Ginzburg-Landau theory, which mathematically describes superconductivity [55], was proposed. It states that the free energy F of a superconductor near the phase transition is expressible by a complete order parameter ψ. This parameter is nonzero below the phase transition and is related to the density of the superconducting component. The free energy is described by

$$F = F_n = \alpha|\psi|^2 + \frac{\beta}{2}|\psi|^4 + \frac{1}{2m}|(-i\hbar\nabla - 2e\mathbf{A})\psi| \ , \tag{2.14}$$

where F_n is the free energy in the normal phase, α and β are phenomenological parameters, m is effective mass, e is the electron charge, $\mathbf{A}$ is the magnetic vector potential, and $B = \nabla \times \mathbf{A}$ is the magnetic field. From equation 2.14, by minimizing the free energy, one can get the Ginzburg-Landau equations:

$$\alpha\psi + \beta|\psi|^2\psi + \frac{1}{2m}(-i\hbar\nabla - 2e\mathbf{A})^2\psi = 0, \tag{2.15}$$

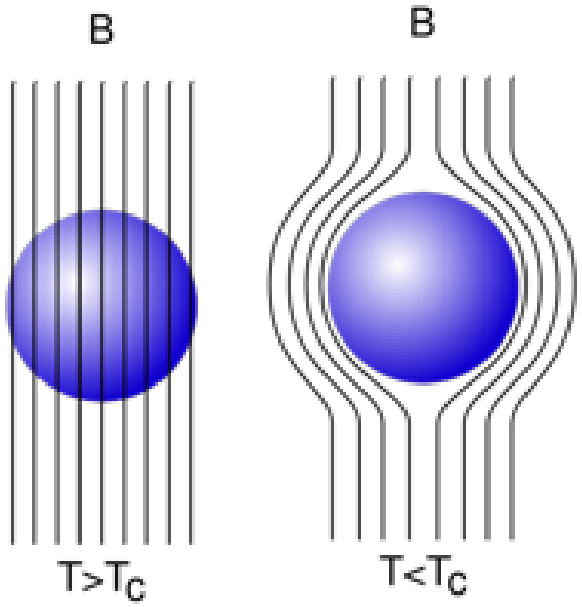

Figure 2.5: Schematic diagram of exclusion of magnetic flux from interior of massive superconductor. λ is the penetration depth, typically only 500 Å [42].

and

$$\nabla \times \mathbf{B} = \mu_0 \mathbf{j} \ ; \ \mathbf{j} = \frac{2e}{m} Re[\psi^*(-i\hbar\nabla - 2e\mathbf{A}]\psi \ , \tag{2.16}$$

where $\mathbf{j}$ is the dissipation-less electric current density and Re is the real part. The first equation describes the order parameter ψ while the second describes the superconducting current. For a homogeneous superconductor equation 2.15 becomes,

$$\alpha\psi + \beta|\psi|^2\psi = 0 \ , \tag{2.17}$$

with the solution $\psi = 0$. This shows that for temperatures above T_c there is no superconductivity. The second non-trivial solution to equation 2.15 is,

$$|\psi|^2 = -\frac{\alpha}{\beta} = -\frac{\alpha_0(T - T_c)}{\beta} \ , \tag{2.18}$$

which shows that below T_c there is superconductivity. From these equations Ginzburg and Landau were able to predict the characteristic length ξ of the superconductor. At temperatures below T_c the superconductor has a length $\xi_0 = a\hbar\nu_F/kT_c$. In this equation a is the numerical constant of order unity, ν_F is the Fermi velocity, and k is Boltzmann's constant.

Based on the Meissner effect, there are two types of superconductors called type I and type II superconductors. Type I superconductors are when superconductivity can be abruptly destroyed when an applied magnetic field surpasses H_c by a first order phase transition, shown in figure 2.6(a) as a function of temperature. This work will focus *solely* on the use of type I superconductors. Type II superconductors exhibit not one, but two H_c's. The first is when the magnetic flux vortices penetrate the material but it stays superconductive. When these vortices become to large the second H_c occurs and superconductivity is destroyed shown in figure 2.6(b) as a function of temperature.

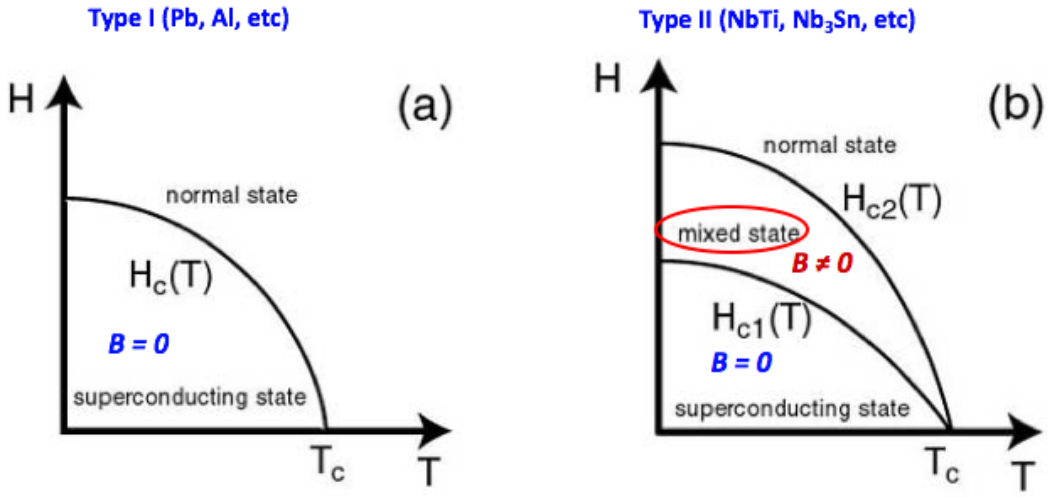

Figure 2.6: Magnetic field H verses temperature T of (a) type 1 superconductors where the Meisnner effect occurs when $H < H_c$ and $H_c = 0.1$ Tesla and (b) type II superconductors with two critical fields where the Meisnner effect occurs as $H < H_{c1}$ with a mixed state at $H_{c1} < H < H_{c2}$ where $H_{c2}(0)$ is very large.

One can now compare the penetration depth λ with the superconducting coherence length. For type I superconductors, λ relative to ξ is $0 < \frac{\lambda}{\xi} < \frac{1}{\sqrt{2}}$ and for type II superconductors, its $\frac{\lambda}{\xi} > \frac{1}{\sqrt{2}}$. These equations govern whether the superconductor is type I or type II.

2.4 Bardeen-Cooper-Schrieffer Theory

To understand the behavior of the superconductor in Andreev Reflection Spectroscopy (ARS), see chapter 4, the BCS theory is needed. In 1957, two papers were written to describe the mechanism of superconductivity and were later awarded the Nobel Prize in 1972 [56, 57]. In this theory, Cooper pairs are essential to superconductivity and must be dominant over the Coulomb force of the interacting electrons. A Cooper pair is described as a weak electron-to-electron bound pair created with a photon interaction. In the material, the Coulomb attraction between the electron and the positive cores of the ions in the material will yield a net positive charge. This, in turn, attracts an electron with opposite momentum and spin creating a Cooper pair. Cooper postulated that, due to the Fermi statics of the electron, the pair state can have energies less then the Fermi energy of the material and consequentially, at low temperatures, the pairs can easily form.

2.4.1 BCS at the Ground State

To satisfy this temperature requirement, they first started with the zero-momentum wave function for two electrons interacting with the Cooper force with a Fermi sea, at T=0:

$$\Psi(\mathbf{r}_0, \mathbf{r}_1) = \sum_k g_k e^{i\mathbf{k}\cdot(\mathbf{r}_1 - \mathbf{r}_2)} \left(|\uparrow\downarrow\rangle - |\downarrow\uparrow\rangle\right) \ , \tag{2.19}$$

where Ψ is the wave fiction as a function of the electron positions, g_k is a perturbation constant and k is the wave vector. Also, noting that anti-symmetry perturbation

states are $g_k = g_{-k}$, using the Schrodinger equation $H\Psi = E\Psi$, one gets the following condition:

$$(E - 2\epsilon_k)g_k = \sum_{k'>k_F} V_{kk'} g_{k'} \ , \tag{2.20}$$

where E is the total energy, ϵ_F is the Fermi energy and ω_c is the cut off frequency. These equations show that only interactions in the material's frequency range are allowed. One can then define $V_{kk'}$ using the mean field approximation:

$$V_{kk'} = \begin{cases} -V, & \text{for } \epsilon_F < \epsilon_k < \epsilon_F + \hbar\omega_c \\ 0, & \text{otherwise.} \end{cases} \tag{2.21}$$

Equation 2.21 can then be inserted into equation 2.20 and will become,

$$\frac{1}{V} = \sum_{k>k_F} \frac{1}{2\epsilon_k - E} = \frac{N_0}{2} \ln\left(\frac{2\epsilon_F - E + 2\hbar\omega_c}{2\epsilon_F - E}\right) \ , \tag{2.22}$$

which becomes the following when simplified:

$$\frac{1}{2\hbar\omega_c}(2\epsilon_F - E) = \frac{1}{e^{\frac{2}{N_0 V}} - 1} \approx e^{-\frac{2}{N_0 V}} \ , \tag{2.23}$$

where N_0 is a constant. Then assuming that $N_0 V \ll 1$, the energy need to create a cooper pair becomes,

$$E = 2\epsilon_F - 2\hbar\omega_c e^{-\frac{2}{N_0 V}} < 2\epsilon_F \ , \tag{2.24}$$

as was stated in section 2.2. So by using the BCS model, the temperature dependence of type I superconductors can be found as shown in figure 2.2.

2.4.2 BCS solution by Variational Method

The main use of the BCS theory is to provide a model for the temperature dependence on the superconducting gap Δ. The results of the following experiments done in this thesis will be fitted using this method and therefore it is crucial to understand this relationship. For the BCS variational form, the ground state is

$$|\gamma_0\rangle = \Pi_{\mathbf{k}=\mathbf{k}_1,\ldots\mathbf{k}_M}(u_{\mathbf{k}} + \nu_{\mathbf{k}} c^*_{\mathbf{k}\uparrow} c^*_{\mathbf{k}\downarrow}) \, |\gamma_0\rangle \ . \tag{2.25}$$

The next step is to use the the paring Hamiltonian at the ground state so that the coefficients can be determined:

$$H = \sum_{\mathbf{k}\sigma} \epsilon_{\mathbf{k}} c^*_{\mathbf{k}\sigma} c_{\mathbf{k}\sigma} + \sum_{\mathbf{kl}} V_{\mathbf{kl}} c^*_{\mathbf{k}\uparrow} c^*_{-\mathbf{k}\downarrow} c_{-\mathbf{l}\downarrow} c_{\mathbf{l}\uparrow} \ , \tag{2.26}$$

where k is the momentum, σ is the spin, and c and c^* are the Fermion creation and annihilation operators, which follow the usual commutation relations. To regulate the mean number of particles, the term $-\mu N_{op}$, where μ is the chemical potential and N_{op} is the particle number operator, is added. Using this term, the expectation value of the ground state $|\psi_G\rangle$ can be minimized to,

$$\delta \langle \psi_G | \, H - \mu N_{op} \, | \psi_G \rangle = 0 \ , \tag{2.27}$$

where the expectation value of $-\mu N_{op}$ is the same as taking the expectation value of kinetic energy. Therefore equation 2.27 simply becomes

$$\delta \langle \psi_G | \sum_{\mathbf{k}\sigma} \xi_{\mathbf{k}} c^*_{\mathbf{k}\sigma} c_{\mathbf{k}\sigma} + \sum_{\mathbf{kl}} c^*_{\mathbf{k}\uparrow} c^*_{-\mathbf{k}\downarrow} c_{-\mathbf{l}\downarrow} c_{\mathbf{l}\uparrow} \, | \psi_G \rangle = 0 \ . \tag{2.28}$$

It is important to note that $\xi_{\mathbf{k}} = \epsilon_{\mathbf{k}} - \mu$ is the single particle energy relative to the Fermi energy. So the first term of equation 2.28 is the kinetic energy of the electrons and the second term is the translation of the phonon mediated electron-electron interaction.

Since each term in equation 2.28 is bi-linear corresponding to the electrons in the Cooper pair, it can be described with,

$$\langle \psi_G | \, H - \mu N_{op} \, | \psi_G \rangle = 2 \sum_{\mathbf{k}} \xi_{\mathbf{k}} \nu^2_{\mathbf{k}} + \sum_{\mathbf{kl}} V_{\mathbf{kl}} u_{\mathbf{k}} \nu_{\mathbf{k}} u_{\mathbf{l}} \nu_{\mathbf{l}} \ , \tag{2.29}$$

where $|u_{\mathrm{k}}|^2 + |\nu_{\mathbf{k}}|^2 = 1$ must be true. Therefore one gets $u_k = \sin\theta_{\mathbf{k}}$ and $\nu_{\mathbf{k}} = \cos\theta_{\mathbf{k}}$. This results in the gap being defined as,

$$\Delta_{\mathbf{k}} = -\frac{1}{2} \sum_{\mathbf{l}} V_{\mathbf{kl}} \ \sin 2\theta_{\mathbf{l}} = -1 \frac{1}{2} \sum_{\mathbf{l}} \frac{\Delta_{\mathbf{l}}}{(\Delta^2_{\mathbf{l}} + \xi^2_{\mathbf{l}})^{\frac{1}{2}}} V_{\mathbf{kl}} \ , \tag{2.30}$$

for $|\xi_{\mathbf{k}}| < \hbar\omega_c$ and zero else where.

Next the summation can be replaced with an integration from $-\hbar\omega_c$ to $\hbar\omega_c$ and, using the symmetry of $-\xi$ and ξ, one gets the final solution of the gap to be,

$$\Delta = \frac{\hbar\omega_c}{\sinh[1/N(0)V]} \approx 2\hbar\omega_c e^{-1/N(0)V} \ . \tag{2.31}$$

2.4.3 BCS Solution by Canonical Transformation

In the normal state, no cooper pairs are expected to pair, therefore the operator $c_{\mathbf{k}\uparrow}c_{-\mathbf{k}\downarrow}$ should average to zero. This then defines the term $b_{\mathbf{k}}$ as,

$$b_{\mathbf{k}} = \langle c_{\mathbf{k}\uparrow}c_{-\mathbf{k}\downarrow}\rangle \ , \tag{2.32}$$

where the energy gap can then be defined as,

$$\Delta_{\mathbf{k}} = -\sum_{\mathbf{k}'} V_{\mathbf{k}\mathbf{k}'}b_{\mathbf{k}'} \ . \tag{2.33}$$

Since the characteristic BCS pair interaction Hamiltonian will give the ground state, there is some phase-coherent superposition of many-body states. Because of this, the operators $c_{-\mathrm{k}\downarrow}c_{\mathbf{k}\uparrow}$ will have a nonzero expectation value rather then averaging to zero. Because the number of particles involved is rather large, the fluctuations should be small and thus one can write the expression with a correction factor,

$$c_{-\mathbf{k}\downarrow}c_{\mathbf{k}\uparrow} = b_{\mathbf{k}} + (c_{-\mathbf{k}\downarrow}c_{\mathbf{k}\uparrow} - b_{\mathbf{k}}) \ , \tag{2.34}$$

giving the modified Hamiltonian called the model-Hamiltonian, in terms of $\Delta_{\mathbf{k}}$:

$$H_M = \sum_{\mathbf{k}\sigma} \xi_{\mathbf{k}} c^*_{\mathbf{k}\sigma}c_{\mathbf{k}\sigma} - \sum_{\mathbf{k}} V_{\mathbf{k}\mathbf{l}}(c^*_{\mathbf{k}\uparrow}c^*_{-\mathbf{k}\downarrow}b_{\mathrm{l}} + b^*_{\mathbf{l}}c_{-\mathbf{l}\downarrow}c_{\mathrm{l}\uparrow} - b^*_{\mathbf{k}}b_{\mathbf{l}}) \ , \tag{2.35}$$

where

$$b_{\mathbf{k}} = \langle c_{-\mathbf{k}\downarrow}c_{\mathbf{k}\uparrow}\rangle_{av} \ . \tag{2.36}$$

Now that the gap can be defined, the gap dependence on temperature can be investigated. Since each term in equation 2.36 is bi-linear corresponding to the electrons in the Cooper pair, the Hamiltonian can be diagonalized by a linear transformation with new Fermi operators $\gamma_{\mathbf{k}}$. The transformation is,

$$c_{\mathbf{k}\uparrow} = u^*_{\mathbf{k}}\gamma_{\mathbf{k}0} + \nu_{\mathbf{k}}\gamma^*_{\mathbf{k}1} \tag{2.37}$$

$$c^*_{-\mathbf{k}\downarrow} = -\nu^*_{\mathbf{k}}\gamma_{\mathbf{k}0} + u_{\mathbf{k}}\gamma^*_{\mathbf{k}1} \ , \tag{2.38}$$

where the numerical coefficients $u_{\mathbf{k}}$ and $\nu_{\mathbf{k}}$ follow $|u_{\mathbf{k}}|^2 + |\nu_{\mathbf{k}}|^2 = 1$. The operator $\gamma^*_{\mathbf{k}1}$ is such that $\gamma_{\mathbf{k}1}$ itself decreases the system's momentum -$\mathbf{k}$ by the complex conjugate which increases it by $\mathbf{k}$. Equation 2.33 now has all the correct formulation and can be written as,

$$\Delta_{\mathbf{k}} = -\sum_{\mathbf{k}'} V_{\mathbf{k}\mathbf{k}'} u^*_{\mathrm{k}} \nu_{\mathbf{k}'} \left\langle 1 - \gamma^*_{\mathbf{k}'0}\gamma_{\mathbf{k}'0} - \gamma^*_{\mathbf{k}'1}\gamma_{\mathbf{k}'1} \right\rangle \ . \tag{2.39}$$

If one further defines $\gamma^*_{\mathbf{k}0}\gamma_{\mathbf{k}0} = \delta(\mathbf{k}-\mathbf{k}') = \gamma^*_{\mathbf{k}1}\gamma_{\mathbf{k}1}$ and note that the probability of the quasi-particle excitation is the normal Fermi function $f(E_{\mathbf{k}}) = (e^{\beta E_{\mathbf{k}}} + 1)^{-1}$, the equation 2.39 can be written as,

$$\Delta_{\mathbf{k}} = -\sum_{\mathbf{k}'} V_{\mathbf{k}\mathbf{k}'} u^*_{\mathrm{k}} \nu_{\mathbf{k}'} [1 - 2(f(E_{\mathbf{k}'})] \ , \tag{2.40}$$

which then becomes,

$$\Delta_{\mathbf{k}} = -\sum_{\mathbf{l}} V_{\mathbf{k}\mathbf{l}} \frac{\Delta_{\mathbf{l}}}{2E_{\mathbf{l}}} \tanh \frac{\beta E_{\mathbf{l}}}{2} \ . \tag{2.41}$$

Using the BCS approximation that $V_{\mathbf{k}\mathbf{l}} = -V$, where $\Delta_{\mathbf{k}} = \Delta_{\mathbf{l}} = \Delta$, one can finally write the self consistency condition equation 2.41 as,

$$\frac{1}{V} = \frac{1}{2}\sum_{\mathbf{k}} \frac{\tanh(\beta E_{\mathbf{k}}/2)}{E_{\mathbf{k}}} \ , \tag{2.42}$$

where this equation will determine the temperature dependence.

Just as was done in the variational method, the summation can now be replaced with an integral from $-\hbar\omega_c$ to $\hbar\omega_c$ and noting the symmetry of $|\xi_{\mathbf{k}}|$ then kT_c becomes

$$kT_c = \beta_c^{-1} = 1.13\hbar\omega_c e^{-1/N(0)V} \ , \tag{2.43}$$

and comparing it with equation 2.42 one can see that the gap at $T = 0$ is indeed comparable in energy to kT_c, which has been tested and found to be reliable:

$$\frac{\Delta(0)}{kT_c} = \frac{2}{1.13} = 1.764 \ . \tag{2.44}$$

2.4.4 Temperature and Energy Gap

Using equation 2.42 or the integral equivalent,

$$\frac{1}{N(0)V} = \int_0^{\hbar\omega_c} \frac{\tanh \frac{1}{2}\beta(\xi^2 + \Delta^2)^{\frac{1}{2}}}{(\xi^2 + \Delta^2)^{\frac{1}{2}}} d\xi \ , \tag{2.45}$$

the gap dependence of T, $\Delta(T)$ can be computed numerically. From equation 2.45, when describing weak coupling superconductors, $\hbar\omega_c/kT_c \gg 1$, $\Delta(T)/\Delta(0)$ is a universal function of T/T_c which monotonically decreases from 1 to zero from $T = 0$ to $T = T_c$. Near $T = 0$ the temperate is exponentially slow and is virtually insensitive to T. This means that the Δ is fairly constant until a significant number of quasiparticles are excited, in which, near T_c, $\Delta(T)$ goes to zero and is described by the tangent. It is approximated to be:

$$\frac{\Delta(T)}{\Delta(0)} \approx 1.74(1 - \frac{T}{T_c})^{\frac{1}{2}} \ ; T \approx T_c \ . \tag{2.46}$$

All of these features are shown in figure 2.2 [58], and this is the approximation used to fit experimental data including figure 2.7 as well as all the data in this thesis.

In figure 2.7(a) it is apparent the conventional superconductors follow very nicely with the BCS approximation. However for unconventional superconductors, such as Aluminum in figure 2.7(b), the BCS approximation may not fit the data as expected.

2.5 Conventional verses Unconventional Superconductors

Just as was stated in section 2.3, there are two types of superconductors, type I conventional and type II unconventional. There are three types of pairing states in superconductors, s-wave, p-wave, and d-wave pairing shown in figure 2.8.

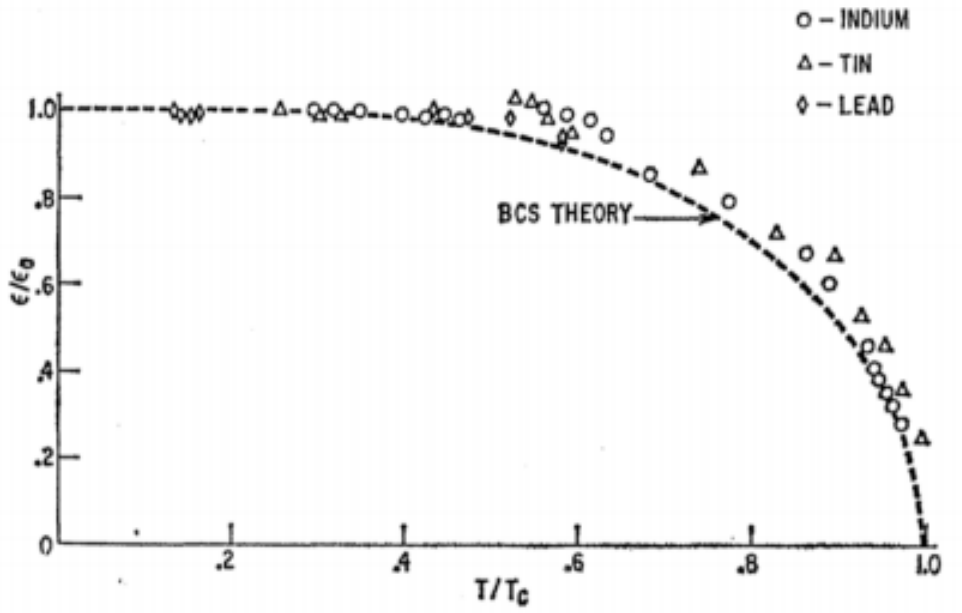

(a) Conventional superconductors

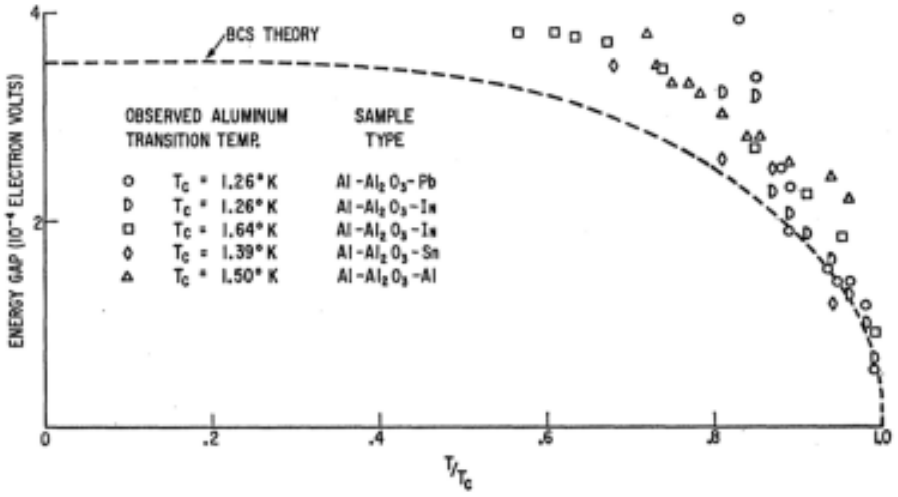

(b) Aluminum

Figure 2.7: Indication that the energy gap is temperature dependent [58]. (a) Indium, tin and lead may then be considered conventional superconductors because their properties may be predicted by BCS theory. (b) Aluminum deviates from the predictions of BCS, and therefore it is not considered a conventional superconductor.

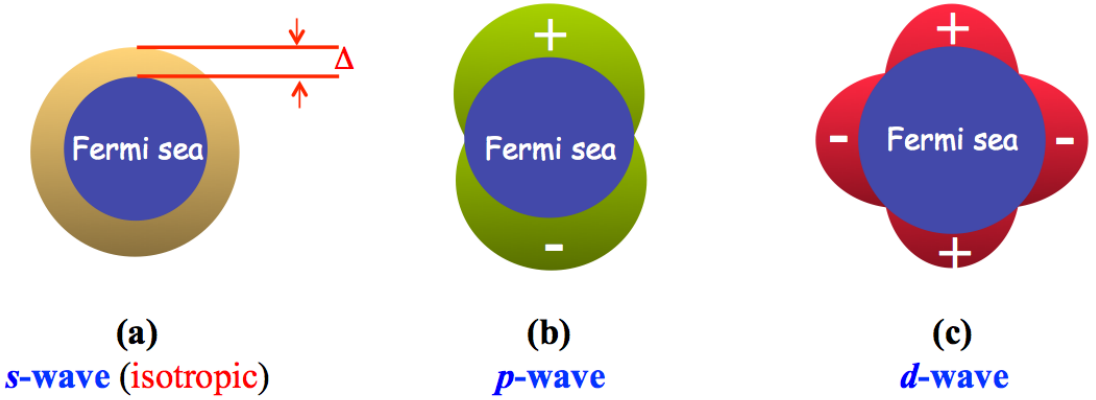

Figure 2.8: The mechanism of superconductivity depends on the superconducting gap. (a) S-wave superconductors have an isotropic gap. Most known superconductors are s-wave superconductors, such as Nb, Pb, and Al, with $T_c < 25K$. (b) P-wave gap with the most well known example super fluid ^{3}He, often with $T_c \approx 1$ mK $-$ 1 K. (c) D-wave gap most often found in cuprates, with CuO_2 plane, or insulating parent compounds and $T_c \approx 5$ K $-$ 140 K. $+$ denotes area with positive momenta $+\mathbf{k}$ and $-$ denotes area with with negative momenta $-\mathbf{k}$.

Figure 2.8(a) illustrates s-wave pairing, which is characterized by the standard BCS model. In s-wave pairing, the two electrons of a Cooper pair have equal and opposite momenta, $\mathbf{k}$, so that the center of mass momentum is zero. This is also known as singlet pairing. The bound states are symmetric and isotropic. The attractive interaction between the two electrons yields a negative energy contribution, which lowers the total energy of the system and thus creates a negative potential energy called the binding energy.

In figure 2.8(c) there is d-wave pairing which is present in high T_c superconductors. For d-wave pairing, the bound state can happen with any attractive force that can overcome the Coulomb repulsion between two electrons. For example, an electron-electron interaction is created by a magnetic spin fluctuation [59–61] which can overcome the this force. The most important distinction is that, unlike s-wave, d-wave pairing is anisotropic, which is described by spin-fluctuation exchange mechanism.

In vary rare case,s a material can exhibit p-wave pairing as shown in figure 2.8(b). With p-wave pairing the electrons may have equal and parallel direction momenta. Therefore, the electrons can either pair with both spin up or both spin down directions, which is referred to as triplet superconductivity. For the purposes of the following work, only the singlet and triplet states are of crucial importance. Referring to the equation for spin polarization, equation 2.1, for a singlet superconductor in contact with a normal metal, see chapter 4, the electrons can have equal and opposite spin to its partner thus creating a nonzero polarization. For a triplet superconductor the spins must have equal spin orientation and direction, be all up or all down spins, such that, when it is in contact with a normal metal, the spin polarization will always yield 0. This characteristic makes it very easy to distinguish the superconductor being measured, where often the material created by a collaborator, is a single or triplet superconductor. See chapter 9 for an example.

Chapter 3

MAGNETIC NANOSTRUCTURES

Today's electronics are becoming smaller and smaller so the need for nanoscale devices such as as MRAM, read heads in hard drives, and spin valves to become increasingly smaller is important. When decreasing the size of these devices, it is crucial to preserve the higher performance speeds and non-volatility. The advantage of nanostructures is that they can take advantage of quantum effects that larger scale devices cannot, such as spin manipulation for spintronics. Magnetic nanostructures add an extra degree of freedom in which the structures can be manipulated and tuned by a permanent or electromagnet. One such effect is the magnetoresistance (MR), which can have very large effects on the resistance at zero magnetic field. There are many different types of MR, however, the giant magnetoresistance (GMR) effect is often considered to be one of the most important. Spin valves used in today's MRAM devices utilize this GMR effect. With this effect, the density of magnetic storage in these devices has substantially increased in the last two decades. GMR nanostructures have been a key component to this field since Parkins found a 60% increase in the GMR response at room temperature as well as an increase of 120% at temperatures around 4 K [62]. Another major advancement has been the recent work with spin-transfer torque (STT), which is the effect in which the orientation of the magnetic layer in a tunnel junction or spin valve can be changed using a spin-polarized current. This is a new way to manipulate the spin properties of the magnet to change the properties of the second layer, and thus one can orient the spin in the desired direction. This is one component to the MRAM devices and it works in conjunction with the spin valve and STT effect. This chapter will describe the different types of

magnetic nanostructures and the different magnetoresistance effects found in these structures.

3.1 Properties of Magnetic Nanostructures

There are many types of magnetic structures where the sample can be divide into many domains to minimize the total free energy. In the early 1900s, magnetic nanoparticles were studied as a method to make permanent magnets from high coercive magnetic materials [63]. In a two dimensional nanostructure, the structure transitions from three dimensional to two dimensional as the thickness of the film decreases. If the thickness is then decreased from the 2D structures, one can even create a single domain particle with added coercivity, superparamagnetism, anisotropy, and many more interesting magnetic properties.

Magnetic behavior depends on the size of the dimension and in 2D, large domain structures dominate the structural behavior. For a magnetic disk structure, all the spin domains are in the plane of the disk to take advantage of the structures anisotropic properties. If one then creates a nano disk by decreasing the diameter of the device, it will cause the domains to create a vortex. The exchange energy wants to be minimized as much as possible, so this causes only small angle changes in the center of the disk, while the edge particles are free to curl over the edge of the disk.

Because of large changes in the angle of the particles at the center of the disk, the distribution of particles will increase the exchange energy. The structure compensates by allowing the spins to gradually turn out of the plane creating a vortex. The behavior of this vortex is determined by the saturation magnetization and exchange stiffness in the nanostructure. Figure 3.1 shows these vortices and shows how the spins turn out of the plane. There can be two different types of vortices, figure 3.1(a) and (b), where one is curled clockwise and the other counter clockwise. When the

vertex is created, a vertical current, which induces a circular field, can switch the directions of the vortexes, which is called the helicity [64]. MRAM devices use this unique property to write data to the device. Even more interestingly, when the vortex is removed, one can create a magnetic nanoring which is shown in 3.1(c) and (d).

This nanoring has less straying fields and has an annular structure which is unique in that whether the helicity of the ring is switched by the current or by the STT effect, only the density of the current will affect the device making it able to use much less current. Less current yields less disturbance and thermal instability in the writing of the memory.

3.2 Ordinary Magnetoresistance

In nonmagnetic metals, the ordinary magnetoresistance (OMR) effect is very small at low magnetic fields. The cylindrical motion of the electrons in the metal create a positive change in the resistivity, $\Delta\rho$, for both magnetic field parallel ($\Delta\rho_{||}$) and transverse ($\Delta\rho_T$) to the current direction where $\Delta\rho_T > \Delta\rho_{||}$. The parallel magnetoresistance of the magnetic field, H, parallel with the current does not vary much with the magnetic field, however the transverse component changes with the magnetic field. The rule for OMR is that the deviation of resistivity from the zero field resistivity, $\rho_)$, must satisfy the equation:

$$\Delta\rho/\rho_0 = F\left(H/\rho_0\right) \ , \tag{3.1}$$

where F is the function related to the metallic properties of the material.

In OMR, the motion of the electrons is a circular or helical orbit. The ratio of the magnetic field to the resistance relies on the number of times electrons can go around the orbit between collisions with neighboring electrons. The relation is described by

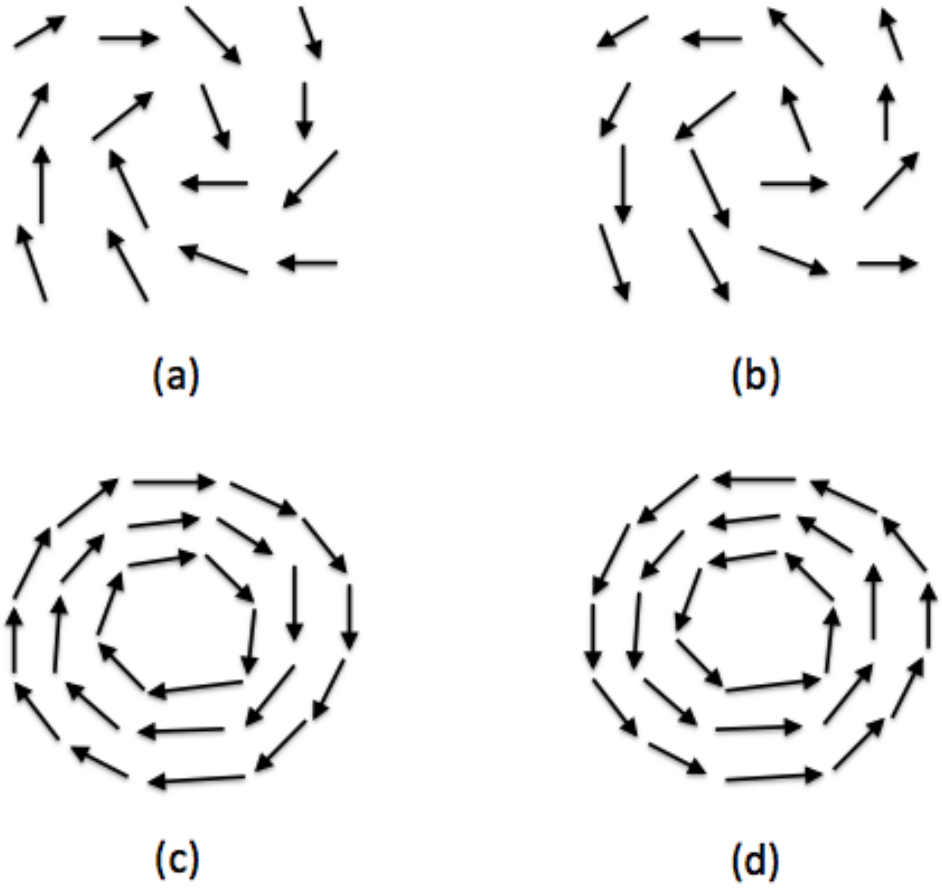

Figure 3.1: Two dimensional magnetic structures: (a) and (b), nanodisk with vortex core, (c) and (d) nanoring.

the Kohler rule:

$$\frac{l}{r} = \frac{H}{\rho_0}\frac{1}{ne} \ , \tag{3.2}$$

where l is the electronic mean free path, r is the orbital radius, n is the number of electrons, and e is the electron charge. From this equation the transverse magnetoresistance behaves in three ways [65]:

i) For metals with close Fermi surfaces, the electrons are constrained by their orbit in k space and as the magnetic field is increase the the cyclotron frequencies also increase. This is typical of In, Al, Na, and Li.

ii) For metals with equal amounts of electrons and holes, the MR increases with H up to high fields, and is independent of the crystallographic orientation. Common metals are Bi, Sb, W, and Mo.

iii) For metal that have open orbits on the Fermi surface, they exhibit large MR effects for fields applied in the crystallographic directions, and will saturate in the other directions as the orbits are closed. Common metals for this behavior are Cu, Ag, Au, Mg, Zn, Cd, Ga, Tl, Sn, Pb, and Pt.

3.3 Anisotropic Magnetoresistance

Anisotropic magnetoresistance (AMR) is a property in which a dependence on the angle between the direction of magnetization is observed in a material. In ferromagnetic metals or alloys the AMR effect is on the order of $\Delta\rho/\rho \approx 2\%$ at low magnetic fields. AMR differs from OMR in that the effect is anisotropic where $\Delta\rho_{||}$ increases with the field, and $\Delta\rho_T$ decreases with the field. In AMR the only dependence is that on the angle $\phi = \psi - \theta$ between the magnetization and current direction. AMR must

follow

$$\rho(\phi) = \rho_T + (\rho_{||} - \rho_T)\cos^2\phi \ . \tag{3.3}$$

The origin of this effect depends on the spin orbit coupling in the material. As the magnetization rotates the electron cloud about the nuclei, deformation will form. This deformation changes the amount of scattering of the conduction electrons when they transverse the lattice. For example it can be due to a larger probability of s-d scattering of electrons in the magnetic field direction, and the net effect is in the electrical resistance which exhibits a maximum when the direction of the current parallel to the applied field.

AMR devices include the measurement of Earth's magnetic field, or for traffic detection, see chapter 11. Honeywell, NXP Semiconductors as well as many other companies utilize this effect in their product designs such as linear position and angle sensing experiments.

3.4 Giant Magnetoresistance

In 1988, two independent groups lead by Albert Fert and Peter Grunberg discovered MR effects of up to 50%, at 4.2 K [3]. This work was carried out on (001)Fe/(001)Cr where the anitferromagnetic coupling between the Fe layers was weakened and lowered the demagnetization field. With an external magnetic field, they were able to produce much higher changes in resistance then AMR so Fert named the effect GMR [3, 66]. In 2007, the Nobel prize was awarded to both Fert and Grunberg for this discovery. Figure 3.2 shows the GMR finding of Fe/Cr super-lattices at 4.2 K.

GMR structures consist of alternating non-magnetic and ferromagnetic conductive layers. Parkin, at IBM, showed that alternating layers of Cu/Co with no insulating barriers were able to produce GMR effects of $\sim 60\%$ at room temperature and as high

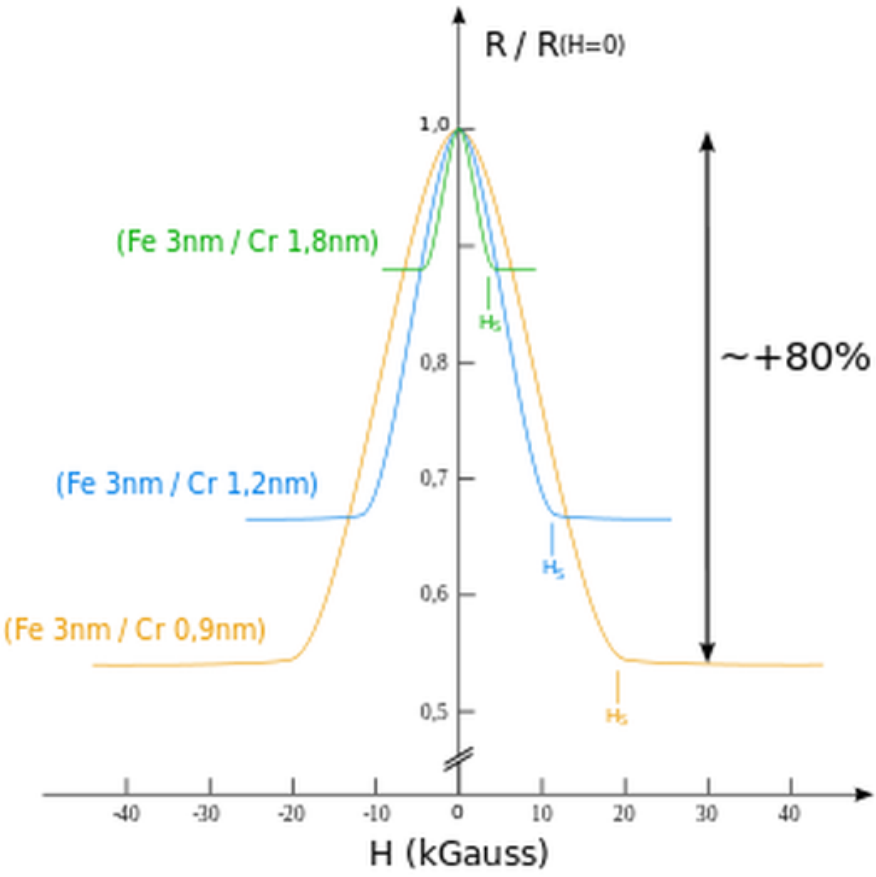

Figure 3.2: Change in resistance of Fe/Cr super lattices at 4.2 K in external magnetic field H. The current and H are parallel to the (110) axis, and the arrow to the rights shows the maximum resistance change where H_s is the saturation field [3, 66].

as $\sim 120\%$ at 4 K [62]. The key to observing the GMR effect lies in the orientation of adjacent ferromagnetic layers. Figure 3.3 shows the two different alignments, antiparallel and parallel. For parallel alignment the resistance is lower and for antiparellel layers the resistance is relatively high. When the electron leaves the first ferromagnetic layer and enters the non magnetic layer, there is an additional scattering process which yields in larger magnetoresistance.

Numerically the GMR percentage is described by:

$$GMR = \frac{R_{\uparrow\downarrow} - R_{\uparrow\uparrow}}{R_{\uparrow\uparrow}} \ , \tag{3.4}$$

where $R_{\uparrow\downarrow}$ is the peak of the resistance at zero field and $R_{\uparrow\uparrow}$ is the saturation or base resistance without being effected by GMR. Figure 3.3 also shows a representative GMR effect with this equation.

To further understand GMR, one an analyzes the electron scattering resistances as a simple circuits composed of resistors. Spin valves demonstrate this analogy and figure 3.4 shows the (a) parallel and (b) antiparallel alignments and the equivalent resistance circuit. Devices which currently utilize the GMR effect include spin-valve sensors, Hard disk drives (MRAM), rectifiers with linear frequency responses, as well as MRAM devices. This work will primarily focus on the GMR effect in Co/Cu multilayer films see chapter 11.

3.5 Colossal Magnetoresistance

Some $LA_xM_xMnO_{3+8}$ perovskite structures have had large MR effects as high as $\Delta R/R(H) = 125,000\%$, named colossal magetoresistance (CMR). If it is normalized to zero field values, this means the resistance can change by 99.9% [67]. The resistivity of these materials undergos a low temperature transition from insulating to metallic characteristics.

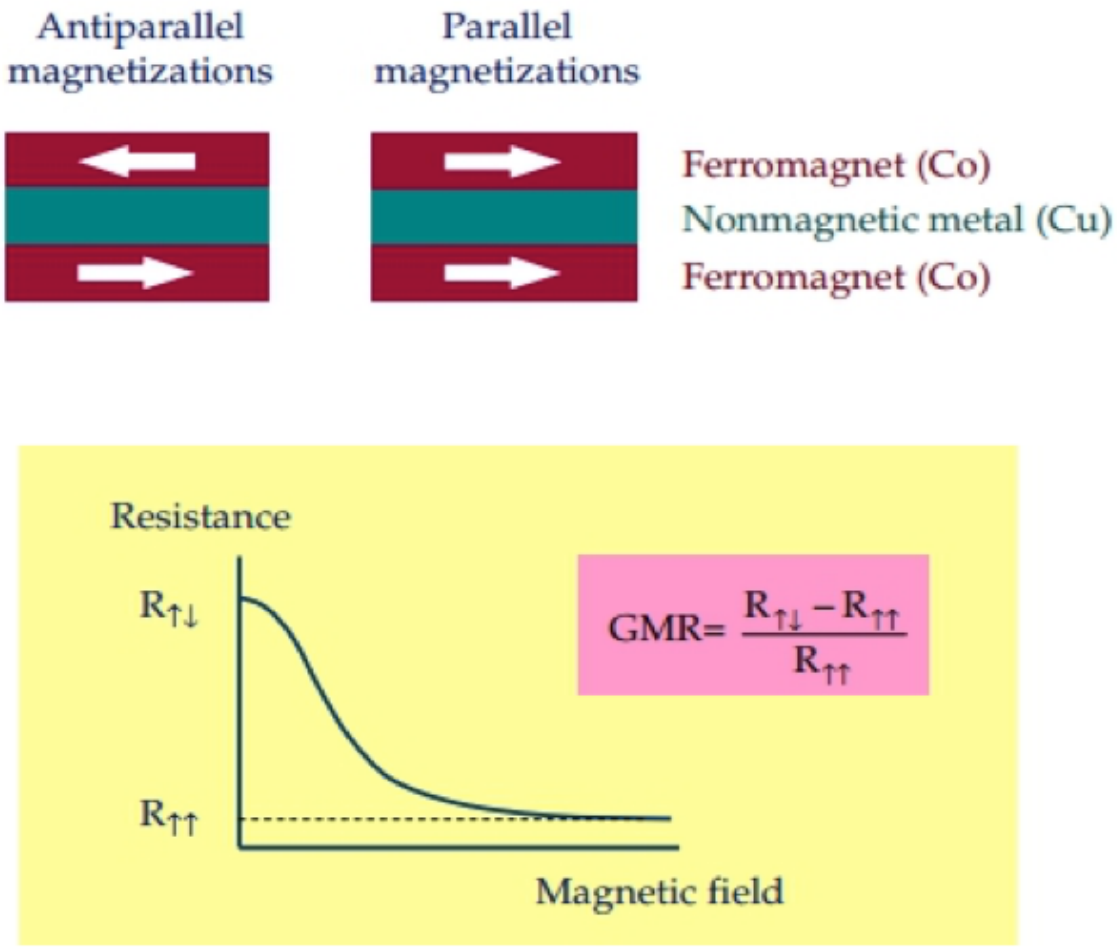

Figure 3.3: Parallel and Antiparallel FM/NM/FM alignments in GMR devices. Representative GMR curve with GMR percentage equation are also shown [62].

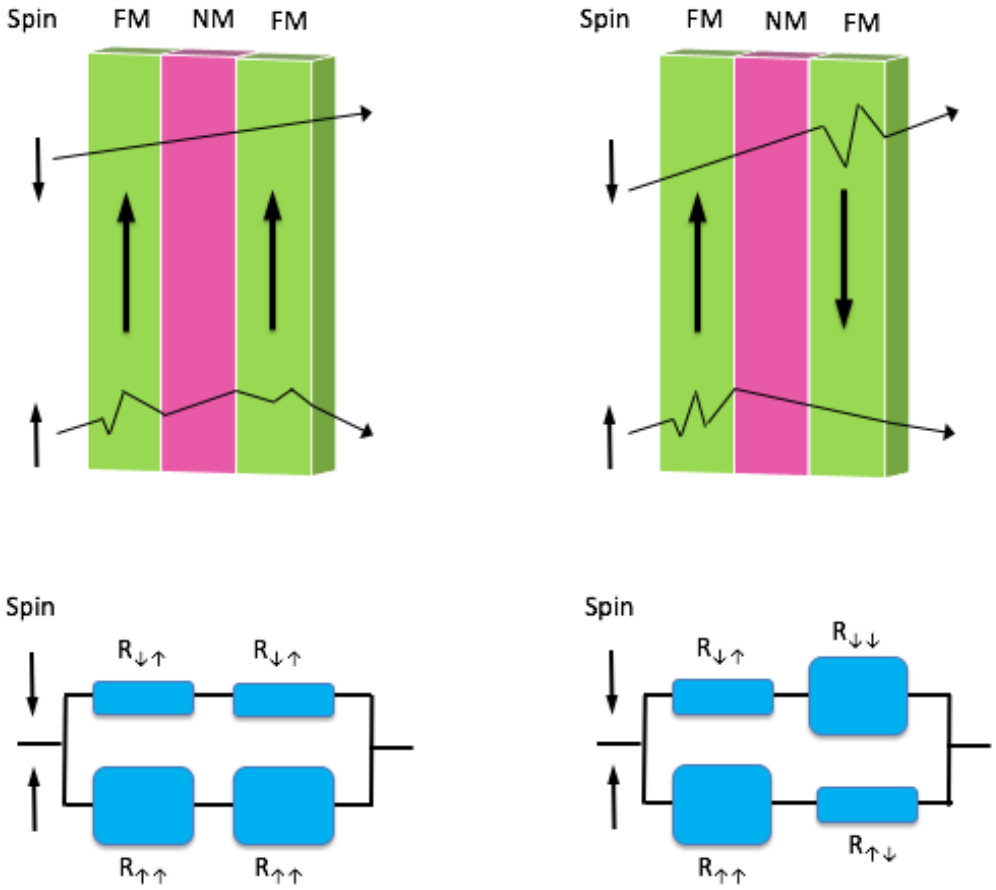

Figure 3.4: Spin valve based on GMR effect. Ferromagnetic layers have arrows indicating the direction of magnetization. For (a) parallel alignment the electrons scatter much less then (b) antiparellel alignment. Corresponding circuit of resistors are shown for (a) parallel alignment and (b) for antiparallel alignment.

HP has designed high quality CMR films at room temperature with a change in resistance of 95%. These results were reported in 1995 by the HP team [65]. There are, however, some disadvantages to these devices, such as the field dependence of the resistance and large magnetic field strengths (on the order of 1 T) which are required to induce CMR.

CMR is induced by a different mechanism then GMR. In CMR materials, conduction occurs by the hoping of the electrons, and not because of the metallic conduction. In GMR magnetic ordering occurs over tens of Angstroms; however, CMR occurs on an atomic scale and is due to an indirect exchange mechanism. The mechanism behind CMR is still hotly debated and much research still needs to be conducted [65].

3.6 Tunneling Magnetoresistance

Tunneling magnetoresistance (TMR) is a quantum effect that occurs when two ferromagnets are separated by a thin insulating layer. The two ferromagnetic layers can change their alignment when a change of the tunneling current is applied to the magnetic tunnel junctions (MTJ). TMR and MTJ utilize the spin-dependent tunneling (SDT) effect which is an imbalance in the electric current carried by up and down spins of the electrons tunneling from the ferromagnet through the insulating film. This effect was discovered by Tedrow and Meservey in 1970 [68].

The TMR effect was first discovered in 1975 by M. Julliere in Fe/Ge-O/Co junctions at 4.2 K with a relative change in resistance of around 14% [69]. The first TMR measurement at room temperature was in 1991 by Terunobu Miyazaki who found a MR response of 2.7% in MTJ of iron separated by amorphous AlO insulators [70]. The first high temperature measurement effect at room temperature was around 70% in Al_20_3. Notably in 2004, Parkin and Yuasa found a TMR effect of 200% in Fe/MgO/Fe MTJs at room temperature [41, 62]. In 2008 an effect of 600% was measured at room

temperature and 110% at 4.2 K in CoFeB/MgO/CoFeB [71]. The main work in this thesis will be on the GMR effect in Co/Cu multilayers in chapter 11.

3.7 Magnetic Random Access Memory

The MRAM was developed in the 1990s as a nonvolatile storage cell, which utilizes large MR effects. RAM devices are used in integrated circuits associated with volatile types of memory that can be lost if power is removed from the system. Present magnetic storage devices include tapes and hard disks, which write data on a rapidly rotating disk coated with magnetic material. Once the data is written it is read sequentially from the same disk.

MRAM is formed from two ferromagnetic plates separated by a thin film insulating layer. One of the ferromagnets is a permanent magnet while the other can change magnetization due to an external field in which memory is stored. This is known as the spin valve and is the simplest magnetic structured for MRAM cells. The simplest method of reading this memory is by measuring the electrical resistance of these cells. The sells consist usually of transistors that switch current from a supply line to the ground end of the cell. By applying power to the transistor, a cell is selected and read. The magnetic tunnel effect can then change the resistance by using the orientation of the fields in the two plates. The current is measured, resistance is calculated and from the polarity of the plates either, when the two plates are the same polarity, a "1" is read, or if they are different polarities ,"0" is read.

Memories used today in computers use dynamic random-access memory (DRAM). DRAM stores each bit in a separate cell that can either be charged or discharged corresponding to a "1" or "0" bit. These capacitors suffer from leakage causing longer charging times, slow discharge, and show losses of information of the capacitor if it is not charged periodically. Because DRAM is volatile, MRAM is superior to DRAM

even with all of its issues. The next generation of hard disk will utilize the MRAM to store memory in computers. Figure 3.5 shows one MRAM prototype which uses two current lines to send current to the ferromagnetic plates which then write the memory. The memory is then read by measuring the GMR of the cell. The field induced by each current line is not enough to switch a bit; however, a bit can be switched by the current and induced field from the two currents combined [72]. Other proposed methods are the STT effect and the recently discovered thermal assisted switching (TAS-MRAM) effect which heats up the magnetic tunnel junction during the writing process to keep the junction stable at colder temperatures. This work will not go into detail of the MRAM device, however it will use the same GMR measurements to characterize other materials.

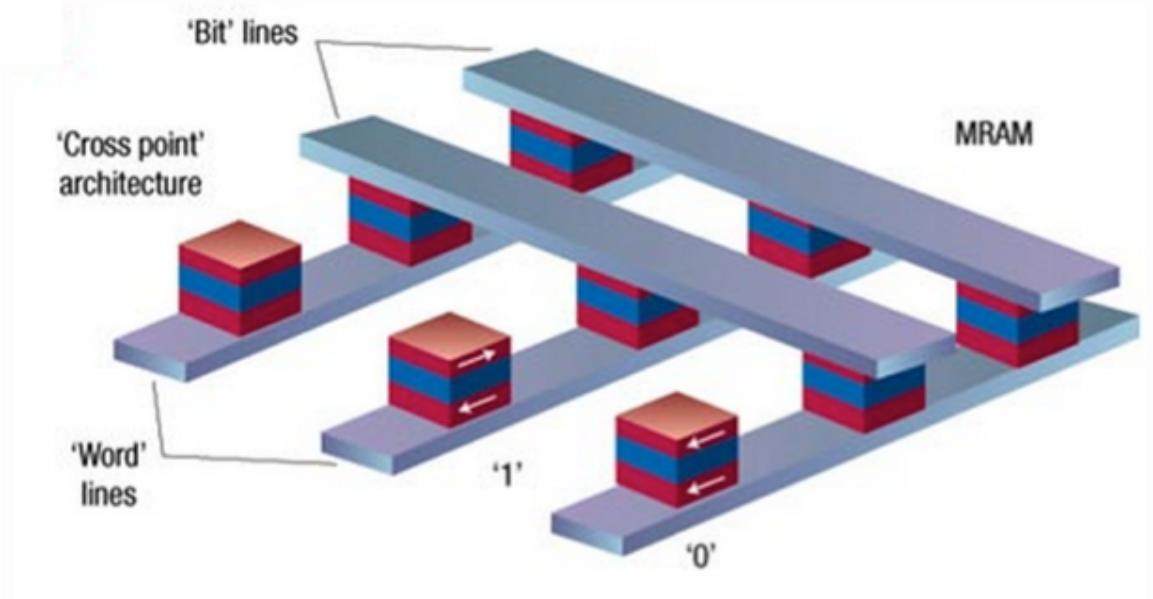

Figure 3.5: Prototype of MRAM device [72].

Chapter 4

ANDREEV REFLECTION SPECTROSCOPY

4.1 Point Contact Spectroscopy

To understand the electronic properties of metals and superconductors, it is important to understand the behavior of electrons close to the Fermi surface, which are responsible for the transport properties of metals. There have been many different techniques for finding this information including angle resolved spectroscopy, photoelectron spectroscopy, optical spectroscopy, and tunneling spectroscopy. This thesis will focus on point contact spectroscopy (PCS) or point contact Andreev reflection spectroscopy (PCAR), which deals specifically with N/S interfaces. Ohm's law states that the applied voltage is linearly proportional to the current flowing in a metal, however, at a point contact, the current voltage characteristic shows deviation from this law. This occurs when the contact size is comparable or less than the electron mean free path of the metal. Electrons in this regime have no scattering but are instead accelerated by the applied voltage and then switch put back to their equilibrium by inelastic collisions with phonons or magnons. It has been shown that the second derivative of the voltage with respect to current d^2V/dI^2 is intimately related to the phonon spectrum of the metals used [73]. Since this discovery, PCS has been used to find the magnon excitations in many metals [16] and in this work to find the spin polarization in ferromagnetic metals. To understand PCS, one must first understand the electron mean free path.

4.1.1 Electron Mean Free Path

The electron mean free path is critical to understanding point contact spectroscopy. In the Drude model, electrons are moving randomly, so the average velocity ν is needed to calculate the mean free path. Each electron will have the velocity $\nu = \nu_0 - e\mathbf{E}t/m$, where ν_0 is the velocity that the electron had after its last collision. The average velocity then becomes:

$$\langle \nu \rangle = \langle \nu_0 \rangle - \frac{e\mathbf{E}\langle t \rangle}{m} = -\frac{e\mathbf{E}\tau}{m} , \tag{4.1}$$

and using $\mathbf{j} = -ne\nu = ne^2\tau E/m$ the conductivity of the metal in the Drude model becomes:

$$\sigma = \frac{ne^2\tau}{m} , \tag{4.2}$$

where n is the conduction electron density, τ is the relaxation time, and e and m are the electron charge and mass. Resistivity ρ is the inverse of conduction therefore equation 4.2 becomes:

$$\rho = \frac{m}{ne^2\tau} = \frac{m\nu_F}{ne^2\tau\nu_F} = \frac{p_F}{ne^2 l_e} , \tag{4.3}$$

where l_e is the mean free path of the electron, and p_F is the Fermi momentum. The mean free path is often in the nanometer range.

4.1.2 Point Contact Resistance

There are two lengths that govern the transport through a metallic point contact. They are the contact size a and the electron mean free path l_e. For these lengths, there are three main regimes that are relevant to PCS. The ballistic regime occurs when $a \ll l_e$, diffusive occurs for $a \gg l_e$, and an intermediate state is anywhere along these two regimes. The contact resistance R_c plays a crucial role and, from it, the contact size can be determined. More information of the resistance in the three different regimes is below.

Ballistic Regime

If the diameter of the point contact a is much smaller then the elastic mean free path l_e, as well as larger then the deBroglie wave length, the contact is in the ballistic regime. In this regime, the electrons statistically do not undergo any scattering in the contact region and, in the precedence of an applied field, they will accelerate and gain energy. Sharvin [74] in 1965—following the lead of Knudsen in 1943 [75] who solved the problem of the flow of a dilute gas through a small hole—was able to find the expression for the contact resistance in the ballistic regime defined by,

$$R_s = \frac{2h}{e^2(ak_f)^2} \ , \tag{4.4}$$

where k_f is the Fermi momentum. This resistance is independent of the bulk resistance and of the purity of the material forming the contact. For a better Sharvin resistance formulation, it is useful to integrate over all possible angles θ and ϕ, which by doing so will correct the resistance by a factor of 4/3:

$$R_{Sharvin} = \frac{4\rho l_e}{3\pi a^2} \ . \tag{4.5}$$

Due to photon or magnon excitation the resistance, shown in figure 4.1, becomes nonlinear and the electrons have a speed of $\Delta\nu = eV/k_F$ where k_F is the Fermi momentum. The current is then changed through the contact by $I = n_0 e\pi a^2(\Delta\nu)$ where n_0 is the free electron density. The contact resistance then becomes

$$R_c = \frac{P_F}{n_0 e^2 \pi a^2} \approx \frac{\rho l_e}{\pi a^2} \ , \tag{4.6}$$

where P_F is the total Fermi momentum and ρ is the resistivity. In the Drude mode there is $\rho = P_F/n_0 e^2 l_e$. For most metals the equation becomes, $\rho l_e \approx 10^{-15} m^2\omega$. It is important to note that even with the 4/3 correction to the Sharvin resistance, the electrons do not behave exactly like an ideal gas, therefore more corrections are

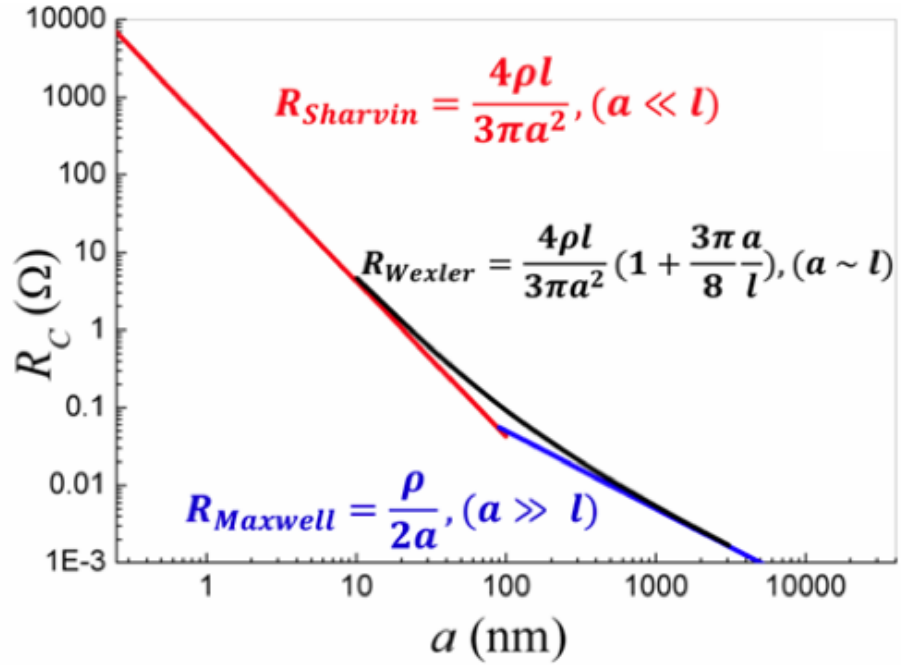

Figure 4.1: Resistance verses the size of the contact a. Point contact is in the diffusive regime with Maxwell resistance when $a \gg 1$, and in the ballistic regime with Sharvin resistance where $a \ll 1$. To preserve spin information, this work use the ballistic regime.

need to be done. When the electron is in an excited state, it can still interact with the crystal lattice and can change the resistance due to the energy absorbed in the inelastic collision by this lattice. Boltzmann has shown that this correction is small, less than 3.6% [76, 77] which can account for this energy absorption. This thesis work will be primarily in the ballistic regime. For PCAR schematics, equipment, and characterization please see section 5.1.

Diffusive Regime

In the diffusive regime, $a \gg l_e$ so that electrons only accelerate within the mean free path and then are elastically scattered. Electrons are able to retain the energy information about inelastic scattering, therefore energy resolved spectroscopy can still be done with a point contact. The scattering causes the current to be linearly proportional to the applied voltage. Maxwell was able to resolve Poisson's equation for potential energy of this system by applying the following boundary condition: [78]:

$$\nabla^2 \phi = 0 \ , \tag{4.7}$$

meaning that the potential energy should have a zero gradient about all applied energies as a function of ϕ. This condition then yields the current flowing in the contact, giving a potential energy of:

$$\phi(r) = \pm \frac{1}{2} eV \left(1 - \frac{2}{\pi} \arctan \frac{1}{\xi} \right) \ , \tag{4.8}$$

where ξ is the potential ellipsoidal surface described by:

$$\frac{1}{a^2 + a^2 \xi^2} + \frac{1}{a^2 \xi^2} = 1 \ . \tag{4.9}$$

The resistance between the the two equipotential surfaces, similar to contact resistance, along the vertical axis of length ξ becomes:

$$R_{\xi} = \frac{\rho}{2\pi a^2} \int_0^{\xi} \frac{d\xi}{a^2 + \xi^2} = \frac{\rho}{2\pi a} \arctan \frac{\xi}{a} \ . \tag{4.10}$$

For distances very far from the contact, the resistance can be simplified to:

$$R_{\xi \to \infty} = \frac{\rho}{4a} \ . \tag{4.11}$$

Finally because there are two contact members, the final resistance is the Maxwell resistance shown in figure 4.1 with the resistance:

$$R_{Maxwell} = \frac{\rho}{2a} \ . \tag{4.12}$$

This resistance is diffusive because it uses Ohm's law $j = \sigma E$ in the calculations. In the purely diffusive regime all energy is dissipated in the contact region, and can cause a temperature increase at the contact. This thesis will deal mainly with the ballistic regime but it is important to understand all three regimes and how they apply to ARS.

4.1.3 Intermediate Regime

The intermediate regime occurs when the contact size is in a state of both ballistic ($l_e \gg a$) and diffusive regimes ($l_e \ll a$). Wexler was able to calculate the resistance of this intermediate regime by solving the Boltzmann equation for a contact using the variational principle [79]. According to this principle the resistance is a linear combination of $R_{Sharvin}$ and $R_{Maxwell}$,

$$R_{Wexler} = \frac{4\rho l}{3\pi a^2} \left[1 + \frac{3\pi}{8} \Gamma \left(\frac{l}{a} \right) \frac{a}{l} \right] \ , \tag{4.13}$$

where $\Gamma(l/a)$ is a slowly varying function with $\Gamma(0) = 1$ and $\Gamma(\infty) = 0.619$ at the two extremes. One can then easily confirm, by taking the limits of the equation, that

this will yield the $R_{Sharvin}$ or $R_{Maxwell}$ using the correct limits in each case. For this regime, the electrons lose momentum information due to elastic scattering but are able to retain energy information due to inelastic scattering.

If the resistivity is in a mixed state of ballistic and diffusive regimes,ρ found in section 4.1.1, the resistance is the Wexler resistance,R_{Wexler}, which can then be simplified to :

$$R_{Wexler} = \frac{116530.12}{n^{2/3} l_e^2} \frac{1}{x^2} \left(1 + \frac{3\pi}{8} x\right) \ , \tag{4.14}$$

where $x = a/l_e$. Further simplifying one gets:

$$R_{Wexler} = 0.0155 n^{2/3} / rho^2 \frac{1}{x^2} \left(1 + \frac{3\pi}{8} x\right) \ . \tag{4.15}$$

The two equations 4.14 and 4.15 can then be used to determine whether the contact in an experiment is indeed in the ballistic regime or not.

4.2 Andreev Reflection Spectroscopy

Andreev reflection has been theoretically proposed to measure the spin polarization of ferromagnetic materials by de Jong [80], and afterwards demonstrated experimentally by two other groups [19–21]. Spin polarization values of many magnetic materials have since been determined by Andreev reflection, including some highly spin-polarized materials and even half metals [22, 23], in which only one spin band is available at the Fermi level.

In section 2.4, superconductivity is described in detail. At a normal metal/superconductor (N/S) interface, in which this work is measured using ballistic PCS described in section 4.1, a normal current must be converted into a supercurrent, meaning that an electron must be accompanied by another electron with opposite spin, as a Cooper pair, to be present in the superconductor. To then conserve angular momentum a hole must be reflected back into the normal metal. This is the Andreev

reflection, as shown in figure 4.3.Therefore, the conductance within the superconducting gap is twice as that outside the gap.

If the current is fully polarized, the conductance is zero within the gap because of the absence of the opposite spin to form the required Cooper pair. This effect of spin polarization on conductance can be used to determine the spin polarization of a ferromagnet as well as the superconducting gap of the superconductor. Theoretically, the N/S interface for a fully unpolarized current has been described by the BTK theory [81] while the interface between a half metal and a superconductor is calculated by Mazin et al. [19]. For the majority of ferromagnetic metals, their spin polarization values are between 0 and 1, and is a linear combination of the fully polarized and fully unpolarized current with the definition of spin polarization P as the coefficient.

In figure 4.3, it describes an ideal interface. In reality, the interface is often not ideal and there is interfacial scattering Z factor and inelastic scattering Γ factor. These scatterings as well as the thermal effect can drastically affect the Andreev spectrum, therefore affecting the analysis of finding the correct value of the spin polarization and gap. When Z is close to zero, the contact is close to the transparent limit while when $Z \gg 1$, the contact is essentially tunneling. As a result the Andreev spectrum includes tunneling spectrum and the effect of Z has been discussed in both the standard BTK theory [81] and fully polarized current [19].

Ideally, the lifetime of quasiparticles in a superconductor is infinite, therefore quasiparticles exist only outside the gap and the DOS diverges right at the gap. The presence of inelastic scattering shortens the lifetime of quasiparticles and thus quasiparticles can appear both inside the gap and recombine to superfluid condensate outside the gap. As a result, the DOS of quasiparticles is broadened. The inelastic scattering has been extensively studied in superconductors using normal metal/insulator/superconductor (N/I/S) and superconductor/insulator/superconductor

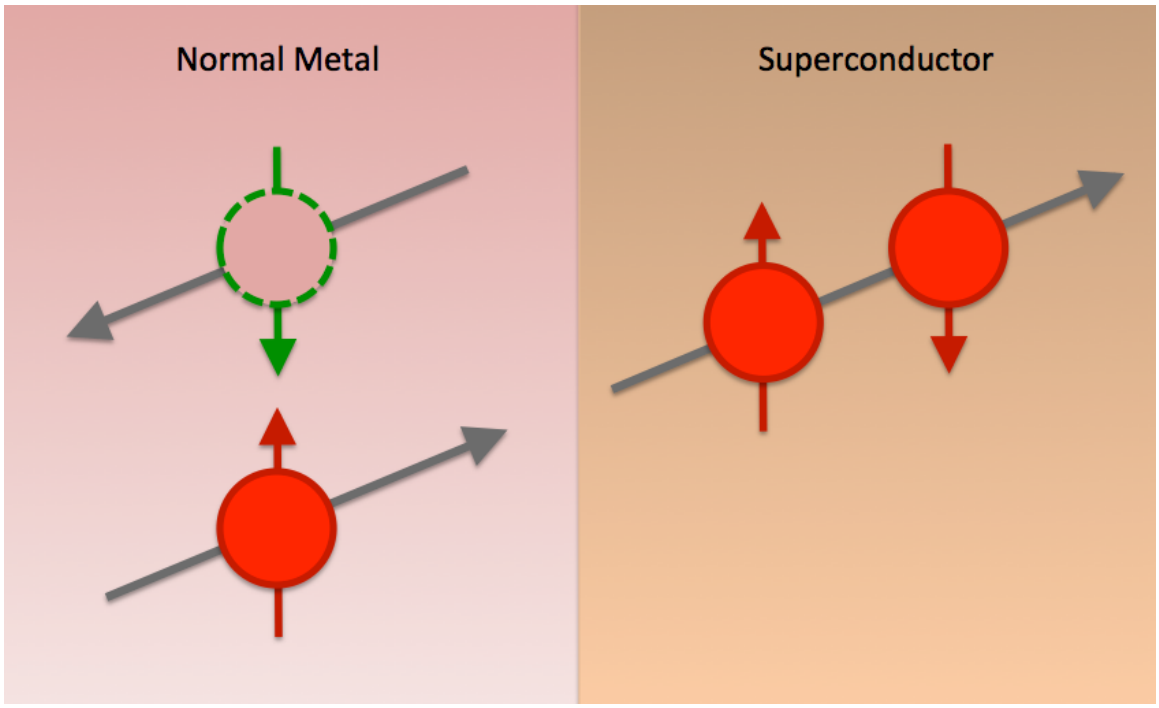

Figure 4.2: Andreev Reflection Spectroscopy: At a normal metal (N) and superconductor (S) interface, an electron (red) tunnels through the potential barrier. To conserve angular momentum, since a Cooper pair must form, a hole (green) is reflected back along the same path as the incident electron.

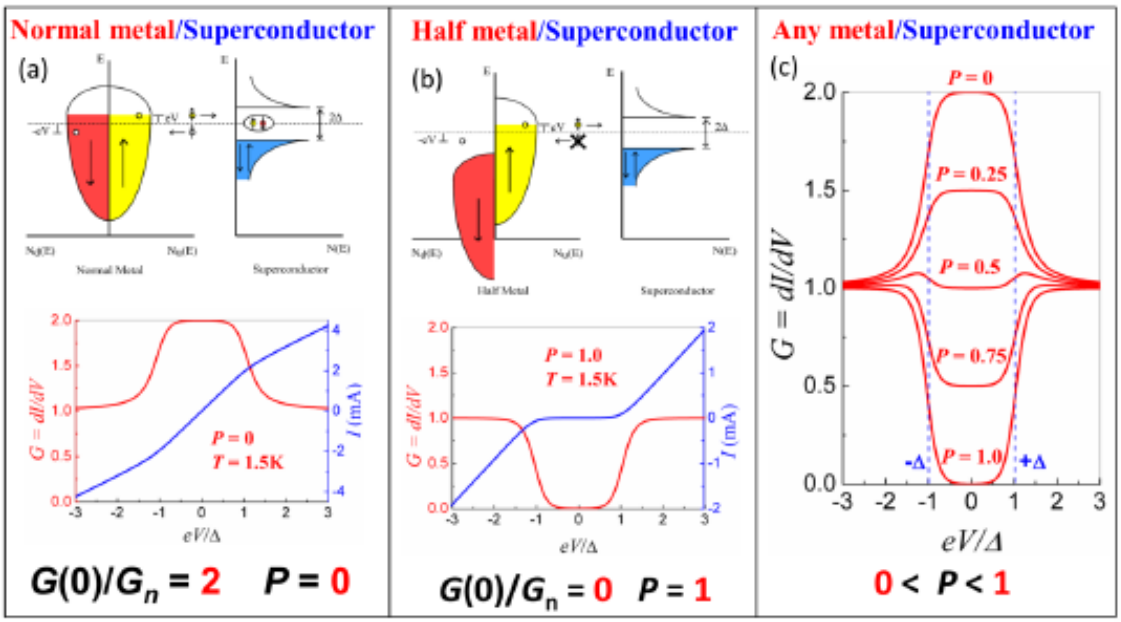

Figure 4.3: Ideal interface Andreev reflection (a) for a normal metal/ superconductor where $P = 0$, (b) half metal/superconductor where $P = 1$, and (c) any metal/superconductor where P is between 0 and 1. The top diagrams are the energy verses number of up and down spins for the metal and superconductor. For the superconductor 2Δ represents the gap due to Andreev reflection. The graphs represent Andreev reflection measurements of differential resistance (G) and current verses voltage for all three metals.

(S/I/S) junctions [82]. Also the conductance spectra are drastically changed by the presence of inelastic scattering. In the analysis, the effect of inelastic scattering has been introduced by adding an imaginary component to the energy. There are several origins that can cause inelastic scattering including magnetic field penetration, electron-electron interactions, electron-phonon interactions, spin fluctuation and spin-flip scattering.

4.3 Blonder-Tinkham-Klapwijk Model

The Blonder-Tinkham-Klapwijk (BTK) model is the theoretical framework that describes the mechanisms of ARS. It is the analysis tool that finds the spin polarization of the normal metal, and superconducting gap of the superconductor. It was created in 1981 to describe the I-V curves of the N/S interfaces [81]. The calculations are based on a generalized semiconductor model using the Bogoliubov-de Gennes (BdG) equations. They generalize the BCS, see section 2.4, to account for the spatially varying pairing strength $\Delta(x)$, chemical potential $\mu(x)$, and the Hartree potential $V(x)$. In this semiconductor model, it is conventional to take advantage of the BCS coherence factors u_k and ν_k which drop out of the computation if the excitations have the same energy E_k, but where the momenta $k < k_F$ and $k > k_F$ are grouped together. The semiconductor model uses the superconductor density of states $N_s(E)$, which distinguishes it from the normal metal. The problem is that, after combining the momentum pairs, information can be lost such as the charge imbalance of Q^* of the quasiparticles. Therefore the BTK model takes into account the the loss of information by using the BdG equations, where it matches the wave functions at the interface boundary. The excitations are described by the following operator $\gamma^\dagger_{e,k_+\uparrow} = u_{k_+} c^\dagger_{k\uparrow} - \nu_{k_+} S^\dagger c_{-k_-\downarrow}$ with the charge e as a two element column

vector:

$$\psi_k = \begin{bmatrix} u_k(x,t) \\ \nu_k(x,t) \end{bmatrix}, \tag{4.16}$$

where u_k and ν_k are described by the equations:

$$\left[-\frac{\hbar^2}{2m}\nabla^2 + V(x) - \mu(x)\right] u_k(x,t) + \Delta(x)\nu_k(x,t) = i\hbar\frac{\partial_{u_k}(x,t)}{\partial t}, \tag{4.17}$$

and

$$-\left[-\frac{\hbar^2}{2m}\nabla^2 + V(x) - \mu(x)\right] \nu_k(x,t) + \Delta^*(x)u_k(x,t) = i\hbar\frac{\partial_{\nu_k}(x,t)}{\partial t}\ . \tag{4.18}$$

Once the excitations are penetrated deep into the superconducting electrode, $\Delta(x)$, $\mu(x)$, and $V(x)$, they become constants, so the solution to equations 4.16 and 4.17 becomes (for $V(x) = 0$):

$$E_k u_k = \left[-\frac{\hbar^2 k^2}{2m} - \mu\right] u_k + \Delta\nu_k, \tag{4.19}$$

and

$$E_k u_k = \left[\frac{\hbar^2 k^2}{2m} + \mu\right] \nu_k + \Delta u_k\ , \tag{4.20}$$

where E_k is the excitation energy which can have four different corresponding k values, where $\frac{\hbar^2 k_\pm}{2m} = \mu \pm \sqrt{E_k^2 - |\Delta|^2}$. The k_+ is the electron-like quasiparticle and k_- is the hole-like quasiparticle. One gets four different equations:

$$u^2_{k_+} = \begin{cases} \frac{1}{2}\left(1 + \frac{\sqrt{E_k^2-\Delta^2}}{E_k}\right), & \text{for } u^2_{k_0} > \frac{1}{2} \\ \frac{1}{2}\left(1 - \frac{\sqrt{E_k^2-\Delta^2}}{E_k}\right), & \text{for } u^2_{k_0} < \frac{1}{2} \end{cases} \tag{4.21}$$

$$\nu^2_{k_+} = \begin{cases} \frac{1}{2}\left(1 - \frac{\sqrt{E_k^2-\Delta^2}}{E_k}\right), & \text{for } \nu^2_{k_0} < \frac{1}{2} \\ \frac{1}{2}\left(1 + \frac{\sqrt{E_k^2-\Delta^2}}{E_k}\right), & \text{for } \nu^2_{k_0} > \frac{1}{2} \end{cases} \tag{4.22}$$

yielding the wave functions for both the superconductor and the normal metal. The wave functions for the superconductor become:

$$\begin{bmatrix} u_{\pm k_\pm}(x)e^{iE_k t/\hbar} \\ \nu_{\pm k_\pm}(x)e^{iE_k t/\hbar} \end{bmatrix} = e^{\pm ik_\pm x} \begin{bmatrix} \sqrt{\frac{1}{2}(1 \pm \frac{\sqrt{E_k^2-\Delta^2}}{E_k}} \\ \sqrt{\frac{1}{2}(1 \mp \frac{\sqrt{E_k^2-\Delta^2}}{E_k}} \end{bmatrix} e^{-iE_x t/\hbar} , \tag{4.23}$$

and for the normal metal become:

$$\psi^N_{\pm k_+} = \begin{bmatrix} u_{\pm k_+}(x)e^{iE_k t/\hbar} \\ \nu_{\pm k_+}(x)e^{iE_k t/\hbar} \end{bmatrix} = e^{\pm ik-x} \begin{bmatrix} 1 \\ 0 \end{bmatrix} e^{-iE_k t/\hbar} \quad \text{(electron-branch)} \tag{4.24}$$

$$\psi^N_{\pm k_-} = \begin{bmatrix} u_{\pm k_-}(x)e^{iE_k t/\hbar} \\ \nu_{\pm k_-}(x)e^{iE_k t/\hbar} \end{bmatrix} = e^{\pm ik-x} \begin{bmatrix} 0 \\ 1 \end{bmatrix} e^{-iE_k t/\hbar} \quad \text{(hole-branch)} . \tag{4.25}$$

The dimensionless barrier height, or interfacial scattering factor, defined as $Z = mH/\hbar^2 k_f$ and $\gamma = u_0^2 + (u_0^2 - \nu_0^2)Z^2$, also must be incorporated into this model since the interfaces are often not ideal. The interfacial scattering factor Z, and inelastic scattering factor Γ will affect this interface. The Γ changes the complex coherence factors to:

$$u = 1/2 + \sqrt{(E - i\Gamma)^2 - \Delta^2}/[2(E + i\Gamma)]^{1/2}, \tag{4.26}$$

and

$$\nu = 1/2 - \sqrt{(E - i\Gamma)^2 - \Delta^2}/[2(E + i\Gamma)]^{1/2} . \tag{4.27}$$

Another parameter that can be defined from the wave functions is that of the spin polarization. Based on the CTC model, $P = \alpha^2/(\alpha^2 + 4)$ [83], where α is the effect of the spin polarization, which can be measured. BTK follows the Dermers and Griffiin models by using a repulsive delta-function potential $V(x) = H\delta(0)$. This yields the

following wave functions for the N/S interface:

$$\psi_N(\mathbf{r}) = e^{i\mathbf{k}_{in}\cdot\mathbf{r}} \begin{bmatrix} 1 \\ 0 \end{bmatrix} + ae^{-(\alpha+i)\mathbf{k}_{AR}\cdot\mathbf{r}} \begin{bmatrix} 0 \\ 1 \end{bmatrix} + be^{i\mathbf{k}_{nr}\cdot\mathbf{r}} \begin{bmatrix} 1 \\ 0 \end{bmatrix} \tag{4.28}$$

$$\psi_S(\mathbf{r}) = ce^{i\mathbf{k}_{elq}\cdot\mathbf{r}} \begin{bmatrix} u \\ \nu \end{bmatrix} + de^{-\mathbf{k}_{hlq}\cdot\mathbf{r}} \begin{bmatrix} \nu \\ u \end{bmatrix} , \tag{4.29}$$

where the first term for the normal metal is the incident electron, second ARS, and third the normal reflection. For the superconductor the first term is transmission without branch-crossing, and second is transmission with branch crossing. The coefficients a,b,c, and d are the coefficients of AR, the normal reflection, and the two transmissions. The coefficients are written below:

$$a = 4u\nu/\gamma \ , \tag{4.30}$$

$$b = [-u^2(2Z) + \nu^2(2Z + 2iZ_-)]/\gamma \ , \tag{4.31}$$

$$c = -2iZ_+u/\gamma \ , \tag{4.32}$$

$$d = 2IZ_-\nu/\gamma \ . \tag{4.33}$$

The probabilities of the Andreev reflection, the normal reflection and the transmission can be calculated by the integration of aa^*, bb^*, $cc^*\nu_g$, and $dd^*\nu_g$ over all solid angles of the interface where v_g is the group velocity:

$$A = u\nu/\gamma \ , \tag{4.34}$$

$$B = (u - \nu)Z(1 + Z)^{1/2} \ , \tag{4.35}$$

$$C = -2iZ_+u/\gamma \ , \tag{4.36}$$

$$D = 2iZ_-\nu/\gamma \ , \tag{4.37}$$

where $Z_+ = 2Z + 2i + \alpha$, $Z_- = 2Z + \alpha = mH/\hbar^2k_f$, and $\gamma = u^2 + (u^2 - \nu^2)Z^2$ with all results depend on Z, α, E, and Γ.

The conductance of the interface can then be found for the bias voltage. It is defined as:

$$\frac{dI}{dV} = \int_{-\infty}^{\infty} \frac{1}{k_B T} \frac{e^{\frac{E-eV-\mu}{k_b T}}}{(1+e^{\frac{E-eV-\mu}{k_B T}})^2}(1+A-B)dE/(1-B_{NN}) \ , \tag{4.38}$$

for a large bias ($eV \gg \Delta$). Therefore $a = 0$, $bb^*_{NN} = Z^2/(Z^2+1)$. The AR spectrum depends on the various parameters. To do the measurements, a conic tip with point angle 2θ is assumed. Figure 4.4 shows the effects of Z and Γ for an ideal interface measuring the differential conductance. From this figure, it can be seen that for temperatures of 0 to 4.2 K, large Z factors will suppress the differential conductance causing a dip at zero bias voltage. It is also shown that for increasing Γ the conductance is again suppressed, but at temperatures of zero, the peak becomes more ridged and the double peak feature is not present. More studies of Z and Γ effects on the interface will be explored in later chapters.

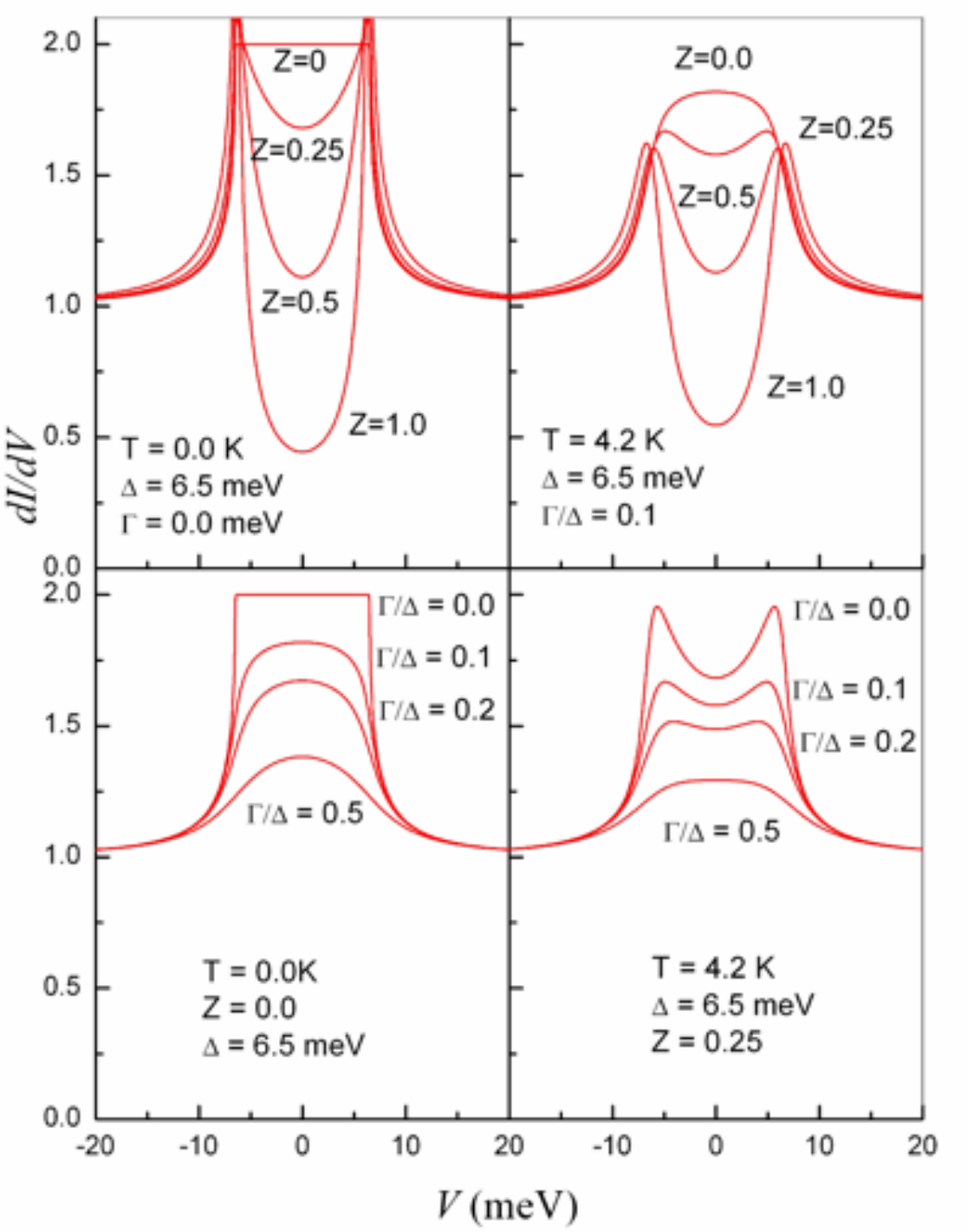

Figure 4.4: Differential conductance for (a) $T = 0K$ with noticeable suppression of the peak at zero bias as the interfacial scattering factor Z is increased, (b) $T = 4.2K$ the same suppression is present at zero bias but the overall conductance is higher then that of $T = 0$ and shows a smoother peak for $Z = 0$, (c) $T = 0k$ the conductance is suppressed for increasing Γ at zero bias, (d) $T = 4.2K$ the same suppression is present at zero bias but the conductance now exhibits smoother, double peak behavior.

4.3.1 Modified BTK Model

In PCAR, it is realized that interfaces are often not ideal and, even with the addition of the interfacial scattering factor Z and the inelastic scattering factor Γ, noticeable thermal smearing due to finite temperatures is present. This will affect the value of the spin polarization P. In the standard ARS model, the point contact resistance (R_C) contains the information to deduce the superconducting gap and spin polarization. However in the four contact PCAR method, extra resistances are present. In figure 4.5 (a) and (b) a contact is formed but an additional resistance is measured along the path. This resistance is called the spreading resistance, or the sample resistance (R_S) [24, 84]. Figure 4.5(c) shows the relative resistances in the sample. In bulk the R_s is so small that only the R_c is measurable, but in the ballistic regime this resistance can be substantial [27].

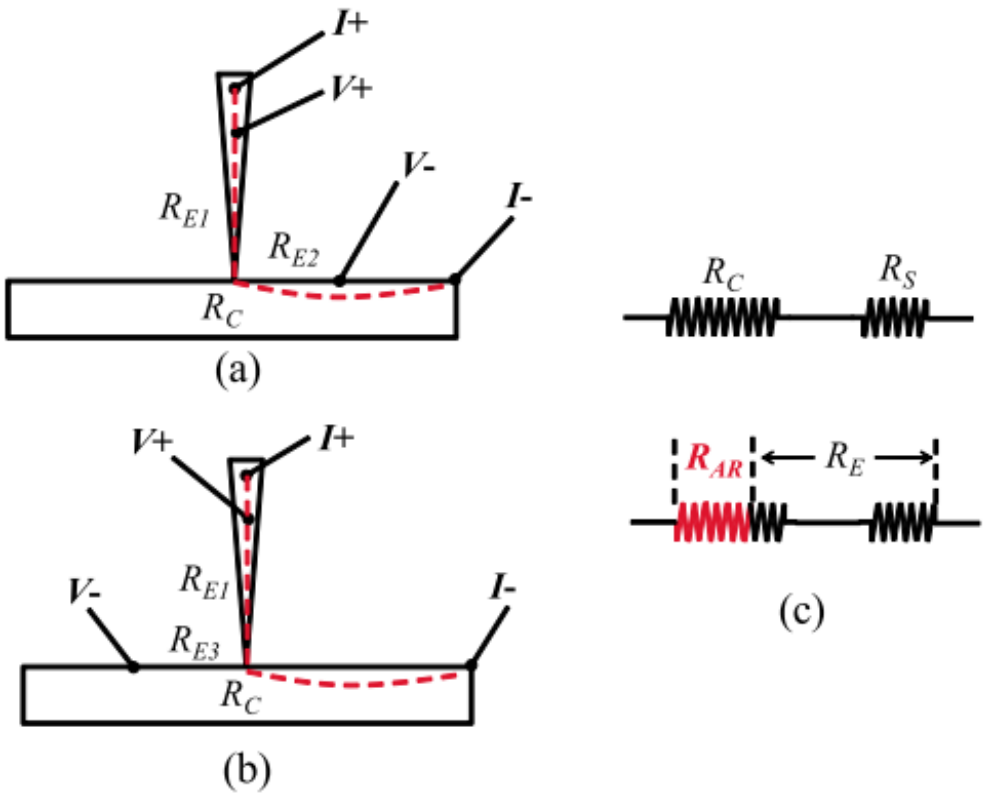

Figure 4.5: Schematics of two typical point-contact experiments with possible causes of extra resistance indicated as R_{E1} and R_{E2} in (a) and R_{E1} and R_{E3} in (b) and with current path indicated as dashed line. (c) Schematics of Andreev resistance R_{AR}, contact resistance R_C, sample resistance R_S, and extra resistance R_E [27].

This resistance originates from the sample but also from the contact itself. The variation of the resistance to the position of the contact is nonlinear, and thus can not methodically be corrected. To account for the resistance in the BTK model, the large sample resistance will be contributed to the additional resistance. For more information see reference [27] which describes this resistance in detail.

In the ballistic regime the contact resistance is the Sharvin resistance $4\rho l/3\pi a^2$, which is defined by the contact aperture radius [85]. Current far from the contact is still diffusive and in the ballistic limit ($l >> a$) the resistance is negligible. In an actual experiment however the resistance is not completely diffusive or ballistic. For AR measurements, this resistance is called R_E which can't be experimentally measured without knowing what region the AR is applied.

By taking into account this additional resistance, the differential conductance of the point contact with bias voltage V_{AR} can be calculated from the current I_{NS}:

$$\frac{dI_{NS}}{dV_{AR}} = 2eS_cN\nu_f \int_{-\infty}^{\infty} \left[\frac{df(E - eV_{AR}, T)}{dV_{AR}}\right] [1 + A - B]dE \ , \tag{4.39}$$

where f is the Fermi distribution function, e is the electron charge, S_c is the effective contact, N is the spin density of states, ν_F is the Fermi velocity, A is the AR probability, B is the normal reflection probability, and V_{AR} is the voltage on the region where the AR contact is made. The main issue with this formalism is that the differential resistance dI_{NS}/dV_{AR} cannot be normalized by $1/R_{NN}$ or the contact resistance because of the additional resistance R_E. The differential conductance is instead:

$$\frac{dI_{NS}}{dV} = \frac{\Delta I_{NS}}{\Delta V_{AR} + \Delta I_{NS}R_E} = \frac{1}{R_{NN}} \frac{\left(\frac{dI_{NS}}{dV_{AR}}\right)_0}{1 + r_E \left(\frac{dI_{NS}}{dV_{AR}}\right)_0} \ , \tag{4.40}$$

where $(dI_{NS}/dV_{AR})_0 = R_{NN}(dI_{NS}/dV_{AR})$ is the normalized conductance and $r_E = R_E/R_{NN}$ is the relative additional resistance. When $V \gg \Delta$ the differential conduc-

tance is 1, therefore the normalized resistance gives the differential resistance:

$$\left(\frac{dI_{NS}}{dV_{AR}}\right)_0 = R_{NN}(1+r_E)\frac{dI_{NS}}{dV} = (1+r_E)\frac{\left(\frac{dI_{NS}}{dV_{AR}}\right)_0}{1+r_e\left(\frac{dI_{NS}}{dV_{AR}}\right)_0}\ . \tag{4.41}$$

This is independent of R_{NN} and allows for the correct normalization of dI_{NS}/dV_{AR}. Using this new differential conductance, figure 4.6 shows an example of PCAR measurements for differing additional resistances. As the resistance increases, the conductance is suppressed for temperatures below 4.2 K [27]. This new model is named the Modified BTK (MBTK) method and this differential conductance is what will be used to fit the data in later chapters.

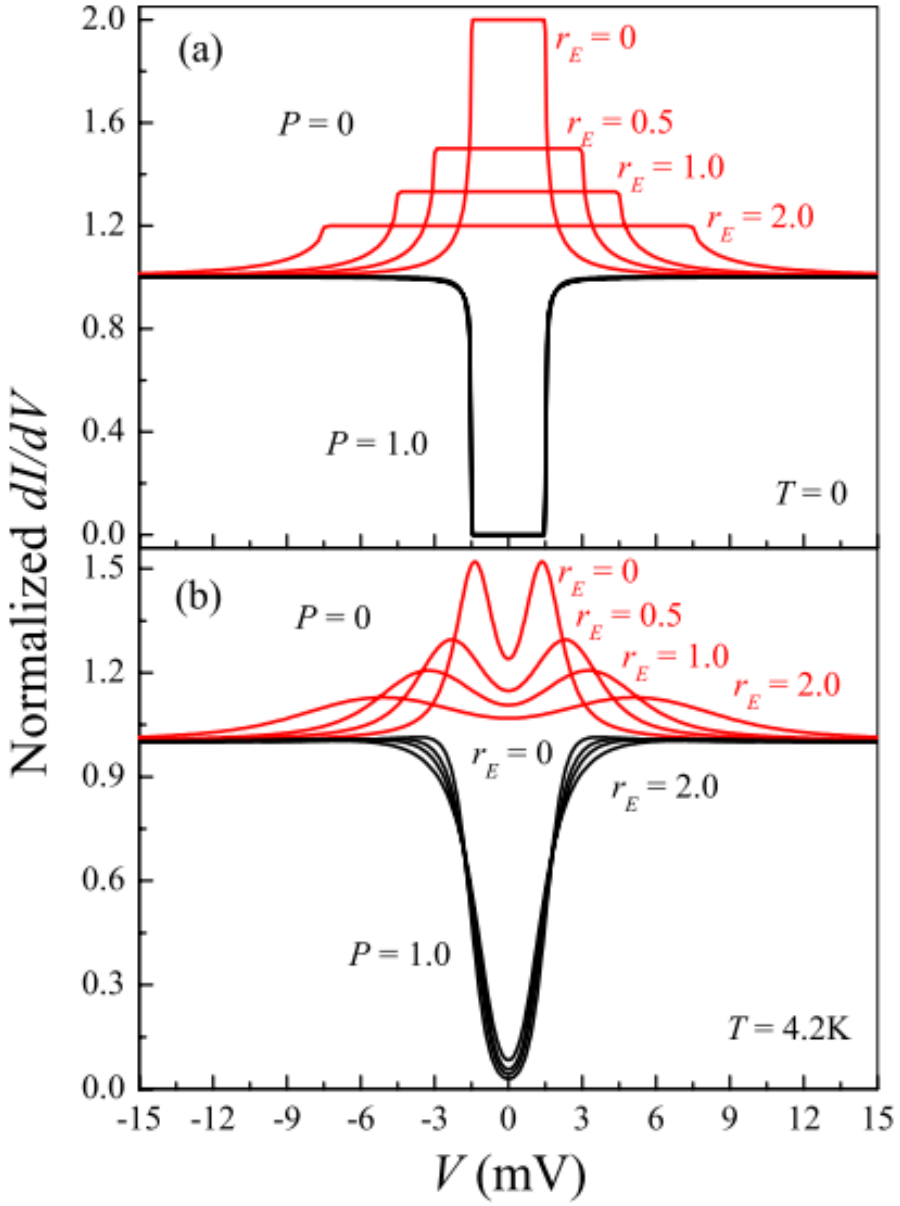

Figure 4.6: Calculated PCAR spectra in the purely ballistic regime with various $r_E = 0.05, 1.0, 2.0$ for $P = 0$ and 1.0 at (a) $T = 0$ and (b) $T = 4.2$ K [27].

4.4 Singlet Superconductivity and ARS

Figure 4.7 shows the three different types of superconductivity, s-wave, p-wave, and d-wave. Each different type displays different ARS effects. In this work singlet s-wave, singlet d-wave, and triplet p-wave superconductivity will be addressed.

For singlet superconductivity it must have an overall antisymmetric wave function and odd parity. The wave function for the singlet superconductor is:

$$\psi_{singlet} = \psi_0(\mathbf{r_1}, \mathbf{r_2})(|\downarrow\uparrow\rangle - |\uparrow\downarrow\rangle) \ . \tag{4.42}$$

The expected normalized conductance is shown in figure 4.8. For a normal metal with small spin polarization, the normalized conductance is expected to increase with decreasing spin polarization, until it reaches its maximum at $P = 0$.

The new question becomes: *How will the differential conductance respond to highly spin polarized materials such as a half metal?* For a singlet superconductor in the presence of the half metal, the electrons will behave by the standard BTK model in which the normalized current will be suppressed for increasing polarizations shown by the red line in figure 4.8. The second question is now: *Will the differential conductance for a normal or half metal behave the same as that of a singlet superconductor?*

4.5 Triplet Superconductivity and ARS

For a triplet superconductor the differential conductance is expected to behave differently due to its even parity. The wave function for a triplet superconductor is:

$$\psi_{triplet} = \psi_{\uparrow\uparrow}(\mathbf{r_1}, \mathbf{r_2})\,|\uparrow\uparrow\rangle + \psi_{\downarrow\downarrow}(\mathbf{r_1}, \mathbf{r_2})\,|\downarrow\downarrow\rangle + \psi_1(\mathbf{r_1}, \mathbf{r_2})(|\downarrow\uparrow\rangle + |\uparrow\downarrow\rangle) \ , \tag{4.43}$$

where blue corresponds to even parity and red odd parity. The half pairs shown in red have parallel spin. This is the key difference from the singlet superconductors. For these triplet superconductors, because of the parallel spins, ARS is not blocked

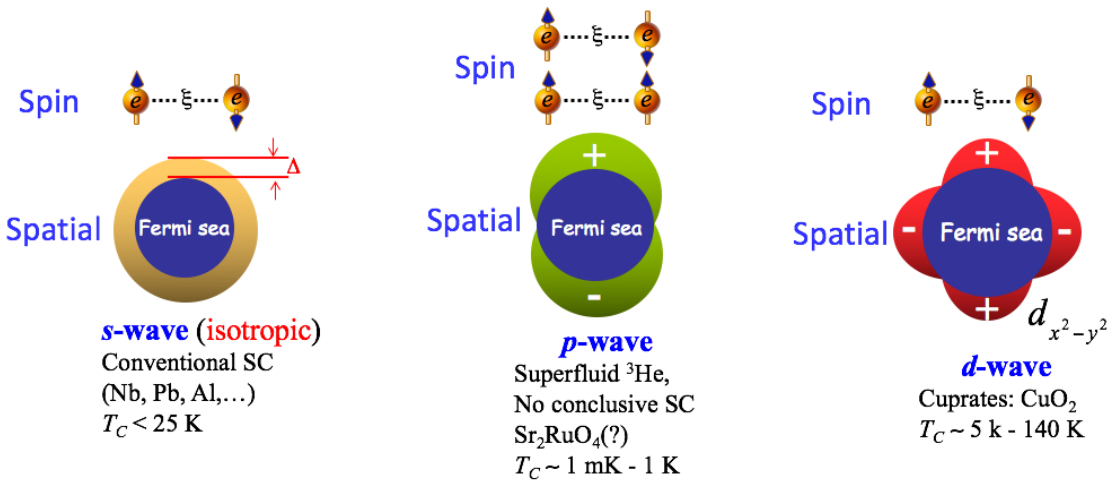

Figure 4.7: (a) s-wave superconductivity, (b) p-wave superconductivity, and (c) triplet superconductivity.

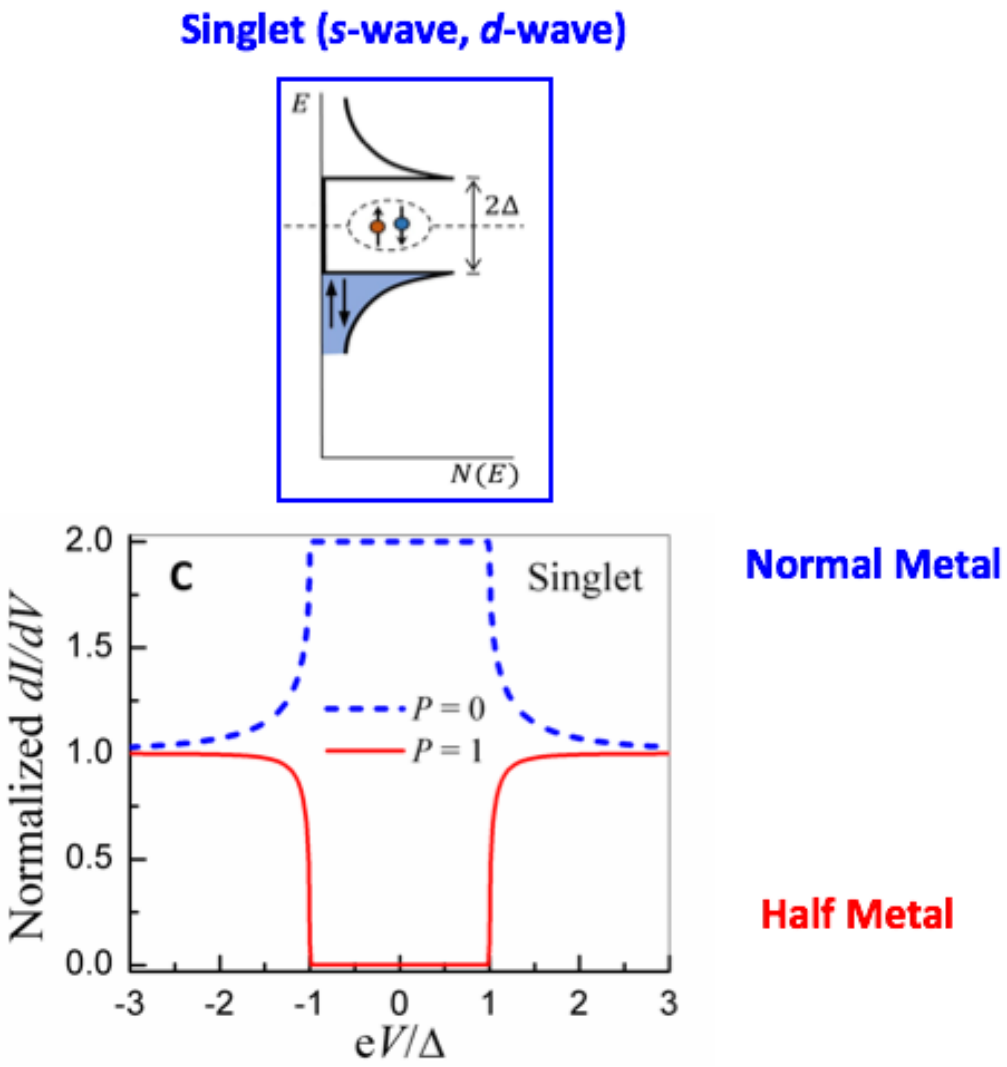

Figure 4.8: Normalized differential conductance of singlet superconductors in ARS contact with a normal metal (blue) and half metal (red).

for half metals. This means that instead of dI/dV being suppressed it will actually grow as show in fig 4.9.

This means that there is a novel way to distinguish whether the superconductor is a singlet or triplet. By measuring the differential conductance using a normal metal and a half metal, one can easily distinguish between the two.

Thus far a p-wave triplet superconductor remains illusive but since the discovery of higher T_c superconductors, there have been strong candidates. Figure 4.10 shows the T_c verses discovery year for many superconductors. The black line correspond to s-wave, blue to d-wave, and red to p-wave. In 1968, Alex Muller and Georg Bednorz discovered the d-wave cuprates and have shown that they are the strongest candidates for high T_c superconductivity. They were awarded the Nobel prize in physics in 1987 for this discovery. In 2008, Fe-SC were discovered and experiments have suggested that they could be p-wave superconductors. Chapter 9 describes the Fe-SCs in more detail and investigates whether they are a candidate for triplet superconductivity.

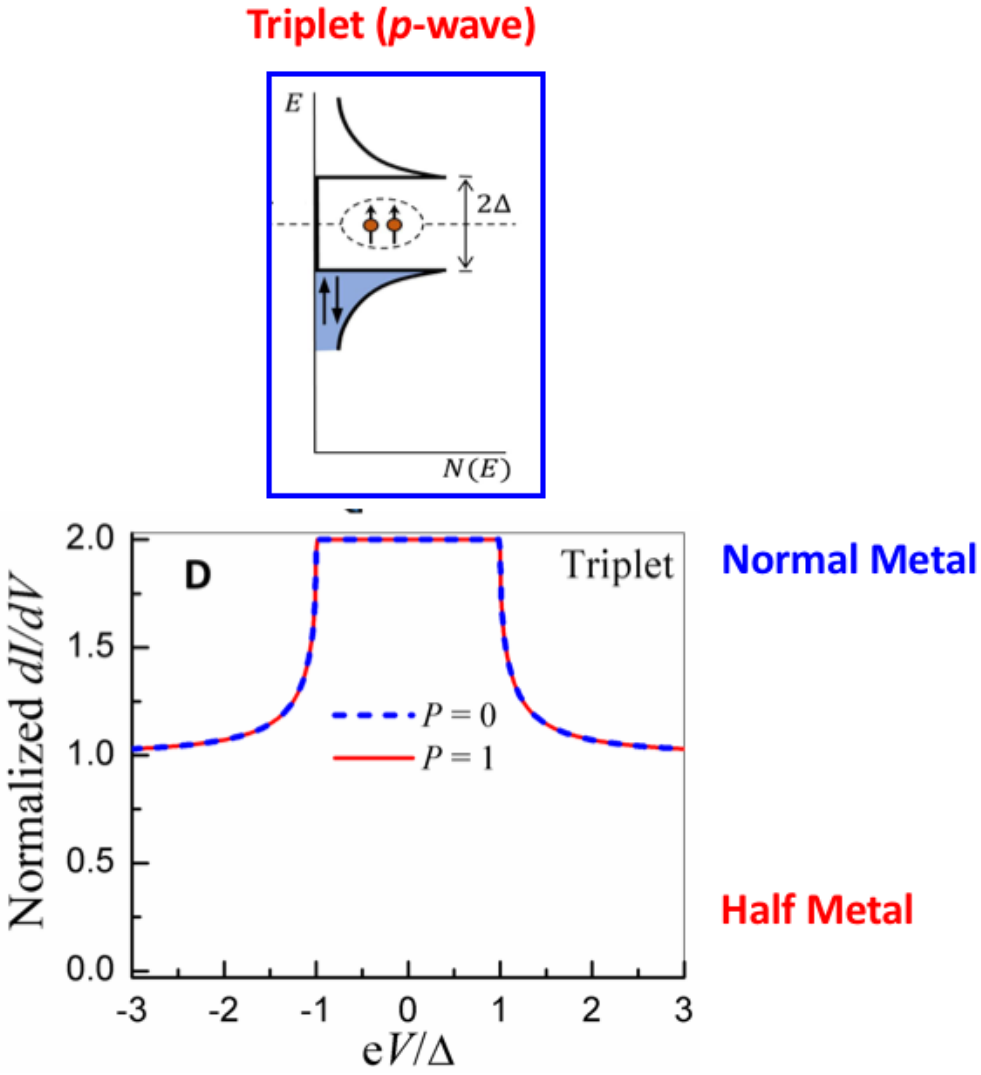

Figure 4.9: Normalized differential conductance of triplet superconductors in ARS contact with a normal metal (blue) and half metal (red).

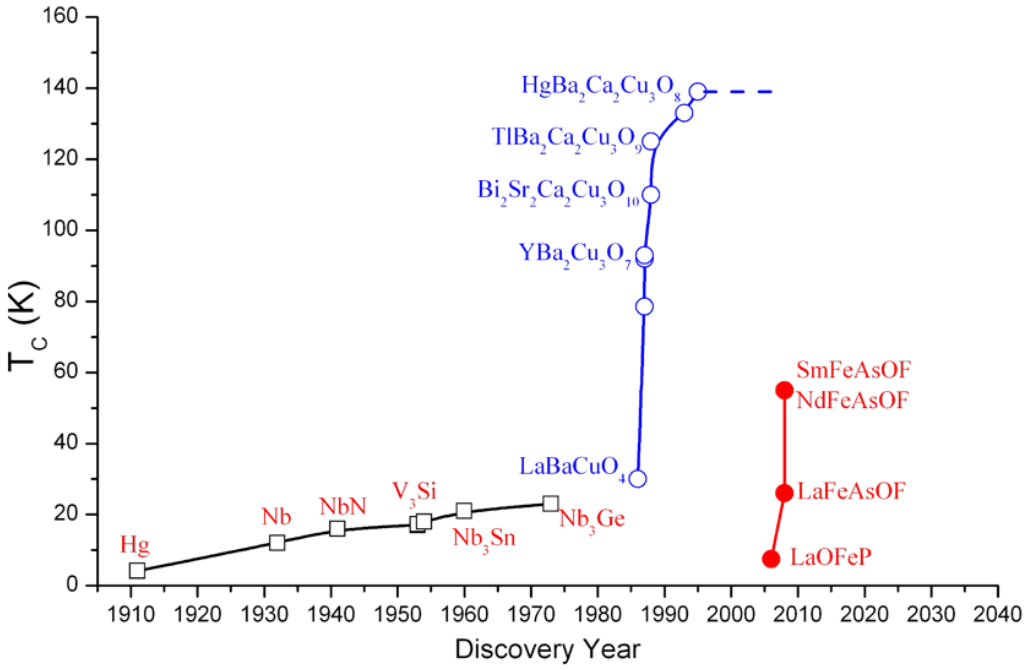

Figure 4.10: The critical temperature T_c verses discovery year for superconductors. Over the years the search for higher T_c superconductors have been of interest and thus far three types have been discovered. Black corresponds to s-wave, blue to d-wave, and red to p-wave superconductors. Fe-SC are hypothesized to be p-wave but not conclusive.

Chapter 5

EQUIPMENT

5.1 Four Point Contact Spectroscopy

For the ARS to correctly measure the superconducting gap of the superconductor and spin polarization of the normal metal, the spin must be preserved at the interface. Therefore, the interface must be ballistic. To create a ballistic interface, one must make the contact at the interface much smaller than the mean free path. Point contact spectroscopy is one of these methods, as shown in figure 5.1.

5.1.1 Experimental Setup

A point contact is formed when a sharp tip is in contact with another material, as in figure 5.1. The contact size can be made from nanometer to macro-size, and can be determined from the contact resistance. Depending on the size a and mean free path l, a point contact is in the diffusive regime with the Maxwell resistance when $a \gg l$, and it is in the ballistic regime with the Sharvin resistance when $a \ll l$. Each different regime is governed by different physics. In point contacts, one mostly operates in the ballistic regime to preserve spin information.

Since PCAR was first demonstrated [86], this technique has been greatly improved, especially with quantum data analysis which finds the spin polarization value. At first, clean contacts are assumed and the P value is found using the conductance ratio $G(0)/Gn = 2\Delta$ between the conductance at zero-bias voltage ($V = 0$) within the superconducting gap and the normal state conductance. However after initial experiments, it was no longer assumed that the contacts were ideal [86–88]. Therefore

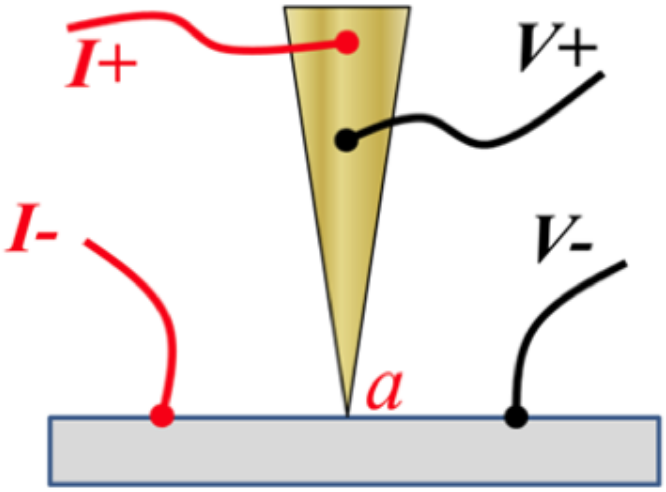

Figure 5.1: Point contact. A sharp point contact is created using a superconducting tip and a normal metal material. Current and voltage is then measured across the contact.

the conductance curve, with the interfacial scattering factor Z and thermal smearing due to finite temperature fluctuations, is used to find the spin polarization value.

5.2 Differential Conductance dI/dV

To detect the small change in conductance, using the point contact method, one needs to measure the differential conductance dI/dV. In the lab, there are two methods for this purpose: a step current sweep method (Step-sweep) and a Lock-in (Lock-in) method.

5.2.1 Step-sweep Method

Differential resistance can be measured by applying current and recording the voltage while using ohms law:

$$R_{differential} = \frac{dV}{dI} = \frac{\Delta V}{\Delta I} \ . \tag{5.1}$$

The step-sweep method is the simplest way to measure differential resistance. The applied current to the N/S interface is a linear staircase sweep. Applying a current, slightly above and below the desired current, is called the 2 step method. In the 2 step method, the differential resistance is integrated with respect to voltage over a fixed time, thus improving the accuracy of the measurement. Since current and voltage have a linear dependence, the measured voltage also follows the same integration (average) to extract ΔI [89], as shown in figure **??**,

$$\Delta I = \frac{(I_1 - I_2) + (I_3 - I_4)}{4} \ , \tag{5.2}$$

where I_n denotes the current step being used.

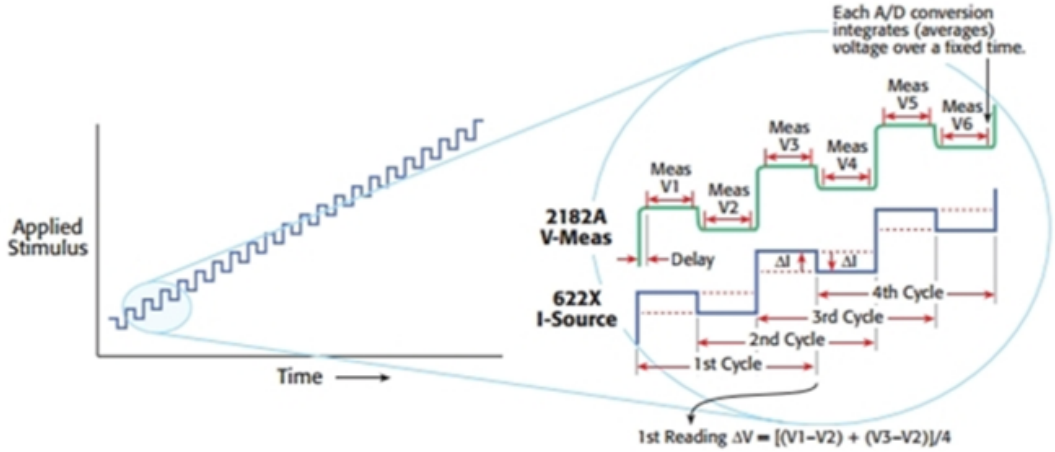

Figure 5.2: Step-sweep 2 step method. Current is applied in steps slightly above and below the desired value, or a linear staircase sweep. The steps are then integrated (averaged) over time. The voltage measured has the same behavior as the current. Using ohms law the differential resistance can then be calculated [89].

5.2.2 Lock-in Method

Unlike the step-sweep method, the lock-in method superimposes a low amplitude AC sine wave on the DC bias step-sweep method, as shown in figure 5.3. This adds a small improvement in noise, however adds the complication of choosing a frequency for the measurement that is usable. This limits the user to about 10-100 Hz, where the noise is five or ten times higher then that of the best conditions. More equipment is needed to superimpose the AC current and measure the differential resistance, however it vastly improves the measurements [89].

In this system, one can measure 10 samples at the same time. This is achieved using a programmable switching box, as shown in figure 5.4. Using either the step-sweep or lock-in method, the experimental set up is the same, show in figure 5.4. Inputs are available for 10 different materials. An input current is applied using the Keithley 6221 current generator. This works in conjunction with the Keithley 7001 SSW system to apply this current to any of the inputs, and the Keithley 2182A volt meter acquires the output voltages.

5.3 Room Temperature Point Contact Spectroscopy

For GMR structures the differential resistance dI/dV is often measured at room temperature (RT) as well as low temperatures of 4.2 K. For these measurements an electromagnet is needed to provide the change in magnetic field. Figure 5.5(a) show the schematic for this set up. A sample mounting rod is connected to the outer rack of the system. On this rod, the electrical contact needed for PCS is guided along the rod to the electrical controls outlined above. The electromagnet sits on a rotation circular plate which allows for angle dependence for GMR measurements. It is also attached to a circular plate in the perpendicular field to allow for both θ and ϕ angular

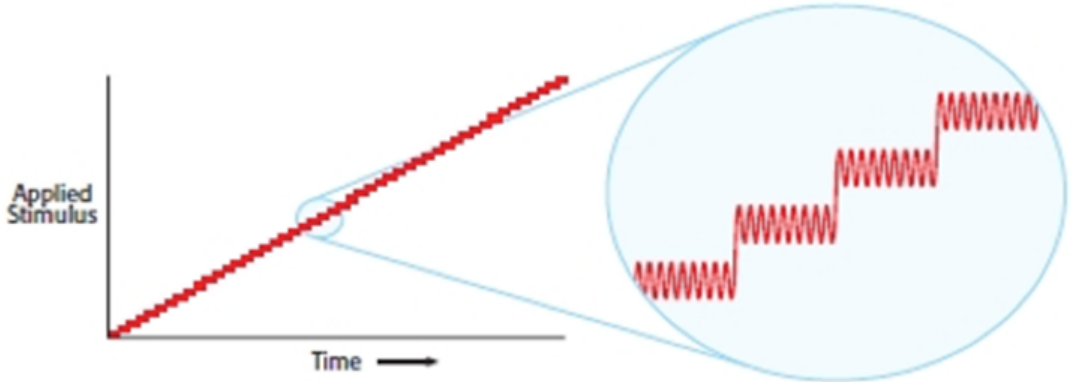

Figure 5.3: Lock-in method measures the response to a AC current while sweeping the DC bias through the desired regime [89].

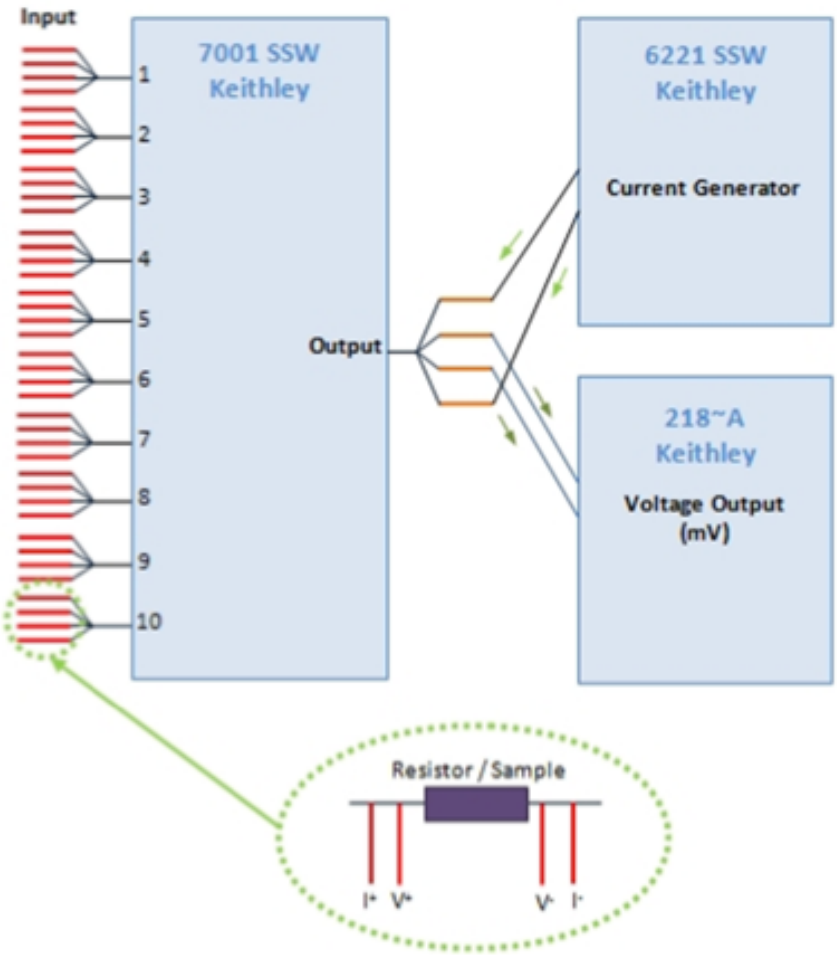

Figure 5.4: Experimental setup for conductance measurements. 10 inputs are used to apply a current to a resistor or sample, as the voltage is measure across the resistor. The 7001 SSW system by Keithley is used to measure and apply this current to any of the 10 resistor inputs. The Keithley 6221 SSW system is a current generator which applies a current to the 7001 SSW to analyze the resistor. Once the current is applied the measurement is outputted to the Keithley 218 A system which is a voltmeter which will measure the voltage from the resistor. Using the applied current and measured voltage the differential resistance can be measured.

dependence. The sample is attached by double sided tape to the mounting rod in the middle of the electromagnetic plates. These plates can be adjusted to change the distance between plates as needed. Figure 5.5(b) is a picture of the actual set up (with an added cold measurement chamber not used in this thesis).

5.3.1 PCAR on known Resistors

Testing of the experimental setup is pivotal to ensuring accurate data acquisition. Initial measurements were done with semi-conductor resistors of known resistances, ranging from 0.5 mΩ to 1 MΩ, at room temperature. Figure 5.6 shows the representative resistance V/I (red) and differential resistance dV/dI (black) of four resistors. The differential resistance dV/dI for each resistor is essentially constant, please note the scale. But the resistance V/I diverges at $V = 0$ for all the resistors. This is because of the contact potential, which I will discuss below.

To check the noise level for all the resistors, one can plot the normalized differential resistance dV/dI of these resistors together as a function of applied current I, as shown in figure 5.7. In this sensitive system, the maximum current that can be sent is 0.1 A and there is also a maximum voltage that the nano-voltmeter can measure. So for large resistances, 100 Ω and up, the applied current is only a fraction of the current that the 1 Ω and 10 Ω can handle. In these experiments, resistance of the point contacts will be between 1 Ω and 100 Ω. One notes that the noise level of dV/dI in this system is about 0.05% for all the measurements up to 100 kΩ. Even for 1 MΩ, the noise level is only about 0.1%. The noise level for 0.5 mΩ is similarly to 0.05%. This indicates that this system is indeed very sensitive, as expected. Furthermore, one can note is that there is a dip at about -0.075 A for both 1 Ω and 10 Ω. It seems that the oscillations of the curves are exactly the same. Various resistors were used in the current range and it can be found that it is due the current source. This is

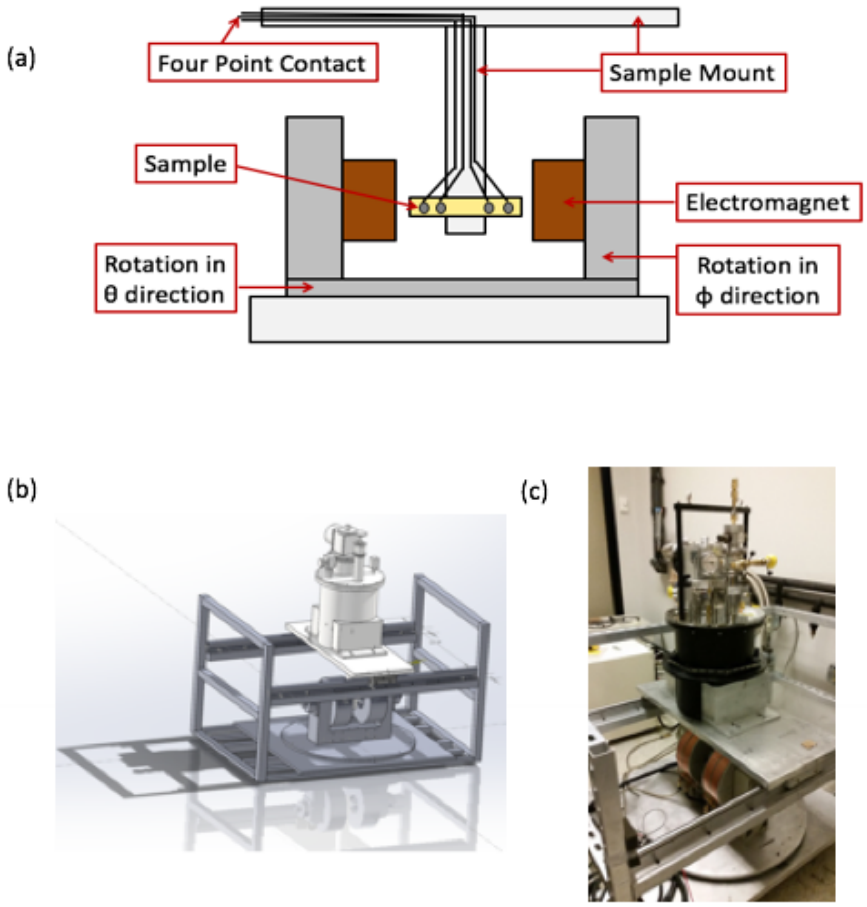

Figure 5.5: (a) Schematic setup of electromagnet used in room temperature measurements. The electromagnet is attached to both a rotating plate in the θ and ϕ direction for GMR angular dependence measurements. The sample it attached to the sample rod which is placed between the movable electromagnetic plates. This rod then guides the PC connection lines to the equipment outlined in the above section, (b) SolidWorks schematic, (c) Actual electromagnetic setup (note that cold chamber between the plates is not part of this thesis).

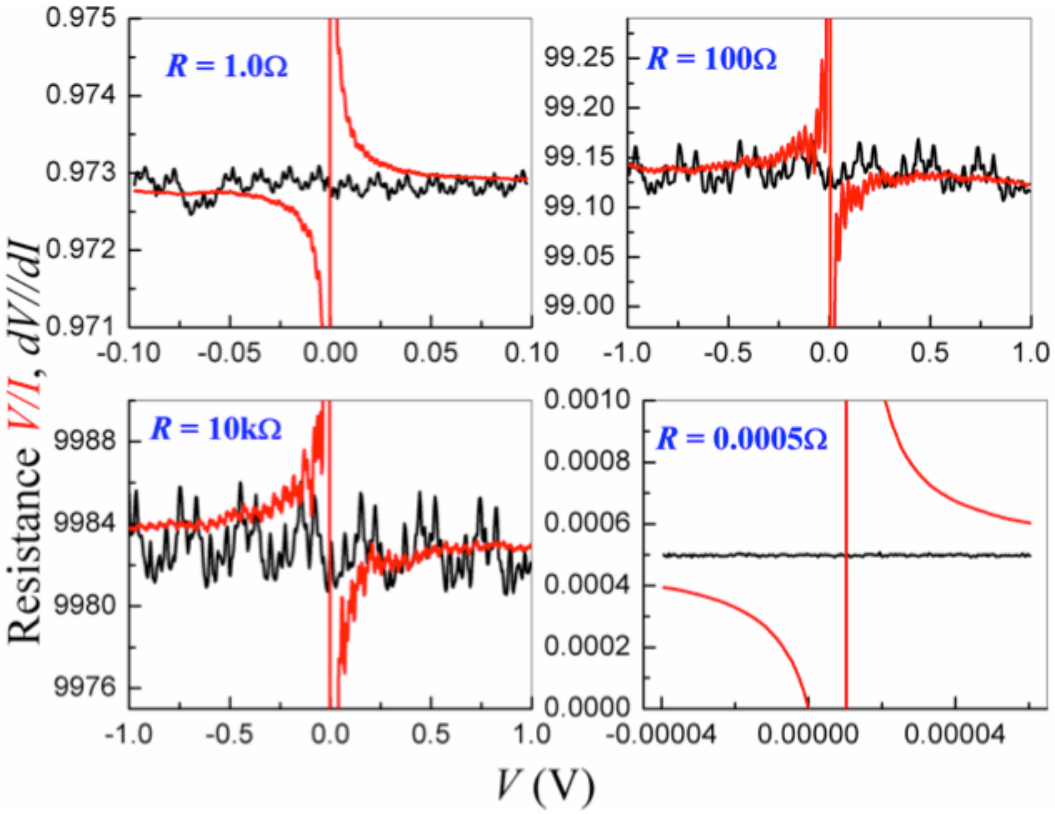

Figure 5.6: Differential (black) and contact (red) resistances for 1.0 Ω, 100 Ω, 10 kΩ, and 0.5 mΩ semi-conductor resistors at room temperature and no applied magnetic field. The differential resistance is virtual constant with fluctuations due to quantum effects in the nano-scale. The contact resistance is virtual constant far from zero voltage and goes to infinite resistance at zero voltage due to ohms law.

due to the systematic error and one can subtract it from the background. After one corrects the systematic error, the noise level is less than 0.01%. In other words, any change of resistance of 0.01% of a nanostructure under different voltage of current can be measured by this system.

The resistance $R = \frac{V}{I}$ is shown in figure 5.6, which is due to the contact potential. For any two dissimilar materials in contact, there is a contact potential due to the difference in Fermi level and work function of the two metals [90]. Because of the contact potential V_0, the actual resistance measurement becomes,

$$R = \frac{V + V_0}{I} \ . \tag{5.3}$$

In other words, even at zero current $I = 0$, there is a voltage V_0, thus the resistance diverges and the sign depends on the sign of the contact potential V_0. In this sensitive system, one can use silver solder to minimize the contact potential. However, there is always contact potential because there are so many connections there. In fact, the contact potential is different for different resistors, as shown in figure 5.7, where the divergence shows a different sign for different resistors.

The contact potential can be corrected using a fitting to the above equation. As shown in figure 5.8, for 0.5 mΩ resistor, it i found that the contact potential is $V_0 = -0.00001041V$. After the correction of the contact potential, it can be found that the resistance V/I is a horizontal line, as shown in figure 5.8 (red).

A typical value of a superconductor gap is a few meV, e.g. it is 1.4 meV and 1.3 meV for Nb and Pb respectively. In the above calibration, this system is very sensitive in the range of 0 to 1 V. In some extreme experiments, a large voltage of several volts is used for an experiment. This system is calibrated for large bias violate up to 36 V. Most semiconductor resistors break down at a few volts, for example, the resistor of 100 Ω of 0.25 W breaks down at about 8 V. Therefore, a graphite resistor

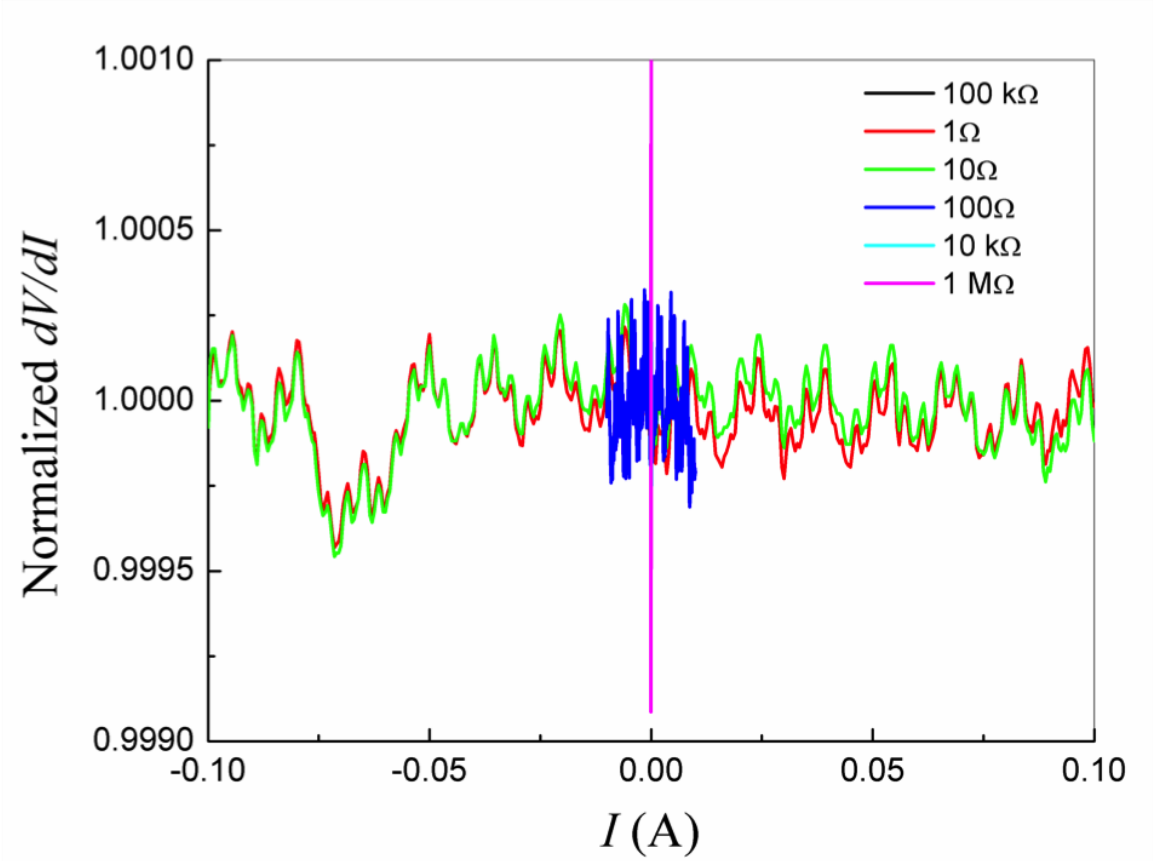

Figure 5.7: Normalized differential resistance for semi-conductor resistors from 1 Ω to 1 MΩ. Larger resistors cannot handle big current ranges and are therefore only a fraction of the total range that was measured. Analyzing the 1 Ω and 10 Ω resistors, it is apparent that since they are virtually identical that there is significant systematic error in the measurement which must be corrected for.

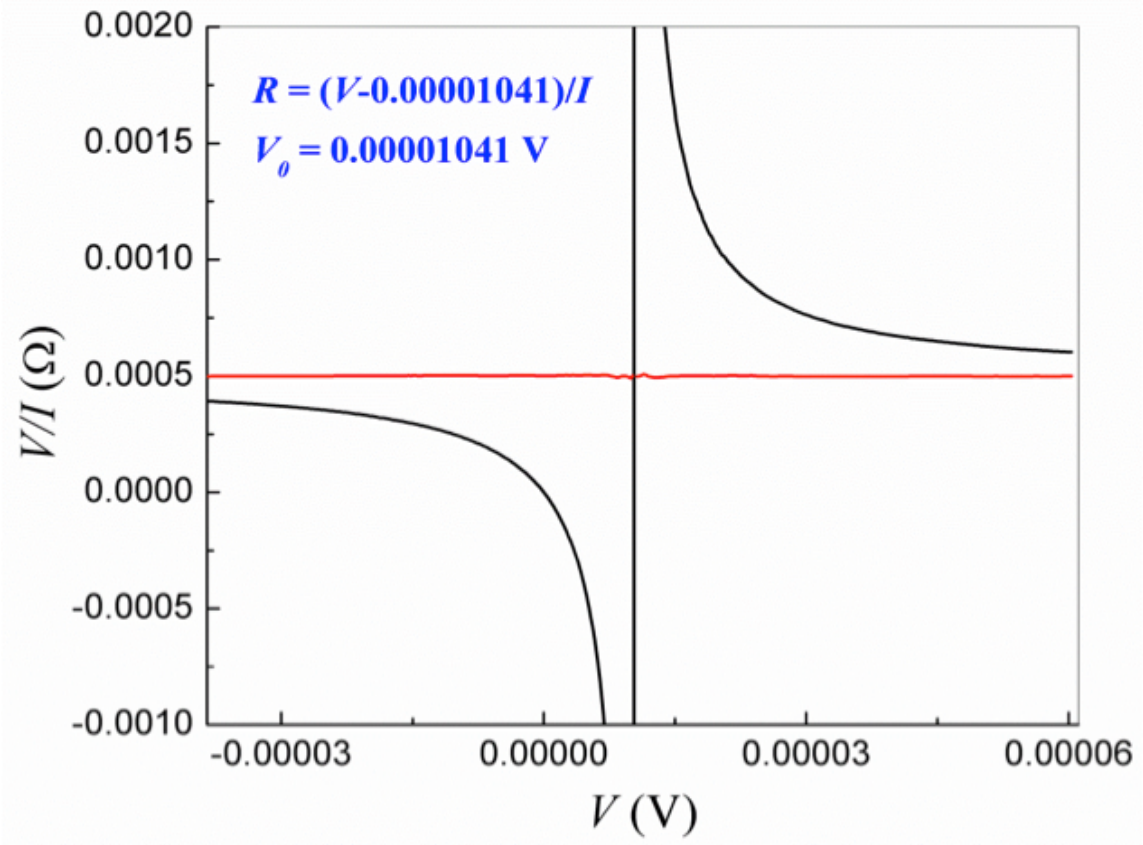

Figure 5.8: Corrected differential resistance (red) and contact resistance (black) for 0.5 mΩ. After accounting for systematic error, correcting the resistance using the voltage intercept of the IV curve, and correcting the zero biased voltage it is apparent that the resistance is more accurate and constant.

was used for the test. Figure 5.9 shows that the noise level in such a large voltage is only about 0.01% after a systematic error correction. In summary, the calibration shows that the resistance measured in this system fluctuates less than 0.02 Ω with a sensitivity of 0.01% and is sustainable up to 10 V, thus demonstrating that this experimental setup is extremely sensitive and accurate.

5.3.2 Test of PCAR Using Nb-SC

After testing this experimental setup, it can be shown that an example of one of this experiments, ARS of a Nb tip in contact with Fe_3Si. Fe_3Si has been proposed a spin injector for spintronics because it has good crystalline match with Si and its spin polarization is predicted to be high. Nb is a superconductor with a T_c of 9.27 K, so its gap is about 1.42 meV. Both the tip and the sample were mounted on the ARS probe in a vacuum jacket. About 50 mτ of He gas is used as exchange to reach low temperature. Then one can inset the probe into the cryostat and cool it down to 4.2 K. Before the experiment, one pumps the sample space in the cryostat and gets temperature about 1.5 K.

Four representative data sets are shown in figure 5.10. Open circles are the experimental data and the solids lines are the best fit to a modified BTK model. One can see that around zero, the conductance peak is suppressed because of the spin polarization. This data can be well described by the modified BTK model. The analysis shows that the spin polarization is close to 100%. But the inelastic scattering is very large. The large inelastic scattering may be due to the oxidation of the surface because the sample has been in air for over 7 months.

The temperature dependence of one of the contacts is shown in figure 5.11. At 1.65 K, there are two peaks associated with the superconducting gap, and the center is suppressed by the spin polarization of the Fe_3Si. At higher temperatures about

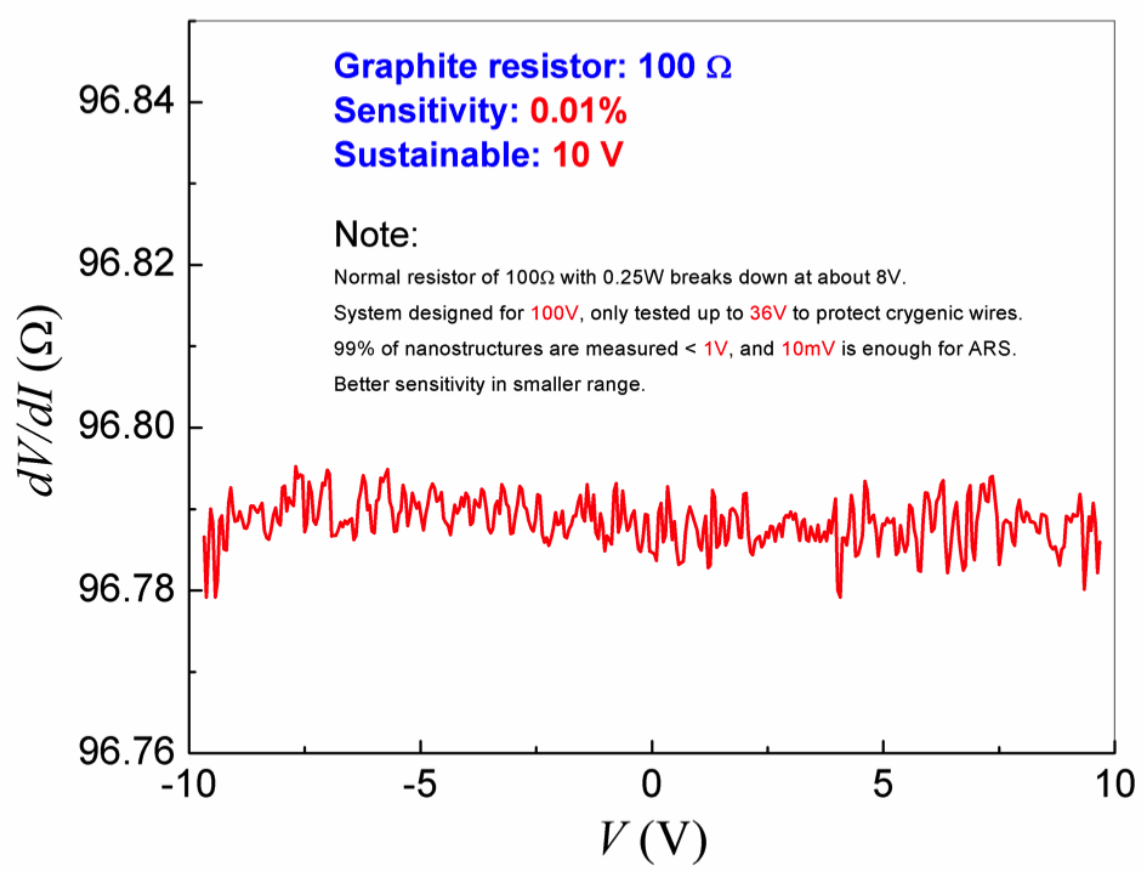

Figure 5.9: Differential resistance measurement (corrected) for a 100 Ω graphite resistor. This system can measure up to 100 V, and the resistor can sustain up to 10 V well within range. The resistance is virtually constant with a sensitivity of 0.01% thus demonstrating the accuracy of the experimental setup. 10 mV is enough for Andreev reflection spectroscopy hence this graphite resistor demonstrates the accuracy and range obtainable, although unnecessary.

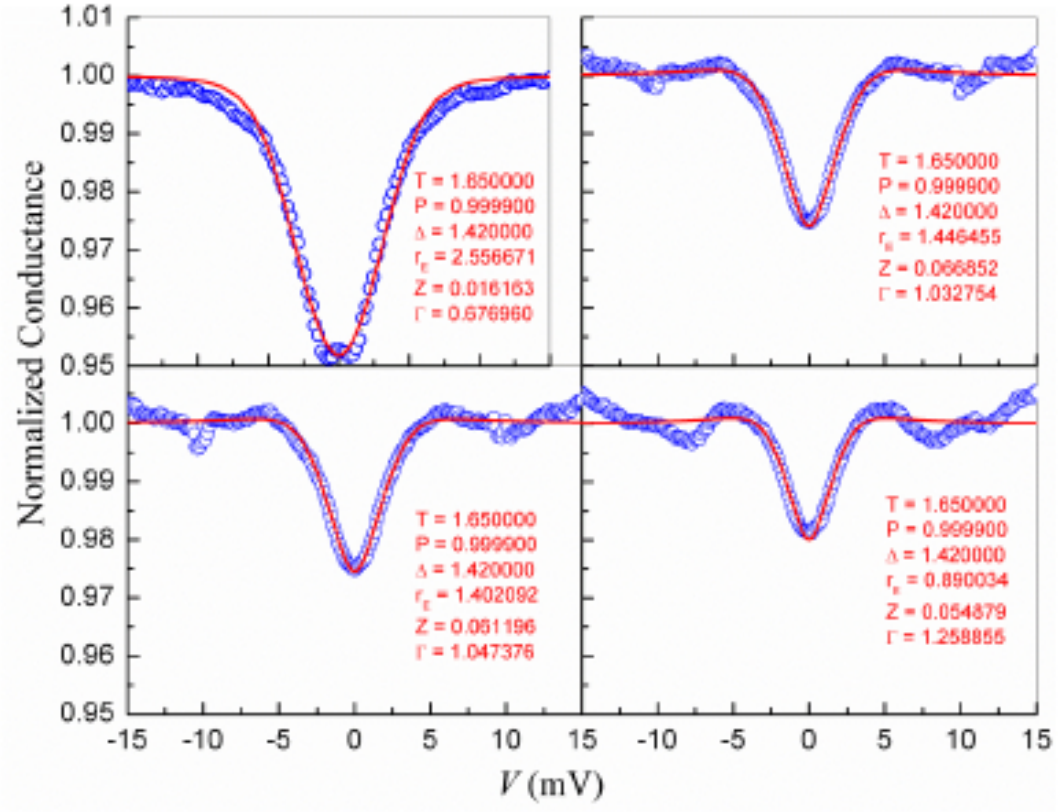

Figure 5.10: Normalized conductance measurements for amorphous Fe_3Si. Blue circles represent the data measured whereas the red lines are the fits to this data using a modified BTK theory, see section 1.3. The data is fitted well, thus Fe_3Si can be well described by this model.

10 K, the two peaks disappear, demonstrating that the two peaks are due to the superconducting state of the Nb.

In summary, Andreev Reflection Spectroscopy is a technique to determine spin polarization of a metal material and the superconducting gap of a superconductor. The ARS system was tested and has the accuracy and sensitivity of 0.01% even at voltage which scan from 0 to 10 V for resistor from 0.5 mΩ up to 1 MΩ. From these calibration experiments, it has been shown that ARS is an important technique for quantitatively measuring spin polarization and superconducting gap of various N/S interfaces.

5.3.3 PCAR Mechanical Setup

For the PCAR measurements, a connection head, a long thin stainless steel turning rod, a vacuum jacket, a differential screw head, and a thin stainless tube make up the mechanical setup for this device. Figure 5.12 shows a schematic set up. The connection head is needed for electrical connections to the sample and for temperature monitoring. The vacuum ports for the pumping and exchange gas (He) and the vacuum seal for the turning rod also rely on the connection head. To establish a point contact, a turning rod is turned outside of the vacuum and is turned by the rotating knob until the contact is created. The rod is attached to a differential screw and moves the tip closer to the sample until it makes contact with the sample. This screw is protected by a vacuum jacket which is immersed in liquid helium so that the tip can become superconducting and low temperature measurements can be obtained. Thermal conduction is often an issue in such systems, therefore, by ensuring the turning rod and tube are thin, this conduction can be minimized. To prevent condensation of air, and non-oxidation of the materials, the system is in vacuum at pressures of $\sim 10^{-6}$ Torr.

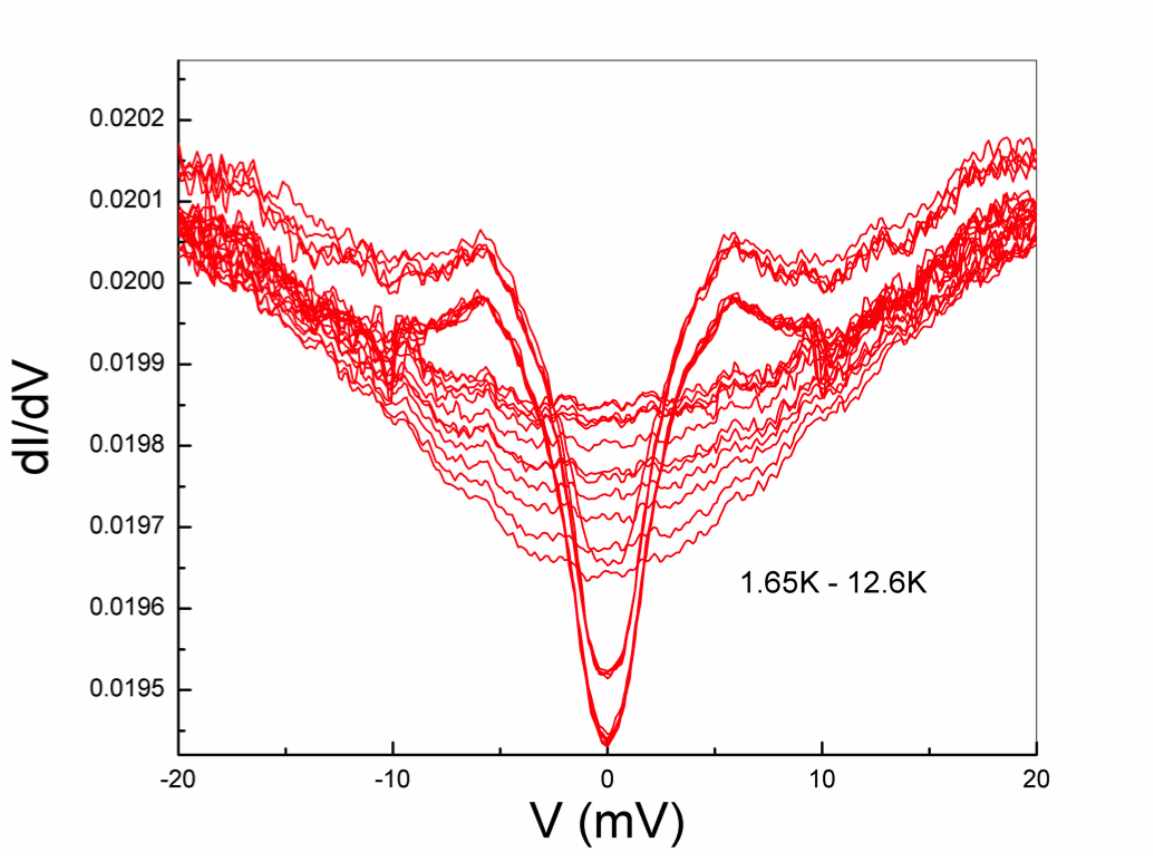

Figure 5.11: Temperature dependence of amorphous Fe_3Si at low temperature. At 1.65 K it is apparent the gap is indicative of Andreev reflection. As the temperature increases this gap begins to vanish until there is no Andreev reflection present.

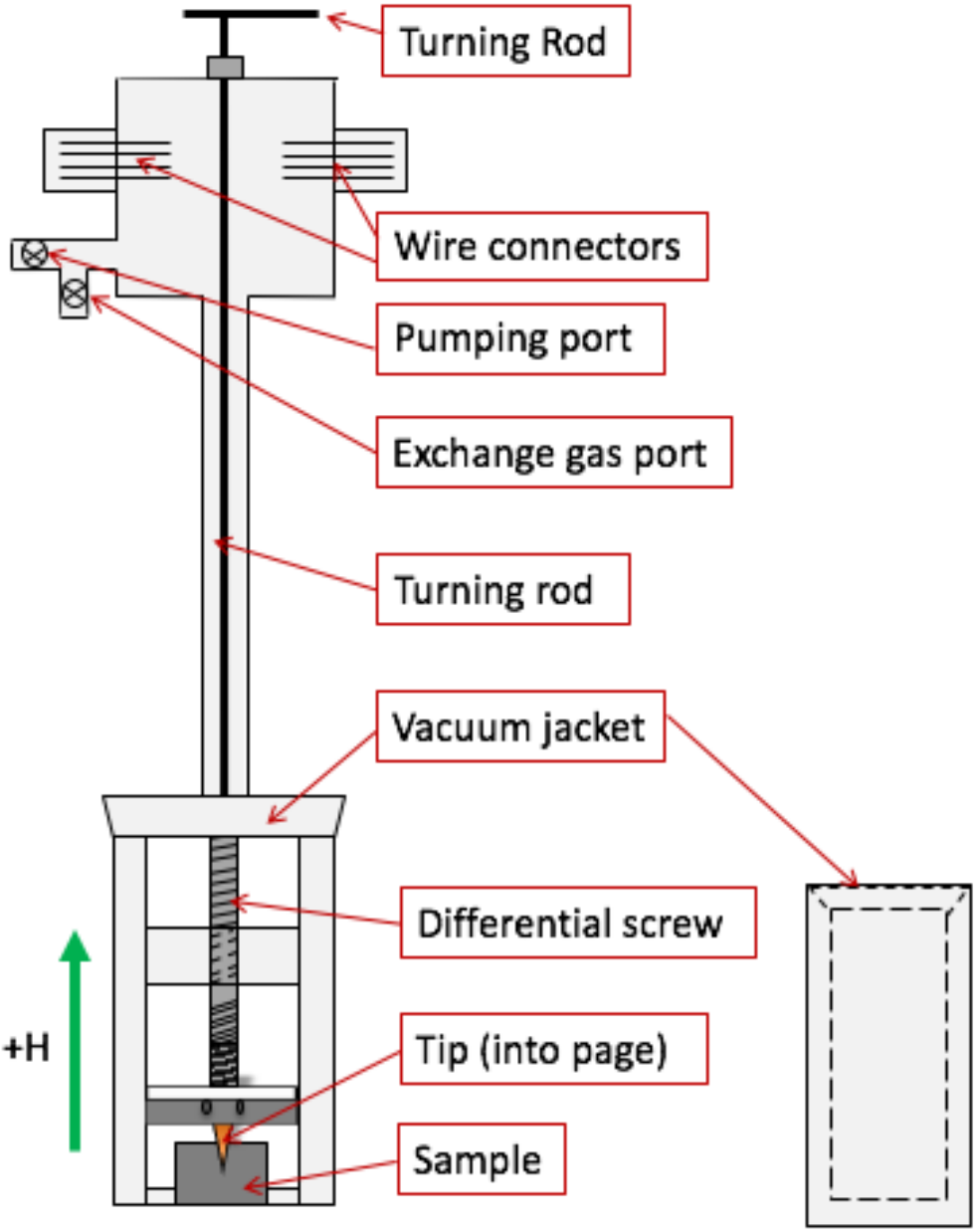

Figure 5.12: Probe for point-contact experiment and vacuum jacket schematic.

The system is also equipped with a magnetic field generator, Cryomagnetics Inc. The system also has a superconducting magnet, Model 4G Superconducting Magnet Power Supply. As shown in figure 5.13, the magnetic field **H** is along the tip perpendicular to the sample plane. The tip is connected to a spring in contact with the vertical tip, and only a small distance is needed to make the contact. Figure 5.13 shows a schematic of the differential screw head. This head utilizes the differences of two threads which can be used to move the device mechanically on a micro-meter scale. The rod is threaded differently with 5-54 and 5-57 threads on either side. Two blocks are trapped with 5-54 and 5-57, where the 5-54 thread is fixed and 5-57 is free to move. As the turning rod is moved clockwise, the thread moves closer to the sample by 1/54 inch every full turn. When the rod is moved counter clockwise the thread moves by 1/57 inch every turn. The differential screw head is made of pure copper to ensure a rapid thermal equilibrium, and non-magnetic brass screws are used to exclude other mechanical forces when the magnetic field is applied. Finally, a low temperature thermometer, Cryo-Coft 32B Temperature Controller, is attached to the differential head so that the temperature of the sample can be monitored and one can see if the critical temperature of the superconductor has been reached.

5.3.4 Electronic Setup

Differential resistance dV/dI is measured during the PCAR measurements and is done so by applying a small ΔI and detecting a small change in voltage ΔV. As described above, a four point PCAR method is used for this work. The current is supplied by a standard Keithley current source and the voltage is measured with a nano-voltmeter. To measure and apply the small changes ΔI a lock-in amplifier is needed as described in section 5.2.2. The lock-in amplifier used is the Stanford Research Systems Model SR830 DSP. It sends out an AC voltage of 0.1 V with a

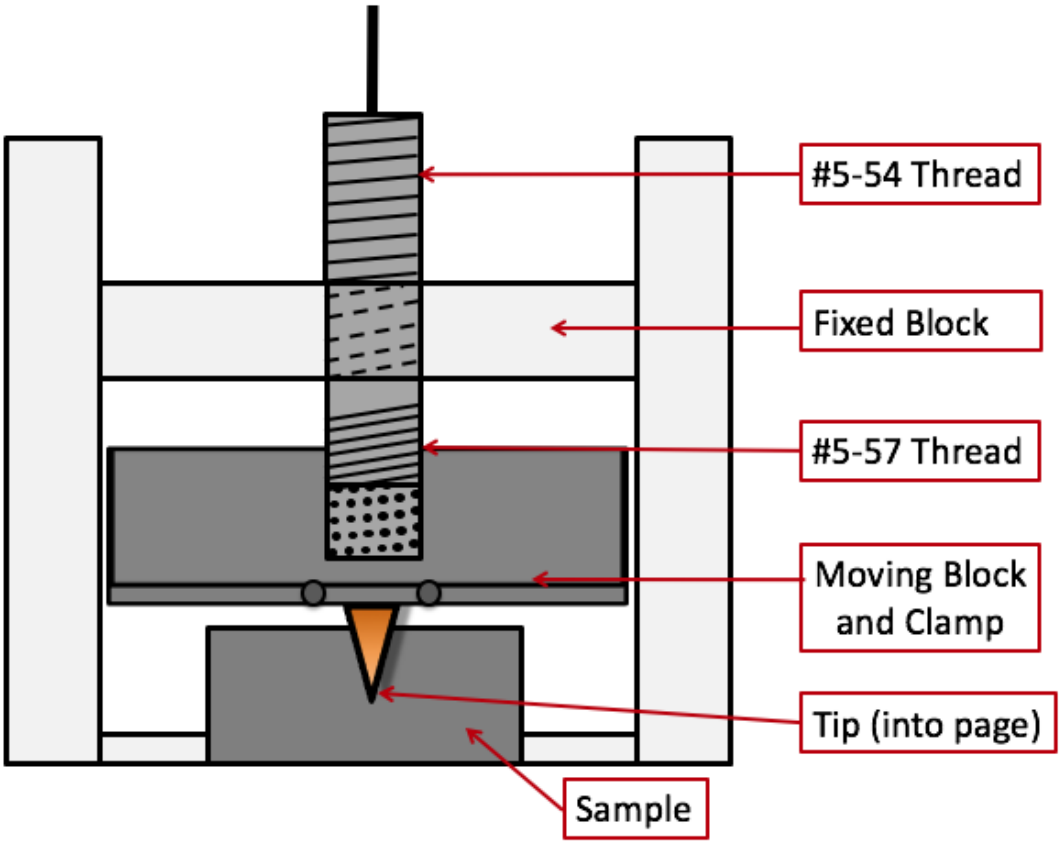

Figure 5.13: The mechanism of the differential screw. Note that the tip is out of plane while sample is in plane with the rest of the schematic.

frequency of 2 kHz. This is converted to a AC current ΔI by a 100 $k\Omega$ resistor. The small AC change is then superimposed on the DC current giving $I + \Delta I$ where ΔI is about $1\mu A$. The lock-in amplifier that detects AC voltage ΔV is connected at the same frequency of 2 kHz. The differential conductance is then measured using LabView by $dV/dI \cong \Delta V/\Delta I$. A switch box can be added so that the instruments so that multiple measurements can be conducted multiple using a computer program without changing the connections. This feature allows the temperature of the system to be measured by switching the box to another channel. All these components are shown in figure 5.14 (a) schematic and (b) actual devices. The LabView program is able to measure data points for $T, I, V, V/I, dV/dI$, and H.

Tip Preparation

Metallic tips are important for PCAR measurements. Many methods can be used to prepare the tips, but in this work two methods are used. The first method is to mechanically polish the tips. For this method often metallic wires of diameters on the order of 10^{-2} inch are used. First the tip is cut using scissors or a razor blade to create a sharp tip, while polishing stones of coarse grade 180-1200 are used to create a finer point. Using this method, the size of the tip is approximately $10\mu m$. One can use electerochemical process to etch the tips to sizes of $1\mu m$, however in these experiments $10\mu m$ is often acceptable.

The second method is to break apart pieces of single crystalline thin metallic films. Using either magnetron sputtering or pulsed laser deposition, thin films, such as LSMO (see chapter 9), can be grow to nano-meter scales. Often these materials are very easy to break apart and by doing so, due to its single crystalline structure, create fine tips. For this method, the process is done by collaborators such as the Nanjing University in China. Often these materials will be the normal metal com-

(a)

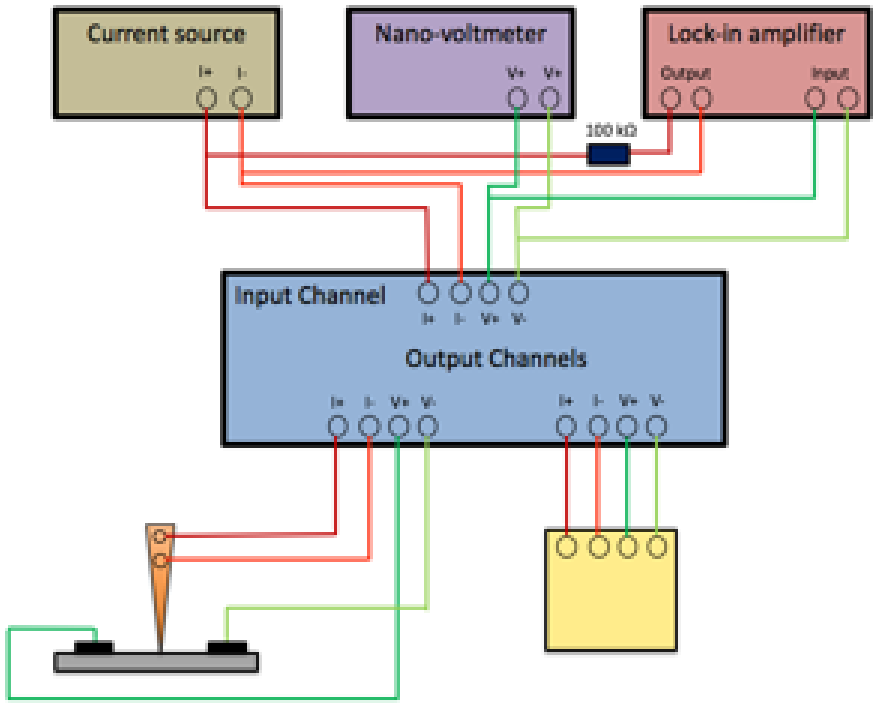

(b)

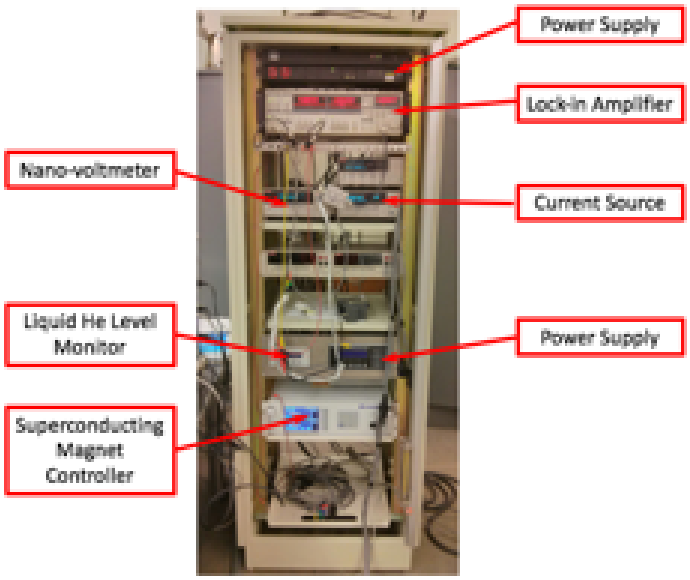

Figure 5.14: The electronic setup for the point-contact experiment (a) schematic (b) actual setup.

ponent of the N/S interface while the samples are the superconducting material. In the PCAR measurements the sample and tip can be switched without effecting any measurements.

5.3.5 Cryogenic Setup

In this work, measurements are all done at liquid helium temperatures. Therefore a cryo system is needed. Figure 5.15 shows the schematic setup. The cryo used is the Janis Cryo System which is comprised of an outer liquid nitrogen dewar, two inner liquid helium dewars, a superconducting magnet, and a sample tube. The superconducting solenoid located at the bottom of the dewar can give a magnetic field of up to 9 T, but in these experiments only a maximum of 2 T is needed, with a polarity pointing up as positive. The or sample tube has a vacuum jacket to thermally insulate the sample from the environment. Outside this inner dewar is a larger helium dewar that can store up to 25 inches of liquid He, measured with Cryomagnetics Liquid Cryogen Level Monitor. The liquid He is refilled every other day for continuous experiments. The liquid He from the outer dewar is released into the smaller dewar which holds the sample tube at the bottom by adjusting the needle valve. The liquid He is then shielded from the rest of the dewar which contains liquid nitrogen to keep the entire system cool and preserve the liquid He for longer. A vaporizer/heater controlled by a temperature controller is used to heat up the system past liquid He temperatures ($, 5K$ to $300K$) when required.

Because the sample tube size diameter is 2 inches, it is very important to avoid trapping air in the sample tube because O_2 as well as N_2 freeze at liquid helium temperatures. If air gets in then it can create an ice blockage which will get trapped in the needle valve between the helium storage tank and the sample tube area. If this occurs the entire system must be heated back to room temperature both wasting

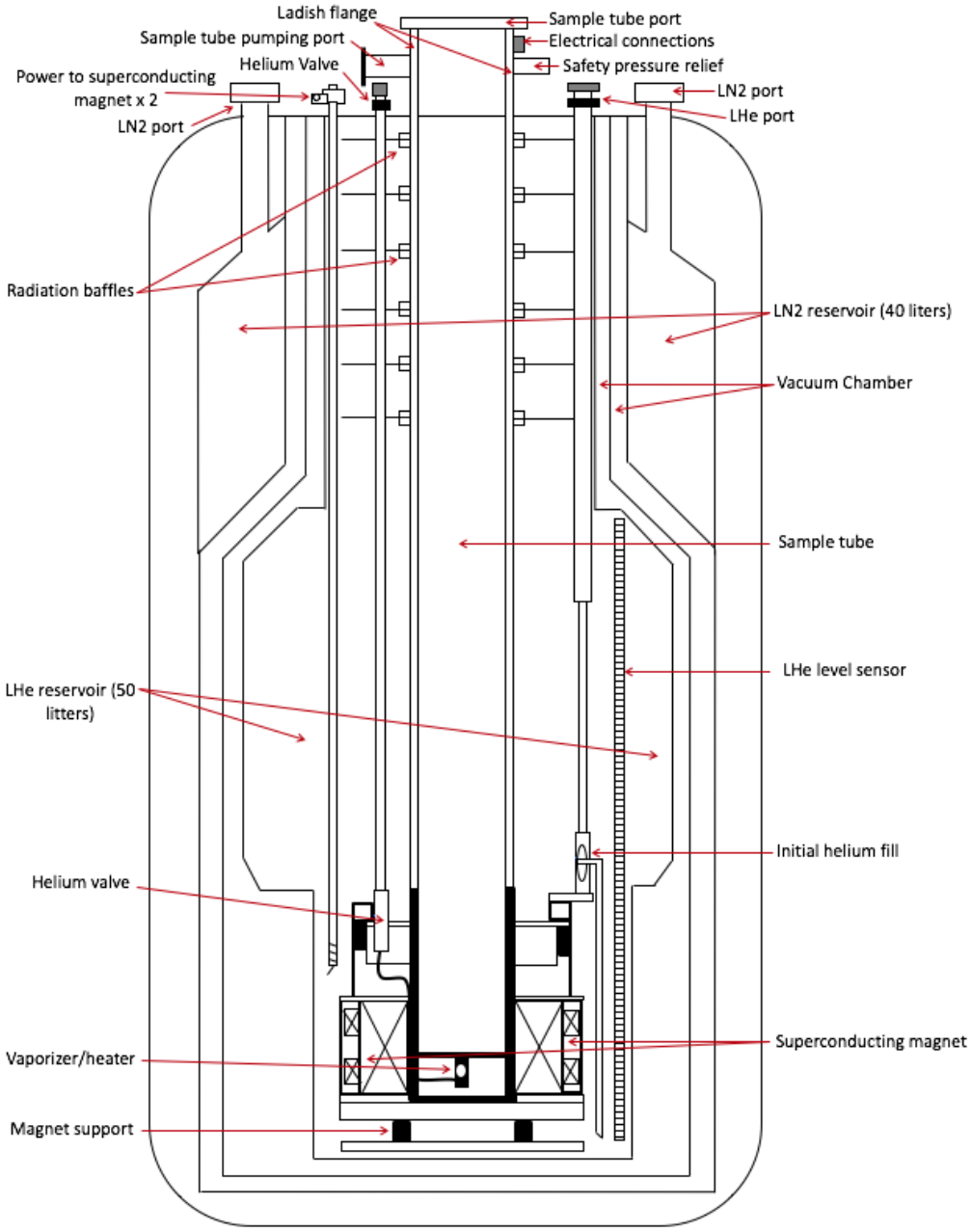

Figure 5.15: The cryogenic setup for the point-contact experiment.

considerable amounts of liquid He as well as a considerable amount of time. By following a few simple steps this can be avoided. Before opening the sample tube, it is important to make sure that it is pressurized with helium gas (which will not freeze). Once this is done then the needle valve in the pumping line can be opened and helium gas can then flow in. The needle valve should be opened roughly 2 turns to release the liquid He into the tube. Once the helium is filled then the ladish flange can open and then the point-contact probe can be loaded into the cryo. A pressure of ≈ 1 psi should be maintained during the cooling process.

It takes an average of 3 hours for the point-contact probe to reach liquid He temperatures of 4.2 K and experiments can start. Often temperatures of less than 4.2 K are required. To do this one simply can close the needle valve and then pump the sample tube. In the cryo temperatures of below 1.4 K can be obtained. For temperature dependent measurements it is often helpful to heat the system higher then 4.2 K, so to do this the heater must be used. On the heating controller the maximum temperature must be set, and once this is done the helium needle valve can be opened slightly while pumping the sample tube. As the temperature increases, the liquid He is vaporized. The temperature is controlled using the Proportional-Integral-Derivative (PID) control which will maintain set points and adjust controls as needed for the experiment. The disadvantage of the PID controller is that it is located at the bottom of the sample tube, therefore the temperature monitor attached to the point-contact tube should instead be used to monitor the sample temperature. LabView will monitor this temperature and record temperature verses time for all experiments.

5.4 Magnetron Sputtering Deposition

There are many different techniques to create thin film samples, but in this work one uses the magnetron sputtering technique. The samples grown are nanostructures which provide structures for fundamental studies of magnetism, superconductivity, and many more physical characteristics. Sputtering has become a well known deposition process for creating more pristine thin films. Using this process layers of atoms are deposited on a substrate with fine control. These films are considered 2D structures but by using lithography, ion milling, and other techniques the films can become 1D nano-line structures or even 0D nano-dot structures. Other techniques such as molecular beam epitaxy, e-beam deposition, chemical vapor deposition, atomic layer deposition, and others are commonly used. Magnetron sputtering is among these techniques and has many advantages such as the ability to make thin films in the angstrom range. Other advantages include increased ionization of argon gas, higher sputtering rates at lower ambient gas pressures, and fewer gas collisions creating a more direct line of the plasma material to the sample.

5.4.1 Magnetron Sputtering

In the basic sputtering process, a target (or cathode) is bombarded by excited ions in the presence of ambient gas which has a pressure of a few mTorr. In the presence of this ionized gas, a plasma is ignited around the target. The bombardment process causes the the target atoms to be ejected, which then condense on the substrate making the thin film. A biased negative DC voltage of ≈-300V is used to ignite the sputtering gun which holds the target. Often the ambient gas used is argon (Ar). The momentum of the Ar^+ is transferred to the surface of the target which causes the atoms to be ejected. Secondary electrons are also emitted from the target as

a result of the Ar^+ bombardment, and these electrons maintain the plasma, which is called diode sputtering. In diode sputtering some electrons and ions drift away from the target which creates a low deposition rate. Figure 5.16 shows a Solidworks schematic of the sputtering gun used in this system.

Magnetron sputtering differs from the basic sputtering technique by increasing the electron path in the plasma. This is done by applying a magnetic field parallel to the target surface which constrains the secondary electrons to the vicinity of the target. The magnets are arranged such that one pole is positioned at the central axis of the target and second pole is formed by a ring of magnets around the outer edge of the target. As shown in figure 5.17(a), the circular magnet below the target supplies the magnetic field. The magnets are soft iron which are used to concentrate the magnetic flux so that the magnetic flux forms a donut shape, called the magnetron. The actual gun is shielded by a gun cap. Because of the high voltages and heat produced in the sputtering target, water cooling is needed. Figure 5.17(b) shows the electrons and ions that would drift away instead being contained by a Lorentz force along the tangent direction of the circle. The electrons become trapped near the gun and form a circulating current instead of driving away electrons. The advantage is that this circulating current creates more Ar^+ which creates a larger sputtering rate on a circle of the target. The magnetron also allows for discharge to be maintained a lower pressures of about 10^{-3} mbar compared to regular sputtering of 10^{-2} mbar. Also lower operating voltages of $\sim$-300 V compared to -3 kV are obtainable.

There are many types of sputtering directions achievable in this system. The substrate holders are connected to a rotating motor which allows us to control the placement and movement of the system. Using LabView, a program was created to move the substrates above the plasma by configuring the number of steps in to do a complete turn in the vacuum chamber, the velocity of the axle of the motor is con-

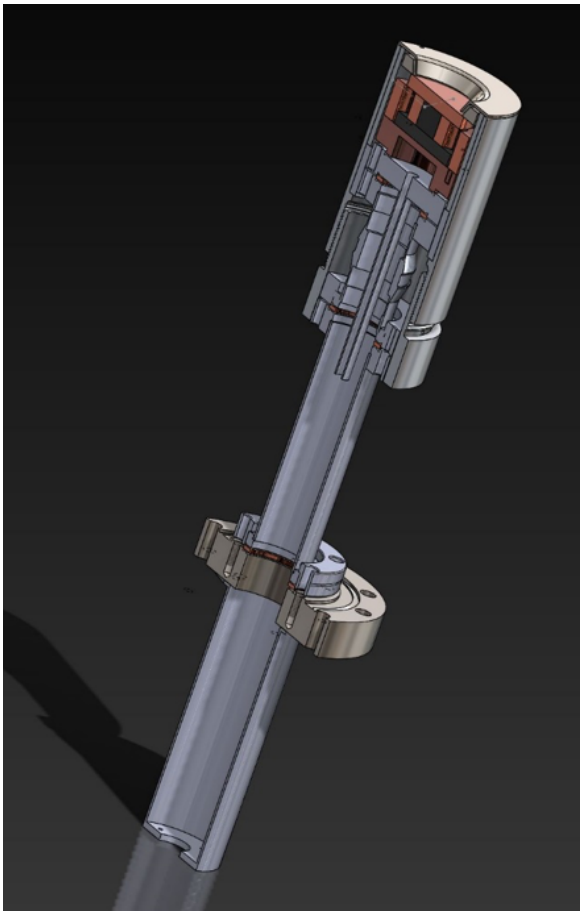

Figure 5.16: SolidWorks schematic of magnetron sputtering gun used in this system.

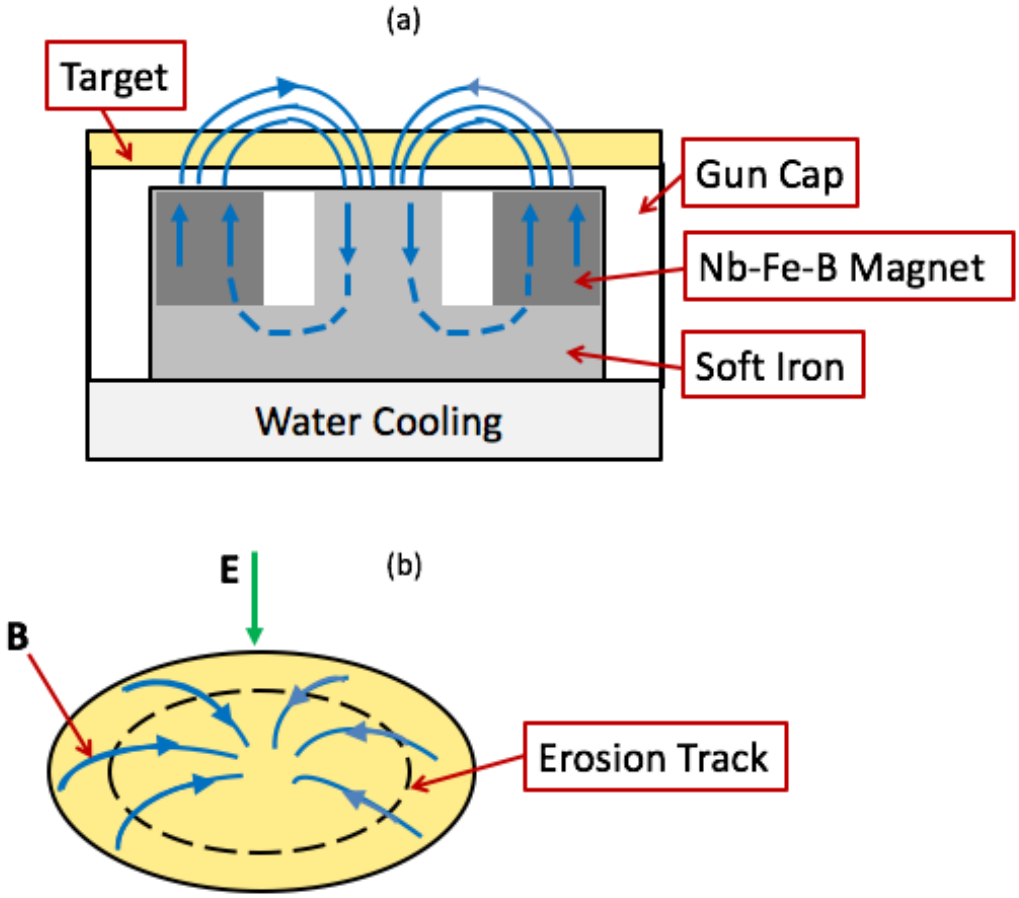

Figure 5.17: (a) The magnetron and (b) the E and B fields of the magnetron.

trolled. When depositing, the sweep method is used to take advantage of the plasma uniformity and uniformity of deposition. The deposition the substrate thickness is inputted (often 2 inches) and the substrate is swept across the target during deposition. This allows each position on the target to be deposited at the center of the plasma and avoids thickness fluctuations at the edges of the samples.

Using the sweep method, various controls can be used. The first is layer by thickness. Using the deposition rate of the target (see section 5.5) the desired thickness is put into LabView and the system will deposit the material by calculating the deposition time. Second, is layer by time with shaking which allows one to deposit the sample by time instead of thickness and the added shaking produces a more uniform field since the substrate will not sweep on this setting. Instead it shakes to allow for the edges to be more evenly coated and produce a more uniform film. Next is layer by thickness without shaking such that the substrate will just sit on top of the target during deposition. Finally a wedge method is used that can deposit gradients of thicknesses on one substrate. The gradient is created by using the sweep method and varying the time the plasma hits the target at different locations. A simple wedge can be deposited or a double wedge which allows two non-zero thickness edges and a finer control for thin gradients. The first wedge will wedge the sample for the thin thickness gradient and then wedge back and deposit the thicker layer onto the thin film. For the GMR structures one uses the double wedge method, see chapter refchap:GMR.

5.4.2 Vacuum System

A vacuum is needed for magnetron sputtering even though sputtering can occur at only a few mTorr of ambient gas. A ultra high vacuum is used with a small base pressure ($\approx 10^{-7}$ Torr) which is needed to prevent the residual gas and materials

sputtered from reacting with each other. The noble gas used must be of high purity and is often Ar in this system. By partially blocking the pumping path as AR gas is allowed to flow, the flow rate (22 sccm) is controlled and helps facilitate a larger plasma areas. The vacuum during sputtering is surprisingly lower than the base pressure during deposition.

In this work, magnetron sputtering is used to make thin film sample including the GMR structures in chapter 9. Figure 5.18 show the vacuum system with the ten available sputtering guns. The chamber is connected to a cryo pump via an electropneumatic gate valve, and a loadlock chamber for loading substrates. It contains a rotating substrate holder connected to the chamber through a UHV bellow that can be rotated and lifted up or down using a LabView program. The loadlock is connected to a smaller turbo pump for the sample chamber which has a rail that can slide into the main chamber to transfer up to 5 samples at a time. By having 10 guns in this system, one can have up to 10 targets and can deposit many different materials with multiple layers without opening the chamber. The gun selection is controlled by placing a shutter over the guns with a 3 in diameter, which is controlled with a motor.

Using LabView one can then pick the target wanted to deposit while covering any other targets turned on with the shutter. This makes depositing many layers much easier because both targets can be on, but the shutter ensures that only the desired material is reaching the substrate for the sample. All deposition times, shutter movement, and sample movement is controlled by LabView, such that one can program a multilayer sample, hit run, and the system will control itself until the entire sample is finished.

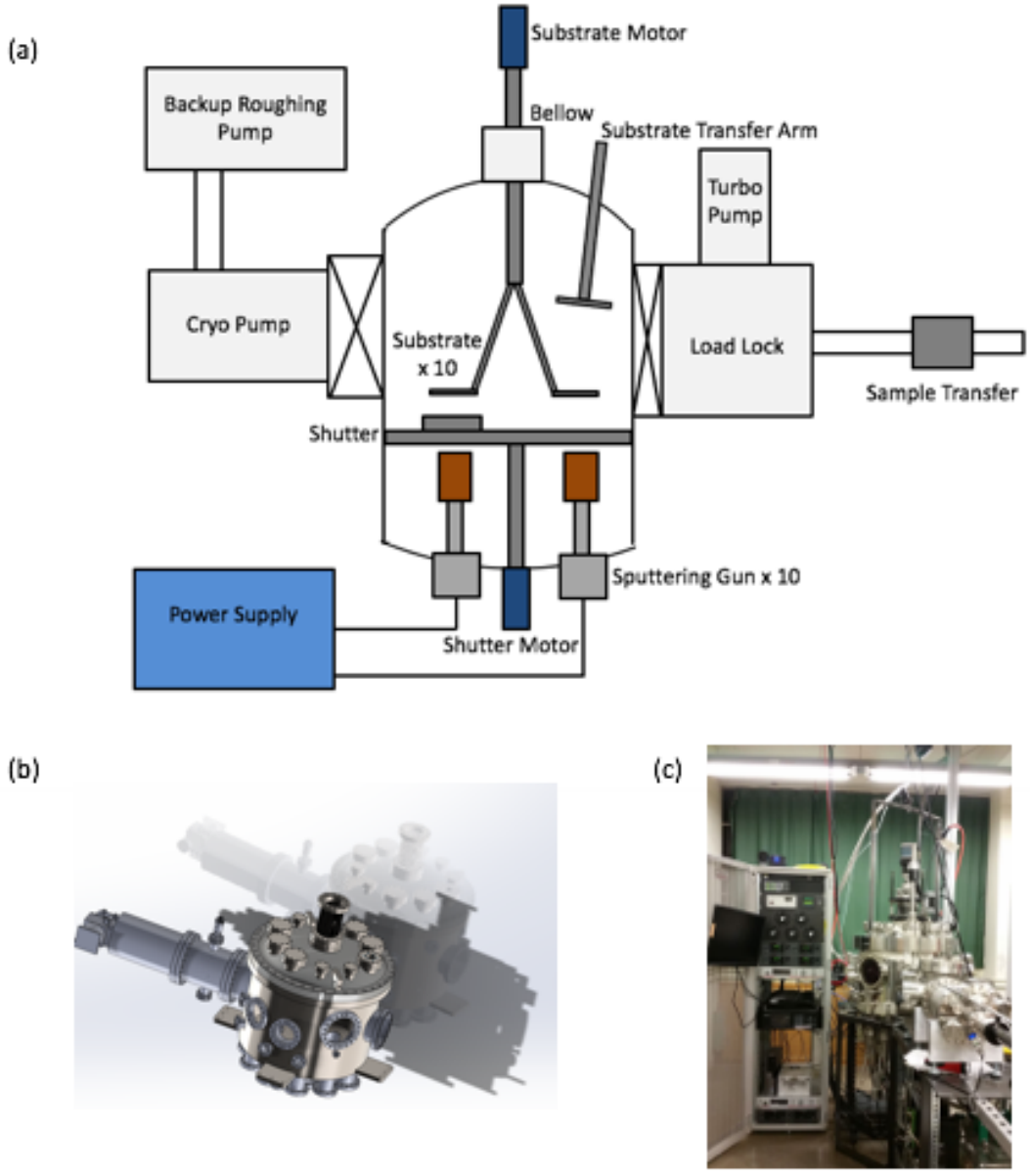

Figure 5.18: The vacuum setup of the sputtering system with 10 guns (a) schematic (b) Solid works model (c) actual chamber.

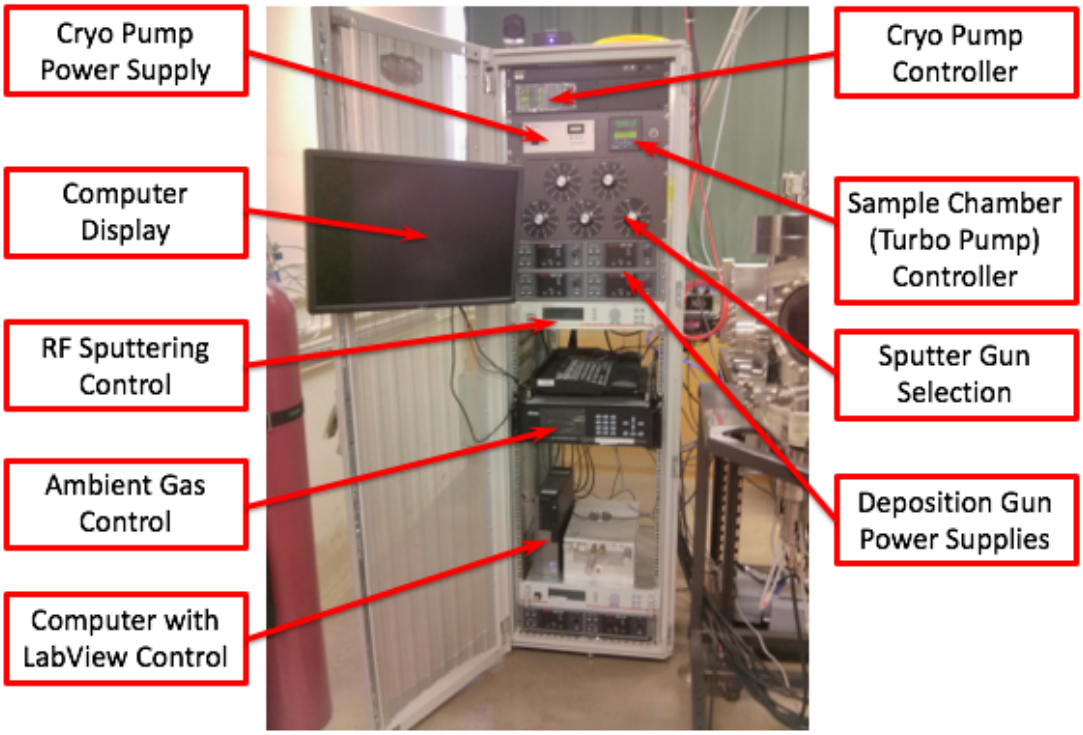

Figure 5.19: Electrical setup and equipment for ultra high vacuum system.

5.5 Rutherford Backscattering Spectroscopy

When getting a new target, the deposition rates of the target must first be found to then ensure thin film depositions are of the correct thickness. To do this an arbitrary thickness, usually tens of angstroms, is assumed with a deposition rate of 1 Å/s. In doing this, the time can be measured for the deposition process and the thickness can be measured, and thus a deposition rate can be found. To calculate the thickness of the samples made, Rutherford Backscattering Spectroscopy is used.

5.5.1 RBS Theory

In 1907, Rutherford worked on alpha particle research and was the first to describe it correctly. At the time. large-angle scattering of alpha particles was used to explain the results of many small-angle scattering using Thomson's "plum pudding model" of the atom [91]. This model states that the atom is made of electrons surrounded by a soup of positive charge to balance the electrons' negative charges, like plums surrounded by pudding in plum pudding. Rutherford did not agree with this model after photographing alpha particles scattered over a few degrees. He wanted to measure their number in relation to the angle of deflection and developed the Rutherford-Geiger tube to do so, which consisted of a vacuum with a metal foil in the middle and fluorescing plate at the end. The alpha particles were created with radiated radium and the flash of each measurement was observed with a microscope. In this experiment they were attempting to remove stray particles believed to be cause by an imperfection in their alpha source. However when positioning the detector on the same side of the foil, he noticed a backscattering signal. The plum pudding model states that these particle should be nonexistent, however, upon their discovery, Rutherford developed his backscattering theory.

The energy of the backscattered particle is

$$E_1 = kE_0 \ , \tag{5.4}$$

where k is the kinematic factor given by

$$k = \left[\frac{m_1 \cos\theta_1 \pm \sqrt{m_2^2 - m_1^2(\sin\theta_2)^2}}{m_1 + m_2} \right]^2 \ , \tag{5.5}$$

where particle 1 is the projectile particle, 2 is the target particle, and θ_1 is the scattering angle of the projectile in the laboratory frame of reference. The energy and the probability of observing an event is given by

$$\frac{d\omega}{d\Omega} = \left[\frac{Z_1 Z_2 e^2}{4E_0} \right]^2 \frac{16}{(\sin\theta)^4} \ , \tag{5.6}$$

where $d\omega/d\Omega$ is the differential scattering cross section, and Z_1 and Z_2 are the atomic numbers of the projectile and target particles. Finally the ion energy loss after passing through a given distance is given by the stoping power S(E):

$$S(E) = \frac{dE}{dx} \ . \tag{5.7}$$

The relative number of particles backscattered from the target atom is related to the differential scattering cross section. By counting the backscattered atoms and measuring their energy, RBS spectra of atoms verses energy can be found where the energy corresponds to the work function of the atoms measured. By analyzing this spectra the thickness of the layer can be calculated.

5.5.2 Instrumentation

There are three main components to the RBS instrumentation: source of He, an accelerator to convert the He ions into high energy alpha particles, and a detector to measure the energies of the backscattered ions. Figure 5.20 shows a schematic of

the tandem accelerator often used in RBS. It uses a positive terminal located in the center of the device. Negatively charge particles are injected into the accelerator and are attracted to the terminal where a stripper element removes two or more electrons from each particle. Thus the particle acquires energy both before and after the terminal. The tandem accelerator has a charged particle beam line in a tank containing high voltage and insulating gas, an electrode called the terminal, an electron charge stripper, and a vacuum system for the charge stripper and beam line.

5.5.3 RBS Measurements of Thin Films

Using RBS, a spectra of the number of backscattered electrons verses energy is measured. The energy position of the peaks correspond to the materials found in the sample. Often the substrate is Si and can span thickness of 0.2 to 1.0 meV due to the many isotopes of Si present in the substrate. The peak is often wide due to the very thick substrate layer compared with the actual thin film. The thickness can be found by the energy width of the peak. Figure 5.21 is a representative spectra of an RBS spectrum on Cu. The peaks of the SiO_2 substrate as well as the thin film are shown. From the width of the peak the thickness can be measured using RBS analysis software XRump, shown in figure 5.21 by the red line.

When fitting the data XRump uses the energy it measured and then the thickness x can be found by expanding the energy of the accelerated particles in a Taylor series and solving for x:

$$E_1 = E_0 + \Delta x \frac{dE}{dx} E_0 + \frac{1}{2} \Delta x^2 \frac{d^2 E}{dx^2} E_0 + ... \tag{5.8}$$

Figure 5.22 shows two more representative spectra for Pt and Co on SiO_2 substrates.

XRump can report the thickness in Å or in atoms/cm^2. Using the first assumes that the element is pure. However, one can see that using the atom density is best to

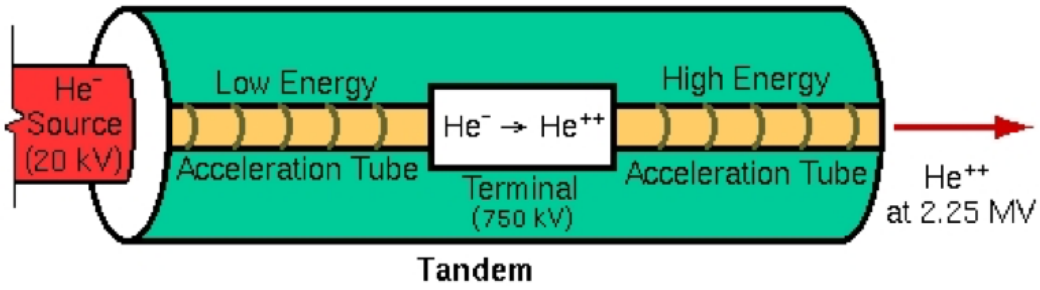

Figure 5.20: Tandem accelerator for RBS schematic. A charged particle beam line in a tank containing high voltage and insulating gas, an electrode called the terminal, an electron charge stripper, and a vacuum system for the charge stripper and beam line are the four main components of the system.

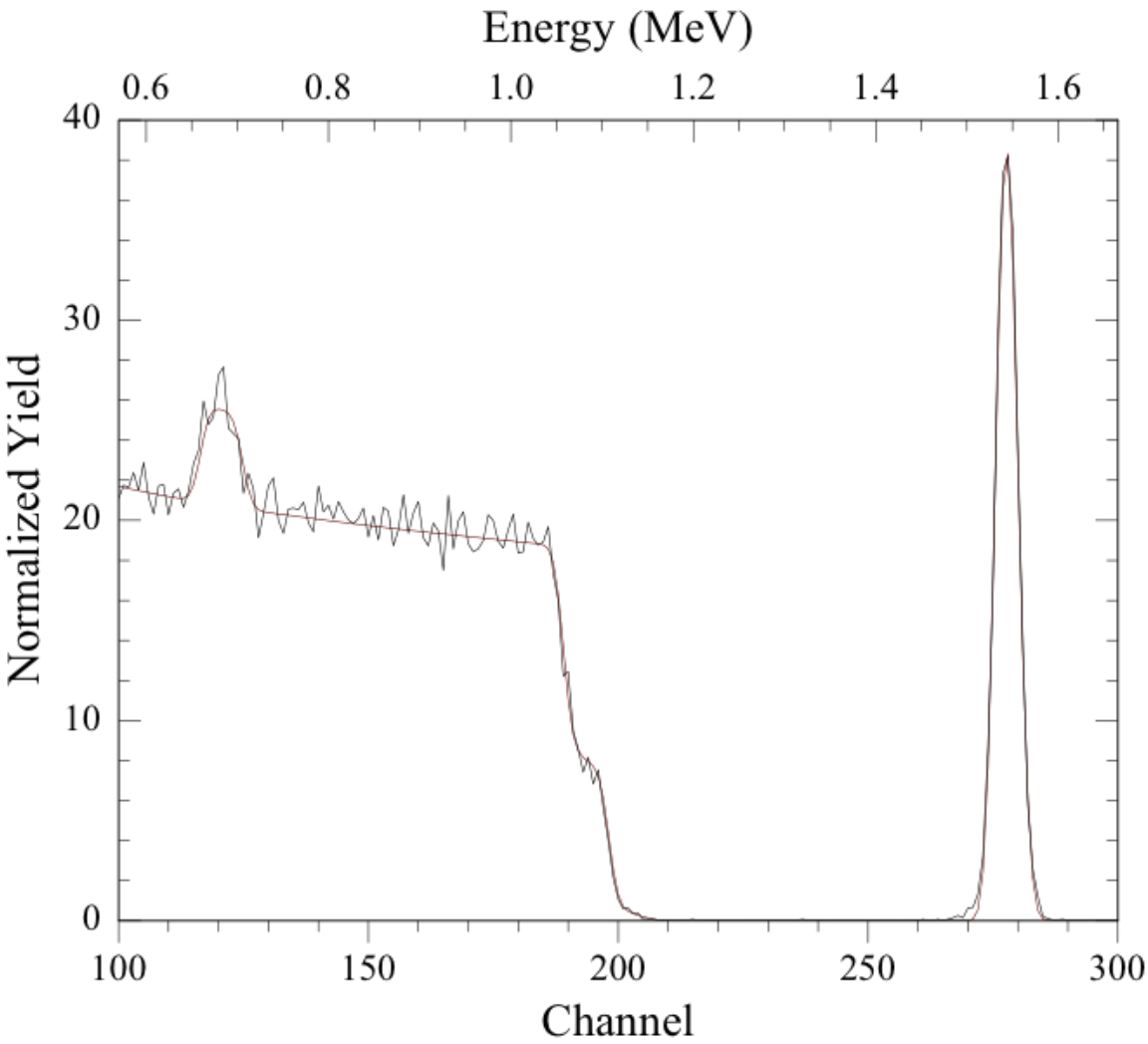

Figure 5.21: RBS spectrum of number of atoms verses energy for Cu thin film. The long peak corresponds to the SiO_2 substrate and skinnier peak at 275 meV is Cu thin film. Using XRump the spectra can be fitted (red line) to find the thickness in atoms/cm^2. This sample was deposited for 240 s and yielded $165 * 10^{15}$ $atoms/cm^2$ or 194.3 Å.

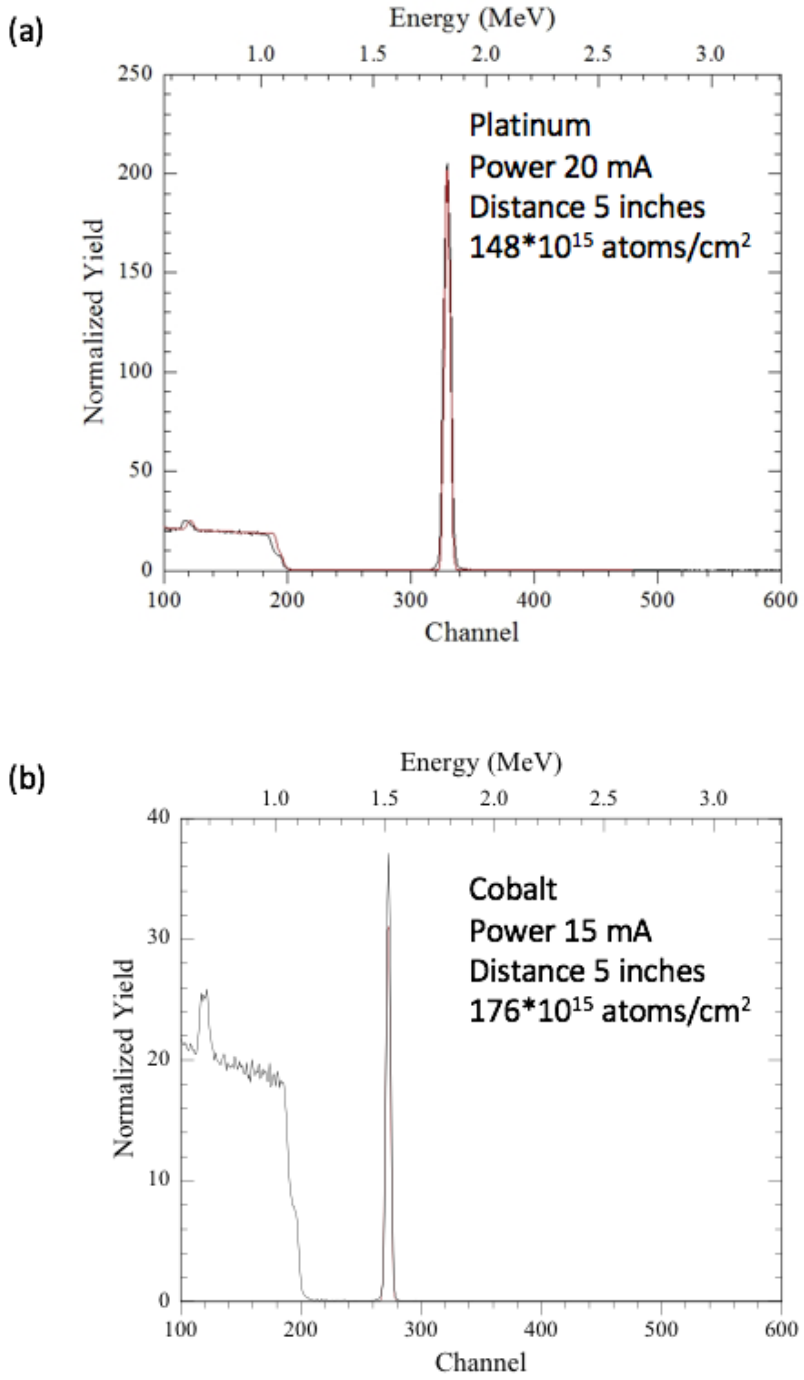

Figure 5.22: RBS spectra of number of atoms verses energy. The long peak corresponds to the SiO_2 substrate and skinnier peak is the thin film. Using XRump the spectra can be fitted (red line) to find the thickness in atoms. (a) Pt sample grown at measured in thickness (b) Co sample grown at 15 mA for 672 seconds measured 222 Å in thickness.

find the actual thickness. Using the atomic weight and density the thickness can be found:

$$Thickness(\text{Å}) = \frac{\text{measured atoms}/cm^2}{\text{density } g/cm^3} \frac{\text{Molar Mass } g/mol}{6.022 * 10^{23}\text{atoms}/mol} \frac{10^8\text{Å}}{cm} \ . \tag{5.9}$$

Note that the thickness of an material with two elements can be found by multiplying the fractional percentage of the element to the weight and density and adding these together for the total weight and density. Using this method each target in this sputtering gun is calibrated with the correct deposition rates. To find the deposition rate one takes the time it took to make the film in seconds and divides the RBS thickness by this number to get $\text{Å}/s$. Figure 5.23 shows the material, power at which the guns are set, distance from target to substrate, thickness of the film in Å using equation 5.9, time to measure the sample, and calculated deposition rates.

Material	Current (mA)	Height (in)	sample-shutter (in)	Thickness (atoms/cm²)	Thickness (Å)	Time (s)	Rate (Å/s)
Cu	10	4	2"-2"	2.40E+017	282.7	369	0.766
Cu	20	4	2"-2"	3.15E+017	371.0	219	1.694
Cu	20	4	3"-2"	2.50E+017	294.4	219	1.344
Cu	10	5	2"-2"	1.18E+017	139.0	369	0.377
Cu	20	5	2"-2"	1.50E+017	176.7	219	0.807
Co	15	4	2"-2"	2.37E+017	299.3	674	0.444
Co	30	4	2"-2"	2.30E+017	290.4	281	1.034
Co	30	4	3"-2"	1.70E+017	214.7	281	0.764
Co	15	5	2"-2"	1.58E+017	199.5	674	0.296
Co	30	5	2"-2"	1.20E+017	151.5	281	0.539
Pt	10	4	2"-2"	1.65E+017	270.4	246	1.099
Pt	15	4	2"-2"	3.05E+017	499.8	328	1.524
Pt	20	4	2"-2"	2.90E+017	475.2	246	1.932
Pt	20	4	3"-2"	2.35E+017	385.1	246	1.565
Pt	10	5	2"-2"	1.10E+017	180.2	246	0.733
Pt	20	5	2"-2"	1.49E+017	244.2	246	0.992
Fe	15	4	2"-2"	1.93E+017	227.7	600	0.380
Fe	30	4	2"-2"	1.90E+017	224.2	291	0.770
Fe	30	4	3"-2"	1.70E+017	200.6	291	0.689
Fe	15	5	2"-2"	1.05E+017	123.9	600	0.206
Fe	30	5	2"-2"	1.00E+017	118.0	291	0.405
Py	20	4	2"-2"	1.36E+017	158.7	303	0.524
Py	30	4	2"-2"	1.96E+017	228.8	213	1.074
Py	40	4	2"-2"	2.20E+017	256.8	161	1.595
Py	20	5	2"-2"	1.25E+017	145.9	303	0.482
Py	40	5	2"-2"	1.25E+017	145.9	161	0.906
Nb	30	4	2"-2"	3.05E+017	549.1	426	1.289
Nb	60	4	2"-2"	3.05E+017	549.1	233	2.356
V	20	4	2"-2"	5.20E+016	80.0	300	0.267
V	40	4	2"-2"	9.80E+016	150.7	200	0.754
Ti	20	4	2"-2"	7.10E+016	121.3	300	0.404
Ti	40	4	2"-2"	9.50E+016	162.2	300	0.541
CoFeB	15	4	2"-2"	8.30E+016	98.7	300	0.329
CoFeB	30	4	2"-2"	1.25E+017	148.7	200	0.744
CoFeB	15	4	3"-2"	1.15E+017	136.8	200	0.684
Cu	20	4	3"-2"	1.34E+017	157.8	219	0.721
Cu	20	4	3"-2"	1.23E+017	144.9	219	0.661
Cu	20	4	3"-2"	1.02E+017	120.1	219	0.549
Cu	20	4	3"-2"	7.40E+016	87.2	219	0.398
Cu	20	4	3"-2"	4.30E+016	50.6	219	0.231
Cu	20	4	3"-2"	2.10E+016	24.7	219	0.113
Co	15	4	2"-2"	2.03E+017	252.3	674	0.374
Co	30	4	2"-2"	1.00E+017	109.7	281	0.390
Co	30	4	3"-2"	1.35E+017	148.1	281	0.527
Co	15	5	2"-2"	1.76E+017	193.1	674	0.286
Co	30	5	2"-2"	9.00E+016	98.7	281	0.351

Figure 5.23: RBS calibration of various targets to find deposition rates. The material, current supplied to the sputtering guns, distance from substrate to target, thickness measured by XRump, calculated thickness using atomic weight and density, time to deposit each sample, and deposition rate are all recorded.

Chapter 6

EFFECT OF THREE DIMENSIONAL INTERFACE IN DETERMINATION OF SPIN POLARIZATIO USING ANDREEV REFLECTION SPECTROSCOPY

A theoretical study of a three-dimensional (3D) normal metal/superconductor interface with arbitrary spin polarization and interface geometry is presented [92]. The interface geometry can drastically affect the Andreev spectrum due to the 3D injection. The 3D effect can be attributed to a larger interfacial scattering factor in the 1D model, yielding the same intrinsic spin polarization and superconducting gap as the 3D model. This demonstrates that the 1D model can be utilized to extract the intrinsic spin polarization and the superconducting gap values for a 3D interface as long as the interfacial scattering factor is not concerned.

6.1 Introduction

The efficiency of spintronic devices will depend crucially on spin polarization (P), which is defined as the normalized imbalance of the number of spin up and spin down electrons at the Fermi level. In a superconductor, the mechanism of superconductivity can be revealed by the superconducting gap (Δ). The spin polarization of a magnetic material and the superconducting gap of a superconductor are thus important quantities, yet there are only a few methods that can measure either of them. Andreev reflection spectroscopy (ARS) is one such method, and is unique, which can measure both the spin polarization and the superconducting gap.

At the Normal metal/Superconductor (N/S) interface, an electron must be accompanied by another electron with opposite spin to form a Cooper pair to be present in the superconductor, with a hole reflected back to the normal metal. This is the

Andreev reflection [93]. The conductance of the interface for electron energies inside Δ is twice that of electrons outside Δ. If the current is fully polarized, the conductance is zero within Δ because of the lack of opposite spin to form the Cooper pair. Thus, the P of the normal metal and the Δ of the superconductor can be measured by the conductance spectra. In an actual experiment, the interface is often not ideal and an analysis of the entire conductance spectrum is necessary to extract Δ and P. The spin polarization of many magnetic materials [15–27] including some half metals [22, 23] has been measured by ARS. Also, the gap of many superconductors, including the recently discovered Fe-superconductors [28, 29], has been determined by ARS. However, most of these experiments have been analyzed using one dimensional (1D) models[83, 84, 86, 94]. In an actual ARS experiment, an interface is often formed using a tip with a certain point angle, thus, it is not exactly 1D. The effects of a three dimensional (3D) interface have been studied before [25, 95–98], but mostly for unpolarized current. Spin polarization has been also incorporated into ARS using the 3D effect [87, 88] where suppression of the Andreev reflection only occurs for electrons within some angular range.

In this chapter, one studies the effect of a 3D N/S interface with arbitrary spin polarization and geometry. The spin polarization is incorporated based on the recent 1D ChenTesanovic-Chien (CTC) model [83]. The 3D interface can drastically change the Andreev spectra which can be well described by the 1D model with a different Z factor but with the same intrinsic spin polarization and superconducting gap. At large $Z(> 1)$, neglect of the 3D effect causes substantial spurious spin polarization.

6.2 Theory

Consider an electron incoming with an angle of θ_N to the normal of the N/S interface, as shown schematically in figure 6.1. The wave vectors of the incident elec-

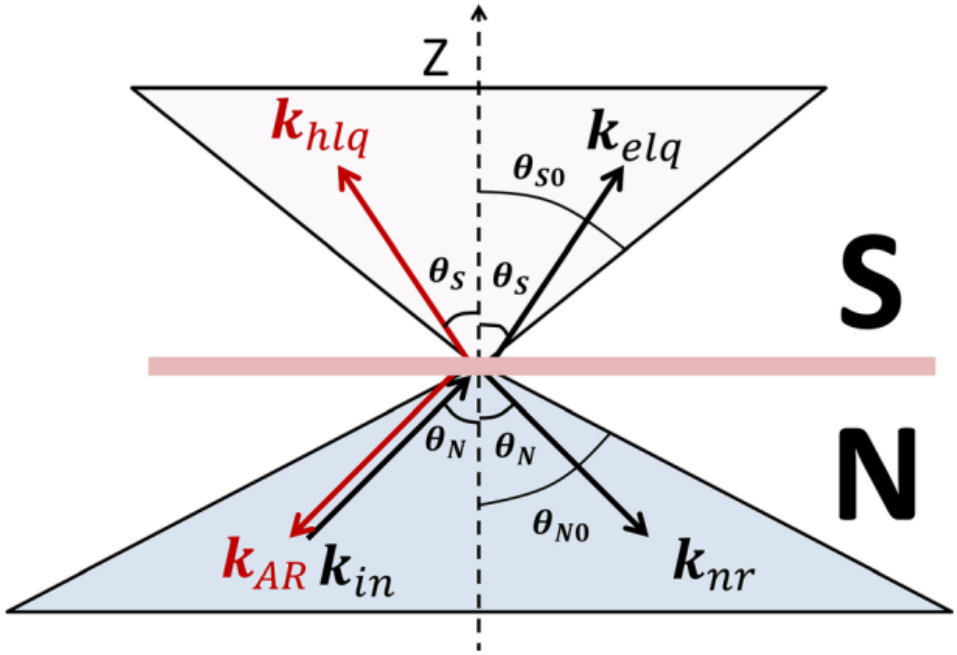

Figure 6.1: Schematic of a N/S interface with point angle of $2\theta_{N0}$ for the magnetic metal side and $2\theta_{S0}$ for the superconductor size.

tron, the Andreev reflection, the normal reflection, and the transmitted quasiparticles without and with branch-crossing can be respectively written as:

$$\mathbf{k}_{in} = (k_{Nx}^{+}, k_{Ny}^{+}, k_{N}^{+}\cos\theta_N) \ , \tag{6.1}$$

$$\mathbf{k}_{AR} = (-k_{Nx}^{-}, -k_{Ny}^{-}, -k_{N}^{-}\cos\theta_N) \ , \tag{6.2}$$

$$\mathbf{k}_{nr} = (k_{Nx}^{+}, k_{Ny}^{+}, -k_{N}^{+}\cos\theta_N) \ , \tag{6.3}$$

$$\mathbf{k}_{elq} = (k_{Sx}^{+}, k_{Sy}^{+}, k_{S}^{+}\cos\theta_S) \ , \tag{6.4}$$

$$\mathbf{k}_{hlq} = (-k_{Sx}^{-}, -k_{Sy}^{-}, k_{S}^{-}\cos\theta_S) \ , \tag{6.5}$$

where $\hbar k_N^{\pm} = \sqrt{2m(\mu_N \pm E)}$ and $\hbar k_S^{\pm} = \sqrt{2m(\mu_S \pm \sqrt{E^2 - \Delta^2})}$. Since $\mu \approx E_F >> \Delta$ or E, one can take the approximations $k_N^{\pm} \approx k_S^{\pm} \approx k_F$. The wave functions in the normal metal and the superconductor can be written as:

$$\psi_N(\mathbf{r}) = e^{ik_{in}\cdot\mathbf{r}} \begin{bmatrix} 1 \\ 0 \end{bmatrix} + ae^{-(\alpha+i)\mathbf{k}_{AR}\cdot\mathbf{r}} \begin{bmatrix} 0 \\ 1 \end{bmatrix} + be^{i\mathbf{k}_{nr}\cdot\mathbf{r}} \begin{bmatrix} 1 \\ 0 \end{bmatrix} \ , \tag{6.6}$$

$$\psi_S(\mathbf{r}) = ce^{i\mathbf{k}_{elq}\cdot\mathbf{r}} \begin{bmatrix} u \\ \nu \end{bmatrix} + de^{-\mathbf{k}_{hlq}\cdot\mathbf{r}} \begin{bmatrix} \nu \\ u \end{bmatrix} \ , \tag{6.7}$$

where a,b,c, and d are the coefficients of the Andreev reflection, the normal reflection, the transmission without branch-crossing, and the transmission with branch crossing, respectively. And u and ν are the BCS complex coherence factors:

$$u = 1/2 + \sqrt{(E - i\Gamma)^2 - \Delta^2}/[2(E + i\Gamma)]^{1/2} \ , \tag{6.8}$$

$$\nu = 1/2 - \sqrt{(E - i\Gamma)^2 - \Delta^2}/[2(E + i\Gamma)]^{1/2} \ . \tag{6.9}$$

The parameter Δ is the superconducting gap and the factor Γ represents the inelastic scattering. In the Andreev reflection term, a denotes the effect of the spin polarization based on the CTC model with $P = \alpha^2/(\alpha^2 + 4)$ [83]. The wave functions must satisfy the boundary conditions of a potential $H\delta(z)$ at the interface and there is

translational invariance in x- and y directions. One notes that this is still valid for a conic tip perpendicular to the interface discussed below since any injection with a valid angle can find valid reflections and transmissions inside the cone.

The calculated coefficients a, b, c, and d are:

$$a = 4u\nu\cos\theta_N\cos\theta_S/\gamma\ , \tag{6.10}$$

$$b = \left(-u^2[2Z + i(\cos\theta_N - \cos\theta_s)]Z_+ + \nu^2[2Z + i(\cos\theta_N + \cos\theta_S]\right)Z_-/\gamma\ , \tag{6.11}$$

$$c = -2iZ_+u\cos\theta_N/\gamma\ , \tag{6.12}$$

$$d = 2IZ_-\nu\cos\theta_N/\gamma\ , \tag{6.13}$$

where $Z_\pm = 2Z + (i+x)\cos\theta_N \pm i\cos\theta_S$ and $\gamma = u^2[2Z - i(\cos\theta_N + \cos\theta_S)]Z_+ - \nu^2[2Z - i(\cos\theta_N - \cos\theta_S)]Z_-$. These results depend on Z, α, E, Γ, θ_S, and θ_N, where Z represents the interfacial scattering, $Z \equiv \frac{mH}{\hbar^2 k_F}$ with k_F the Fermi velocity. These are the general results for an interface between a magnetic metal and an s-wave superconductor. The probabilities of the Andreev reflection, the normal reflection, and the transmissions can be calculated by the integration of aa^*, bb^*, $cc^*\nu_g$, and $dd^*\nu_g$ over all the solid angles of the interface, where ν_g is the group velocity. One can readily verify that if $\nu_g = (uu^* - \nu\nu^*)\cos\theta_S/\cos\theta_N$ for any Z, α, E, and Γ, consistent with the boundary requirements. The result reduces to the 1D CTC model when $\theta_N = \theta_S = 0$. The conductance of the interface under a bias voltage can be calculated following the classic Blonder-Tinkham-Klapwijk (BTK) approach [81]:

$$\frac{dI}{dV} = \int_{-\infty}^{\infty}\frac{1}{k_BT}\frac{e^{\frac{E-eV-\mu}{k_bT}}}{\left(1+e^{\frac{E-eV-\mu}{k_BT}}\right)^2}(1+A-B)dE/(1-B_{NN})\ , \tag{6.14}$$

where A and B are the probabilities of the Andreev reflection and the normal reflection. At large bias ($eV >> \Delta$), $a = 0$, $bb^*_{NN} = [4Z^2+(\cos\theta_N-\cos\theta_S)^2/[4Z^2+(\cos\theta_n+\cos\theta_S)^2]$, which reduces to previous results with $\theta_N = \theta_S$ [99]. The probability B_{NN} is calculated from bb^*_{NN} by the average of the solid angles of the interface.

The AR spectrum of a 3D interface depends on the parameters Z, α, Γ, Δ, and the geometry of the interface. For simplicity, one can choose two conic tips with point angles of $2\theta_{N0}$ and $2\theta_{S0}$ for the interface, as illustrated in figure 6.1. 1. One can verify that the Andreev spectra depends on the geometry (θ_{N0} and θ_{S0}) of the interface. In a ballistic contact, the components of the wave vectors along the interface are conserved, $k_N \sin\theta_N = k_S \sin\theta_S$ (Ref. [100]). Here one can neglect the Fermi wave vector mismatch, so one can have $\theta_N = \theta_S$. In the following, one can focus the discussion on the 3D model with $\theta_N = \theta_S$ and the coefficients are obtained by setting $\theta_N = \theta_S$.

6.3 3D Model verses 1D Model

The comparison between the 1D and the 3D AR spectra is illustrated in figure 6.2 with $2\theta_{N0} = 2\theta_{S0} = \pi$ and $T = 0K$. The black solid curves are for the 1D interface while the dashed red curves are for the 3D interface. At $Z = 0$, the 1D and 3D AR spectra are the same (figure 6.2(a)) but they are very different when $Z = 0.5$. The 3D spectrum is much lower than the 1D spectrum, as shown in figure 6.2(b). For larger Z, such as $Z > 1$, the difference becomes smaller. Since the 3D effect appears at $Z > 0$, the plot of the 1D and the 3D spectra with various P values for $Z = 0.1$ in figures 6.2(e)(h) is obtained. Again, the 3D spectra are different from the 1D spectra with different P values. The difference is small only for a half-metallic current of $P = 1$, as shown in figure 6.2(h).

As shown above, the 3D and the 1D Andreev spectra can be very different. This may affect the value of spin polarization and superconducting gap determined using ARS. Previously many experiments [15–22, 22–27] have been done using only the 1D model to extract spin polarization and superconducting gap. In the following, one can analyze the 3D interface using the 1D model, in particular, one uses the 3D model

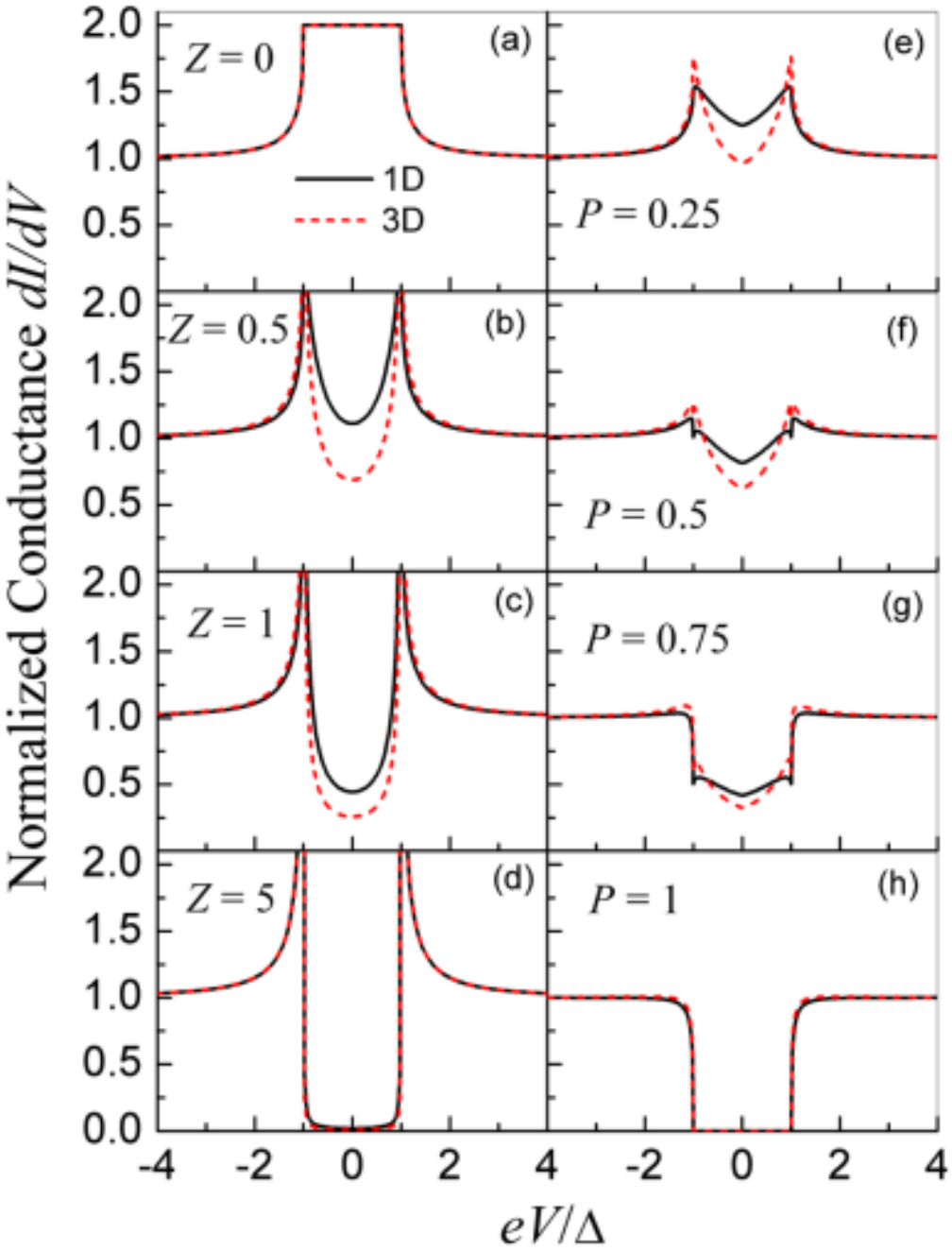

Figure 6.2: Representative Andreev spectra of the 1D (solid black) model and the 3D model with $\theta_N = \theta_S$ (dashed blue line) at $T = 0K$ ((a)(d)) for various interfacial scattering factors $Z = 0, 0.5, 1, 5[P = 0, \Gamma = 0]$ and (e)(h) for various spin polarizations $P = 0.25, 0.5, 0.75, 1.0[\Gamma = 0, Z = 0.1]$.

to generate data, then fit the data with the 1D model.

As shown in figure 6.3, three different polarizations $P = 0, 0.45$, and 0.9 with various Z factors at $T = 1.5K$ normalized at high bias are examined. In analysis, one can take three cases to mimic actual experimental scenarios: using a superconductor with a known gap to fit an unknown polarization (black solid curve), and using a metal with a known polarization to fit an unknown gap (red dashed curve). In the third case, both the superconductor and the magnetic metals are assumed to be unknown (blue dotted curve). The 3D data can be well described by the 1D model, as shown in figures 6.3(a)(c) for all the P values and Z factors. In fact, the analysis curves of the three cases, black solid, red dashed, and blue dotted curves, are almost indistinguishable from each other.

6.4 3D verses 1D Fitting Parameters

The parameters of the best fit are plotted in figure 6.3(c) and (d). For $P = 0$ in the 3D data, the spin polarization obtained using the 1D model is very close to zero (within 2%) for $Z < 1$, as shown by the squares in figure 6.3(c). However, P increases for $Z > 1$ and it reaches about 20% at $Z = 2$. This is a spurious spin polarization caused by neglecting the 3D injection. At large $Z > 1$, the conductance within the gap is very close to zero thus causes large uncertainty in extracting spin polarization. For a material with modest spin polarization of 45%, again the spin polarization obtained using the 1D model only deviates from the 3D value for $Z > 1.0$, as shown by the open and solid circles in figure 6.3(c). For highly spin-polarized materials, such as $P = 0.9$, the 1D model always gives an value that is within 1% of the 3D value, as shown by the triangular symbols in figure 6.3(c). For the three cases, one obtains the intrinsic spin polarization by extrapolating Z to zero, and both the 1D and the 3D models give exactly the same values.

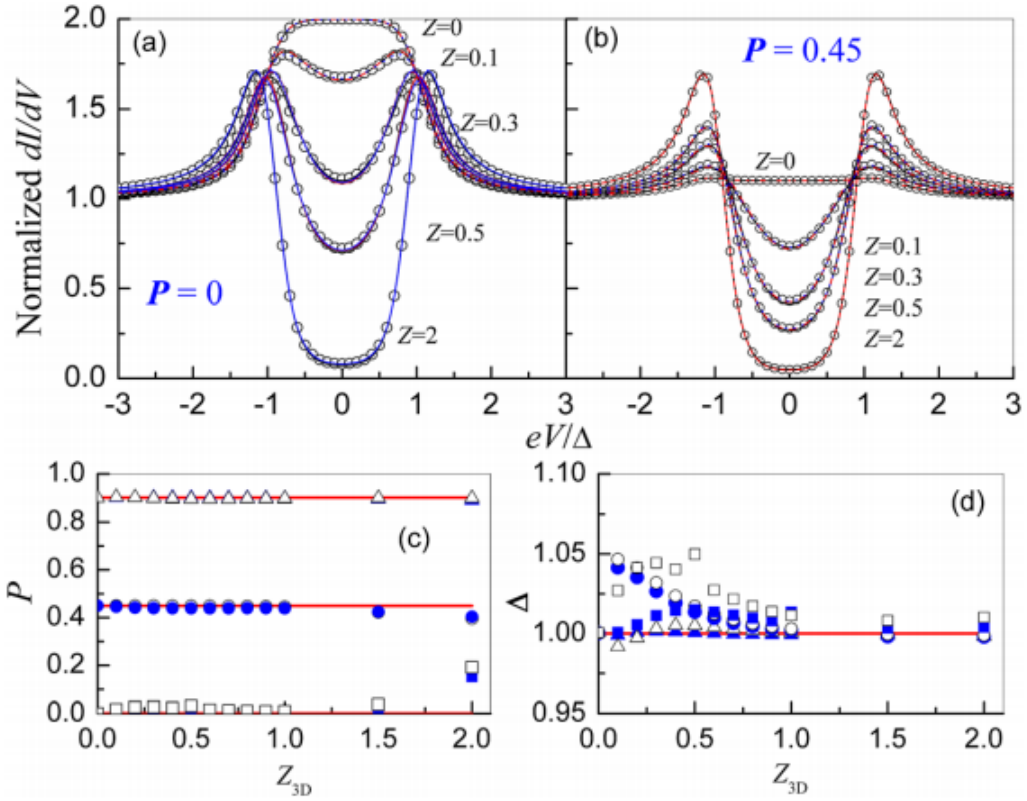

Figure 6.3: (a)(b) Andreev reflection spectra with 3D interface ($\theta_{S0} = \theta_{N0} = \pi/2$) fitted by the 1D model for different Z factors (open circles are generated by the 3D model, solid black lines, dashed red lines, and dotted blue lines are the best fit using the 1D model with fixed gap, fixed spin polarization, and variable gap and polarization), (d) spin polarization of the best fit in ((a)(b)) as a function of Z factor, (e) superconducting gap of the best fit in (a)(c) as a function of Z factor.

The superconducting gap obtained using the 1D model is always within 5% of the 3D value, regardless of the analysis method, as shown in figure 6.3(d). The largest discrepancy actually occurs at small Z factor of 0.1. This shows that a superconducting gap can always be determined using a 1D ARS model without considering 3D effects, for all the ranges of spin polarization and interfacial scattering Z. Finally the Z factor using the 1D model is very different from that of the 3D model. The difference of the Z factor is zero only when the Z factor of the 3D model is zero. It increases monotonically for increasing Z factor (not shown). Previously, it has been attempted to determine the effect of interfacial scattering on spin polarization [101]. The results show that one should take the 3D effect into account to obtain the correct interfacial scattering Z factor for the analysis.

6.5 Conclusion

In summary, one can calculate the Andreev reflection spectra of a three-dimensional interface between a normal metal and an s-wave superconductor. The spectra can be drastically altered by 3D injection, depending on the interface geometry. It is shown that the effect due to 3D injection can be attributed to an apparent larger Z factor using a 1D model for small $Z(Z < 1)$ but with the same intrinsic spin polarization and the superconducting gap. For a 3D interface at large Z factor ($Z > 1$), one must know the interface geometry and use the 3D model to extract the spin polarization. Finally, one can carry out Andreev reflection experiments of the Co/Nb interface and the analysis is consistent with the theory.

Chapter 7

FABRICATION OF HIGHLY SPIN-POLARIZED $CO_2AL_{0.5}SI_{0.5}$ THIN FILMS

Ferromagnetic Heusler $Co_2FeAl_{0.5}Si_{0.5}$ epitaxial thin-films have been fabricated in the $L2_1$ structure with saturation magnetizations over 1200 emu/cm^{3}3. Andreev reflection measurements show that the spin polarization is as high as 80% in samples sputtered on unheated MgO (100) substrates and annealed at high temperatures. However, the spin polarization is considerably smaller in samples deposited on heated substrates.

7.1 Motivation

A Heusler alloy, named after German mining engineer Chemist Friedrich Heusler in 1903 [102], is a ferromagnetic metal alloy with a Heusler phase. This phase contains intermetallics with face-centered cubic crystal structures. Due to the double-exchange mechanism, they become ferromagnetic. If an electron transfers to a certain central site than the neighboring sites should have the same spin as the central site or it will break Hund's rule. The magnetic properties of these alloys are the most interesting and researched aspect of these materials. Most Heusler alloys order ferromagnetically and will saturate in a weak applied magnetic field. Even though these alloys are metals, these alloys have localized magnetic properties and are great models for the study of atomic disorder and changes in electron concentrations on magnetic properties. The localization of the magnetic moment is caused by the large exchange splitting of the Mn d-states which implies that Mn atoms support d-states of only one direction of spin.

The study of Heusler alloys is of the greatest interest because it has the best

potential to realize half-metallicity, or P of 100%, at room temperature. So far only CrO_2 has been shown to be half metallic so the hunt for other materials is one of the most important searches in the spintronic field. Since 1983, theoretical calculations have predicted that the energy gap for minority electrons demonstrates half metallicity for half-Heusler compound NiMnSb [32, 103], which after extensive studies still remains rather controversial [104–106]. Kubler showed that the minority spin densities at the Fermi energy nearly vanish for Co_2MnAl and Co_2MnSn which he then states that this should lead to a particular transport properties because only the majority density of electrons will contribute the the Fermi states [107].

Research groups have recently incorporated these alloys into spintronic devices. One example is the implementation of MTJs using Co_2MnSi Heusler alloys. At 20 K a TMR ratio of 95% with a spin polarization of 66% was measured. At room temperature they found a TMR of 33%. They conclude that this device, based on these values, is superior to 3D based magnetic elements currently used in current MTJs [108].

The explosion of interest (over 700 publications) since 2000/2003 was caused by the observation of large negative magnetoresistance in powder compacts of $Co_2Cr_{0.6}Fe_{0.4}Al$ [109]. A MR effect of 30% in a magnetic field of 0.1 T at room temperature was observed. This showed that, for the first time, a cheap and simple magnetic sensor based on Heusler alloys would remain stable and that 88% GMR could then be found if Al_2O_3 is mixed into the powder. Inomata lead a group of scientists who then incorporated this alloy to make a spin value and showed that a TMR ratio of 16% at room temperature was feasible [110]. Many other groups created thin films based on this design [111–114]. The disadvantage, however, was that the TMR ratios found indicated small spin polarizations, especially at room temperature. Therefore the search for a half-Heusler material which could still produce these MR ratios is still

crucial for emerging technologies.

It has also been stated that MTJs are less favorable for HDD read heads due to the much larger intrinsic resistance-area product of $1\Omega cm^2$, compared with all-metallic GMR devices [115]. However a bigger advantage is that Co-based Heusler compounds have much lower saturation magnetizations and damping constants compared with conventional ferromagnetic materials [116, 117]. This is extremely important because of the reduction of the switching current and power consumption of the current STT devices. Because they also show perpendicular magnetic anisotropy, it suggest that the feasibility of the application of the Heusler compounds in perpendicular FM electrodes of the MTJs is obtainable. They show high thermal stability and a reduction in dimension [118]. In this work, one characterizes the electronic properties, and conduct ARS measurements to determine the spin polarization of a Co-based Heusler alloys and whether they are a good candidate for MTJ and TMR applications.

7.2 Introduction

The performance of spintronic devices depends on generating highly spin-polarized carrier populations [41, 62, 71]. In theory, perfectly spin-aligned carrier populations can be injected from half metals (HF) [32, 119] since they have an electronic structure with one spin band at the Fermi level. However, the injection efficiency from most HFs measured to date is far below 100% and is strongly temperature dependent [39]. This presumably arises from the presence of spin-wave excitations and energy band(s) with opposing spin near the Fermi level [39].

Co-based full-Heusler alloys [107, 120–122] have been proposed for use as electrodes to improve spintronic device performance, although these alloys spin polarization are typically observed to be below 75% by direct measurements [123–125]. Recently, very large giant magnetoresistance (GMR) values have been inferred from

measurements on epitaxial CPP (current perpendicular to film plane) [126, 127], and TMR6, [128] structures fabricated with $Co_2FeAl_{0.5}Si_{0.5}$ (CFAS) electrodes. Of particular interest is the large CPP GMR measured in devices with resistances smaller than that found in MgO-based MTJs. This finding may have important implications for hard-drive read-head applications.

The half metallicity of CFAS has been indirectly verified using crystalline MTJs [39, 128] and the spin polarization is deduced to be over 90%. This, however, does not prove that the electrodes are highly spin polarized since spin-filtering during transport can occur from the coherent tunneling and interface scattering processes [129]. This effect is well documented in MRAM devices using Fe electrodes and MgO tunnel barriers where the current is almost 100% spin polarized [130], even though Fe is known to have a spin polarization of $\sim 50\%$ at the Fermi level [86]. Thus, a direct measurement of the intrinsic spin polarization of the CFAS is imperative both to understand the origin of the large CFAS-based GMR and TMR and to improve the performance of CFAS-based spintronic devices.

In this chapter, it is reported that the results of the systematic study are used to understand the effect of the growth method and thermal processing on the spin polarization in CFAS [131]. One can directly measure the spin polarization using Andreev reflection (AR) spectroscopy in pointcontact and vertical tunnel junction configurations. One can show that the extent of polarization of the injected charge carriers depends strongly on the growth method used and the thermal processing conditions. One observes a spin polarization value as high as 80% in samples sputtered on unheated MgO (100) substrates and *in situ* annealed at high temperatures. These results are expected to be useful for the development of spintronic devices with improved performance.

7.3 Experimental Setup

CFAS films were synthesized using magnetron sputtering on MgO (100) substrates in a cryopumped ultra-high vacuum (UHV) chamber with an unbaked base pressure of 210^8 Torr. For comparison, a few films were grown using pulsed laser deposition in a similarly equipped system. Figure 7.1 is a schematic of the set up. Stoichiometric $Co_2FeAl_{0.5}Si_{0.5}$ polycrystalline targets were used for both growth methods. Sputtered films were grown in 5 mTorr Argon gas at a plasma power of 100 W, while pulsed laser deposition films were grown in 5 mTorr Ar with a frequency of 10 Hz and 450 mJ/pulse excimer laser power. Rutherford backscattered spectroscopy (RBS) measurements and analysis were used to infer the composition and thickness of the thin-films. High-resolution x-ray diffraction (PANalytical XPert PRO) was used for structural characterization. The magnetic properties of the films were characterized using a vibrating sample magnetometer (VSM) from 41000 K (Quantum Design, Model PPMS with oven option). An atomic force microscope (Veeco, Dimension 300) was used to measure the surface quality and roughness of the thin-films.

Two growth processes 1-step and 2-step processes were used to compare and optimize the structural and magnetic properties of the CFAS thin-films. CFAS was deposited at an elevated growth temperature (T_g) in the 1-step process, whereas it was deposited at room temperature (RT) and then in situ annealed at higher temperature (T_a) in the 2-step process.

Spin polarization values (P) of the CFAS films were measured by point contact Andreev reflection (PCAR) operated at 4.2 K using superconducting Pb tips. Vertical Pb superconductor/insulating barrier/CFAS thin-film trilayer junctions were also fabricated and characterized. To form the device, two types of tunnel barrier layers were prepared on 50 nm thick CFAS layers: (a) a CFAS native oxide produced by air-

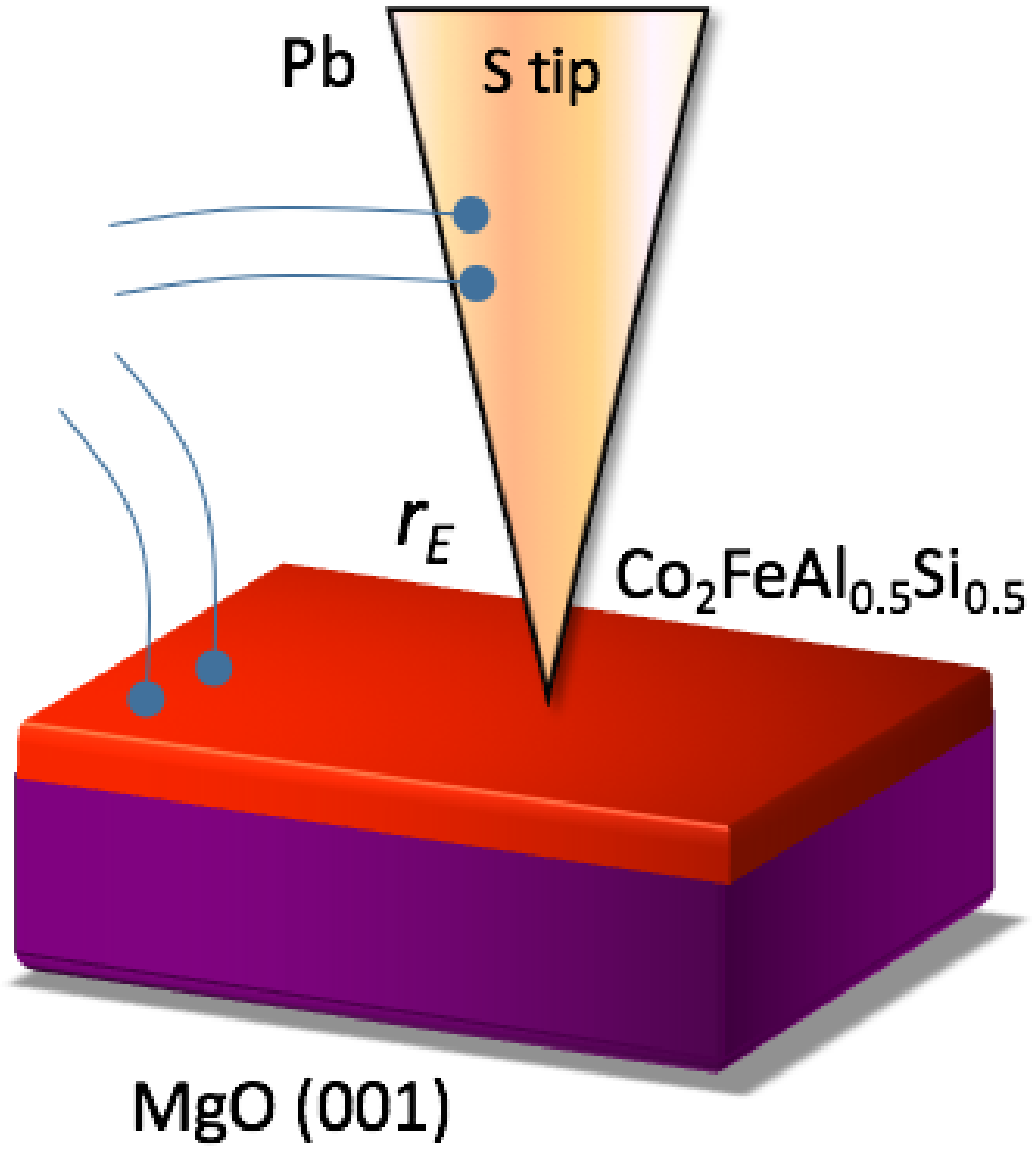

Figure 7.1: CFAS films were grown using magnetron sputtering on MgO (100) substrates in a cryopumped ultra-high vacuum (UHV) chamber with an unbaked base pressure of 210^8 Torr.

exposure, and (b) an AlOx layer produced by oxidizing a $\sim$ 4 nm Al layer deposited in situ on an ion-milled CFAS surface [132]. Then a 1 mm wide barrier/CFAS strip was patterned using photo lithography and reactive Ar ion etching (RIE). A Ge layer was then deposited at RT over the entire substrate, except on top of the barrier/CFAS strip, to act as a low temperature insulator to prevent shorting between electrodes. Finally, the 200 nm thick Pb layer was deposited using thermal evaporation through a shadow mask. The electrical characteristics of the device were measured using a 4-point measurement with a dipping probe in a liquid He Dewar.

7.4 Electronic Properties

RBS results showed that the CFAS thin-films are stoichiometric and have a thickness of $\sim$ 50 nm. Figure 7.2 shows the effect of annealing and growth temperature on the magnetic moment (μ_B), magnetization (M_s), coercive field (H_c), and resistivity (ρ) of sputtered thin-films synthesized in 1-step and 2-step processes. The saturation magnetization is found, in general, to increase with both annealing (2-step) and growth temperature (1-step), as shown in figure 7.2(a). The saturation magnetization of >1200 emu/cm^3 was achieved with both 1-step and 2-step processes. This corresponds to a moment of $\sim 6\mu_B$ for both growth methods when $T_g = T_a = 600$ °C. According to the Slater-Pauling rule, the CFAS moment is expected to be 5.5 μ_B, although a value of 6 μ_B is expected for nonstoichiometric and structurally disordered CFAS material [133]. The coercivity of the samples slightly decreases with increasing T_g or T_a, then increases for T_a and T_g greater than 350 °C, as shown in figure 7.2(b). The coercivity was found to be considerably larger for the CFAS films prepared by the 1-step procedure compared to the 2-step procedure when processing temperatures above 350 °C were used. The resistivity of the CFAS samples at RT is shown in 7.2(c) and it decreases with increasing T_a or T_g due to the formation of enhanced degrees of

crystallinity. The magnetization was measured from 4 to 1000 K on a CFAS thin-film prepared using the 2-step process with an annealing temperature of 600 ° C [figure 7.2(d)]. One can fit the data to the empirical equation, $M_s/M_{s0} = [1 - (T/T_C)^{\alpha}]^{\beta}$, where Ms0 is the zero-temperature magnetization, T_C is the Curie temperature, and α and β are fitting parameters.As shown in 7.2(d), the least squares fit to the data gives a Curie temperature of $\sim 1150 \pm 50$ K, with the best fit to the experimental data for α and β of 1.5 and 0.45, respectively. The Curie temperatures for similar Co based Heusler alloys, Co_2MnSi 9 and Co_2FeSi,10 are 985 and 1100 K, respectively. The magnetic properties of these samples grown by both methods are comparable to the best results reported by Wang et al. [128, 134] for CFAS films grown on MgO substrates and SiO_x/Si substrates with a 20 nm MgO buffer layer (which ranges from 900 emu/cc to 1160 emu/cc) for samples grown at RT without any post annealing and with 680 °C post annealing process, respectively [128].

As illustrated in figure 7.2(c), the room-temperature resistivity for most of the samples is below 100 $\mu\omega cm$. One can also observe that the resistivity of samples at 4.2 K remains very near that value, with less than a 10% change, which indicates a mean free path of a few nm, as inferred from the Drude model. For each sample, one can measure over 10 spectra with contact resistances ranging between 80 ω and 300 ω. This corresponds to a contact size of a few nm using the Wexler [79] formula. These values suggest that transport at the contact is close to the ballistic regime.

7.5 ARS using Heusler Metal

Since the moment of samples grown by both the 1-step and 2-step methods both attain a value of $\sim 6\mu_B$, one anticipates they will have similar levels of polarization. The measured AR spectra on representative films are shown in figure 7.3. One analyzes the AR spectra using both the modified Blonder-Tinkham-Klapwijk (BTK)

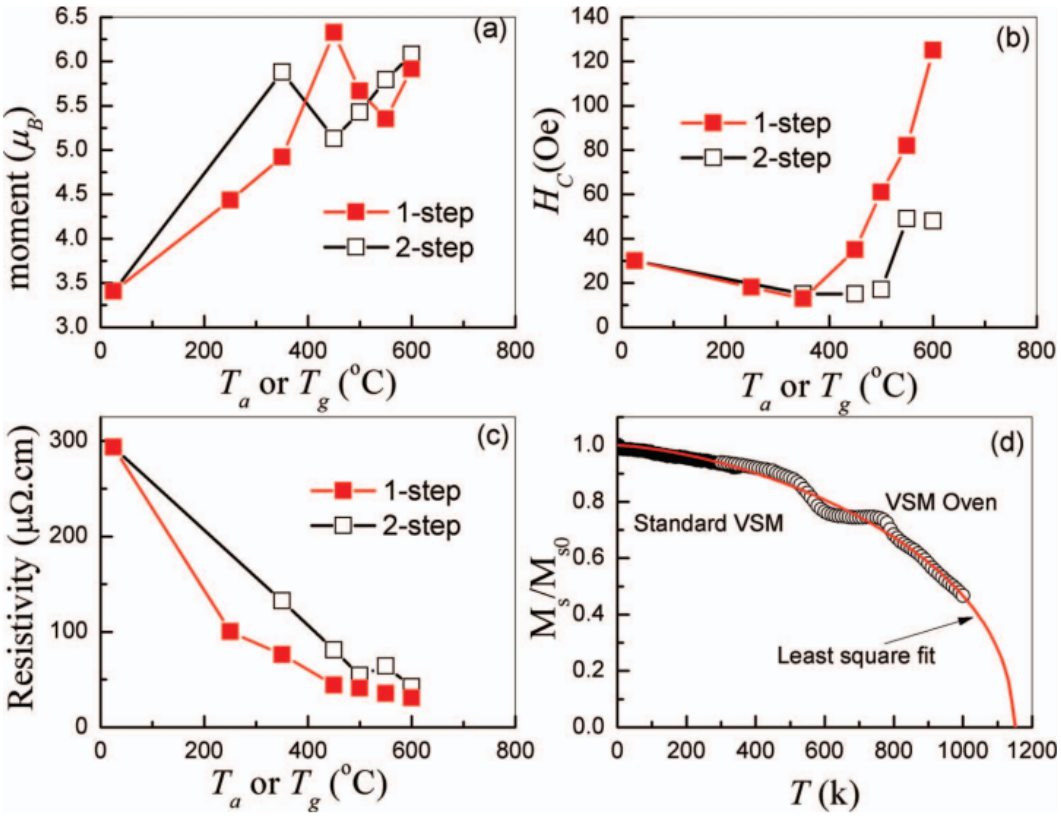

Figure 7.2: Magnetic properties and spin polarization of CFAS samples. (a) Magnetic moment, (b) coercivity, and (c) resistivity of films deposited by sputtering as a function of growth and annealing temperatures. (d) Magnetization as a function of temperature for film deposited at RT and annealed at 600 °C.

[25, 27, 81, 84] and the more recent Chen-Tesaonv and Chien (CTC) models [83]. Representative data (open circles), along with the best fit to the CTC model (red solid line) and the best fit to the modified BTK model (blue solid line), are shown in figure 7.3. Since both fits are near identical, the red and the blue curves are indistinguishable to each other and the obtained P values (as listed inside each figure with the designated color) are very similar. The Z factor represents the interfacial scattering [25, 27, 79, 81, 84] in both models and rE corresponds to the additional resistance that occurs when small point contacts are used on high resistivity samples [25]. For the sample grown at 600 °C, the normalized conductance (dI/dV) is $\sim$ 1.0 at zero bias [figures 7.3(a) and 7.3(b)]. For the samples annealed at 600 °C, the normalized conductance is below 0.7 at zero bias [figures 7.3(c) and 7.3(b)]. This indicates a much higher polarization value for samples annealed at 600 °C. The best fits to both models show that the P value of the 2-step sample is about 0.74, while it is below 0.5 for the sample grown by the 1-step process. One also notes that the conductance shoulders, often referred to as Andreev peaks, occur at $\sim$ 5 mV, a value much larger than the 1.3 meV superconducting gap of the Pb tip at 4.2 K. This is due to the additional contact resistance (r_E) inherent to high resistance films, which has been incorporated in the analysis for both models.

Since point-contact AR spectra indicate that samples annealed at 600 °C exhibit the highest polarization value, 11mm^2 Pb/insulator (CFAS native oxide or Al_2O_3)/CFAS trilayer thin-film junctions were fabricated. The AR spectra of these two junctions are shown in figures 7.3(e) and 7.3(f). As illustrated in Fig. 2(f), the junction with the native CFAS oxide layer shows no shoulders at the peak, indicative of a smaller barrier at the interface. This can be compared to the Al_2O_3 oxide layer junction measurements, figure 7.3(e), that show characteristics very close to the tunneling regime. Furthermore, the conductance of both junctions are about 0.3 at

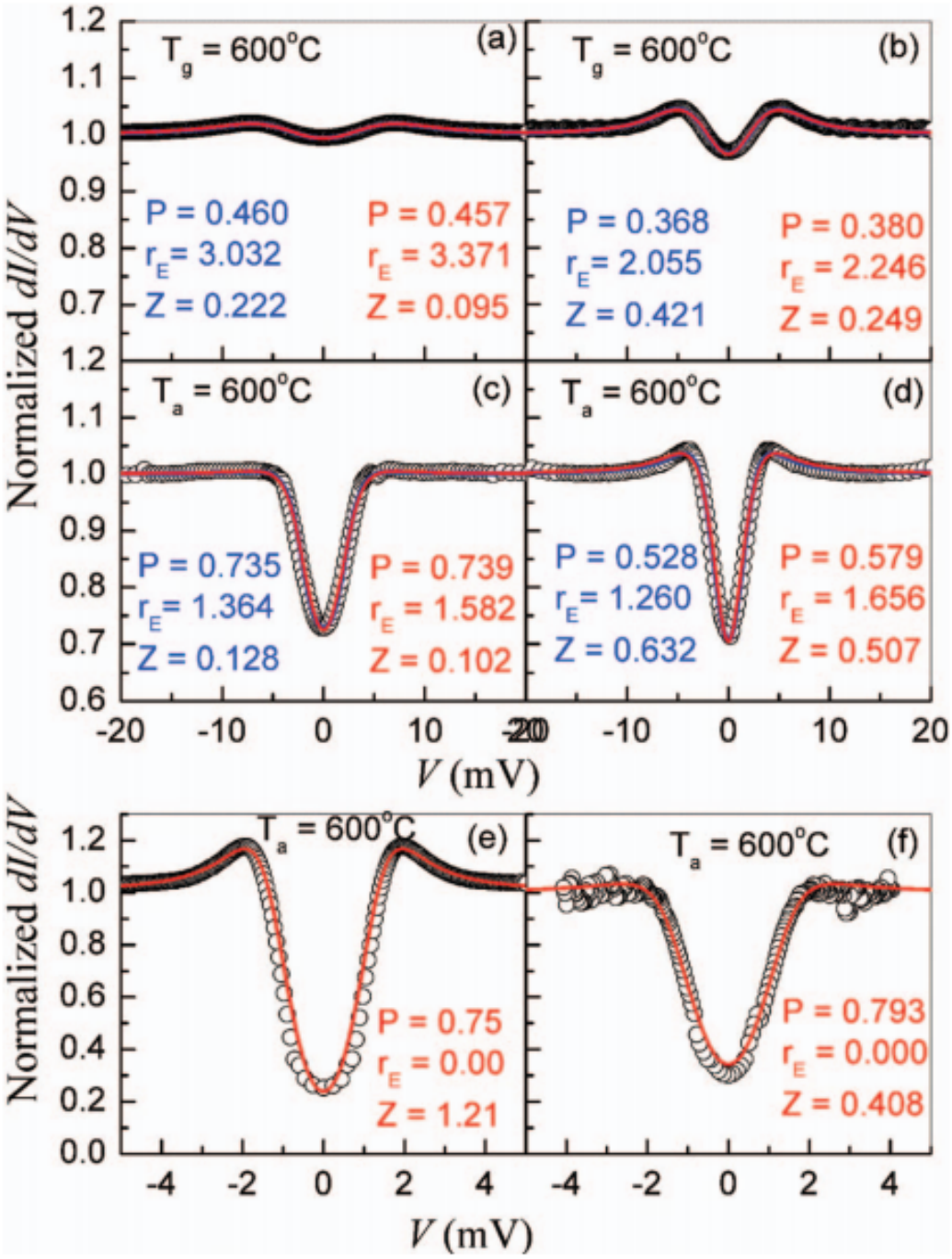

Figure 7.3: Representative point contact Andreev reflection spectra of sputtered CFAS samples with different interfacial scattering factors: (a) and (b) sample grown at 600 °C, (c) and (d) sample grown at RT with 600 °C post annealing, (e) and (f) vertical junctions of Pb/Al_2O_3/CFAS and Pb/native CFAS oxide/CFAS, respectively, with 600 °C post annealed CFAS layer.

zero bias, indicating a high polarization value. Both methods of analysis find that the spin polarization of these junctions is very close to 80%.

The dependence of the P values as a function of the interfacial scattering Z factor for representative samples are shown in figure 7.4. For all the samples, the P values decrease with increasing Z factor due to spin flip scattering at the interface, although there are important differences in the trends. For example, the P value of the sample grown at RT decreases rapidly from 0.47 at $Z = 0$ to zero at $Z \sim 0.3$, figure 7.4(a). In contrast, the P value of the sample annealed at 600 °C (figure 7.4(d)) is higher and is reduced by only a small amount over the same Z range. One also notices that the P values obtained for the trilayer junctions are higher, as shown by the solid squares in figure 7.4(e), and are virtually independent of the Z factor. This can be attributed to higher quality junction interfaces. From the P vs Z curves, one notes that the polarization decreases more rapidly with Z for samples with smaller P values, presumably from stronger spin flip scattering.

By extrapolating to $Z = 0$ using a polynomial fit (dashed curve), one can obtain the intrinsic P value of each sample. Values for $P(Z = 0)$ are presented in figure 7.4(f). The highest $P(Z = 0)$ is about 80% for the sample annealed at 600 °C. The red solid circle denote the the samples grown with a 2-step pulsed laser deposition (PLD) process that used 550 °C and 780 °C in situ anneals. The $P(Z = 0)$ value for the sample fabricated with the 2-step sputtering process ($T_a = 550$ °C) is very similar to that grown by PLD, indicating that $P(Z = 0)$ values do not appear to strongly depend on the growth method. However, the $P(Z = 0)$ of the samples grown with the 1-step sputtering process (solid blue square) is much lower. $P(Z = 0)$ is equal to $\sim 50\%$ for the sputtered sample grown at 600 °C.

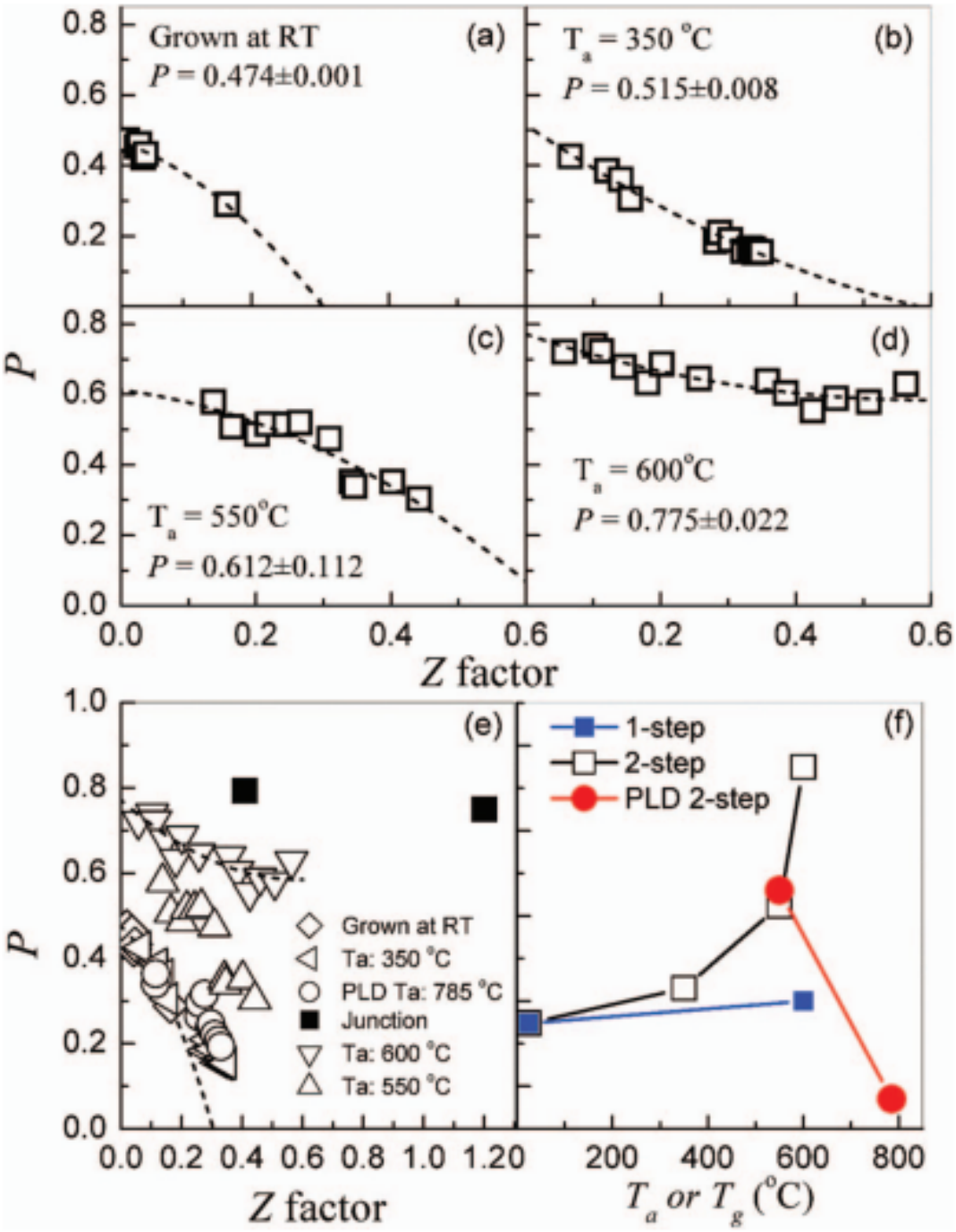

Figure 7.4: Representative curves of spin polarization of the sputtered CFAS samples as a function of the interfacial scattering factor Z for (a) sample grown at RT, (b) sample with 350 °C post annealing, (c) sample with 550 °C annealing, (d) sample with 600 °C annealing, and (e) for all the samples including sample grown by pulsed laser deposition and post annealed at 785 °C. The dashed curves are polynomial fitting. (f) Intrinsic spin polarization $P(Z = 0)$ of samples fabricated by 1-step sputtering, 2-step sputtering and 2-step pulsed laser deposition.

7.6 X-ray Diffraction and Φ Scans

The films were measured using x-ray diffraction (XRD), as shown in figure 7.5. The XRD results indicate that the films grown with the 1-step process are epitaxial when T_g is larger than 250 °C, figure 7.5(a). The intensity of the (002) and (004) CFAS peaks is enhanced with increasing growth temperature, indicating that crystal quality improves under these conditions. XRD Φ scans of the off-axis Bragg peaks have been used to identify the presence of L21 ordered structure [128, 135]. Φ scans of the off-axis CFAS(111) peak on the samples [figure 7.5(a) inset] showed fourfold symmetry in the diffraction patterns. This is direct evidence that films grown at T_g over 350 °C have the L21 CFAS structure. One can conclude that the films are epitaxial with the CFAS L21 structure and the L21 ordering improves with increasing growth temperature. It is interesting that these samples show poor spin polarization of $\sim$ 50%. A P value of 50% is similar to that measured by ARS on bulk CFAS samples [133].

The presence of epitaxy in the coupled $\theta - 2\theta$ XRD data of films with high P values grown with the 2-step process were not detected [figure 7.4(f)]. However, by using XRD grazing angle measurements, one could detect the evidence of the polycrystalline CFAS structure with broad XRD Bragg diffraction peaks for film without post annealing [0.7° full width at half maximums (FWHMs) of (220) peak]. The quality of films, as inferred from the intensity and the width of the XRD peaks, was found to improve with increasing annealing temperature. The (220) Bragg diffraction peak of the film annealed at 600 °C had a FWHM of 0.46°. Wang et al. reported a high spin polarization value of 71% for TMR structure with polycrystalline CFAS electrodes.16 This value is very similar to the value observed (70%) for CFAS electrodes with B2 ordering structure [135]. In addition, Tezuka et al. [135] reported that CFAS

MTJs with the highly ordered structure ($L2_1$) have much lower spin polarization than devices containing electrodes with the less ordered structure (B2). The authors attribute the difference in the polarization results to the higher roughness in the films with $L2_1$ ordering than found in films with B2 ordering [83]. The samples fabricated with the 2-step process are smoother [figure 7.5(b)] than those produced with the 1-step process. Since the contact diameter of the probe in the AR spectra experiments is only a few nm, the surface roughness, which is believed to strongly influence the MTJ characteristics, may not significantly affect the measurement results.

The direct ARS measurements show that the P value of CFAS films can be as high as 80% and depends crucially on the fabrication process. This value is consistent with the large CPP GMR and TMR values reported in the literature [39, 126–128]. The observation of a range of polarization values that can be found for films with similar magnetic properties is interesting and should provide valuable information to researchers developing spintronic devices.

7.7 Conclusion

In summary, CFAS thin-films have been fabricated using both the 1-step and 2-step methods and measured the samples intrinsic spin polarization values. One finds that the magnetic properties of the samples are similar, although the spin polarization is different. Spin polarization as high as 80% has been observed by Andreev reflection spectroscopy for the CFAS samples grown at room temperature followed by post annealing.

7.8 Acknowledgment

This work was supported by the Office of Naval Research through Contract Nos. N00014-09-C-0292 and N00014-13-1-0069 and by IARPA through Contract No.

IARPA-BAA-10-07-AB-8553. The use of facilities in the LeRoy Eyring Center for Solid State Science at Arizona State University is acknowledged.

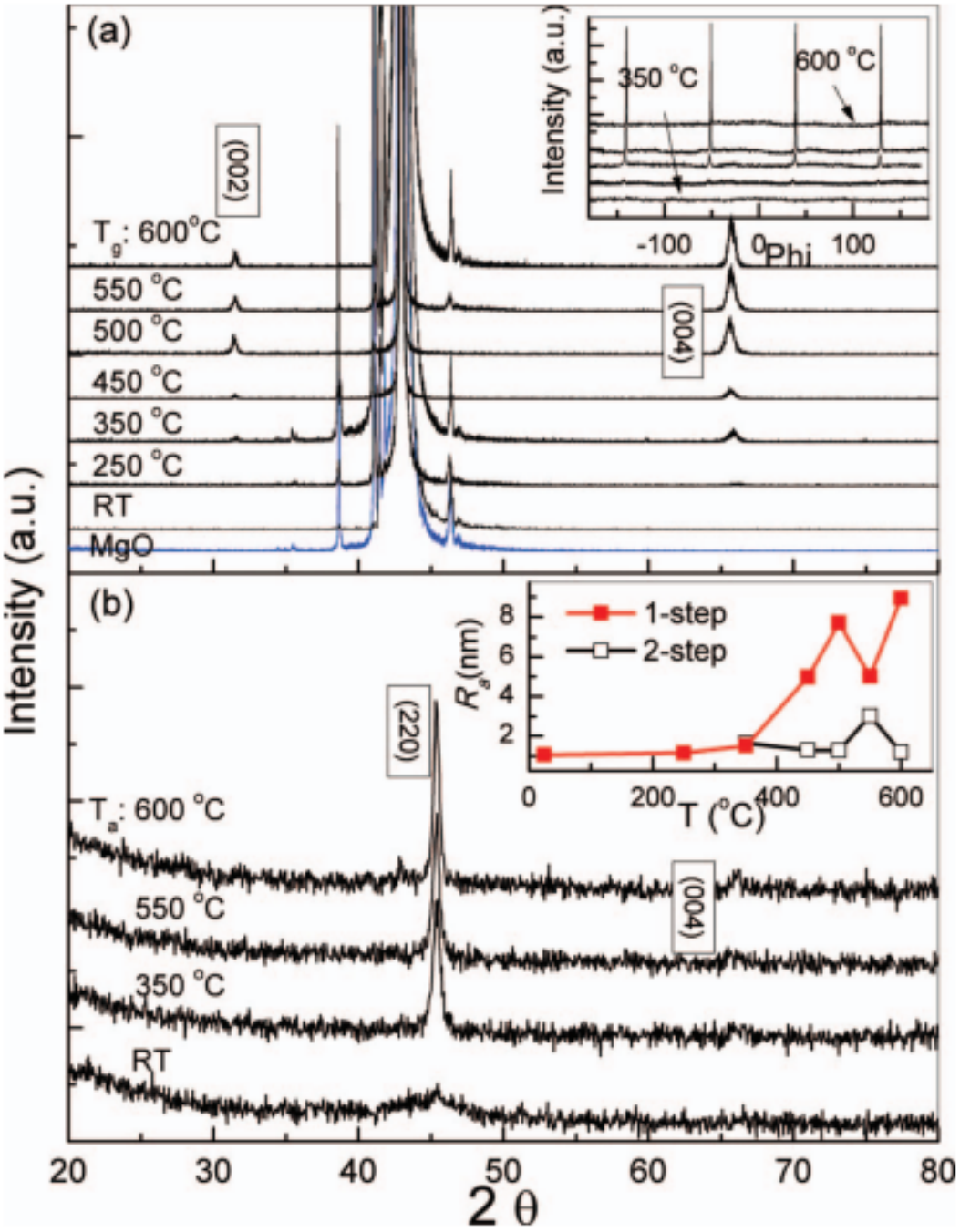

Figure 7.5: (a) X-ray $\theta 2\theta$ diffraction of the CFAS samples fabricated by 1-step method. The inset illustrates the Φ-scans of the off axis (111) peak. (b) XRD grazing angle of the CFAS samples made using the 2-step method. The inset summarizes the roughness of the CFAS samples, as inferred from atomic force microscopy measurements.

Chapter 8

DETERMINATION OF SPIN POLARIZATION OF AMORPHOUS AND EPITAXIAL $FE_{0.65}SI_{0.35}$ FILMS USING ANDREEV REFLECTION SPECTROSCOPY

Ferromagnetic Fe_xSi_{-x} alloys have been proposed as potential spin injectors into silicon with a substantial spin polarization. Experimentally, however, the observed spin polarization of the alloys still remains low. Ideally, spin polarization of a metal is defined as the imbalance of density of states at the Fermi level, but in amorphous alloys it is different since the Fermi level is not well defined. Recently, it has been found that the magnetic properties of the amorphous Fe_xSi_{-x} alloys are very different from the crystalline phase. In this work, one can utilize Andreev Reflection Spectroscopy (ARS) to determine the spin polarization of both amorphous and crystalline $Fe_{65}Si_{35}$ alloys. One can show that the additional resistance in ARS is quite high because of large resistivity of these alloys and must be taken into account to correctly extract the spin polarization. The obtained spin polarization values are very different: the amorphous phase has a significantly higher spin polarization than that of the crystalline phase.

8.1 Motivation

In traditional metals, magnetism is highly influenced by the local atomic structure. Magnetic studies on amorphous and crystalline alloys Fe_xB_{1-x}, Fe_xP_{1-x}, Fe_xZr_{1-x}, Fe_xCo_{1-x}, and Ni_xFe_{1-x} have been conducted and compared with amorphous studies on (FeCo)G and (NiFe)G [136–139]. The disadvantages of these studies however is that the crystalline analog has a very specific stoichiometric phase, and even though

the amorphous films have a wide composition range, the amorphous phase is formed by metalloids which affect the magnetic properties [139]. In these studies, it has been shown that, by changing the Fe concentration, the magnetic ordering critical temperature decreases sharply such that it can have T_c as high as 760 K in $Fe_{72}B_{28}$ [136]. The advantage to using amorphous materials is the availability to grow them and vary the degrees of both the chemical and structural order, tune their T_c, and manipulate the structure to make a better spin-injector.

The main advantage is that the these amorphous films can be manipulated through structure, composition, and confinement to change material properties such as the magnetic moment, anisotropy and coercivity [140]. Amorphous films are highly uniform and have good layer perfection [141]. This makes them ideal candidates for hetero-structures and magnetic tunnel junctions [142]. An added advantage is, that since the lattice matching to neighboring layers is not an issue for amorphous films, anisotropy can be imprinted in the layers by applying a magnetic field during growth [143, 144]. $Co_{40}Fe_40B_20$ is one amorphous structure that has caught the eye of scientists. These amorphous structures have high strength and hardness as well as superior wear resistance [145–148]. This material has been used in GMR, TMR, MTJs, and MRAM studies because of its high spin polarization and low coercivity. The very short mean free path in the alloys yields a higher MR ratio [149–153] and the path is much smaller than in crystalline materials. Therefore, the thickness needed for MR devices is much less then standard materials used today [151]. Since its discovery, many more amorphous materials are gaining attention such as Fe_xSi_{1-x}.

A spin injection device posed is comprises of two different semiconductor materials (AlGaAs, GaAs, GaN, InSb, or InP) and a ferromagnetic material imposed in between them [154]. Typical spin injection devices do not use semiconductors but, with the discovery of amorphous highly spin polarized materials, they can be semiconducting

which has created a new branch of devices with both spintronic and insulating properties. Previously it has not been possible to transfer spin alignment to superconductors because ferromagnetic materials used have been had a higher electrical conductivity then a semiconductor. There are less electrons that move through a semiconductor compared to a metal, and for this reason spin alignment in semiconductors has been unsuccessful. For spin injection from a ferromagnetic to a semiconductor to occur, the conductivity of the two must be closely matched [155]. Because amorphous materials are highly tunable, it has been found that the semiconductors Si, Ge, or SiGe can be added to the amorphous material and make a magnetic semiconductor. So not only can these amorphous materials become ferromagnetic, but they can now be be used in spintronic devices and they also can retain their semiconducting properties. The conductivity can be in the range of $1 \times 10^4(\Omega\ cm)^{-1}$ to $1 \cdot 10^{-10}(\Omega\ cm)^{-1}$. The resistivity of the amorphous materials can also be adjusted so that the resistivity is within eight orders of magnitude of the resistivity of the material adjacent to it, such a ferromagnetic metal [155]. One such amorphous semiconductor is Fe_xSi_{1-x}.

It has been shown that the amorphous Fe_xSi_{1-x} thin films have significantly larger magnetization than the crystalline films [156, 157]. This chapter investigates the magnetic and spintronic properties of epitaxial and amorphous $Fe_{0.65}Si_{0.35}$ films. The goal is to determine if the amorphous or epitaxial films are better suited for spin injection and for high spin polarization applications. Thus far, no papers have investigated the ARS measurements of this amorphous material.

8.2 Introduction

Spintronics utilizes both charge and spin for information process. To take advantage of the technology of the conventional Si-based electronics, efficient spin injection into silicon is necessary for semiconductor spintronics, [4, 158–160]. However, spin

can be efficiently injected from a ferromagnetic metal into normal metals such as Cu and Al [161, 162] but not semiconductors because of the mismatch in conductivity, carrier density, crystal lattice, and other complexities [163]. One way to circumvent these difficulties is to use an appropriate spin injector such as Fe_xSi_{-x}, which can grow epitaxially on Si [164–167] and have relative large resistivity. Spin injection into Si has been demonstrated at low temperature (< 40K) using expitaxially grown Fe_3Si/Si Schottky-tunnel-barrier contacts [167]. In addition to an appropriate interface, a spin injector with a high spin polarization is also important to realize efficient spin injection.

The spin polarization (P) of a metal is defined as the normalized imbalance of the density of states (DOS) of the two spin orientations at the Fermi level, $P \equiv [N(E_{F\uparrow}) - N(E_{F\downarrow})]/[N(E_{F\uparrow}) + N(E_{F\downarrow})]$, with $N(E_{F\uparrow})$ and $N(E_{F\downarrow})$, respectively, as the spin-up and spin-down DOS. The DOS of crystalline solids are a result of energy band depending on the crystal structure, so is the magnetism of the ferromagnets. Magnetism in alloys of transition metals depends crucially on the local atomic environments [136–139].

In particular, a Fe atom in amorphous Fe-based alloys often displays a moment less than 2.2 B of that in pure metallic Fe. Interestingly, striking enhancement of magnetism has been observed in amorphous Fe_xSi_{1-x} ($0.45 < x < 0.75$) [165] compared to the same crystalline chemical composition. As a potential spin injector for spintronics, it is important to determine the P value of the crystalline Fe_xSi_{1-x} as well as the amorphous alloys to reveal the effect of the enhancement of magnetism on the P value. This chapter will focus on compairing the spin polarization of epitaxial and amorphous Fe_xSi_{1-x} to observe which crystal structure is the highest spin polarized [168].

8.3 Experimental Setup

The amorphous $Fe_{0.65}Si_{0.35}$ films of 150 nm were grown by electron beam co-evaporation of Fe and Si at room temperature on amorphous SiN_x on Si substrate, while the epitaxial $Fe_{0.65}Si_{0.35}$ films of the similar thickness were fabricated using (001) MgO substrate at 200 °C. Figure 8.1 shows the schematic setup for this material. The amorphous and crystalline nature has been confirmed by the X-ray diffraction and high-resolution transmission electron microscopy. Both samples are ferromagnetic at 300 K and the magnetic, structural, and growth details have been described elsewhere [165]. A thin Al over layer of 1.5 nm is covered on both samples to protect the surface for the spin polarization experiments. This work determines the spin polarization of the amorphous and the crystalline $Fe_{0.65}Si_{0.35}$ alloys using Andreev Reflection spectroscopy (ARS). A superconductor tip of a few nm in size is used in the experiments. The sample and the tip are enclosed in a vacuum jacket then cooled down to low temperature of 1.5 K. A point contact is then established and the differential conductance dI/dV and resistance V/I were measured using a Lock-in method. Both superconducting Nb and Pb tips have been utilized and there is no observable difference in the determined P values. The resistivity of the epitaxial sample is 54 ωcm while it is about 156 ωcm for the amorphous samples. In the experiments, the contact resistance is between 71 ω and 300 ω where the corresponding contact size is a few nm, less than or comparable to the mean free path estimated from the resistivity based on the Drude model. Thus all of the contacts are approximately in the ballistic regime.

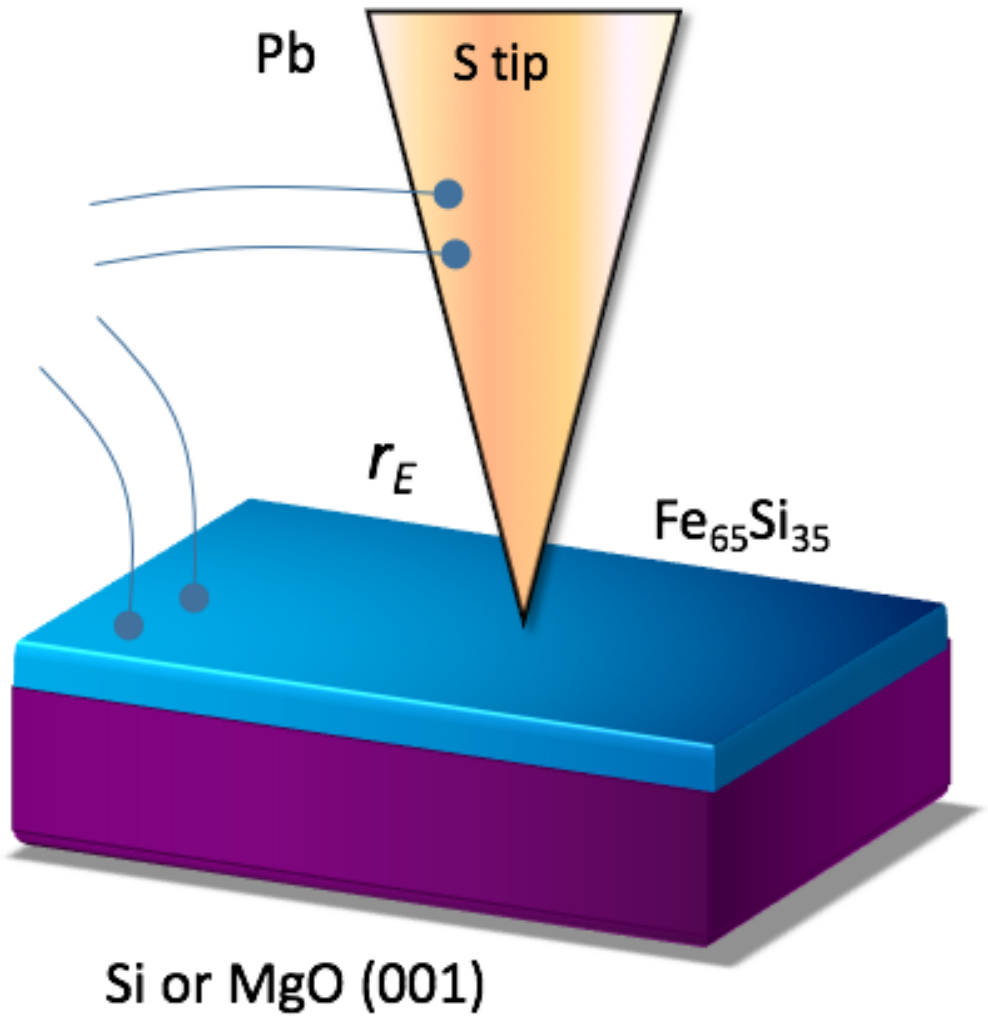

Figure 8.1: The amorphous $Fe_{0.65}Si_{0.35}$ films of 150 nm were grown by electron beam co-evaporation of Fe and Si at room temperature on amorphous SiN_x on Si substrate. The epitaxial $Fe_{0.65}Si_{0.35}$ films of the similar thickness were fabricated using (001) MgO substrate at 200 °C.

8.4 ARS using Amorphous Material

Representative ARS spectra are shown in figure 8.2 for Pb tips in contact with the crystalline $Fe_{0.65}Si_{0.36}$ sample. The open circles are the experimental data and the solid lines are the best fit using the Chen-Tesanovic-Chien (CTC) model [25, 27, 84], which gives the same P value as the modified Blonder-Tinkham-Klapwijk (BTK) model [169]. The parameters of the best fit are listed inside each panel with T the experimental temperature, P the spin polarization, the superconducting gap, the additional resistance, and Z the interfacial scattering factor. The data can be well described by the CTC model. As Z increases, the P value of the epitaxial $Fe_{0.65}Si_{0.35}$ sample decrease from about 50% at $Z = 0$ to 22% at $Z = 0.4$, showing a typical reduction of the P value by the interfacial scattering also observed in other ferromagnets [17, 18, 22, 23]. The superconducting gap value is often indicated by the two Andreev should peaks but in the data the two Andreev peaks are at about 2.5 meV, much larger than the experimental superconducting gap value 1.34 meV of the Pb tip calculated from the T_c using the BCS theory. This is due the additional resistance because of the high resistivity of the sample. The address of the additional resistance has been previously described [27]. In the analysis, the temperature and the superconducting gap are fixed as experimental values while only r_E , P and Z factor are varied. In fact, even with all the parameters varied, the resultant T and Δ are very similar to the experimental values, demonstrating that it is important to taken the additional resistance into account for data analysis in these samples with high resistivity.

One can also measure the P value of the amorphous $Fe_{0.65}Si_{0.35}$ sample using Pb tips but the ARS spectra are different from that of the crystalline sample. The representative spectra are shown in figure 8.3 where a dip, much lower than that in

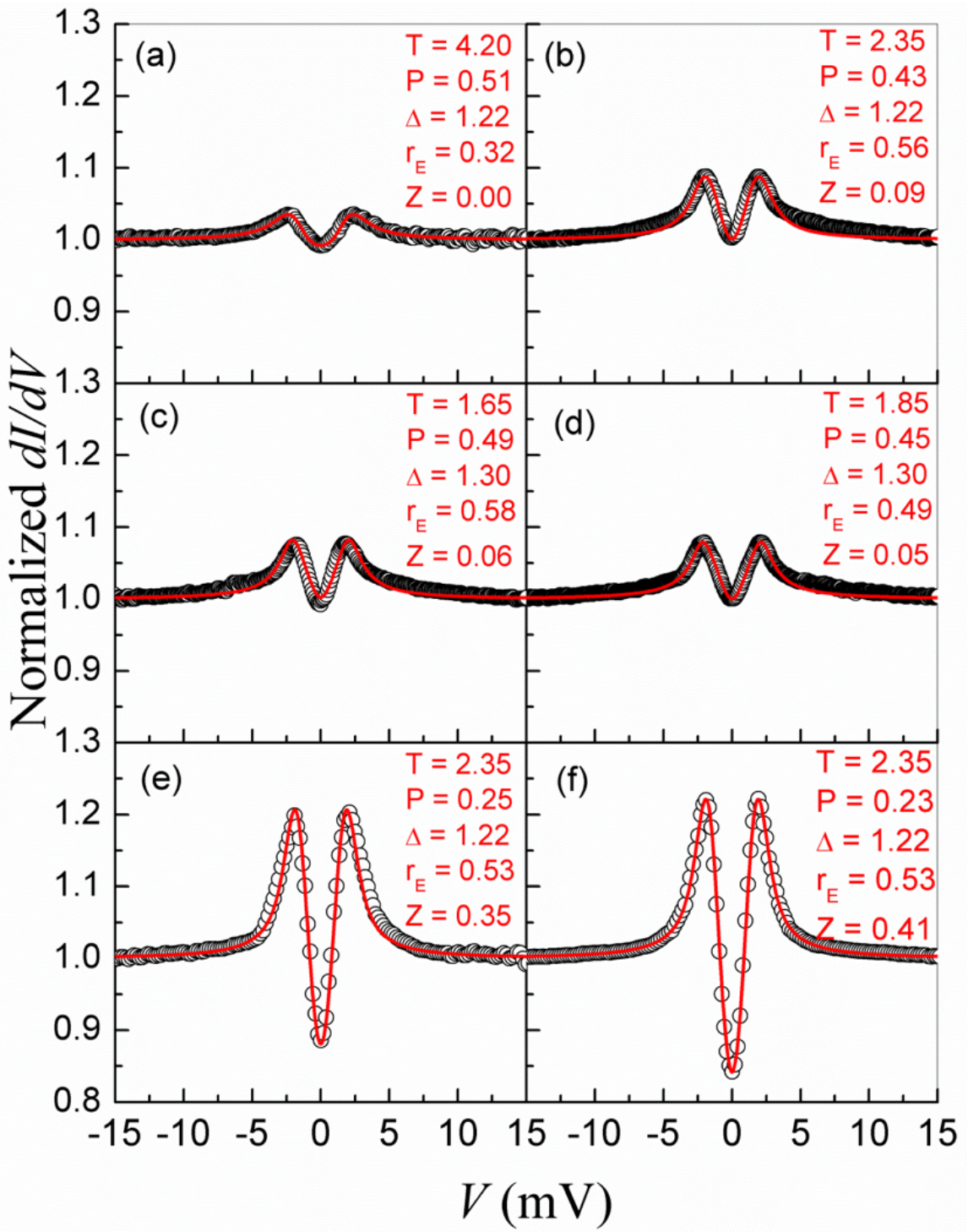

Figure 8.2: Representative Andreev spectra (open circles) of different Z factor from 0 to 0.41 of point contacts on an epitaxial $Fe_{0.65}Si_{0.35}$ sample and the best fit (solid lines) by the BTK model (Insert are the parameters of the best fit with P as the spin polarization, Δ the superconducting gap, r_E the additional resistance and Z the interfacial scattering factor).

the spectra of the crystalline sample, appears at zero bias voltage. One notes that the Andreev peaks now appear almost at 5 mV, which cannot be the superconducting gap of the Pb tip, but due to the additional resistance r_E resulting from the high resistivity of the amorphous sample. The data (open circles) can still be well described by the CTC model (solid lines) and the parameters of the best fit are listed inside each panel. The obtained additional resistance r_E is indeed much larger than that in the epitaxial sample. The P value of the amorphous sample decreases as Z increases, showing a similar trend as that of the crystalline sample. ARS determines the P value based on the suppression of the Andreev reflection by a spin polarized current. For a normal current of $P = 0$ of an ideal interface, the conductance is 2 at zero bias while for a half-metallic current of $P = 1$, the conductance is zero at zero bias because the Andreev reflection is completely suppressed. With similar values of the Z factor, the conductance curve for the amorphous sample is much lower than that of the crystalline sample, indicating a higher P value in the amorphous sample.

Indeed, two conductance spectra of similar Z factors are compared in figure 8.4(a, b). The conductance (black squares) for the crystalline sample is about 1.05 at zero bias for $Z = 0.05$ while the conductance (black circles) for the amorphous sample is only 0.75, indicating a much higher P value of the amorphous sample. Even for large Z factor of about 0.4, the conductance spectrum of the crystalline sample is still much higher than that of the amorphous sample, as shown in figure 8.4(b). Over 40 conductance curves were measured for each sample and the obtained P values are plotted in figure 8.4(c). The P value decreases for increasing Z factor but at any Z factor, the P value of the amorphous sample is always higher than that of the crystalline sample. Extrapolating the Z factor to zero, the intrinsic P value was observed. For the crystalline $Fe_{0.65}Si_{0.35}$ sample, the P value is 49.20.7% , close to the previously reported value in epitaxial Fe_3Si of $45 \pm 5\%$ [170]. However, the P value

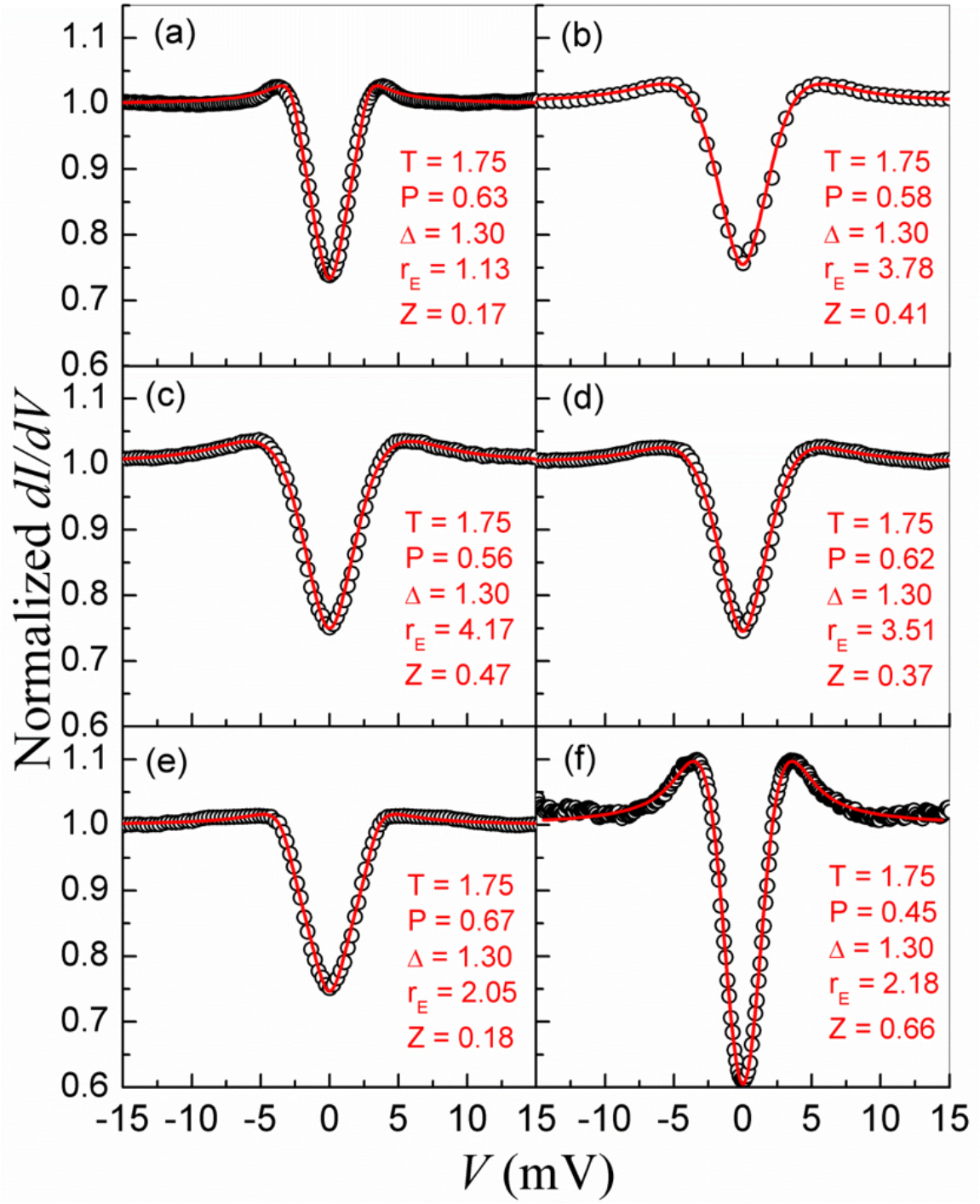

Figure 8.3: Representative Andreev spectra (open circles) of different Z factor from 0.17 to 0.66 of point contacts on an amorphous $Fe_{0.65}Si_{0.35}$ sample and the best fit (solid lines) by the BTK model (Insert are the parameters of the best fit).

for the amorphous $Fe_{0.65}Si_{0.35}$ sample is 68.53.1%, substantially higher than that of the crystalline sample.

One notes that the P value of a solid depends on the DOS, which in a crystalline solid is the result of the energy band depending on the crystal structure. Band structure curves $E(k)$ are not well defined in an amorphous ferromagnet, in which only short-range ordering exists. Nevertheless, there is still a well defined Fermi energy E_F and density of electron states $N(E)$, and the conduction electrons in an amorphous ferromagnetic metal should remain polarized. In the $Fe_{0.65}Si_{0.35}$ alloy, the magnetism is actually enhanced in the amorphous sample due to the reduction of the number of Fe-Si bonds [165]. The experiment shows that the P value of amorphous $Fe_{0.65}Si_{0.35}$ is also substantially higher than the P value of the crystalline alloy of the same composition. Previously, enhanced P value has also been reported in amorphous FeCoB [27]. The enhanced P value may be due to the modified magnetism because of the change of the local environment in the amorphous sample, as also demonstrated by the enhanced magnetism. The work shows that in transition metal alloys, in addition to magnetism, the spin polarization can also be modified by changing the structure. Theoretically, a substantial P value has been predicted [171] in the amorphous $Fe_{0.65}Si_{0.35}$ alloy, which is similar to that of the crystalline alloy in magnitude but with a negative sign [165]. Further experiments are necessary to determine the sign of the P value since the ARS cannot detect the sign of the spin polarization.

8.5 Conclusion

In summary, one can determine the spin polarization of both the amorphous and the epitaxial $Fe_{0.65}Si_{0.35}$ alloys using Andreev reflection spectroscopy. The spin polarization of the crystalline $Fe_{0.65}Si_{0.35}$ is about 49%, similar to that of common magnetic metals, indicating that it is a good spin injector for semiconductor spintronics. In-

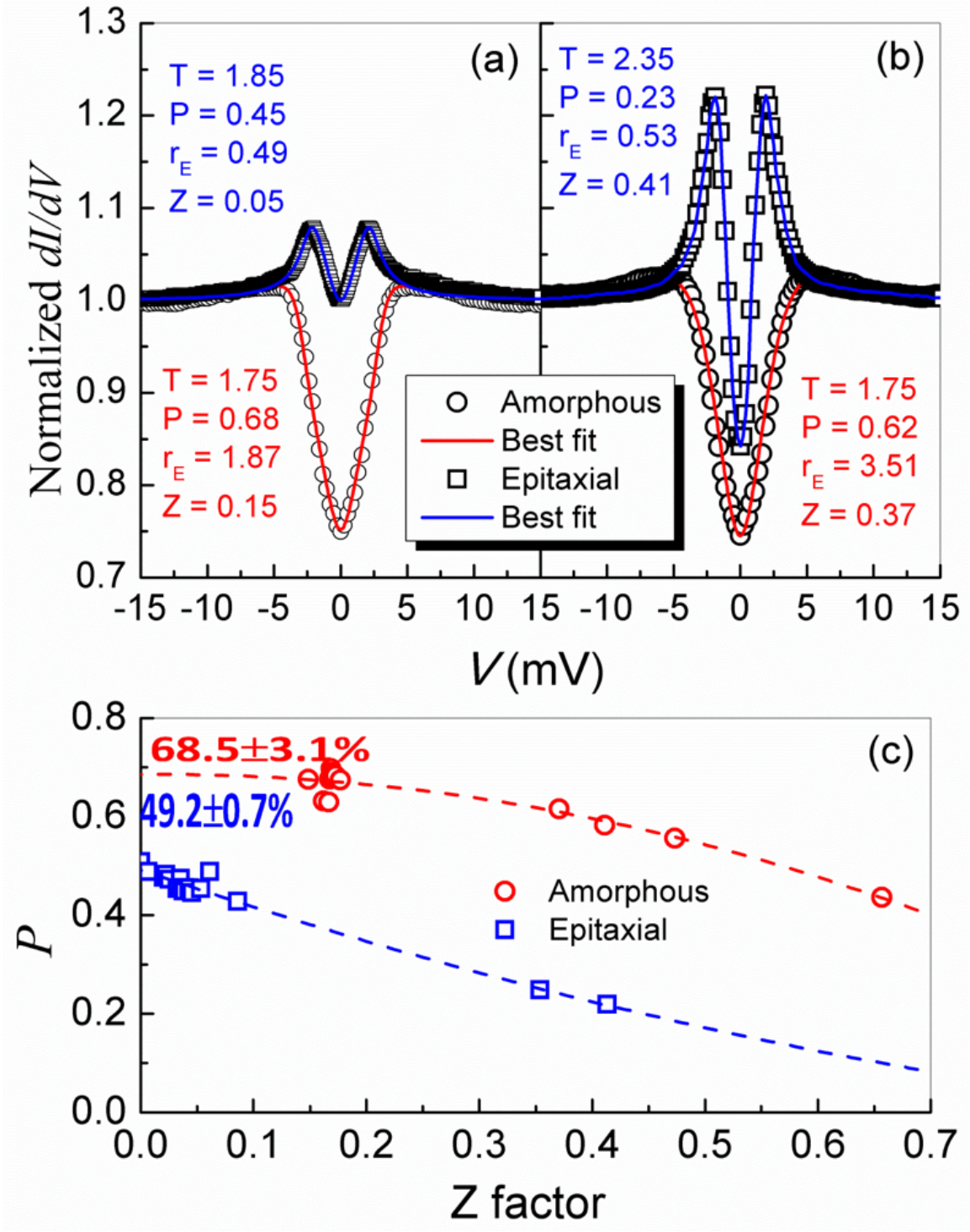

Figure 8.4: (a, b) Comparison of Andreev spectra of two contacts on the amorphous and the epitaxial $Fe_{0.65}Si_{0.35}$ samples with small Z factor close to zero and large Z factor of about 0.4 where open symbols are the experimental data and the solid lines are the best fit to the BTK model, (c) spin polarization (open symbols) of the epitaxial and the amorphous $Fe_{0.65}Si_{0.35}$ samples as a function of the Z factor (dashed lines are a quadratic fit to guide ones eyes).

terestingly, the spin polarization of the amorphous $Fe_{0.65}Si_{0.35}$ alloy is substantially higher, demonstrating that a modified magnetism by the amorphous nature can also be utilized to tune the spin polarization for spintronics.

8.6 Acknowledgments

Magnetism program at Lawrence Berkeley National Lab, supported by the U.S. Department of Energy, Office of Basic Energy Sciences, Materials Sciences and Engineering Division, under Contract No. DE-AC02-05CH11231.

Chapter 9

DETERMINATION OF SPIN POLARIZATION USING FE-SUPERCONDUCTOR $SMO_{0.82}F_{0.18}FEAS$

This work utilizes a (1111) Fe superconductor $SmO_{0.82}F_{0.18}FeAs$ and Pb to measure the spin polarization of a highly spin-polarized material, $La_{0.67}Sr_{0.33}MnO_3$. The determined spin polarization value using the Fe superconductor is the same as that using Pb, indicating that the Fe superconductor can be utilized to measure spin polarization of magnetic materials. Furthermore, one can show that the spin polarization can be measured up to 52 K, the transition temperature of $SmO_{0.82}F_{0.18}FeAs$. Based on the behavior of the differential conductance for highly spin polarized LSMO and small polarization of Au, it can be concluded that the Fe-Sc is not a triplet superconductor but a singlet superconductor.

9.1 Motivation

The first high temperature superconductor was discovered in 1986 by IBM researchers Georg Bendnorz and K Alex Muller [172]. Unlike conventional superconductors, which often have transition temperatures below 10 K, some high temperature superconductors do not require cooling using liquid helium. This is a huge advantage since liquid He systems are often very expensive, require specialists to operate them and the cost of liquid helium is about \$10-\$22 per liter. For typical superconducting measurements, that would run about a week, one would need 100 liters of liquid He. High temperature superconductors do not need to be cooled to such low temperatures so, in some cases, this can be done with liquid nitrogen [173]. Almost every university and laboratory has easy and affordable access to liquid nitrogen which has

an evaporation temperature of 77 K, costs only around $0.50 per liter, and is much less dangerous then liquid He. For almost 20 years, only compounds of Cu and O_2, known as cuprates, were found to have high temperature properties. The discovery of these materials was surprising because, according to the BSC theory, the upper limit for superconductivity was thought to be 30 K. It was found that the larger the transition temperature the larger the fraction of the Fermi temperature was available, meaning there is a wider range in superconducting temperatures for unconventional materials.

There are many technological applications that would benefit from the higher transition temperatures, and some have transition temperatures higher then the boiling point of liquid nitrogen. These devices would benefit from higher critical magnetic fields. Some cuprates have shown to have critical fields of up to 100 T [174]. One obvious technology that would benefit from high T_c superconductors would be spintronic devices such as STT or spin valves. If these devices could operate at temperatures higher then needed for liquid He, these devices could be much more commercially available and weigh a lot less. Other devices such as qubits and Josephson junctions would also benefit from high temperature superconductors such that a quantum computer would be less expensive, less complex, and weigh less. Microwave devices have also benefited from the discovery of cuprates, such as microwave communication devices for orbiting satellites. Approximately 1/8 of the total weight is made of microwave filters, filter bank mechanical support, and cable harnesses [175]. This means the remaining weight is from the passive radiation cooling systems which cool the microwave superconducting components to low temperatures. If these were replaced with high T_c elements most the the weight could then be replace with the microwave filters and produce a more efficient system [176].

In 2008, Hideo Honsono was the first physicist to investigate, using flourine-doped

LaFeAsO, a new family of superconductors called the Fe-SCs [177] where the critical temperatures are around 26 K. Following his work, groups in Japan and China were able to raise the superconducting transition temperate T_c of LaFeAs to 43 K under lower pressures [178], and have critical temperatures of over 55 K have, since then been, discovered. There are many advantages of using the Fe-SC over cuprates. The first is that cuprates are often brittle and are difficult and costly to fabricate into wires, such as the wires used in MRI systems. Therefore MRI devices still use conventional materials such as NbTi, however they are still expensive to operate due to the use of liquid helium. Fe-SC are easier to make and less costly. An added bonus is that they have a higher critical temperature, and do not need liquid He to cool them lower then there critical temperature. Secondly, Fe-SC have values of T_c that exceed most cuprates and have critical fields that exceed all cuprate materials. Thus they are the ideal candidate for high magnetic field and large current driven devices. Thirdly, the chemical versatility of these Fe-SC is important. Because the chemical flexibility is better then cuprates ,this allows scientist to tailor the properties they need for specific devices [179]. An open question about Fe-SC is how superconductivity arises. Many have argued that, do to measuring a spin polarization of zero, the Fe-SC must be of even parity and thus be a triplet superconductor [180, 181], while others have argued that Fe-SCs are just s-wave or odd parity superconductors [182–184]. This chapter will investigate whether Fe-SC can be used to measure the spin polarization of highly spin polarized materials—for example LSMO. This work compare these results with the conventional s-wave Pb superconductor, as well as compare the normalized dI/dV of Au, which has a small polarization, and use the ARS methods to investigate whether this Fe-SC is a singlet, like Pb, or a triplet superconductor.

9.2 Introduction

Spintronic devices critically depend on the spin polarization (P), which is the normalized imbalance of the number of spin up and spin down electrons at the Fermi level. Many spin devices, such as giant magnetoresistance sensors and read-heads in hard drives, can achieve big enhancements if highly spin-polarized materials are used. The discovery of these highly spin-polarized materials, especially half metals with $P = 100\%$, has been a main topic in spintronics [4]. For most conventional superconductors, the Curie temperature (T_c) is below 10 K, which makes it difficult to measure the spin polarization in these highly spin-polarized materials. Recently Fe-superconductors have been shown to have T_c of up to 55 K, consequentially allowing them to fix this issue. Andreev reflection spectroscopy (ARS) is the method used to measure P as well as the superconducting gap (Δ) of a superconductor, which describes the mechanism of superconductivity.

P is defined as the imbalance of spin up and down electrons at the Fermi energy $P = \frac{n(\uparrow)-n(\downarrow)}{n(\uparrow)+n(\downarrow)}$. At a normal metal/superconductor interface, a current injected from the normal metal to the superconductor must be converted to a supercurrent. Therefore within the superconducting gap, at the Fermi level, to conserve superconductivity, an electron must be accompanied by another electron with opposite spin to form a Cooper pair. Consequently a hole must be reflected back into the normal metal. This is what is known as Andreev reflection [93]. The conductance at the interface for the electrons inside the Δ must be twice that outside the Δ. For a half metal/superconductor interface, the conductance within the gap is zero because only one spin orientation is allowed at the Fermi level and thus a Cooper pair cannot be formed. This leads to $P = 100\%$. The P of the normal metal and Δ of the superconductor can be measured by the conductance spectra. For real experiments

the interface is not ideal and therefore an analysis of the whole spectrum is needed to find P and Δ. Using ARS, the spin polarization of many materials have been measured as well as the superconducting gap [15–27] of many superconductors. Recently Fe-superconductors having T_c as high as 55 K have been measured using ARS [28, 29]. To better find P of highly spin-polarized materials, such as LSMO, higher T_c dependent materials such as these Fe-superconductors are needed [185].

Point-contact Andreev Reflection (PCAR) is the method used to perform these experiments which uses the density of states of the superconductor to measure the P of the material. In a spin-polarized current from a ferromagnet, the loss of electrons with one spin orientation suppresses the AR process, which yields PCAR spectroscopy. From the spectra, the P value and Δ can be determined [28] using the effects of the 3D interface [87, 88, 95–98]. More recently, it has been shown that these values can be determined using the 1D effects as shown in the previous work [92]. To find P the conductance ratio $G(0)/G_n = 2(1-P)$ between zero-bias voltage ($V = 0$) within the Δ was determined using the standard Blonder-Tinkham-Klapwijk (BTK) model [81]. In real experiments the contacts used are often not ideal and therefore the inclusion of the interfacial scattering factor Z, thermal smearing due to finite temperature, and residual resistances must also must be taken into account. The spin polarization is based on the recent 1D Chen-Tesanovic-Chien (CTC) model [83]. This PCAR technique has been used to determine the P values of highly spin-polarized materials and half metals [22, 23].

This chapter investigates whether Fe-superconductors, specifically $SmO_{0.82}F_{0.18}FeAs$ [185], can be used to determine the P value for highly spin-polarized materials. Fe-SCs have shown to have critical temperatures ranging from 26 K to 55 K [186–190, 190–195] well above the critical temperatures of around 10 K for conventional superconductors such as Pb. For comparative analysis both a conventional superconductor Pb

and unconventional superconductor $SmO_{0.82}F_{0.18}FeAs$ were used to find the P value of a highly spin-polarized material, $La_{0.67}Sr_{0.33}MnO_3$ (LSMO). Both materials yielded similar behavior in normalized conductance and showed similar intrinsic P values and temperature dependence, which is not obvious until all data is normalized.

9.3 Experimental Setup

First, the temperature dependence of the conductance using the Pb superconductor is studied and then the P and Δ dependence on temperature is extracted. Figure 9.1 shows the schematic setup for PCAR measurements. Using the pulsed laser deposition method (PLD), samples of $La_{0.67}Sr_{0.33}MnO_3$ were epitaxially grown to a thickness of 150 nm on single crystalline $SrTiO_3$ substrates by the collaborators at Nanjing University in China. For PCAR measurements a sharp superconducting tip made of either Pb, with T_c 7.2 K, or Fe-superconductor, with T_c 55 K, and were placed on the sample to create the AR contact needed. To measure the conductance of the material four contacts were used, two being the input and output current and two being the measured in and out voltage. To measure temperature dependence of the material, each sample was cooled to temperatures of about 1.5 K and allowed to heat up to room temperature. If the samples are heated too quickly the contacts can become damaged due to the quadratic temperature gradient induced, therefore each measurement was cooled down over the time frame of about 8 hours.

9.4 ARS Using Conventional Pb Superconductor

Figure 9.2 is representative analysis of the normalization of the dI/dV conductance using the Pb superconductor for temperatures between 1.54 K and 7.67 K. It can be observed that for $T > 7.42$ K the conductance curves are the same and have a resistance of 57.4 Ω. Therefore to normalize the conductance each measurement was

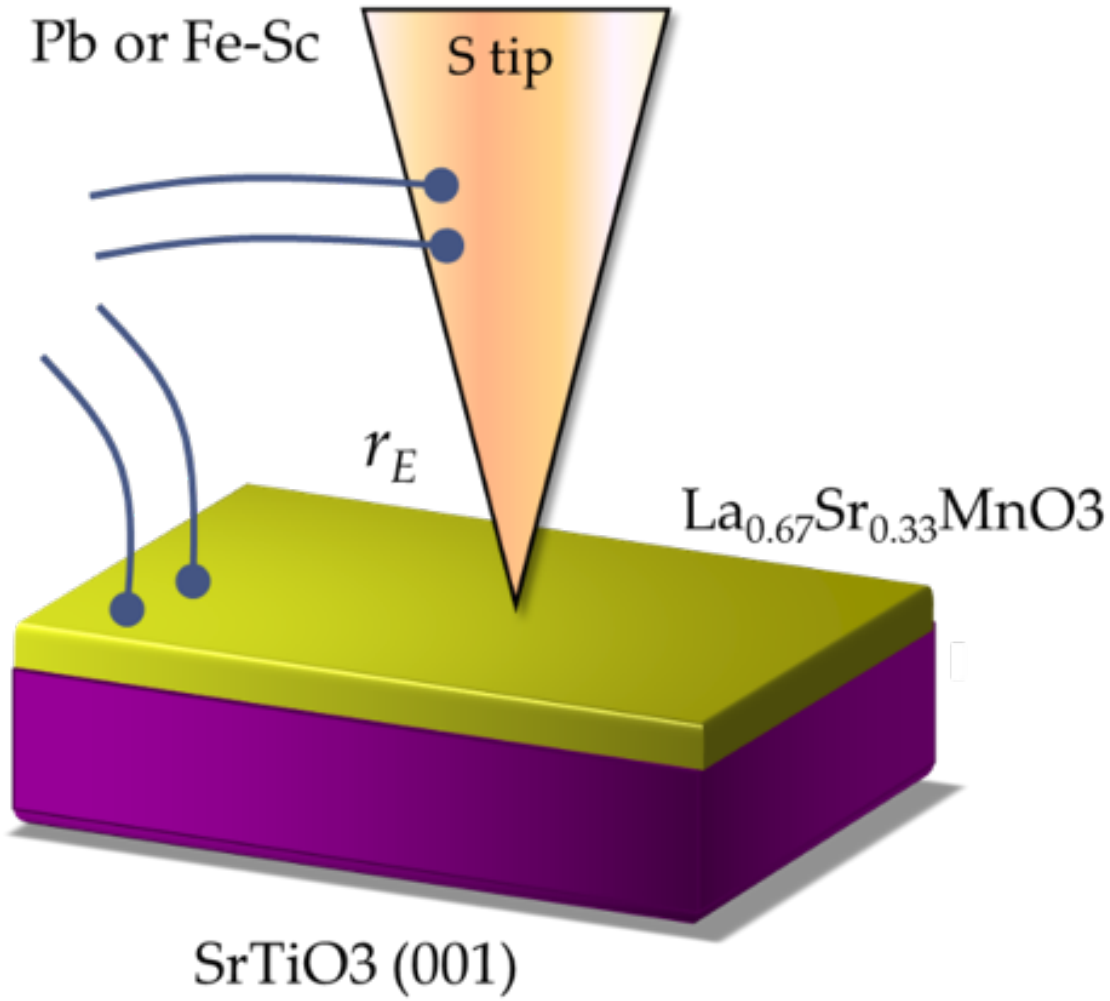

Figure 9.1: Schematic setup for Point contact Andreev reflection (PCAR) measurements. Epitaxial $La_{0.67}Sr_{0.33}Mn0_3$ samples of 150 nm thick are deposited on single crystalline $SrTiO_33$ substrates. Samples are grown by pulsed laser deposition (PLD) by collaborators at Nanjing University in China. A sharp superconducting point is made in contact with the sample. The superconductor is either Pb or Fe-superconductor $SmO_{0.82}F_{0.18}FeAs$. Four contacts are needed: two for input and output current, and two to read the incoming and outgoing voltages.

divided by the conductance at 7.42 K. The figure shows that for increasing T there is increased conductance. The conductance curves are slightly asymmetric about zero voltage which can be attributed to surface defects in the sample.

Figure 9.3 shows the normalized conductance measurements, open circles, with their fit to the MBTK model, red lines. It is apparent that the conductance data are symmetric about zero bias and can be well described by this model. Using the MBTK model the polarization P, superconducting gap Δ, and interfacial scattering factor Z can be calculated.

Using the MBTK theory the fitting parameters P, Δ, r_E, and Z are calculated. Figure 9.4 shows the fitting for 4 different temperatures 1.54, 5.27, 6.85, and 7.02 K. Open circles are the measured data and red lines are the MBTK fit. For each data set the Z factor is the same. This is because Z depends on the contacts used during PCAR and, for all temperatures shown, the same contact was used. The r_E is also assumed to be constant since all measurements were done on the same contact. For larger temperatures the P value decreases from 0.385 to 0.367. This decrease is very small and all values are within 5%, so the P is considered to be constant with an average value of 0.376. Finally Δ can be seen to decrease with increasing temperature. To better understand the temperature dependence the Δ verses temperature is plotted in figure 9.5.

Figure 9.5(a) shows the Δ dependence with T for all temperatures measured from 1.54 K to 7.67 K, open squares. For $T < 3.25$ K the gap remains constant. For $T > 3.25$ K the gap decreases non-linearly with increasing temperature. The BCS model is shown by the red dashed line to help guide the eye. Even though the data is not fitted with this model, it can be seen that the gap does follow a BCS trend. Figure 9.5(b) shows the P dependence on T for the same temperatures measured, open blue squares. The P value varies slightly, all values within 5%, and shows that

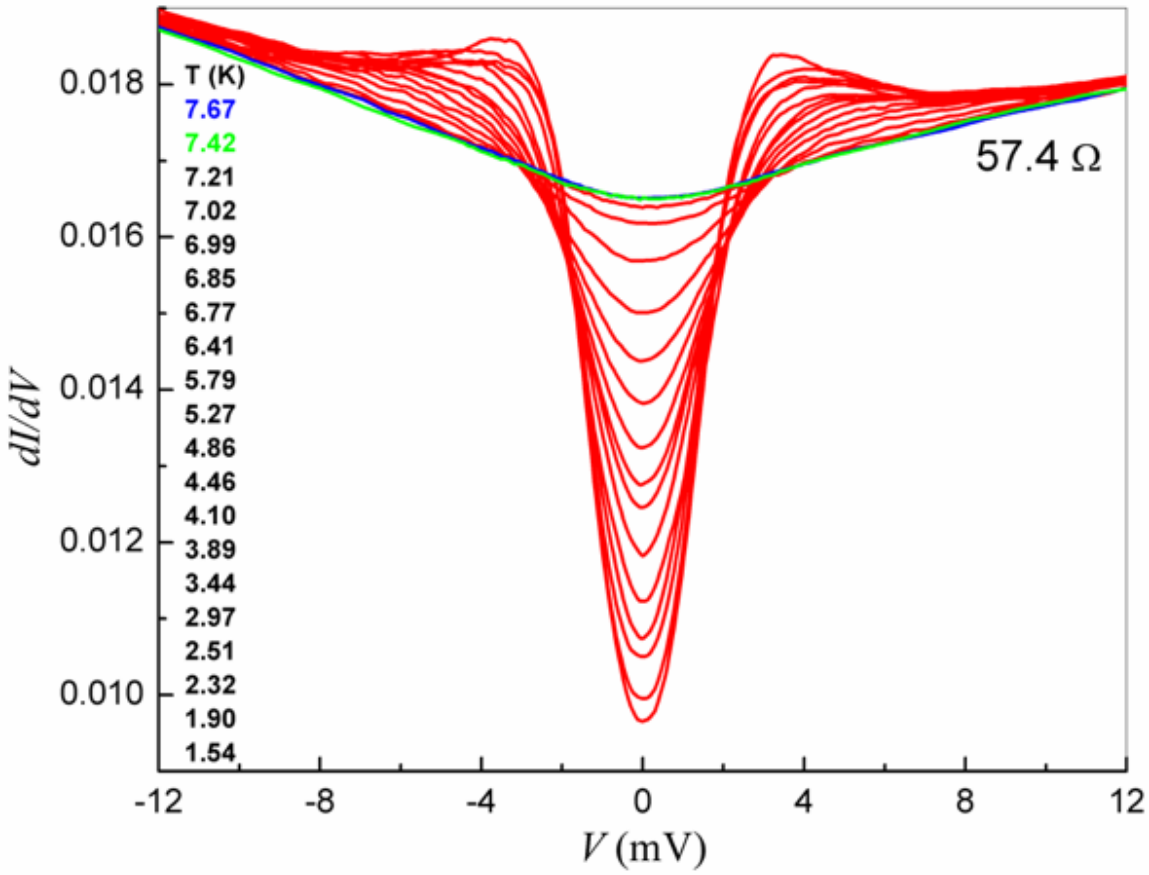

Figure 9.2: Normalized conductance dI/dV verses voltage conducted at temperatures from 1.58 K to 7.67 K for LSMO measured with Pb superconducting tip. At 53.73 K (green curve) the conductance is the same for higher temperatures and has a resistance of 57.4 ω. This conductance curve is used to normalize the other curves. As temperature increases so does the conductance and all are symmetric around zero. There is slight asymmetry due to the surface quality of Pb.

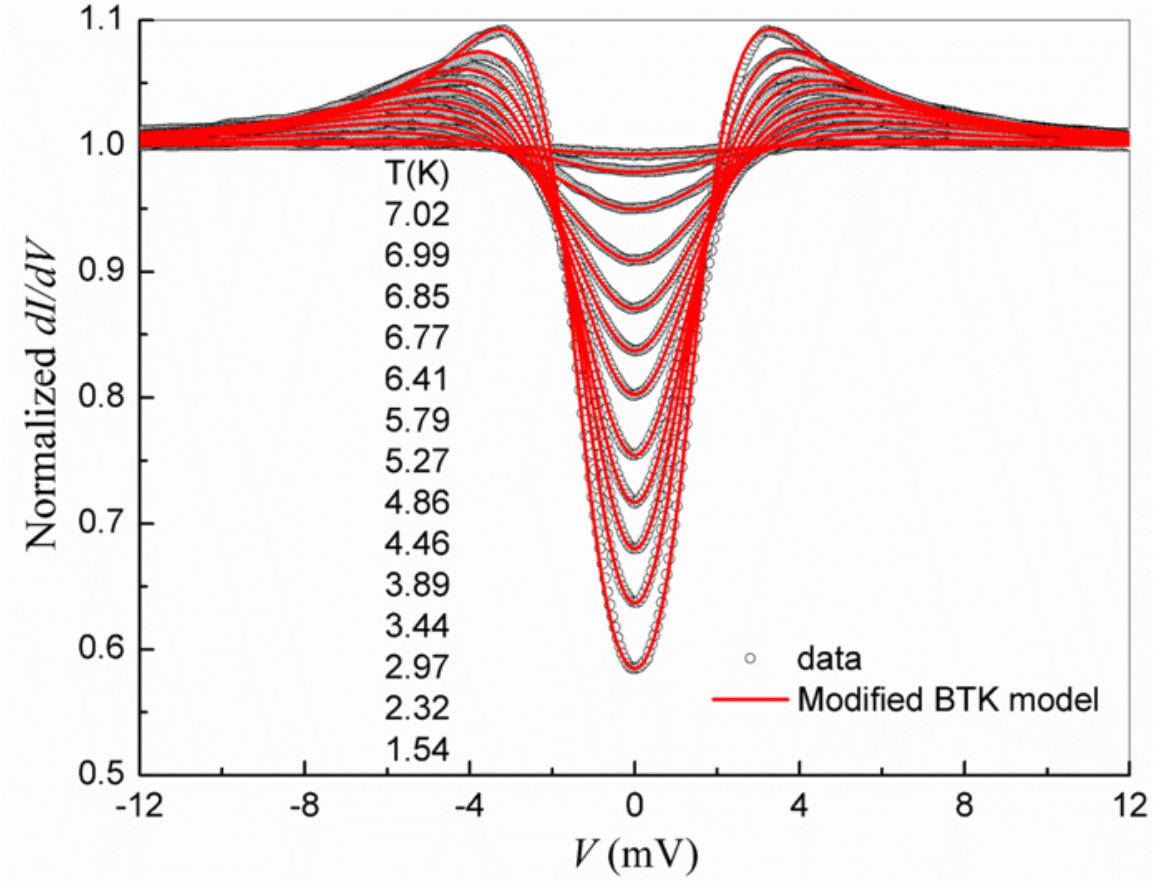

Figure 9.3: Normalized conductance using PCAR fitted with MBTK model using Pb superconducting tip. Open circles are the measured normalized conductance and red lines are the MBTK fit. Conductance curves are shown for T between 1.54 K and 7.02 K. Conductance is symmetric about zero as expected and is well explained by the model.

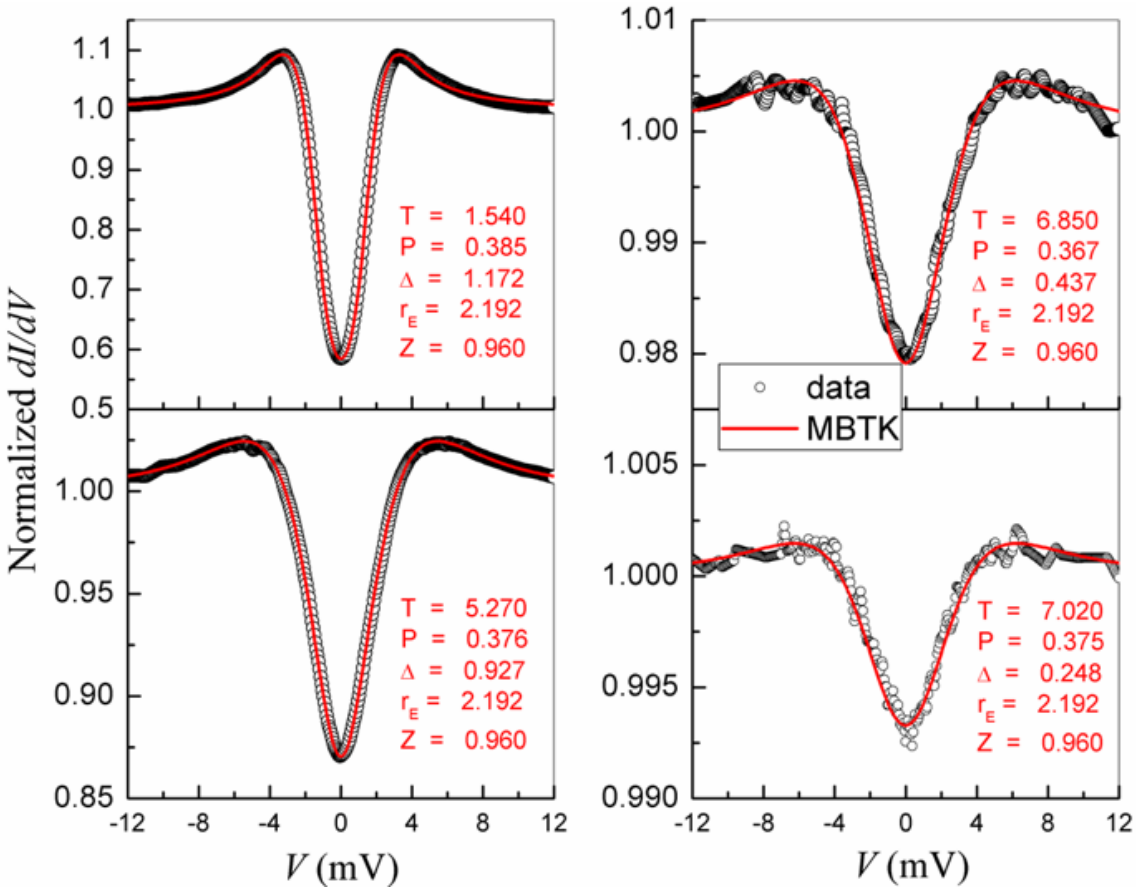

Figure 9.4: Normalized conductance fitting parameters using PCAR fitted with MBTK model. Open circles are the measured normalized conductance and red lines are the MBTK fit. Conductance curves are shown for T 1.54 K, 5.27 K, 6.85 K, and 7.02 K. The interfacial scattering factor Z is 0.960 for all measurements because the same contacts were used in each measurement. Since the same contacts were used it was also assumed that r_E would remain constant with a value of 2.192 ω. As the temperature increases the polarization changes slightly but remains fairly constant. The P value is 0.376. The Δ decreases from 2.192 to 1.172 with increasing T.

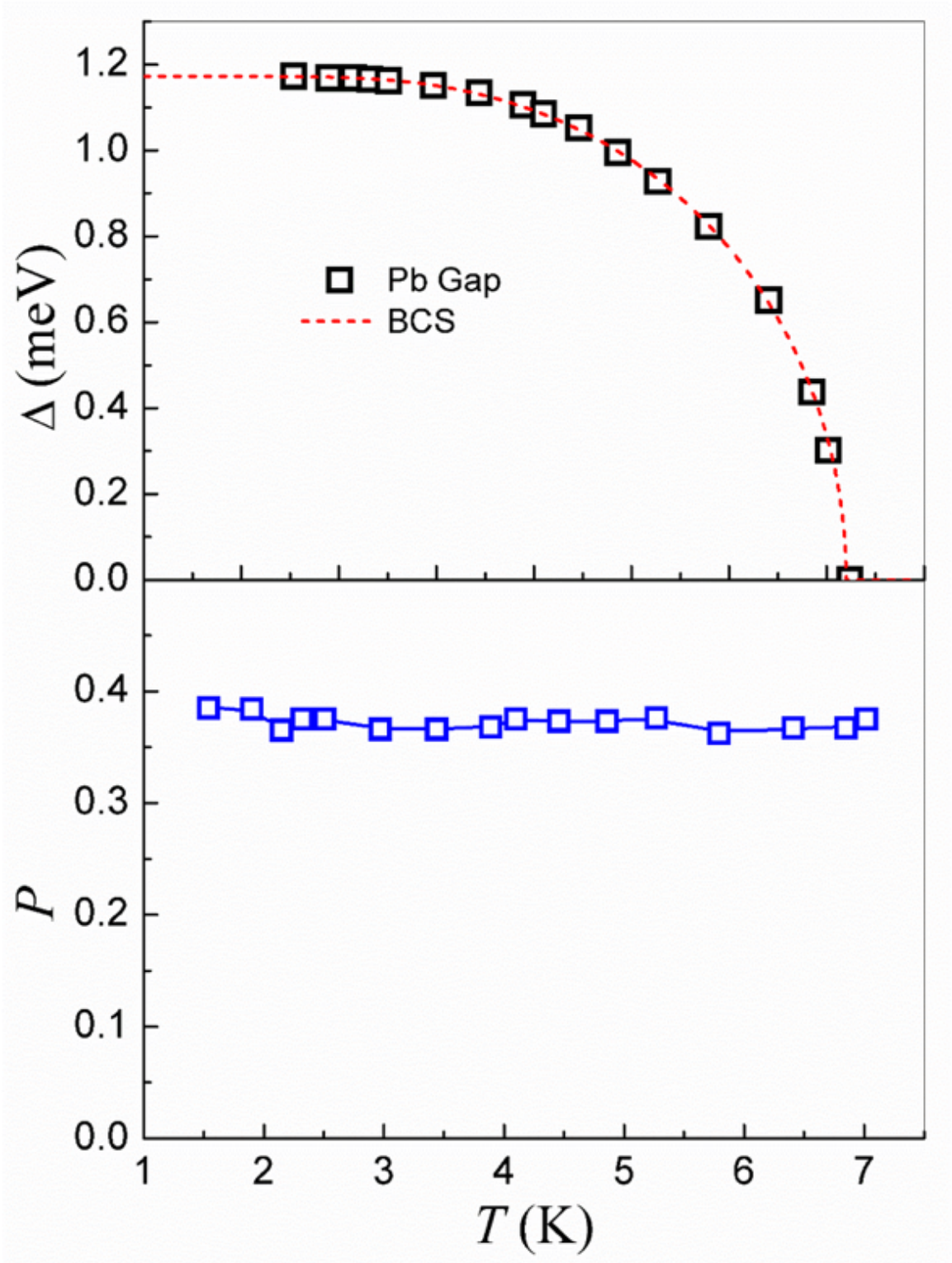

Figure 9.5: (a) Δ dependence on T for LSMO measured using Pb superconductor. For $T < 3.25$, Δ remains constant at about 1.18 meV and then for $T > 3.25$ meV, Δ decreases non-linearly to 0 meV. (b) P dependence on T for Pb superconducting tip on LSMO. Polarization has negligible T dependence with a constant P of 0.376.

for all T the P value is 0.376.

To obtain the P dependence on Z factor the conductance was calculated for the same T of 1.80 K using different contacts for each measurement. Figure 9.6(a) shows the normalized conductance at 1.80 K for four different measurements. Again red lines are the MBTK model fitting used. For these measurements, Δ was held at a constant 1.20 eV, and the r_E is fitted. The r_E changes (from 0.35 ω to 1.83 ω) with surface quality and varies depending on the contact used. The conductance curves display a small asymmetry due to the surface quality of the Pb superconductor used. It can be seen that for increasing Z from 0.035 to 0.6 the P value decreases from 0.070 to 0.859. To better understand the behavior, the P values for many more temperatures were plotted verses the Z factor in figure 9.6(b). For increasing Z from 0 to 1, P decreases non-linearly from 0.83 to 0.35. The red curve is to guide the eye. The P value behaves as expected and is dependent on the contacts used.

9.5 ARS Using Unconventional Fe Superconductor

Next the Pb-SC tip was replaced with the unconventional Fe-SC. Figure 9.7(a) shows the raw conductance data for various temperatures from 1.78 to 53.73 K. The behavior is very similar to the temperature dependence of Pb with conductance increasing with temperature and symmetry about zero voltage. To normalize this conductance the temperature at which the conductance curves no longer change (temperatures above 53.73 K) was found and the conductance curve at 53.73 K was used to normalize the rest of the data. Figure 9.7(b) is a representative data of this normalized conductance at 1.78 K. Again using the MBTK model, the data (open circles) was fitted (red line) and shows good agreement with the model. This yielded a P of 0.82 and gap of 8.15 eV. This spin polarization is different than Pb because this is not purely intrinsic spin polarization. Therefore one must extrapolate to $Z = 0$

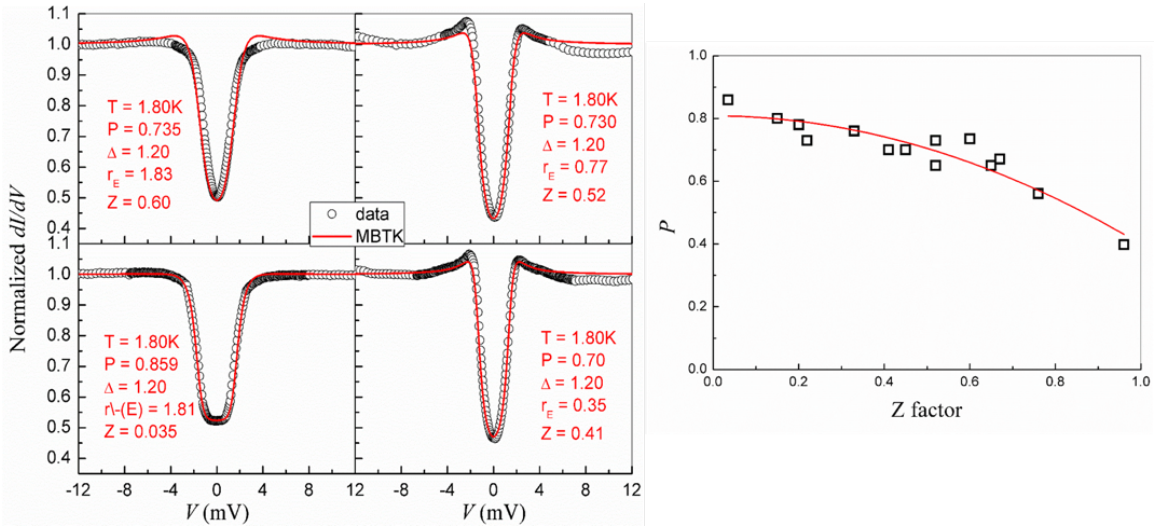

Figure 9.6: (a) Normalized conductance using Pb superconducting tip with fitting parameters, P, ω, r_E, and Z for T of 1.80 K using different contacts for each measurement. Open circles are the measured data while red lines are MBTK fit. Z factor changes for each contact between 0.60 and 0.035 because each measurement is a different contact. The Δ is the same since the same tip was used. Because Z varies with contacts so does the r_E from 0.35 to 1.20 ω. P also varies with Z and decreases for increasing Z. (b) P dependence on Z. As Z factor increases from 0 to 1 the P value decreases from 0.80 to 0.40. The red line is to guide the eyes.

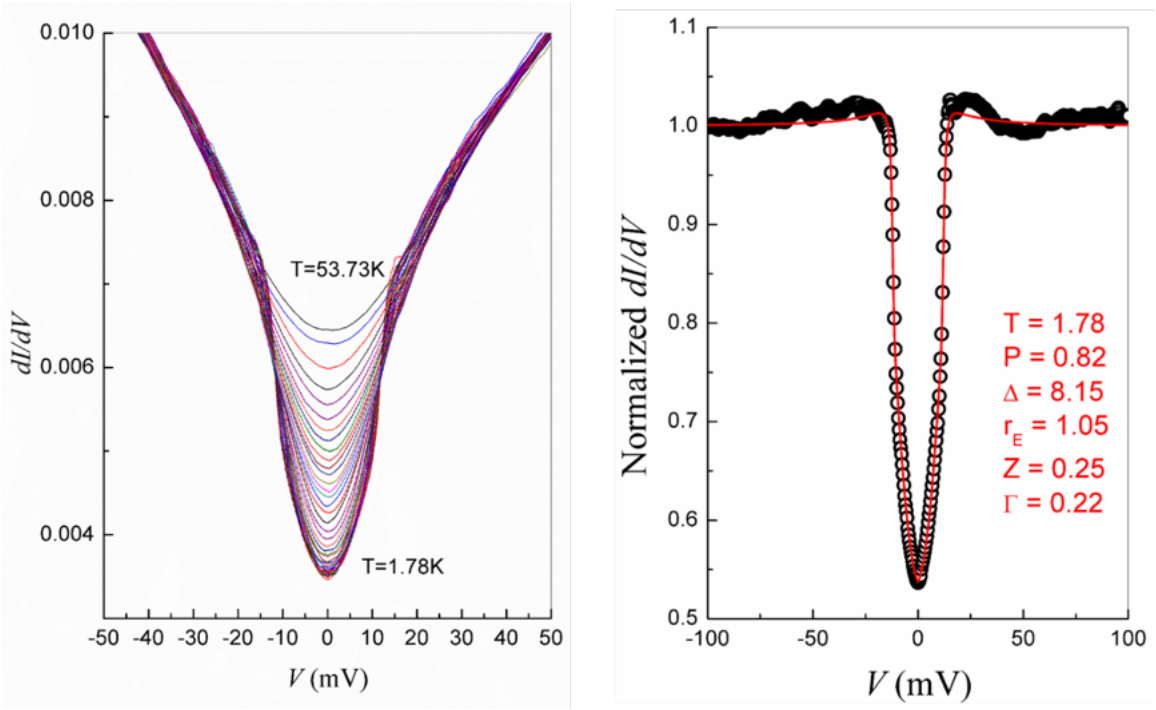

Figure 9.7: Raw dI/dV verses voltage conducted at temperatures from 1.78 K to 53.73 K for LSMO measured with Fe-superconducting tip. At 53.73 K the conductance is the same for higher temperatures. This conductance curve is used to normalize the other curves. As temperature increases so does the conductance and all are symmetric around zero. There is slight asymmetry due to the surface quality of Pb. (b) Normalized conductance at 1.78 K. Open circles are measured data and red line is the MBTK fit. Using the MBTK fit the P value was found to be 0.82, Δ 8.15 meV, r_E 1.05 ω, and Z of 0.25.

to find the intrinsic spin polarizations for each superconductor used.

The normalized conductance curves using the Fe-SC for T between 1.78 K and 51.26 K are shown in figure 9.8. The open circles are the measured data and red lines are the fit using the MBTK model. Just as for Pb, the Fe-superconductor conductances fit well with this model. Figure 9.9 shows the fitting parameters at 1.78 K and 1.80 K from the MBTK fit. Figure 9.9(a) shows two conductance curves, one for 1.78 K and 53.73 K for one contact. The conductance increases for the higher temperature. Figure 9.9(b) shows the conductance curves at 1.8 K and 53.25 K for a different set of contacts. The conductance also increases with T. Figure 9.9(a) and 9.9(b) should have the same conductance since the temperature is almost the same, however there is a shift in conductance due to the change in interfacial scattering factor Z. Figure 9.9(c) and (d) are the fitting parameters and MBTK fit for both 1.78 and 1.80 K. Notice that the Z factors are indeed different. Just as Pb, the P value decreases from 0.824 to 0.71 as the Z factor changes from 0.250 to 0.405. One can also see the Δ decreases with temperature from 8.15 eV to 8.11 eV as T increases from 1.78 K to 1.80 K. The r_E also changes from 1.05 ω to 0.679 ω, but this is due to the change of contacts. It is not obvious that the behavior of Fe-SC is the same as for Pb until the data is normalized.

Figure 9.10 shows the comparative analysis for both the conventional Pb superconductor and the unconventional Fe-superconductor. Figure 9.10(a) shows P verse Z for different contacts at the same temperature. Orange circles are from the Fe-SC tip and open squares are from Pb. It is obvious that the behavior for both tips are the same and both fit the BCS model (red line), to guide the eye, well. Using figure 9.10(a) one can find the intrinsic spin polarization of 0.8 by extrapolating each measurement at $Z = 0$. Figure 9.10(b) is P verses T for both tips. For Fe-SC open squares P changes minimally and has an average value of 0.8. The polarization for

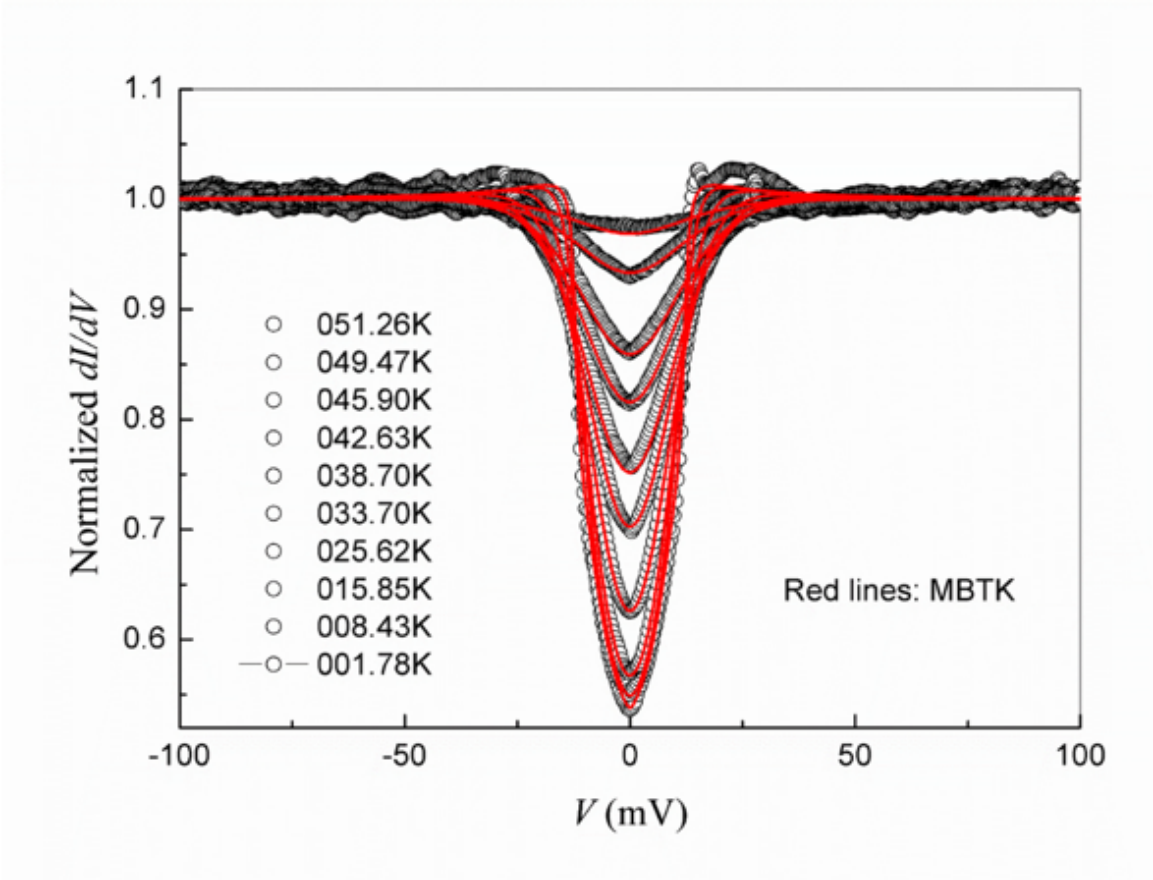

Figure 9.8: Normalized conductance using PCAR fitted with MBTK model for Fe-superconducting tip. Open circles are the measured normalized conductance and red lines are the MBTK fit. Conductance curves are shown for T between 1.78 K and 51.26 K. Conductance is symmetric about zero as expected and is well explained by the model.

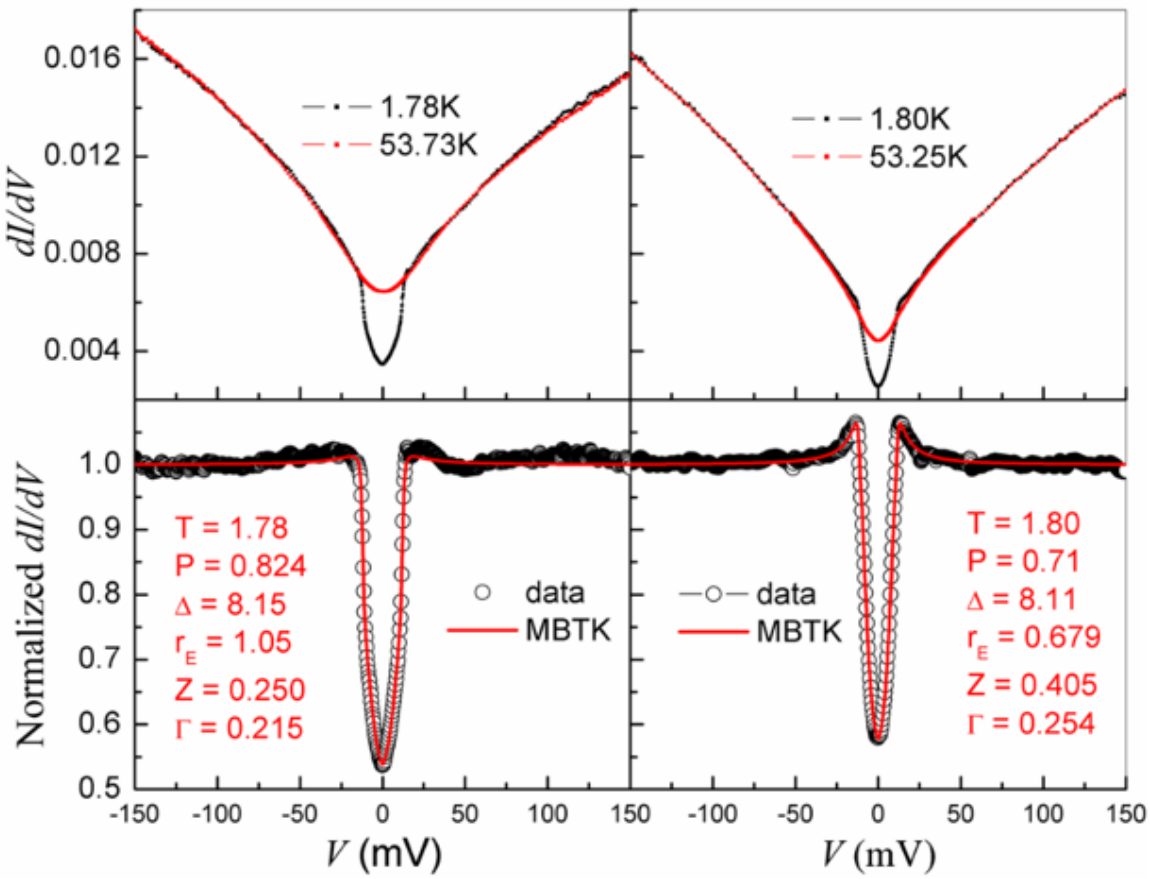

Figure 9.9: (a) Normalized conductance using Fe-superconducting tip for T 1.78 K and 53.73 K. Conductance increases with T. (b) Normalized conductance for T 1.80 K and 53.25 K. Conductance fits same behavior as (a) but the values have shifted. This is due to different contacts being used in (a) and (b) and therefore slightly different conductances are measured. (c) Fitting parameters, P, Δ, r_E, and Z for T of 1.78 K. Open circles are the measured data while red lines are MBTK fit. (d) Fitting parameters for T of 1.80 K. For (c) and (d) as the Z factor increases from 0.250 to 0.405, P decreases from 0.824 to 0.710, and the Δ and r_E change slightly as Z changes.

Pb (open blue circles) is also constant with an average value of 0.376, all of which are within 5%. Both tips give us the same intrinsic polarization. Finally one can show the normalized SC gap verses the normalized T for both Fe-SC (open squares) and Pb (open blue circles) in the inset of 9.10(c), the gap for each superconductor follows a similar decrease as T increases but one does see different Δ values for each. The gap decreases from 8 meV for the Fe-Superconductor, open squares, and decreases from 1.5 meV for the Pb superconductor (open blue circles). It is not obvious that both tips behave the same until one normalizes the data. Figure 9.10(c) shows the normalized Δ verses T for both tips and they both follow the same characteristic BCS behavior, red dashed lines to guide the eye. One can show that the sample can be measured up to T of 52 K and is consistent with Pb measurements.

9.6 Fe Superconductor is Not a Triplet Superconductor

As discussed in section 4.5, s-wave and p-wave superconductors exhibit different dI/dV dependence. For a s-wave superconductor in contact with a highly polarized metal, the normalized differential conductance will decrease using highly spin polarized metals; however, for a p-wave superconductor at both large and small spin polarized metals, dI/dV will always increase at zero bias.

Figure 9.11 shows the spin polarization of known singlet superconductors Nb and Pb on common normal metals. Figure 9.11(a) the normalized dI/dV is shown for s-wave Nb and Pb using Au and Cu metals. These are metals show that the polarization is only 0 and the change in dI/dV is only 0.60 and 0.80 respectively. Figure 9.11(b) shows highly spin polarized materials $Co_2FeAl_{0.5}Si_{0.5}$ and the half metal CrO_2 with polarizations of 75% and 96%. Figure 9.11(c) shows the normalized dI/dV for Fe and Cu with polarizations of 40% and 45%.

The main question becomes: *Because one can show that LSMO is highly spin*

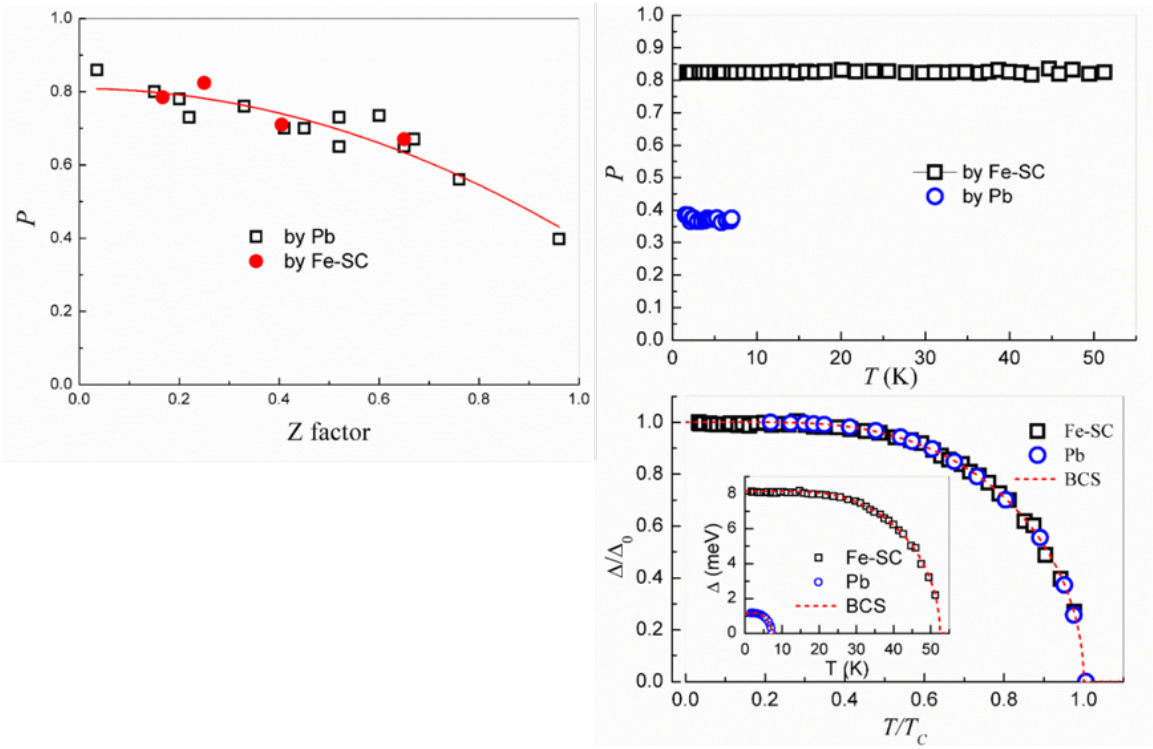

Figure 9.10: (a) P dependence on Z for both Pb, open squares, and Fe-superconductor, solid orange circles. As Z factor increases from 0 to 1 the P value decreases from 0.80 to 0.40 for both tips. The red line is to guide the eyes. (b) P dependence on T for Pb superconducting tip, open circles, and the Fe-superconductor, open squares. Polarization has negligible T dependence with a constant P of 0.376 for Pb and 0.82 for Fe-superconductor. The values are different but one finds the same intrinsic P for both of 0.8 when extrapolating the data at $Z = 0$. (c) Δ dependence on T for LSMO measured using Pb superconductor, open blue circles, and Fe-Superconductor, open squares. The inset shows the temperature dependence for each and it is not obvious both tips follow the same behavior until you normalize the Δ and T as done in the main plot. For both tips $T/T_c < 0.45$ the $\Delta/\Delta(0)$ remains constant at about 1 and then for $T/T_c > 0.45$ meV the Δ decreases non-linearly to 0.

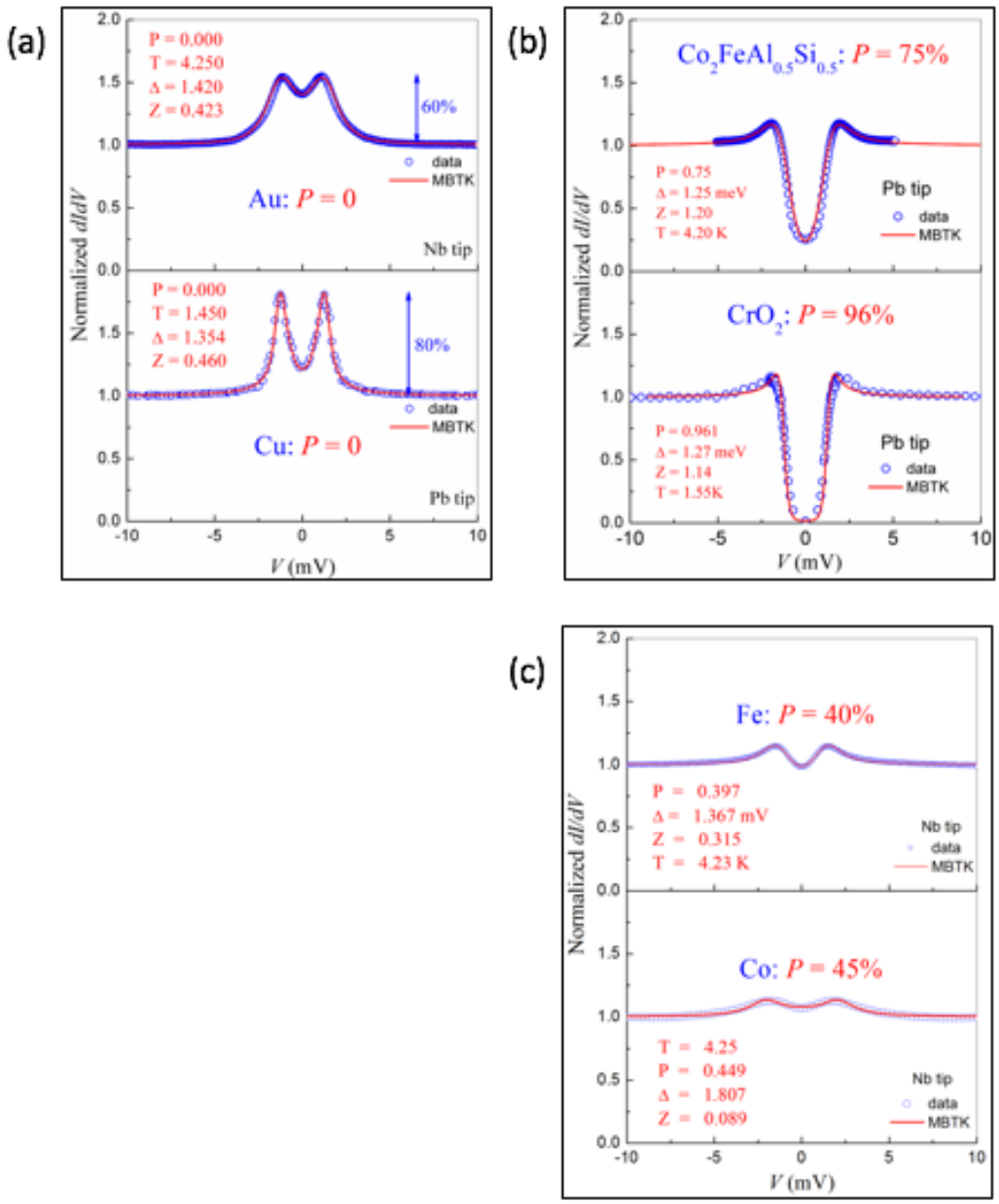

Figure 9.11: Polarization of common normal metals using known singlet superconductors Nb and Pb (a) on Au and Cu with $P = 0$, (b) $Co_2FeAl_{0.5}Si_{0.5}$ and the half metal CrO_2 with P of 75% and 96%, (c) Fe and Co with P of 40% and 45%.

polarized, can it be measured by Fe-SC? Is this superconductor actually a p-wave or rather a singlet s-wave superconductor? This answer can be found by measuring the differential conductance using the highly spin polarized LSMO and then measuring with a known singlet SC and comparing the behavior. To do this the normalized dI/dV, using the unconventional Fe-SC and conventional Pb-SC on both highly spin polarized LSMO and small polarized Au. Figure 9.12 shows these results. For the Au measurements both dI/dV dependence is as expected for $P = 0$ wherein the conductance increases at zero bias. If the Fe-SC is a triplet, one would expect the differential conductance to increase as well; however, because for both Au and LSMO both decrease at zero bias, one can conclude that the Fe-SC is not a triplet superconductor, but rather because it behaves similarly to the known singlet Pb-SC then it must also be a singlet superconductor.

9.7 Conclusion

In summary, one can demonstrate that both a conventional Pb-superconductor and unconventional Fe-superconductor can be used to extract the intrinsic P value of the metal and Δ of the superconductor in PCAR experiments. One can show that PCAR can yield the dI/dV conductance of the material and normalization can be calculated using the conductance curves at temperatures above T_c, in this case 55 K for the Fe-superconductor. The same P of LSMO was determined using both Pb-and Fe-superconductor at a value of 0.8. Both superconductors showed negligible T dependence on P for $T < 55$ K and all values of P at these temperatures were within 5% of each other. Finally one can conclude, based on the PCAR measurements, that Fe-superconductors can be used to find the P of the metal and Δ of the superconductor especially for high spin-polarized materials such as LSMO. After investigating the behavior of the differential conductance on highly spin polarized

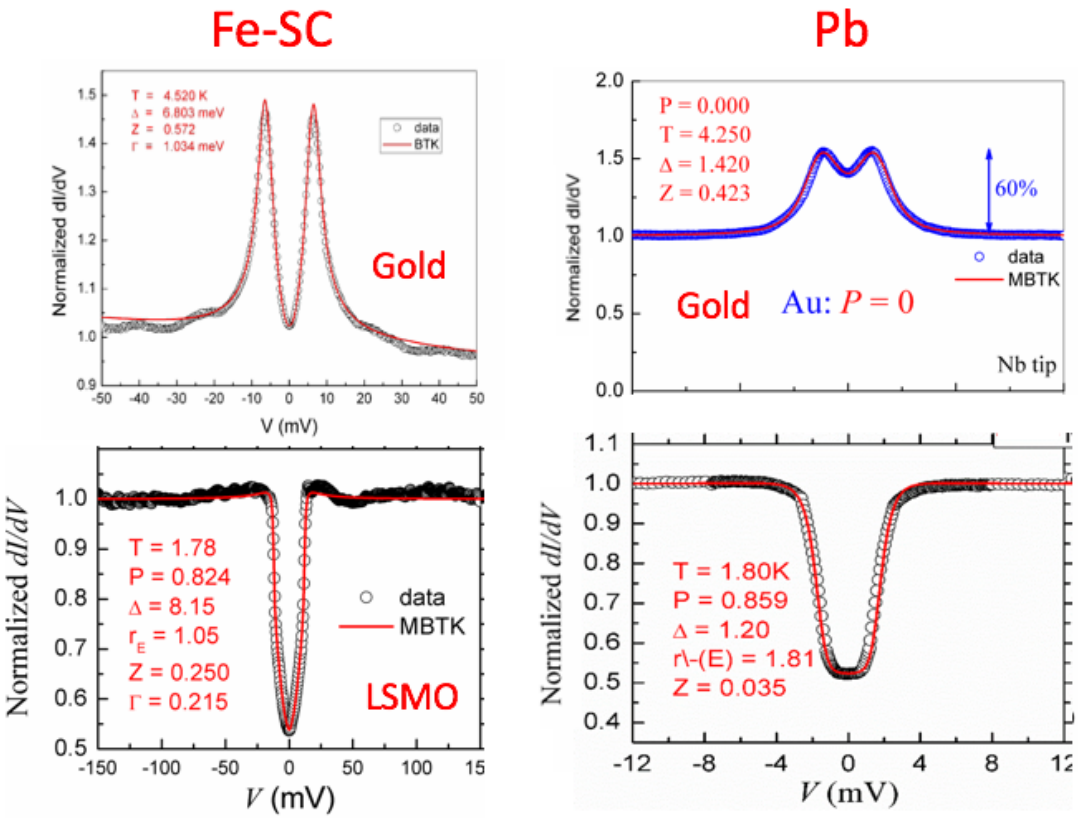

Figure 9.12: Normalized dI/dV for Au and LSMO using both a singlet superconductor Pb and unconventional superconductor Fe-SC. Because both behave the same the Fe-SC cannot be a triplet superconductor but rather a singlet.

LSMO with $P = 0.8$, and small polarized Au $p = 0$, both differential conductances decrease at zero bias. One can conclude that the Fe-SC is not a triplet superconductor, but rather, because it behaves similarly to the known singlet Pb-SC, it must also be a singlet superconductor.

9.8 Acknowledgments

This work was supported as part of SHINES, an EFRC center funded by the U. S. Department of Energy, Office of Science, Basic Energy Science, under award SC0012670.

Chapter 10

ZERO BIAS ANOMALY IN POINT-CONTACT ANDREEV REFLECTON SPECTROSCOPY

Zero bias anomaly (ZBA) in point contact Andreev reflection (PCAR) has been utilized as a characteristic feature to reveal many novel physics including superconductivity with nodes, topological superconductivity, Majorana states, and two band superconductivity. However, complexities at a superconductor/normal metal interface often cause nonessential ZBA-like features, which may be readily mistaken as ZBA. In this chapter, it is shown that an intrinsic ZBA in a d-wave superconductor, which is due to the Andreev reflection, can be suppressed by a spin-polarized current while a nonessential ZBA cannot be affected by a spin-polarized or half-metallic current and can be induced in conventional superconductors, therefore it is extrinsic to the superconductor. By systematically varying the contact resistance, one finds that the non-essential ZBA depends on the contact resistance and evolves from properties of a specific interface while the intrinsic ZBA is independent of point contacts. This work demonstrates that it is crucial to administer PCAR correctly in the proper region to obtain the intrinsic properties of the materials in question to reveal new physics.

10.1 Motivation

D-wave superconductivity has been a highly studied field since its discovery in the 1980s by Bednorz and Muller [196]. Since this discovery the transition temperature (T_c) has risen to 134 K [197] and many more experimental and theoretical studies of the properties of these materials have been conducted [60, 198–200]. For these d-wave

superconductors, many exhibit the zero bias anomaly (ZBA) which is the appearance of a large increase in the differential conductance when in contact with a metal at zero bias. For different materials this ZBA peak behaves differently. The three most interesting materials that exhibit different ZBA dependence are quasicrystals, topological superconductors, and Majorana fermions.

The Nobel Prize in 2011 was awarded to the discovery of quasicrystals, which have atoms that are ordered over long distances by non-periodic arrangement [201]. In 1982, Schechtman found a five fold forbidden symmetry in rapidly cooled alloy of aluminum and manganese. Shortly after, Levine and Steinhardt theorized that it is indeed possible to have five fold symmetry as long as the structure was quasi-periodic [202]. Since these two papers, quasicrystals have been studied extensively. Figure 10.1 shows the Andreev reflection of one such quasicrystal, AlNiCo. It shows ZBA at zero bias and is similar for crystals with a counterelectrode 25 mK and 500 mK made of an Al film[203]. As the temperature increases this peak vanishes. Extra dips can be seen as the temperature decreases, which can identify a material as a quasicrystal.

Another interesting material is the topological superconductor. The topological superconductor (TSC) is a topological state of matter that is characterized by a structure of the quantum-mechanical wave function in the Hilbert space [204–207]. $Cu_xBi_2Se_3$ is of particular interest because of its band structure and strong spin-orbit coupling [208]. The ZBA in these structures was measured in figure 10.2 for (a) a large range of energies, (b) a narrower range, and (c) at 0.35 K measured in a perpendicular magnetic field from 0-0.8 T [209]. For topological superconductors the ZBA is suppressed by the energy and the temperature. These two characteristics distinguish them from other materials.

Lastly, Majorana fermions also possess interesting ZBA effects. Majorana fermions are particles that are identical to their own antiparticles and are believed to exist in

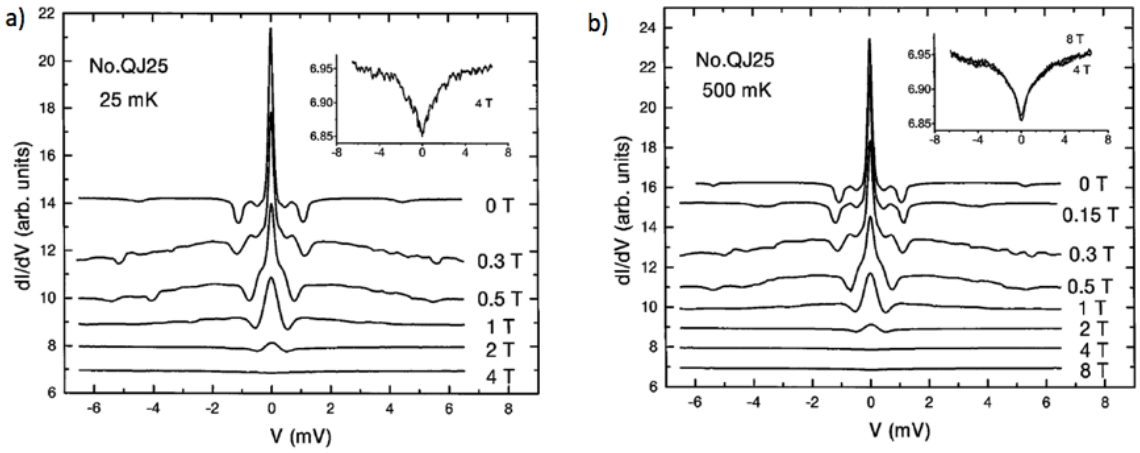

Figure 10.1: Tunneling spectra of diagonal AlNiCo single quasicrystal, QJ25, with an Al film as a counterelectrode at (a) 25 mk and (b) 500 mk. Fine structures can be seen in low magnetic fields and they disappear above 4 T. [203]

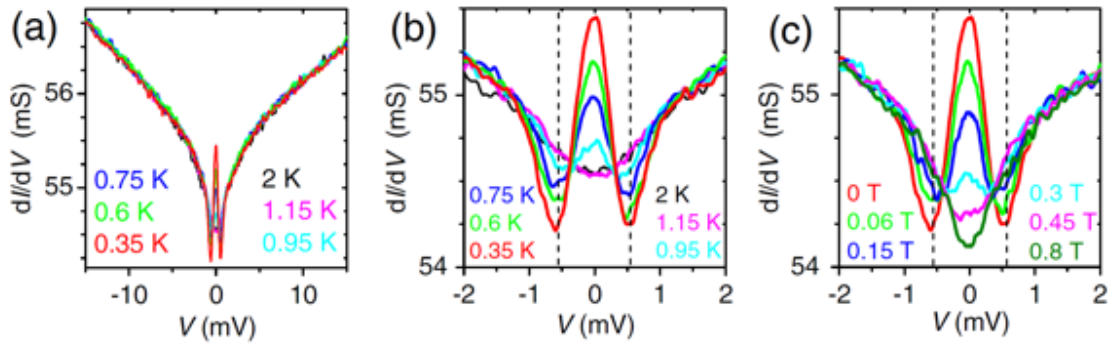

Figure 10.2: Zero-bias conductance peak. (a) PCAR of $Cu_xBi_2Se_3$ with $x = 0.3$ for 0.35-2 K measured in 0 T for a wide energy window. (b) A narrower window of (a). (c) The spectra at 0.35 K measured in perpendicular magnetic field of 0-0.8 T. The vertical dashed lines in (b) and (c) indicate the energy position of the dips [209].

topological superconductors. The can appear naturally as elementary particles or as charge-neutral and zero-energy quasi-particles [210, 211]. ZBA is used to characterize these materials through tunneling spectroscopy [212–214]. ZBA peaks are shown to rigidly stick to zero energy over large magnetic field ranges. This ZBA vanishes at zero magnetic field, for a magnetic field parallel to the spin-orbit field, or if superconductivity is removed [215]. By changing the gate voltage, and analyzing the temperature dependence of ZBA shown in figure 10.3 for InSb nanowires [216], the data suggests that without the Majorana fermions ZBA could not occur in these structures. They further show that ZBA can disappear and reappear by systematically changing the PCAR parameters [215].

The ZBA occurs for many of these materials, as well as conventional superconductors but not much is know about the mechanisms behind it. To better understand the mechanisms, more materials with this effect need to be measured. Measurements of conventional and d-wave superconductor and their ZBA appearance may be the gateway into understanding this effect. There are two different types of ZBA: extrinsic and intrinsic defined below. Often measurements may seem to indicate intrinsic ZBA however it is essential to systematically varying the contact resistance, to ensure that the PCAR is administered correctly in the proper region to obtain the intrinsic properties of the materials in question and to reveal new physics. This chapter will focus on proper point contact Andreev reflection (PCAR) analysis of conventional materials and will show that intrinsic ZBA results only correctly define the ZBA when the ZBA is independent of point contact.

10.2 Introduction

There are several claims to explain the mechanism behind the zero bias anomaly (ZBA), which occurs in superconductivity by the appearance of an anomalous peak

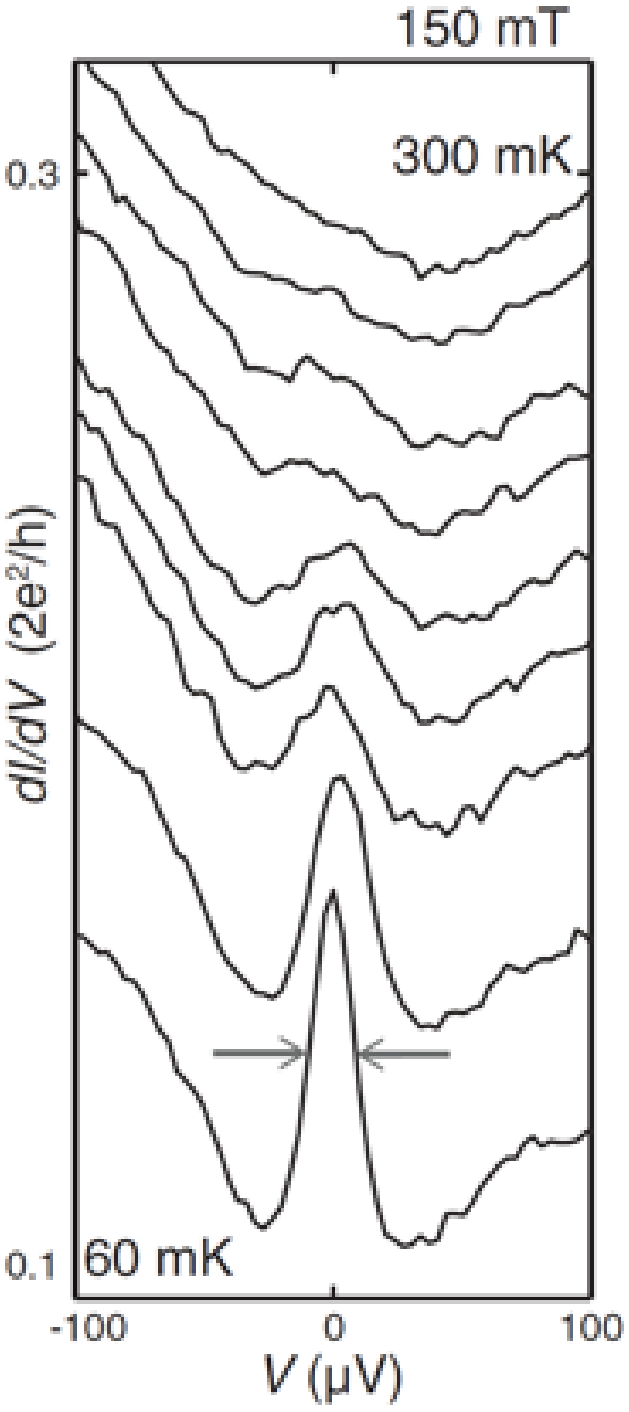

Figure 10.3: Temperature dependence of InSb nanowires, dI/dV verse V at 150 mT. Traces have an offset for clarity and are taken at different temperatures from 60 to 300 mK. A FWHM of 20 μeV is measured between the arrows [215].

in the conductivity at zero bias. The proposals to explain this effect include the presence of quasi-particle tunneling, the proximity effect, or localized magnetic states in junctions [217, 218]. Overall ,the dependence of the current I on an applied bias V is understood and at low voltages V. At high voltages, I depends on V exponentially [219]. In 1960, ZBA was first observed by Hall, who observed, in a III-V semiconductor diode at 4.2 K, a narrow dip in the conductance at zero bias [220]. In the same year Fisher and Giaver investigated the tunneling through two electrodes and also measured the same effects [221]. Shortly after, ZBA was observed in p-n junctions, tunneling through oxide layers, and dilute magnetic alloys [219, 222–231]. Shen and Rowell were the first to identify the giant zero bias resistance peak in Cr-I-Ag junctions, and have proposed that ZBA is due to tunneling electrons by a localized magnetic moment in the barrier [219, 232–235].

For unconventional SCs such as a d-wave SC, there are nodes in the gap [**?**]. At a certain direction, the interference of the AR from positive and negative gap directions causes a zero-bias anomaly (ZBA) in conductance [**?**]. However, many other effects can also cause ZBAs at the interface with a SC. For example, it has been predicted that a topological insulator can induce Majorana fermions when it contacts with a SC, which can induce resonant AR and result in a ZBA [212]. Recently, ZBA has also been utilized as a signature for Majorana fermions in superconductor-semiconductor nanowires [215], signature of topological superconductors [209], and decagonal quasicrystals [203]. Therefore, many phenomena, including some of the most recent exciting phenomena, have been utilizing ZBAs as signatures to characterize the essential physics of these materials. [203, 209, 212, 215**?** **?**]. Furthermore, for an interface associated with a SC, many other parasitic effects such as Oersted field, multiple contacts, diffusive transport and interfacial scattering can occur. These effects can cause complexities and difficulties in finding the intrinsic properties, including ZBAs,

to the materials in question.

This chapter will utilize ARS to observe the ZBA effect on both extrinsic conventional superconductors Nb and Pb, as well as the intrinsic superconductor YBCO [236]. As previously stated, one way to measure this ZBA effect is to use Andreev Reflection Spectroscopy (ARS) [93] shown in figure 10.4. At the Normal metal/Superconductor (N/S) interface, an electron must be accompanied by another electron with opposite spin to form a Cooper pair to be present in the superconductor. A hole must then be reflected back to the normal metal, which is called Andreev Reflection. The conductance of the interface for electron energies inside Δ is twice that of electrons outside Δ. If the current is fully polarized, the conductance is zero within Δ because of the lack of opposite spin electrons needed to form the Cooper pair. Thus, the P of the normal metal and the Δ of the superconductor can be measured by the conductance spectra. In an real experiment, the interface is often not ideal and an analysis of the entire conductance spectrum is necessary to extract Δ and P. The spin polarization of many magnetic materials [15–27] including some half metals [22, 23] has been measured by ARS. Also, the gap of many superconductors, including the recently discovered Fe-superconductors [28, 29], has been determined by ARS.

Figure 10.5(a) is another representative ARS but for d-wave superconductors. These are the wave vectors for AR where the incident electron either normally reflects back into the normal metal, or goes into the superconductor creating a electron-like and hole-like quasi-particle and a hole is reflected back. For the PCAR measurements, figure 10.5(b) shows the point angle, which is amused to be 2θ [92]. The point angle then depends on the contact resistance and is defined by the point angle β.

ARS has been measured for Andreev bound states (ABS) of d-wave superconductors in figure 10.6. Figures 10.6 (a) and (b) show the differential conductance verses

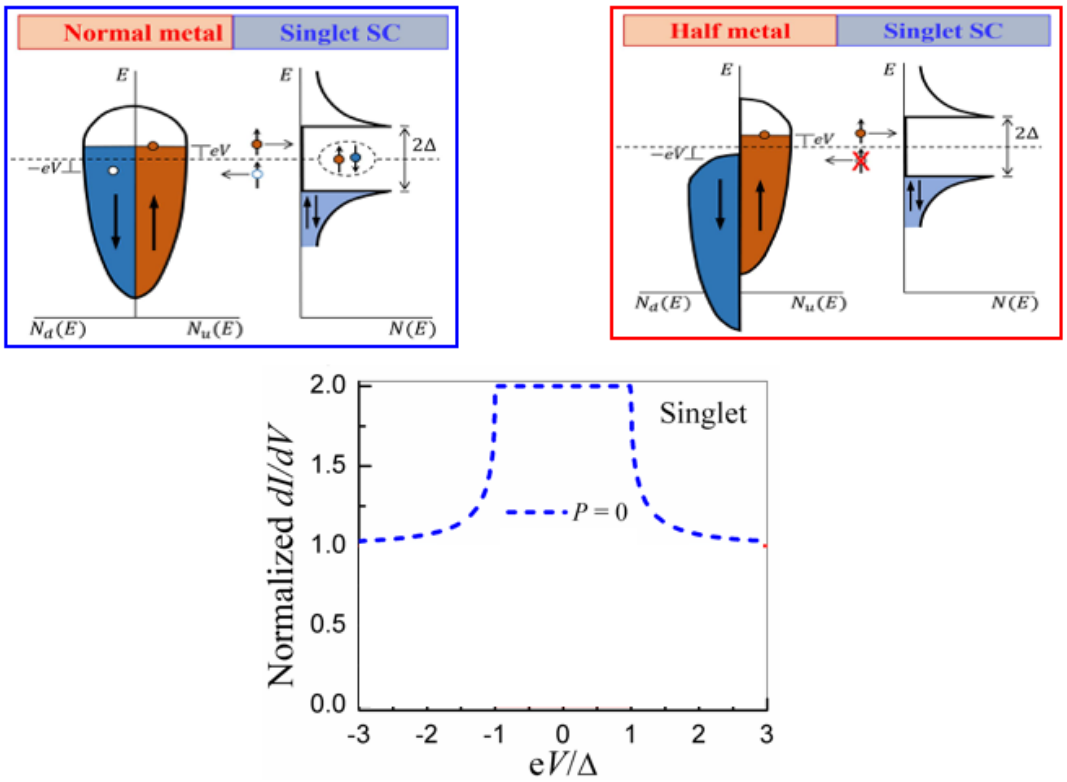

Figure 10.4: At a normal metal (N) and superconductor (S) interface, an electron (red) tunnels through the potential barrier. To conserve angular momentum, since a Cooper pair must form inside the gap making the conductance inside the gap twice that outside the gap (blue) and a polarization of $P = 0$. A hole is reflected back along the same path as the incident electron. For a half metal only one spin band is available at the Fermi energy therefore a Cooper pair cannot be formed inside the gap (red). This gives $P = 1$.

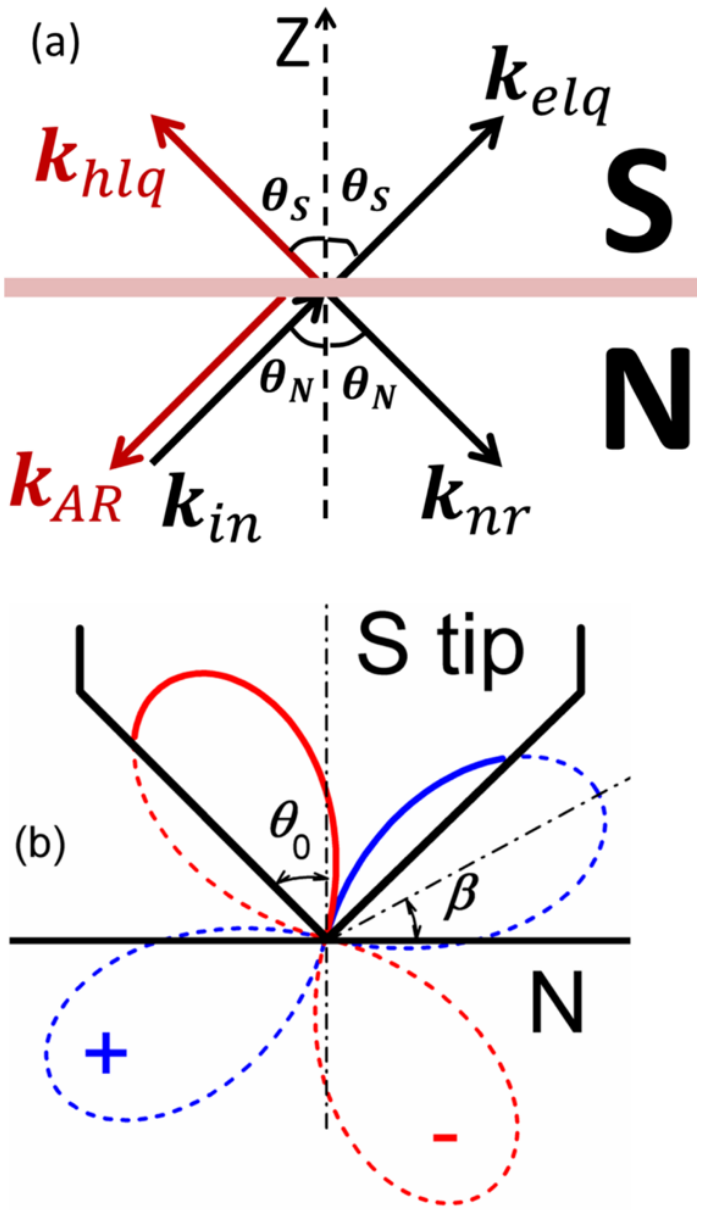

Figure 10.5: (a) ARS representation using wave vectors. k_{in} is the incident electron which will either be normally reflected, k_{nr}, or go into the superconductor and create a electron-like quasi-particle, k_{elq}, and a hole-like quasi-particle, k_{hlq}. A hole must be reflected back into the normal metal which is called AR, k_{AR}. (d) For PCAR measurements the point angle is assumed to be 2θ. The point contact then depends on the contact resistance and is defined by the point angle β [92].

energy and point contact angle β for two different point angles $2\theta = \pi/3$ and π for the interfacial scattering factor $Z = 0.25$. The ABS occurs at zero bias and it can be seen that they only occur for some β. By changing the point angle β, th larger the contact resistance the smaller contact size, which means that more ABS are available. This can also be seen for $Z = 5$ in fig 10.6 but more pronounced. For larger Z there are more ABS, which corresponds to ZBA since both occur at zero bias.

Figure 10.7 shows more ABS but now for different spin polarizations P. The ABS peak is suppressed by the spin polarization. As P increases from 0.5 to 1 the peaks disappear for both $P = 0.5$ and 1. In the cases of only a 50% polarization, it suppresses some of the peaks. When its 100% spin polarized, all the peaks are suppressed. The small peaks at $\beta = \pi/4$ and $3\pi/4$ are not ABS peaks but are instead due to the zero gaps at each of these βs. For $Z = 5$ and $P = 1$ all of the ABS peaks are suppressed.

Even though it is still controversial as to what drives it, ZBA itself is a great tool to find extrinsic and intrinsic properties of materials. In this work, one shows that an intrinsic ZBA, which is due to the Andreev reflection being changed, can be suppressed by a spin-polarized current, which demonstrates two cases. The first is intrinsic ZBA, which is independent of the point contact. The second is nonessential, or extrinsic, ZBA, which cannot be affected by a spin-polarized or half-metallic current and can be induced in conventional superconductors, which is crucially dependent on the point contact. Extrinsic ZBA also depends on the critical field applied to the superconductor. As the critical field increases, the ZBA vanishes at magnetic fields higher then the critical field H_c. This is one way to distinguish between the two types of ZBA. By systematically varying the contact resistance, one finds that it is essential to administer PCAR correctly in the proper region to obtain the intrinsic properties of the materials in question to reveal new physics.

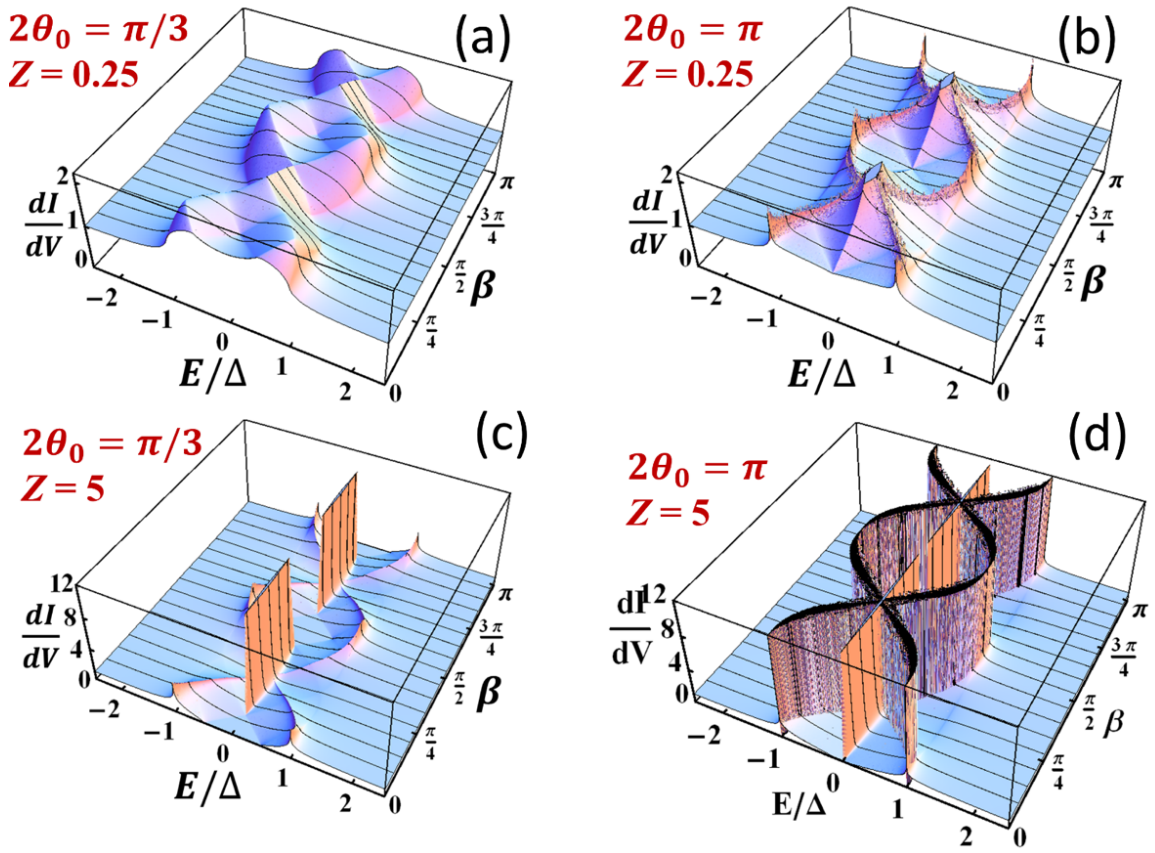

Figure 10.6: ABS for d-wave superconductors (a) point angle $2\theta = \pi/3$ with $Z = 0.25$, (b) point angle $2\theta = \pi$ with $Z = 0.255$, (c) point angle $2\theta = \pi/3$ with $Z = 5$, (d) point angle $2\theta = \pi$ with $Z = 5$. For different angles and Z more ABS can be created.

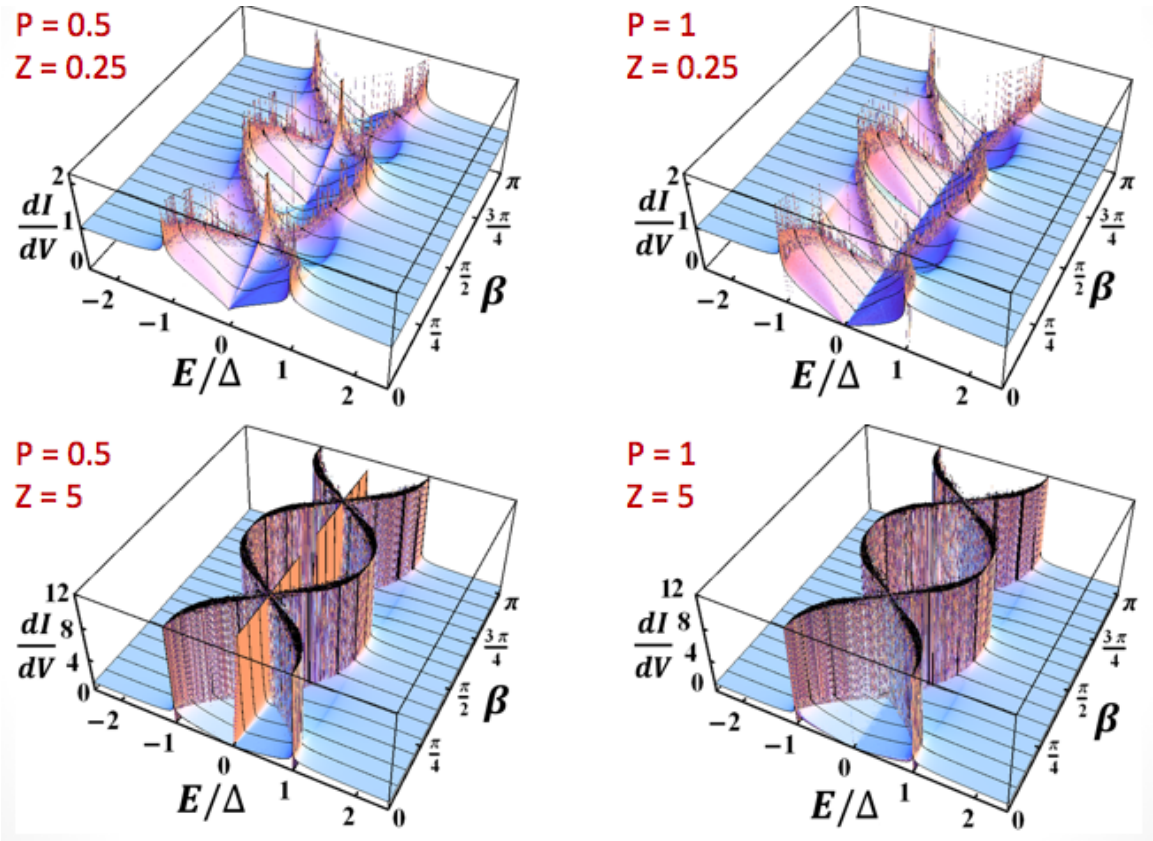

Figure 10.7: ABS peaks for different P. For both $Z = 0.25$ and 5 ABS is suppressed but is more suppressed for higher spin polarizations.

10.3 ZBA of Conventional Superconductors Nb and Pb

Some examples of ZBAs are shown in figure 10.8. It shows large ZBA in the Nb superconductor in contact with (a) a normal metal Cu at 100 nm. The ZBA is 6.5, which is much larger than the Andreev limit of 2. ZBA was observed in Pb (b) in contact with bulk Bi from 4.2 K to 8.0 K. If Pb is in contact with Bi as in (c) one can observe the temperature dependence and see that the peak is again much higher then the Andreev limit of 2. As the temperature increases the ZBA is suppressed. Right above the critical temperature (T_c) the ZBA disappears which indicates its due to the superconductivity of Pb. For Pb in contact with CoS_2 (d) a high spin polarization of 60% is observed, and by applying an external field, ZBA can be killed slightly above H_c of Pb. However, the filed dependence does not exactly follow the critical field of Pb, which is about 800 Oe [**?**]. The ZBA has a big drop at 600 Oe but it remains up to 5 kOe, as shown in figure 10.8(d). If the origin of the ZBAs is due to Andreev reflection, which is suppressed by a spin polarized current and completely suppressed by a half metallic current, then the ZBA in Nb or Pb should be reduced by a highly spin-polarized current. However, the ZBA in Pb/CoS_2 is about 4, twice of that of the Andreev limit even for a highly spin-polarized current of 60% from CoS_2 [21, 26]. Using a half metal $La_{2/3}Sr_{1/3}MnO_4$, (LSMO), the ZBA from Pb cannot be suppressed at all, as shown in figure 10.8(c). This indicates that the ZBAs have nothing to do with the AR.

10.4 Evolution of ZBA in Nb on normal metal

To further understand the origin of these ZBAs observed in conventional SCs, one studies the evolution of the ZBAs depending on a series of contact resistance (R_C) for contacts with both the normal current and the half metallic current, as shown in

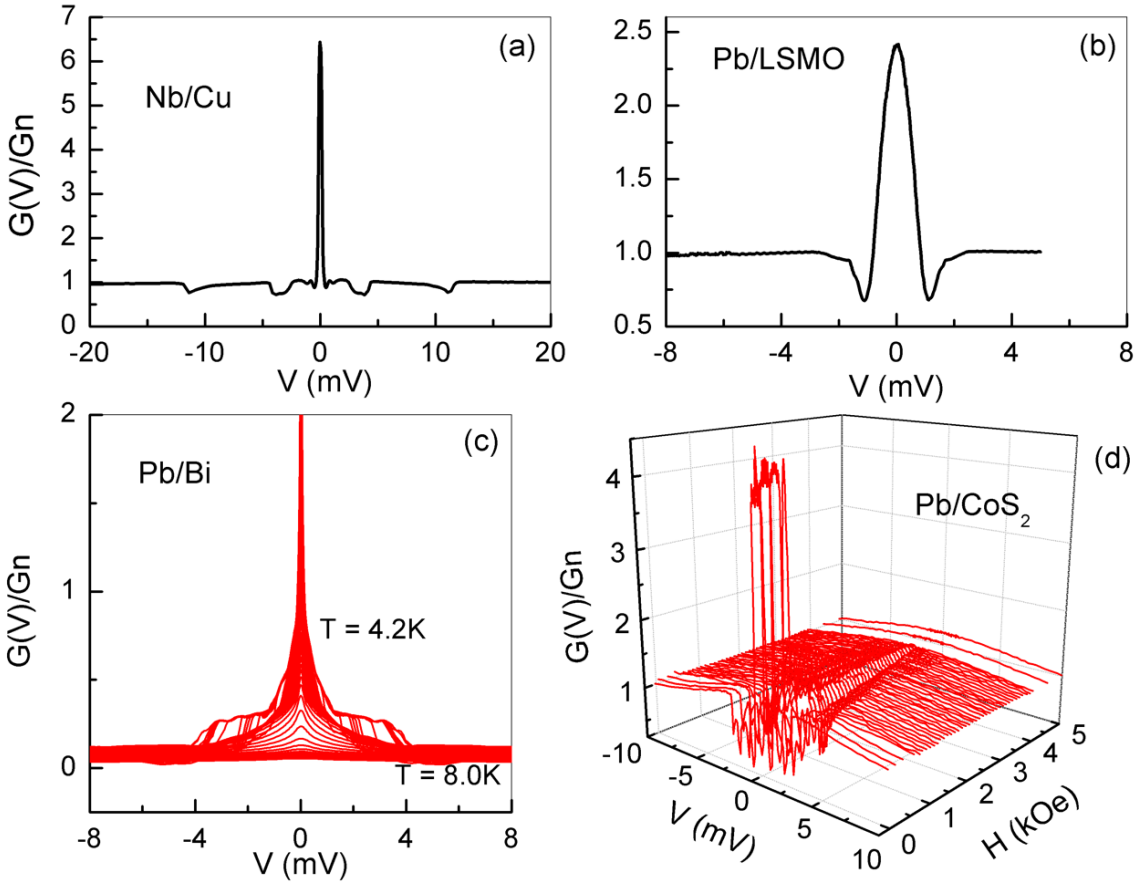

Figure 10.8: Various ZBAs in (a) Nb superconductor in contact with Cu with a large ZBA dependence, (b) Pb superconductor in contact with LSMO with a large ZBA, (c) Pb superconductor Pb in contact with Bi which shows suppression of ZBA at temperatures slightly higher then T_c, and (d) Pb superconductor on Pb superconductor in contact with CoS_2 at $P = 0.60$ with a large ZBA that can be suppressed by magnetic fields higher then H_c.

figure 10.9. The series of ARS spectra with various R_C are obtained by gradually pushing the point contact from small contact size with large R_C to large contact size with small R_C. As shown in figure 10.9(a) for a series of Nb/Cu contacts, the occurrence of ZBA depend crucially on R_C. For large $R_C = 10.7$, the ARS spectrum can be well described by the modified BTK model and the correct $P = 0$ for Cu and $\Delta = 1.34$ meV for Pb are extracted, as shown in figure 10.9(b), with the exception of the two dips outside the gap. For increasing contact size or decreasing R_C, the two dips move into the gap, causing complex multiple peaks inside the gap ($R_C = 2$), where eventually a sharp ZBA appears for $R_C = 1.2$. For a half metallic current, the suppression of AR is indeed observed for small contacts with large $R_C = 141$, as shown in figure 10.9(c). The data can be well-described by the MBTK model and the obtained $P = 79\%$ for LSMO and $\Delta = 1.32$ meV for Pb are consistent with previous reports [20]. For large contacts, two dips appear outside the gap and they move into the gap for increasing contact size or decreasing R_C. Eventually, a sharp ZBA forms, as shown in figure 10.9(d).

Next the ARS of Nb and Cu are decomposed to observe the possible similarities. This ZBA is not from Nb or Cu alone. When Nb is in contact with Au the additional dips outside the gap show similar dependence as figure 10.9. Figure 10.10 shows this similarity. For Cu on MgB_2 one observes the suppression of the ZBA as a function of contact resistance as seen with Nb/Cu. When the contact resistance is small with large contact size, the ZBA gradually forms.

10.5 Evolution of ZBA in Half Metal LSMO using Pb

For a half metallic metal a very large contact with small resistance, the AR is not suppressed by the half metallic current. This is shown in figure 10.11. The differential conductance verses voltage is shown for different contact resistances which are shifted

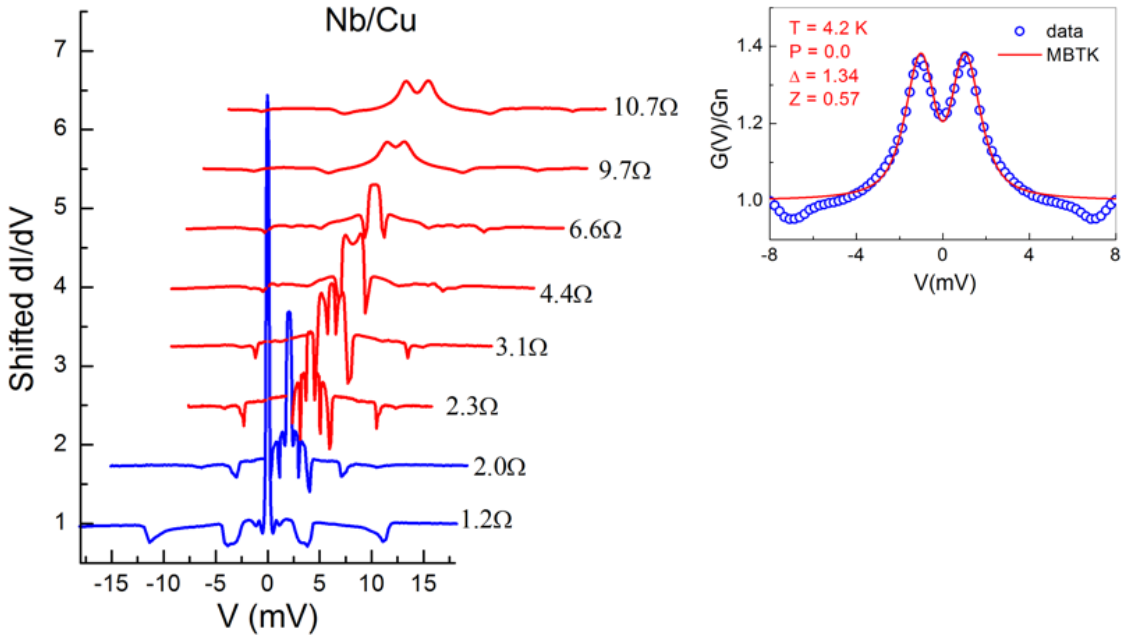

Figure 10.9: Evolution of ZBA in normal metal Cu in contact with Nb superconductor. Differential conductance is plotted verse voltage and the contact resistance is changed. The ARS is shifted up and to the right to observe the ZBA effect for each curve. Dips occur outside the gap and when the resistance is increased the dips move inside the gap inducing structures inside the gap and creating ZBA.

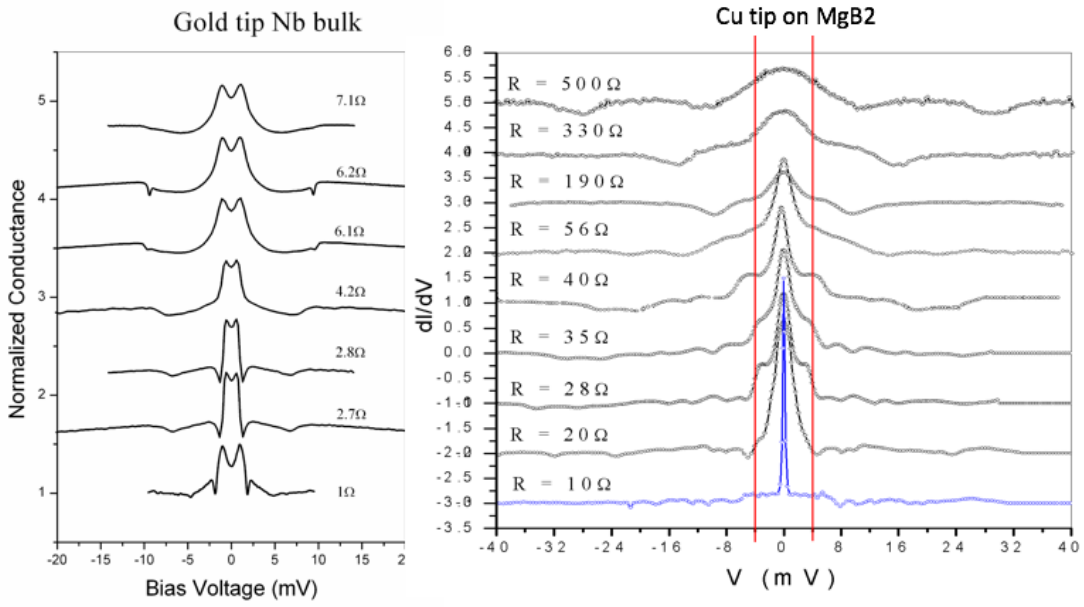

Figure 10.10: Decomposition of ARS on Nb and Cu. ZBA is not due to just Nb or Cu alone. Au on Nb and Cu on MgB_2 show similar features to Nb/Cu ARS analysis. When the contact resistance is small with large contact size the ZBA gradually forms.

up and to the right to observe the ZBA peaks. Just as for Nb/Cu, for large contact the contact resistance is small and can be well described by MBTK. Again dips outside the gaps appear and once they reach the gap ZBA occurs.

Since the ZBA cannot be suppressed by a half metallic current, it cannot be ascribed to AR which is suppressed by a highly polarized current. The evolution of the ZBA observed in both unpolarized current and fully spin-polarized current indicates that the ZBAs are related to the dips outside the gap. When the dips move into the gap, ZBA occurs. Thus these dips hold the key to understanding the ZBAs. Dips far from the gap have been studied before [**?** **?**] and have been attributed to the critical field of the contact. The BTK model where the contact resistance, R_c, is defined as,

$$\left(\frac{dI}{dV}\right)_{NN} \equiv \frac{1}{R_c} = \frac{N(0)e\nu_F\pi a^2}{2(Z^2+1)} \ , \tag{10.1}$$

where $N(0)$ is the density number of electrons, e electron charge, ν_F the Fermi velocity, a the contact size, and Z the atomic number of the material. The dip voltage, V_d can also be defined and is due to the critical field of the contact:

$$V_d = R_c I_c \ , \tag{10.2}$$

where

$$2\pi a H_c = I_c. \tag{10.3}$$

The dip voltage can then be written in terms of R_c,

$$V_d = R_c 2\pi a H_c = \frac{2(Z^2+1)}{N(0)e\nu_F\pi a^2} 2\pi a H_c = \frac{4(Z^2+1)H_c}{N(0)e\nu_F a} = k\sqrt{R_c} \ , \tag{10.4}$$

where

$$k = \sqrt{\frac{8\pi(Z^2+1)H_c}{N(0)e\nu_F}} \ . \tag{10.5}$$

From this, it is apparent that H_c is proportional to the root of R_c. Therefore when the ZBA is suppressed by the contact resistance it is due to the critical field, known

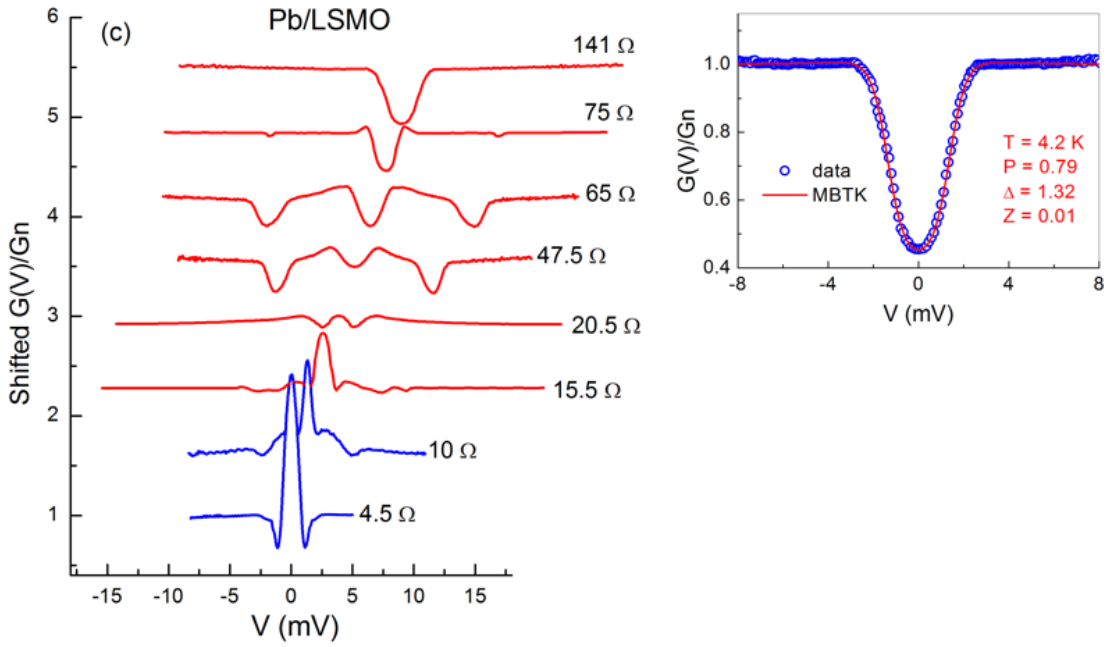

Figure 10.11: Evolution of ZBA in half metallic metal LSMO in contact with Pb superconductor. Differential conductance is plotted verse voltage and the contact resistance is changed. The ARS is shifted up and to the right to observe the ZBA effect for each curve. Dips occur outside the gap and when the resistance is increased the dips move inside the gap inducing structures inside the gap and creating ZBA.

as extrinsic ZBA. One notes that there are two dips outside the gap of Nb but there is only one dip outside the gap of Pb, this indicates that Nb is a type II SC, which has two critical fields while Pb is a type I SC. The slope k depends on the Z factor of the interface a well as the H_C and specific properties of the normal metal including $N(0)$ and ν_F.

10.6 Dip Voltage and Critical Current Dependence of ZBA

To further prove this, the voltage dip verses the contact resistance is plotted in figure 10.12 for NbFe, Nb/Cu(H_c2), Nb/Au, Nb/Cu(H_c1), and Pb/LSMO. The voltage dip follows a linear curve for each material. For Nb the slopes are almost similar which depend on the critical current. The Pb has a different slope which depends on the Z factor and critical field as well as other material properties. However, the Pb has a different slope which is most likely due to the large field of the critical field of Nb, thus Pb has a smaller slope because its critical field is less then that of Nb. This farther proves that the dips are due to the critical field of the point contact.

Looking back on the evolution of ZBA using Pb and LSMO, figure 10.11, the ZBA is due to the critical current because the contact size is too large. The results conclusively show that the voltage dips are due to the critical field of the contact interface. Since the ZBA occurs right after the dips approach the gap, it must be due to the critical field of the contact. A typical gap value of a conventional SC is about a few meV. The current density from such a voltage can be as high as 108 A/cm^2 depending on the current size [**?**]. The Oersted field inside a uniform current density is proportional to the diameter. For large contacts with small R_C, the field increases drastically for decreasing R_C. Eventually, the Oersted field kills the SC, so that the contact region becomes normal, which cause a large change of resistance which displays a ZBA much larger than 2. One notes that the effect of the magnetic

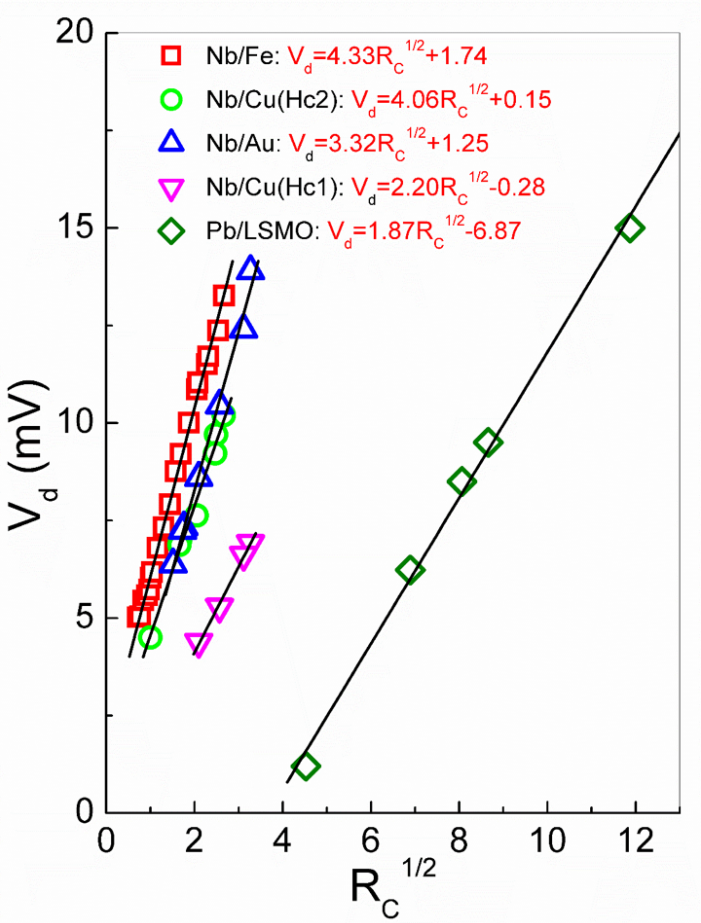

Figure 10.12: Dip voltage, V_d, verses contact resistance, R_c, for (red square) Nb/Fe, (green circle) Nb/Cu(H_c2), (blue triangle) Nb/Au, (pink upside down triangle) Nb/Cu(H_c1), and (green diamond) Pb/LSMO.

field is not exactly as that of the Meissner effect. This may be due to the fact that the Oersted field is circular and the applied external field is added to the circular field on one side but is subtracted on the other. In addition, the point contact is under pressure, which is another factor that could affect the unusual behavior of the field dependence.

10.7 Intrinsic ZBA of YBCO

In the following, it is shown that the measurement of the intrinsic ZBA in $YBa_2Cu_30_{7-x}$. The YBCO is a bulk polycrystal made by the sol-gel method and its transition temperature is about 82 K. A series of contacts of a Au tip in contact on the YBCO sample are shown in figure 10.13. A ZBA has been observed for contacts with all the contact resistances from 120 Ω to about 1300 Ω. Furthermore, the width and shape of the ZBA do not change much for all R_Cs. This demonstrates that the ZBA is independent of the contacts, thus intrinsic to the YBCO SC.

10.8 Conclusion

In summary, it is shown ZBA can be observed at an interface between a conventional superconductor and a normal or half metal. The temperature dependence indicates that it is due to superconductivity but the magnetic field does not exactly follow the Meissner effect. From the evolution of ZBAs, the ZBAs are determined to be due to the Oersted field of the current exceeding the critical field of the point contact, which is not intrinsic to the superconductor. The intrinsic ZBA from YBCO is independent of the point contact. This work demonstrates that it is important to administer the PCAR properly to find the intrinsic properties to reveal new physics.

10.9 Acknowledgments

This work was supported as part of SHINES, an EFRC center funded by the U. S. Department of Energy, Office of Science, Basic Energy Science, under award SC0012670.

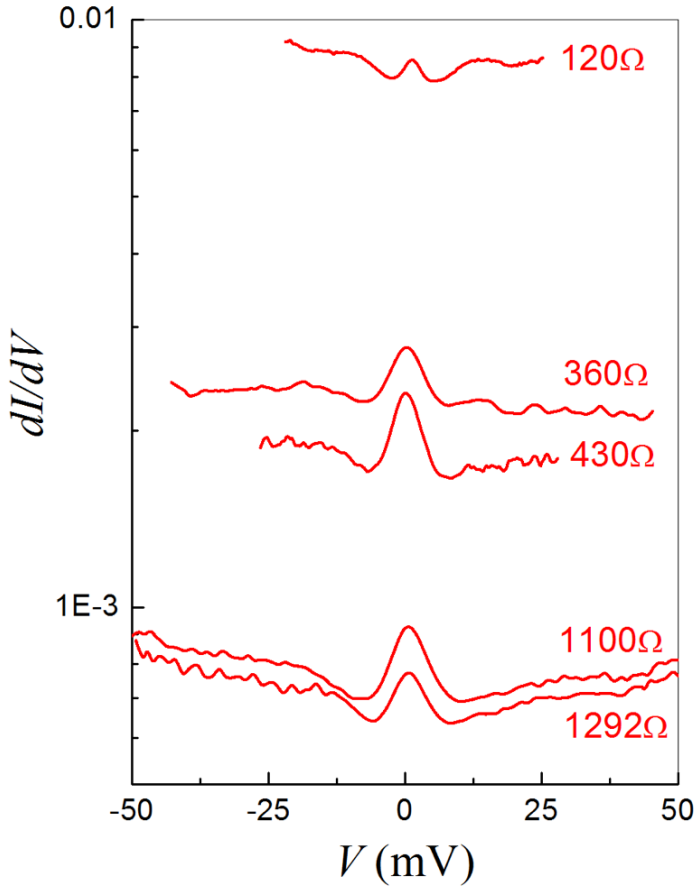

Figure 10.13: d

Differential conductance verses voltage for YBCO using Au tip as a function of the contact resistance R_c. Because the ZBA is independent of the contact resistance this indicates that this is intrinsic ZBA.

Chapter 11

STUDY OF GMR EFFECT AND ARS MEASURMENTS ON MULTILAYER OF CU/CO

It has been stated that GMR structures have the ability for tunability of the material's spin polarization by changing the applied magnetic field. Using the wedge deposition method it is shown that the sample Si/Fe 135 $\mathring{A}$ /[Co 15 $\mathring{A}$ /Cu (0 - 20) $\mathring{A}$]x 40/ Co 15 $\mathring{A}$ has the highest GMR% of 63% at room temperature with a Cu thickness of 10$\mathring{A}$. At 4.5 K, the GMR% is 115%. It is also shown that this GMR response is dependent on the materials used and not the applied current or voltage. Then the Andreev Reflection response of this film is measured and fit the data using the MBTK method. It is shown that the spin polarization can indeed be tuned by applying different magnetic fields. It is also shown that, for the case of this Cu/Co GMR structure, the spin polarization can be tuned from 0.386 to 0.415 from $H = 0$ kOe to $H = 15$ kOe.

11.1 Motivation

Beside MRAM, which is described in detail in section 3.7, giant magnetoresistance (GMR) is used in many more applications. One of the first technologies introduced was the use of GMR sensors consisting of nanometer thick layers [237]of ferromagnetic non-magnetic materials. Most magnetic sensors only yield a few percent increase in resistance when a magnetic field is applied, but GMR sensors have a typical 10-20% increase in resistance. The sensor also have high spatial resolution as well as a frequency range of 100 MHz [238]. One application used in differential current measurements is a GMR sensor placed between two Helmholtz coils, where two currents

in each coil are compared [239]. When both currents are identical the magnetic field in the middle of the coils is zero as well as the voltage of the sensors. The system was used in a house hold application and showed that it can be used for detecting differential currents below 30 mA.

Another proposed application are the GMR compass devices. They have expanded the market for electronic compasses due to their high sensitivity and large dynamic ranges [240]. There are significant issues including noise, hysteresis and sensitivities problems. To address these issues, magnetic pole pieces are used to enhance the directionality of the device [241]. Hill compared GMR sensors to spin-vale sensors and discovered that the more traditional multilayer GMR structures are better vector devices and more suitable for compass applications [242].

Not only is the GMR effect important for computing, sensing, and navigation, but it also helps with today's basic technologies such as traffic regulation. For linear and rotary position sensing, gear tooth sensing, and current sensing, GMR devices are being used [243]. The large magnetic fields are used to distinguish the fields from the background magnetic fields, such as as Earth's magnetic field and the field from every day ferromagnetic objects. For traffic lights, a biasing magnet such as the Earth's field is used to detect magnetic parts of the automobile by magnetic sensors. Small, low-powered GMR sensors allow the sensors, electronic, memory and battery to be packaged in a small protective aluminum housing the size of a person's hand [243]. An added benefit is that, unlike non GMR sensors which need a substantial current to be applied to sense the changes in conductance, the GMR sensors only need small voltages or currents to be applied, saving money in the long run.

GMR devices have also become present in biology such as magnetic resonance imaging (MRI) and electromyogram (EMG) machines. EMG machines track the movements of the eyes or limbs and the data can be correlated with other information

readings to diagnose movement disorders [244]. A small magnet can be attached to the body to be monitored. GMR magnetic sensors can then be used to track the position. A 3-D image of the motion of a limb can be done using 3 orthogonal GMR sensors which measure the vector components of the Earth's magnetic field together with 3 accelerometers [245]. Since these sensors are very small, the patient can wear these sensors while doing long term studies. MRI machines use magnetic fields to image the inside of the body, and bio-sensors, using GMR sensors with magnetic micro-beads, have been fabricated to measure molecule and chemical behaviors of different types of materials making up the micro-beads [246].

Co/Cu multilayer films have gained a lot of attention in GMR studies. Not only are the materials rather inexpensive but GMR ratios of up to 80% have been found at room temperature and 120% at 4 K [62]. Thus far no ARS measurements have been conducted on Co/Cu multilayers. Must research has been conducted on the GMR effect on these multilayers, but, with the added information of ARS measurements and spin polarization, one can investigate whether they are highly spin polarized and would be good materials for not only the read heads but also the writing of data onto the HDD. They could be used in MRAM with high spin polarizations and a large spin injection efficiency. In this chapter, the conductance of GMR and ARS measurements are studied to characterize Co/Cu multilayer thin films to see if this multilayer is a good candidate for not only GMR devices but low temperature spintronic devices.

11.2 Introduction

GMR structures consist of alternating non-magnetic and ferromagnetic conductive layers. For this chapter, Cu and Co are used. Parkin, at IBM showed, alternating layers of Cu/Co, with no insulating barriers, were able to produce GMR effects of $\sim$ 60% at room temperature and as high as $\sim$ 120% at 4 K [62]. To measure this

ratio, the difference of the resistance peak at zero field from the saturated resistance is normalized by the saturation resistance giving the GMR ratio $GMR = \frac{R_{\uparrow\downarrow} - R_{\uparrow\uparrow}}{R_{\uparrow\uparrow}}$, shown in chapter 3 figure 3.3. This chapter will investigate the GMR response at both room temperature and 4 K as well as measure the spin polarization of these structures. Previously, studies have only measured the fixed polarization of a material. GMR structures however have the advantage of controlling the spin polarization by applying different magnetic fields. This chapter demonstrates that, by using ARS with different magnetic fields, one can control the spin polarization of the Cu/Co multilayers.

Spin polarization (P) is very important for spin injection and the higher the spin polarization the better spin injection efficiency. P is defined as the normalized imbalance of the number of spin up and spin down electrons at the Fermi level normalized by the total number of electrons, $P = \frac{n(\uparrow) - n(\downarrow)}{n(\uparrow) + n(\downarrow)}$. Many spin devices, such as GMR sensors and read-heads in hard drives, can achieve big enhancements if highly spin-polarized materials are used. Half metallic materials have spin polarizations of $P = 100\%$, but only CrO_2 has been shown to be half metallic with $P = 96\%$. Therefor the hunt for other half metals has guided the spintronics field.

Andreev reflection spectroscopy (ARS) is the method used to measure P as well as the superconducting gap (Δ) of a superconductor, which describes the mechanism of superconductivity, shown in figure [**?**]. At the normal metal superconducting interface, the normalized differential conductance can give the spin polarization and superconducting gap of the materials which are often very hard to measure by other techniques. At a normal metal/superconductor interface, a current injected from the normal metal to the superconductor must be converted to a supercurrent. Therefore, within the superconducting gap at the Fermi level, to conserve superconductivity, an electron must be accompanied by another electron with opposite spin to form a Cooper pair. Consequently a hole must be reflected back into the normal metal.

This is what is known as Andreev reflection [93]. The conductance at the interface for the electrons inside the Δ must be twice that outside the Δ. For a half metal/superconductor interface, the conductance within the gap is zero because only one spin orientation is allowed at the Fermi level and thus a Cooper pair cannot be formed. This leads to $P = 100\%$. The P of the normal metal and Δ of the superconductor can be measured by the conductance spectra. For real experiments the interface is not ideal and therefore an analysis of the whole spectrum is needed to find P and Δ. Using ARS, the spin polarization of many materials have been measured as well as the superconducting gap [15–27]. Recently Fe-superconductors having T_c as high as 55 K have been measured using ARS [28, 29]. To better find P of highly spin-polarized materials, such as LSMO, higher T_c dependent materials such as these Fe-superconductors are needed [185].

Point contact Andreev Reflection (PCAR) is the method used to perform ARS. From the spectra, the P value and Δ can be determined [28] using the effects of the 3D interface [87, 88, 95–98]. More recently it has been shown that these values can be determined using the 1D effects as shown in previous work [92]. To find P the conductance ratio $G(0)/G_n = 2(1 - P)$ between zero-bias voltage ($V = 0$) within the Δ was determined using the standard Blonder-Tinkham-Klapwijk (BTK) model [81]. In real experiments the contacts used are often not ideal and therefore the inclusion of the interfacial scattering factor Z, thermal smearing due to finite temperature, and residual resistances must also be taken into account. The spin polarization is based on the recent 1D Chen-Tesanovic-Chien(CTC) model [83]. This PCAR technique has been used to determine the P values of highly spin-polarized materials and half metals [22, 23].

This chapter investigates the spin polarization and ARS dependence of Co/Cu multilayer GMR structures. At low temperatures there should be a huge enhancement

on the GMR ratio, in these experiments 4 K. It has already been shown that GMR at room temperature has a large enhancement [62] and that these structures are therefore good materials to use in read-heads. The question becomes: *Can one prove, that by applying different magnetic fields, that one can control the spin polarization of the these multilayers to create a highly spin polarized material and tune the spin polarization?*

11.3 Fabrication of Co/Cu Multilayer Films

The Co/Cu multilayers were fabricated using magnetron sputtering on single crystalline Si substrates. The substrates were cleaned using hydrofluoric acid for 25 seconds to clean any oxides and residue off the surface. During deposition, a thin film of Fe at a thickness of 135 $\mathring{A}$ was deposited to smooth out the surface for the actual GMR structure deposition. For a typical GMR structure, shown in figure 11.1, the Co and Cu are deposited at constant thicknesses. In the structures used in this chapter, the Co is deposited antiferromagnetically to enhance the GMR response. 40 bilayers of alternating Co and Cu are fabricated with a final capping layer of Co.

The relative thickness of the Co and Cu layers plays an important role in the GMR ratio. To find the best thicknesses for Fe, Co, and Cu a wedge deposition method is used such that it makes a gradient of thicknesses. By wedging the layers, one material at a time, one can save a lot of material and time by making one large sample. This sample is then cut into many pieces ($\sim$ 30 pieces) so that each smaller sample only changes by a fraction of a nano-meter in the thickness. One can then compare all thicknesses to determine the dependence of the thickness on GMR. Figure 11.2 shows the wedge method on the Cu layers. The Fe and Co were previously wedged and the thicknesses of 135 $\mathring{A}$ and 15 $\mathring{A}$, respectively, were found to give the largest GMR response. The Cu layer from was deposited from 0 to 20 $\mathring{A}$.

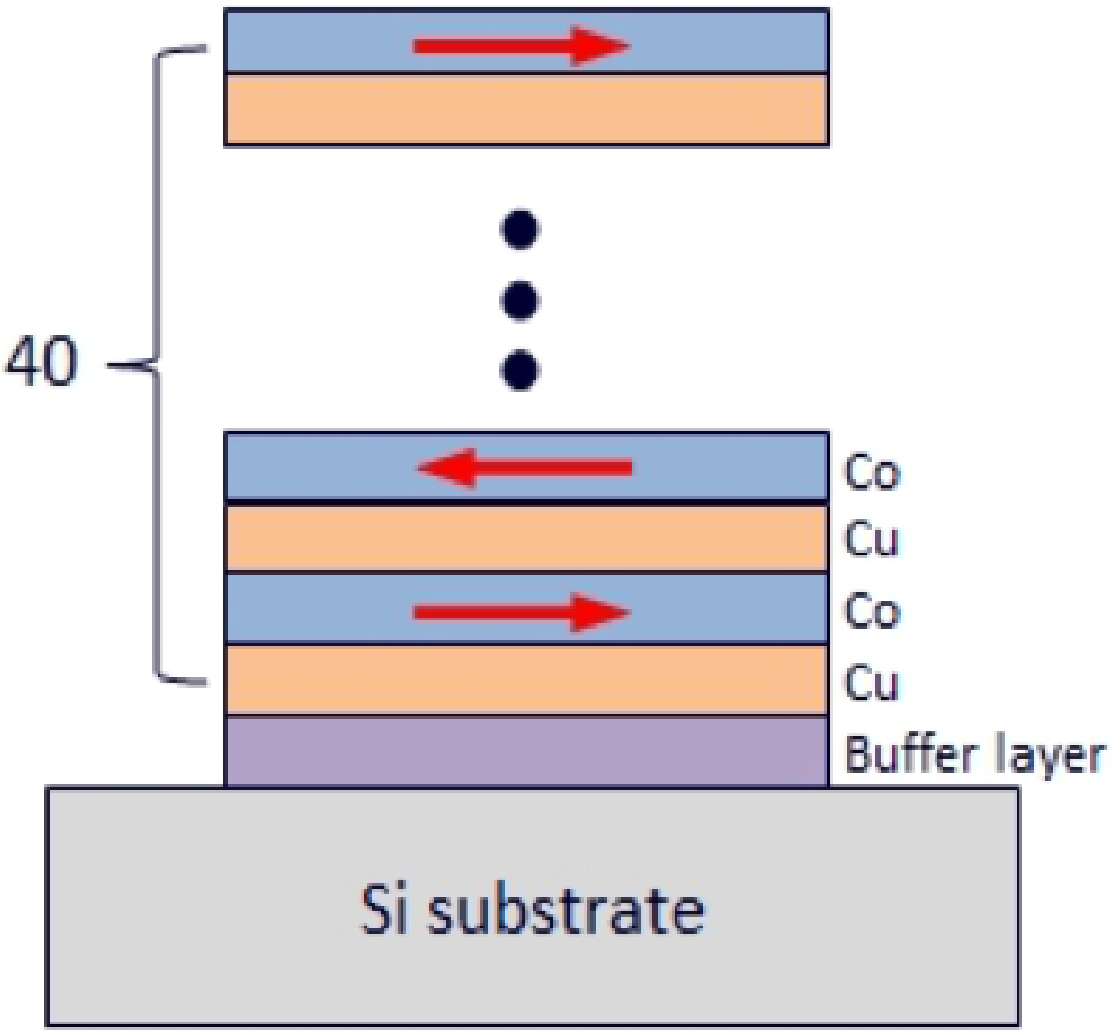

Figure 11.1: GMR structure of Co/Cu multilayer films with alternating magnetic directions of Co. A Si substrate is cleaned using hydrofluoric acid for 25 seconds and an Fe buffer layer of 135 $\mathring{A}$ is added to smooth the surface. 40 bilayers of Co and Cu are deposited with a capping layer of Co.

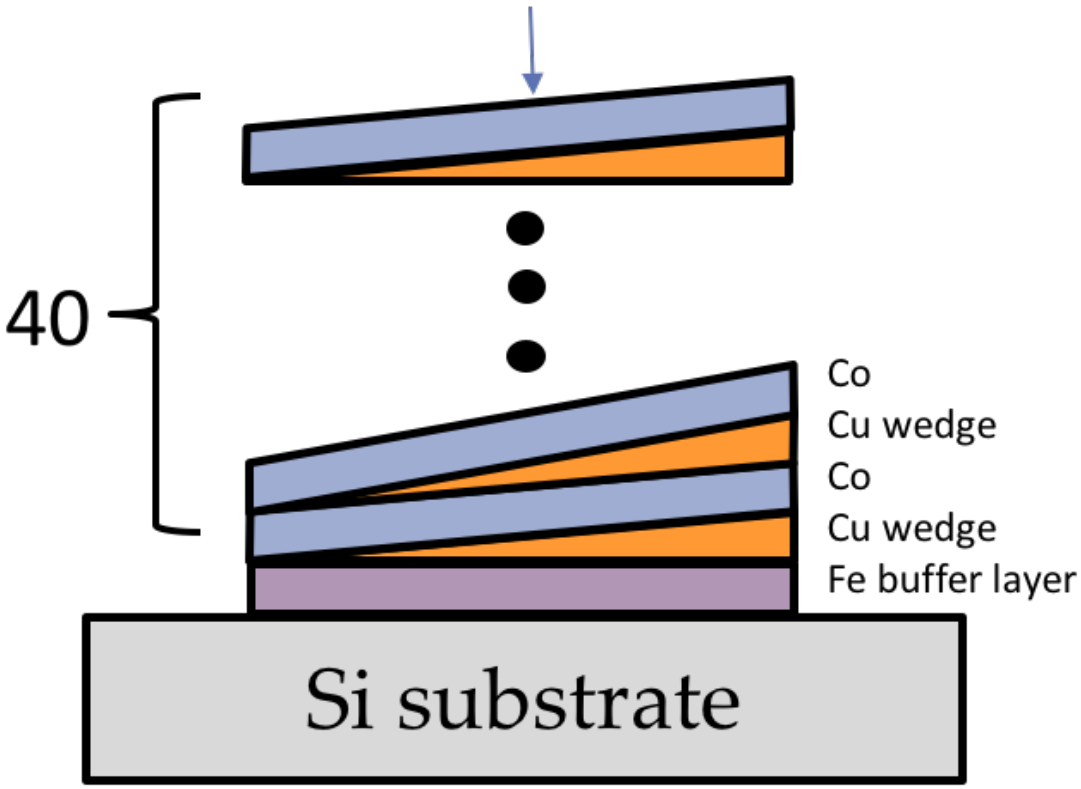

Figure 11.2: GMR structure of Co/Cu multilayer films with alternating magnetic directions of Co using the wedge method. A Si substrate is cleaned using hydrofluoric acid for 25 seconds and an Fe buffer layer of 135 $\mathring{A}$ is added to smooth the surface. 40 bilayers of Co at 15 $\mathring{A}$ and wedges of Cu of 0 to 20 $\mathring{A}$ are deposited with a capping layer of Co at 15 $\mathring{A}$.

The thickness dependence of the GMR ratio as a function of the Cu thickness is shown in figure 11.3. As the relative thickness of Cu reaches 10 $\mathring{A}$, it is observed that the highest GMR ratio is 63%. Therefore the sample used in the ARS analysis is Si/Fe 135 $\mathring{A}$ /[Co 15 $\mathring{A}$ /Cu 10 $\mathring{A}$]x 40/ Co 15 $\mathring{A}$.

11.4 ARS and GMR Analysis at Low Temperature

Using the sample Si/Fe 135 $\mathring{A}$ /[Co 15 $\mathring{A}$ /Cu 10 $\mathring{A}$]x 40/ Co 15 $\mathring{A}$ the GMR response is measured from -15 kOe to 15 kOe, shown in figure 11.4. It is found that the GMR% was 63% at 300 K and as high as 115% at 4.5 K, shown in figure 11.4(a). This large increase in the resistance at zero field confirms that this structure is indeed a good GMR material. Figure 11.4(b) shows the growth of the multilayers using tunneling electron microscopy (TEM). The image shows a smooth surface with little defects. Before measuring the AR of the multilayers it is important to understand the AR of Co and Cu alone. In figures 11.4(c) and (d), the differential conductance verses applied voltage is shown for Cu and and Co. The superconductor used was NbTi. Fitting the data using the MBTK model for Cu at 4.25 K one gets $P = 0$ and for Co 4.22 K one gets $P = 0.41$. These polarizations are consistent with other findings. Both spectra show AR for both $H = 0$ and $H = 2$ T and show that there is no change in the spectra due to this applied field.

The GMR response shown in figure 11.4 is only shown for one applied current. The inset of figure 11.5 shows the point contact used, where NbTi is the superconducting tip. The resistance of the point contact is plotted as a function of the applied field for three different applied currents in figure 11.5. These currents are 0.01 mA, 1 mA, and 1 mA with contact resistance 1.48Ω. There is a clear GMR response at zero field for each measurements. The resistance of the point contact decreases with increasing field. However, the GMR ratio of this resistance remains constant for all

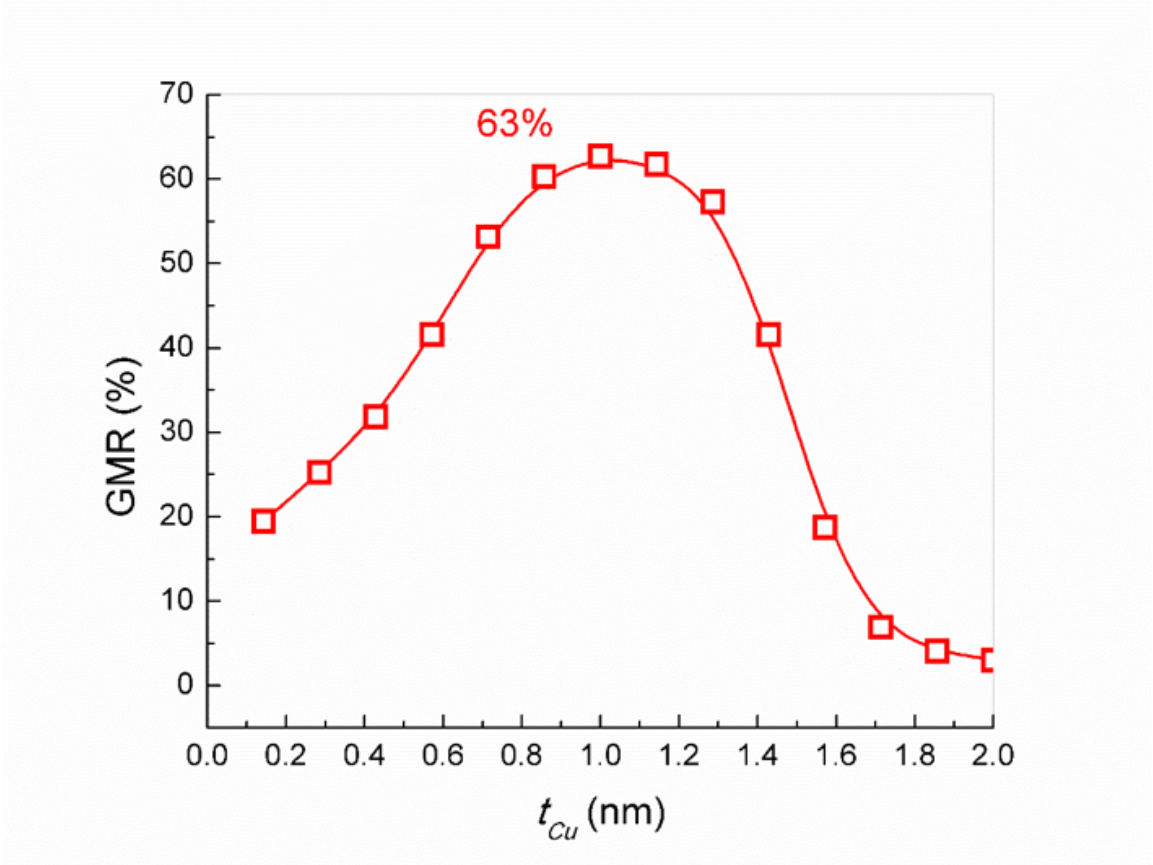

Figure 11.3: GMR% as a function of Cu thickness. At 10 $\mathring{A}$ one gets the highest GMR% of 63%. Therefore will use the sample Si/Fe 135 $\mathring{A}$ /[Co 15 $\mathring{A}$ /Cu 10 $\mathring{A}$]x 40/ Co (0-20) $\mathring{A}$ for ARS.

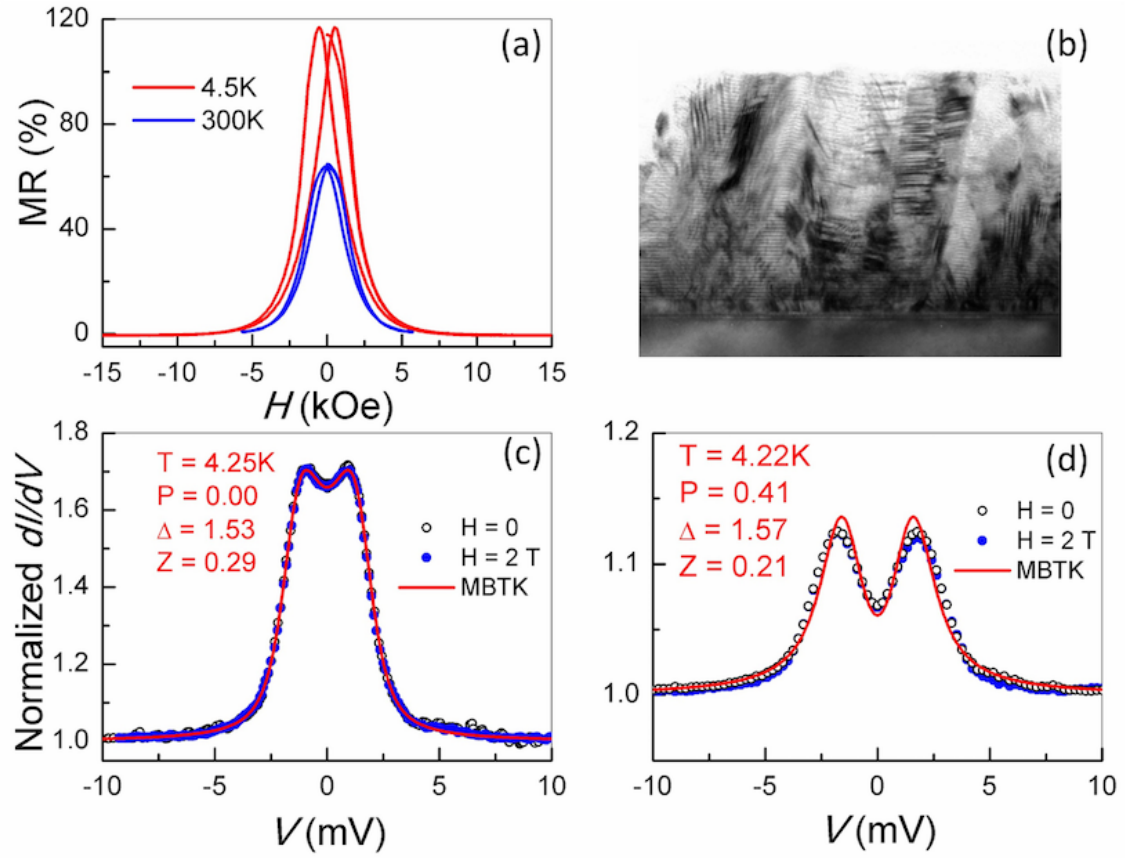

Figure 11.4: (a) MR% as a function of applied field for Co/Cu multilayer films. At 300 K a MR% of 63% is observed and 4.5 K 115% is observed. (b) TEM image of multilayer surface. (c) Differential conductance verses voltage for Cu at 4.25 K with $P = 0$. (D) Differential conductance verses voltage for Co at 4.22 K with $P = 0.41$. Both (c) and (d) are plotted for $H = 0$ and $H = 2$ T and show no dependence on the applied field.

three measurements. This shows that the GMR response is not dependent on the current applied, but rather only dependent on the applied field. This shows that the GMR enhancement is an inherent property of the material itself and that it is not dependent on experimental parameters such as the applied current.

Figure 11.6(a) shows the conductance verses voltage of the multilayers at two different applied magnetic fields $H = 15$ kOe and $H = 0$ kOe using ARS. Both measurements are done at $T = 4.2$ K using the same contact. The interfacial scattering factor Z and the superconducting gap of NbTi Δ are also used to fit the data (solid lines) using the MBTK model. Z is dependent on the contact used and, since each measurement is done using the same contact, no difference in the values is seen. When the magnetic field is increased, one sees that the AR peak decreases as well. This will change P of the material and in this case changes it from $P = 0.386$ to $P = 0.415$. Therefore, the higher the field, the larger the spin polarization. Figure 11.6(b) shows the P dependence on the magnetic field. For small fields, P is small and as the field is increase as well as the spin polarization. One sees that P becomes saturated at $P = 0.415$ at around $H = 6$ kOe. Because the spin polarization changes with applied field one can confirm that for GMR structures P is not fixed and can be tuned by using different magnetic fields. Since P only reaches 0.415, these structures are not highly spin polarized, but P can be manipulated to give larger values.

11.5 Conclusion

It is shown that the ratio of Co to Cu in GMR multilayer structures is important to fabricate the best sample with the highest GMR ratio. Using the wedge deposition method the group showed that the sample Si/Fe 135 $\mathring{A}$ /[Co 15 $\mathring{A}$ /Cu 10 $\mathring{A}$]x 40/ Co 15 $\mathring{A}$ has the highest GMR% of 63% at room temperature. The group used this sample in the ARS analysis to measure the GMR% at low temperatures of 4.5 K

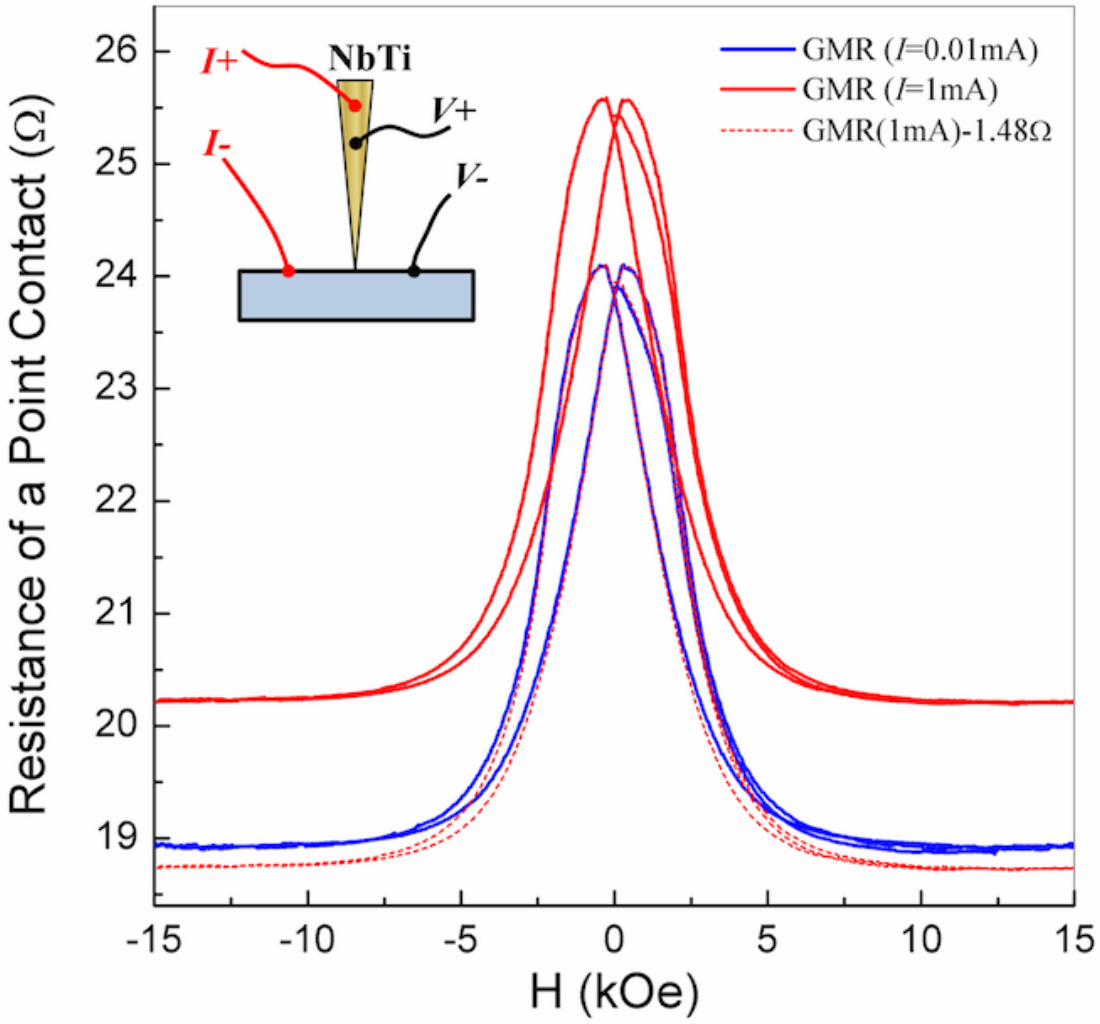

Figure 11.5: Resistance of a point contact verses applied magnetic field for Cu/Co multilayers. Blue curve is for a 0.01 mA applied current, red solid line is for a 1 mA applied current, and red dashed line is for a 1 mA with contact resistance 1.48Ω. The GMR% does not depend on applied current but is a property of the material itself. The inset shows the point contact used with a NbTi superconducting tip.

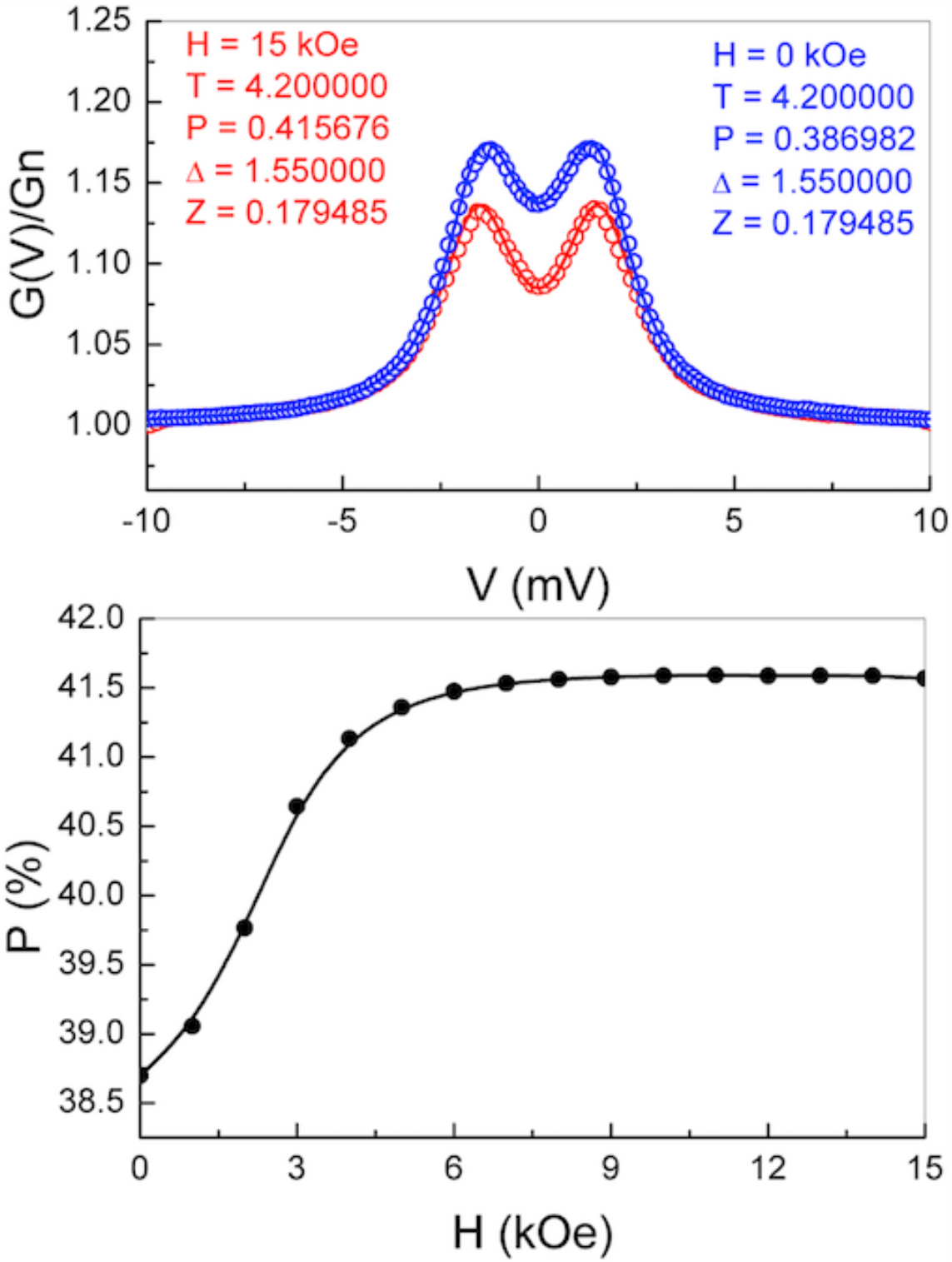

Figure 11.6: AR analysis on Cu/Co multilayer films. (a) Conductance verses voltage at (red open circles) 15 kOe and (blue open circles) 0 kOe. The solid lines are the MBTK fit to find the polarizations. (b) Spin polarization verses applied magnetic field. P can be tunable in this structure and changes with the applied field.

as well as measure the spin polarization of the structure at low temperatures. The MR% at 300 K as well as 4.5 K was measured and showed an increase of 63% and 115% respectively. At low temperatures, one can see that this material is indeed a GMR structure with a large increase in the resistance. I can be shown that this GMR response is dependent on the materials used and not the applied current or voltage. The AR response of this film and fit the data using the MBTK method is measured. It is shown that the spin polarization can indeed be tuned by applying different magnetic fields. It is shown that for the case of the Cu/Co GMR structure the polarization can be tuned from 0.386 to 0.415 from $H = 0$ kOe to $H = 15$ kOe.

11.6 Acknowledgments

This work was supported as part of SHINES, an EFRC center funded by the U. S. Department of Energy, Office of Science, Basic Energy Science, under award SC0012670.

Chapter 12

CONCLUSION

Spintronics will be the next generational leap in electronic devices. By using the spin of the electron, one can read and write data much faster then by writing it using charge alone. Spintronics allow for smaller sizes, non-volatility, and spin injection which are being implemented in everything from MRAM devices to highway traffic control. The main disadvantage, however, is that, previously, there are no easy was to determine the spin polarization and superconductive properties of such devices. It is shown that using ARS one can determine the spin polarization of a normal metal and superconducting gap of a superconductor in a consistent reproducible way.

Point-contact spectroscopy is a novel technique which can be used to get a high current density in the ballistic regime ($\sim 10^9 A/cm^2$), which makes it possible to probe for the fundamental physics related to the ballistic or high current density transport. This simple technique makes it easy to quickly study new phenomena in new samples and orientations at both room temperature and low temperature applications. In this thesis, it is shown that one can develop a new theory for 3D effects in PCAR measurements and show that one could characterize the spin polarization of amorphous alloys, Heusler alloys, and Fe-Sc on LSMO sample. Using this model, one is able to measure high spin polarizations in these materials, which brings scientists one step closer to finding a true half metallic material. In this thesis, it is also shown that one can use ARS to characterized not only highly spin polarized materials, but also determine if a superconductor is a singlet or triplet superconductor. It was also shown that an Fe-SC is not a triplet superconductor. It was also shown that one can measure the AR dependence in GMR structures of Co/Cu and measure the spin

polarization to see if they can not only read data from MRAM devices, but to see if they are highly spin polarized and could also be used as spin injectors to write the data to the disk. Below are more specific conclusions to each experiment conducted in this thesis.

Andreev Reflection Spectroscopy (ARS) is another technique of importance which measures the spin polarization of the normal metal and superconducting gap of the superconductor at a normal metal superconductor interface at $T < T_c$. ARS, in conjunction with point-contact spectroscopy, measures the differential conductance and fits this data to find spin polarization, gap, interfacial scattering factor, additional resistance, as well as inelastic scattering factor of each measurement. Using the 3-D model of ARS one is able to theoretically show that all 3D ARS measurements can be analyzed with the 1-D ARS model. It is shown that the effect due to the 3D injection can be attributed to a larger interfacial scattering factor using a 1D model. Even though the interfacial scattering factor differs, it was shown that the same intrinsic spin polarization and superconducting gap value was measured with both models. ARS experiments were conducted on Co/Nb interface and the analysis was consistent with the theory. The next step for this projects is to develop a model bases on this theory that accounts for anisotropy and the majority and minority spins.

Next a ferromganetic Heusler alloy $Co_2FeAl_{0.5}Si_{0.5}$ was investigated. ARS measurements showed that the spin polarization was as high as 80% in samples sputtered on unheated MgO(100) substrates annealed at high temperatures. The samples that were fabricated on heated substrates showed much smaller spin polarizations and therefore are inferior to the unheated ones. The magnetic properties of the samples were found to be similar, although the spin polarization varied substantially. It was found that the CFAS samples grown at room temperature followed by post annealing on unheated substrates were the highest spin polarized samples and therefore the

best material to consider for spintronic devices. The next step is to investigate other Heusler alloys to see if their results are comparable. It would also be interesting to see if other caping layers could imporve the spin polarization even more then the Pb/AlO_3 layer.

Ferromagnetic Fe_xSi_{-x} alloys have been proposed as potential spin injectors into silicon with a substantial spin polarization. ARS was used to determine the spin polarization of both amorphous and crystalline $Fe_{65}Si_{35}$ alloys. It was shown that the additional resistance in ARS is quite high because of large resistivity of these alloys and must be taken into account to correctly extract the spin polarization. The spin polarization of the crystalline $Fe_{0.65}Si_{0.35}$ is about 49%, similar to that of common magnetic metals, indicating that it is a good spin injector for semiconductor spintronics. Interestingly, the spin polarization of the amorphous $Fe_{0.65}Si_{0.35}$ alloy is substantially higher, demonstrating that a modified magnetism by the amorphous nature can also be utilized to tune the spin polarization for spintronics. The next step is to investigate why these amorphous samples yield such higher spin polarizations. To do this multiple samples of the same materials with small changes in the chemical or structural properties in the amorphous film need to be systematically measured to determine what in this amorphous form give a higher results. Another issue is that for amorphous films the interface effects can be substantially different. The electron k vector may will not behave the same as described in the 3D model and may reflect differently or cause more effects in the Z. Therefore a ARS model for amorphous materials should be developed to obtain more accurate results which may then lead to an explanation on why this amorphous material is better.

Since transition temperatures of most conventional superconductors are below 10 K, spin polarization is measured only at low temperatures by ARS. The recently discovered Fe-superconductors are shown to have a transition temperatures close to

60 K, much higher than that of the conventional superconductors. In this work, a (1111) Fe superconductor $SmO_{0.82}F_{0.18}FeAs$ and Pb were utilized to measure the spin polarization of a highly spin-polarized material, $La_{0.67}Sr_{0.33}MnO_3$. The same intrinsic P of LSMO was determined using both Pb and Fe-superconductors and had a value of 0.8. Both superconductors showed negligible T dependence on P for $T < 55$ K and all values of P at all temperatures were within 5% of each other. It is concluded, based on the PCAR measurements, that Fe-superconductors can be used to find the P of the metal and Δ of the superconductor, especially for high spin-polarized materials such as LSMO. Based on the behavior of the differential conductance for highly spin polarized LSMO and small polarization of Au, it can be concluded that the Fe-Sc is not a triplet superconductor. The next step would be to measure other Fe-SCs to see if different chemical combinations could yield a material even more highly spin polarized. Another direction to go is to use this ARS technique to look at other materials which may be triplet superconductors. This is currently being done for one sample of Bi/Ni by other members of the group.

It is shown that the ratio of Co to Cu in GMR multilayer structures Si/Fe 135 $\mathring{A}$ /[Co 15 $\mathring{A}$ /Cu (0 - 20) $\mathring{A}$]x 40/ Co 15 $\mathring{A}$ is important to fabricate the best sample with the highest GMR ratio. Using the wedge deposition method, one can show that the sample has the highest GMR% of 63% at room temperature with Cu thickness $\mathring{A}$. The MR% at 300 K as well as 4.5 K was measured and showed an increase of 115% at 4.5 K. It is also shown that this GMR response is dependent on the materials used and not the applied current or voltage. The AR response of this film was then measured and was fitted using the MBTK method. It is shown that the spin polarization can indeed be tuned by applying different magnetic fields. It is shown that for the case of this Cu/Co GMR structure the polarization can be tuned from 0.386 to 0.415 by changing the field from $H = 0$ kOe to $H = 15$ kOe. The next step for this project

would be to change the ferromagnetic layers or non magnetic layers and see if other materials will yield comparable, or better GMR responses then the one measured here. One can also vary the bilayers in the sample to see if adding more layers could increase the response as well.

REFERENCES

[1] Igor Žutić, Jaroslav Fabian, and S. Das Sarma. Spintronics: Fundamentals and applications. *Rev. Mod. Phys.*, 76:323–410, Apr 2004.

[2] M. Cahay S. Bandyopadhyay. *Introduction to Spintronics*. RC Press, Raton, Florida, 2008.

[3] Mario Norberto Baibich, Jean Marc Broto, Albert Fert, F Nguyen Van Dau, Frédéric Petroff, P Etienne, G Creuzet, A Friederich, and J Chazelas. Giant magnetoresistance of (001) fe/(001) cr magnetic superlattices. *Physical review letters*, 61(21):2472, 1988.

[4] SA Wolf, DD Awschalom, RA Buhrman, JM Daughton, S Von Molnar, ML Roukes, A Yu Chtchelkanova, and DM Treger. Spintronics: a spin-based electronics vision for the future. *Science*, 294(5546):1488–1495, 2001.

[5] Gary A Prinz. Magnetoelectronics. *Science*, 282(5394):1660–1663, 1998.

[6] VP LaBella, DW Bullock, Z Ding, C Emery, A Venkatesan, WF Oliver, GJ Salamo, PM Thibado, and M Mortazavi. Spatially resolved spin-injection probability for gallium arsenide. *Science*, 292(5521):1518–1521, 2001.

[7] Min Ouyang and David D Awschalom. Coherent spin transfer between molecularly bridged quantum dots. *Science*, 301(5636):1074–1078, 2003.

[8] Gene Siegel, Megan Campbell Prestgard, Shiang Teng, and Ashutosh Tiwari. Robust longitudinal spin-seebeck effect in bi-yig thin films. *Scientific reports*, 4, 2014.

[9] Johan Åkerman. Toward a universal memory. *Science*, 308(5721):508–510, 2005.

[10] Mark Durlam, P Naji, M DeHerrera, S Tehrani, G Kerszykowski, and K Kyler. Nonvolatile ram based on magnetic tunnel junction elements. In *Solid-State Circuits Conference, 2000. Digest of Technical Papers. ISSCC. 2000 IEEE International*, pages 130–131. IEEE, 2000.

[11] Dmytro Apalkov, Alexey Khvalkovskiy, Steven Watts, Vladimir Nikitin, Xueti Tang, Daniel Lottis, Kiseok Moon, Xiao Luo, Eugene Chen, Adrian Ong, et al. Spin-transfer torque magnetic random access memory (stt-mram). *ACM Journal on Emerging Technologies in Computing Systems (JETC)*, 9(2):13, 2013.

[12] Yiming Huai. Spin-transfer torque mram (stt-mram): Challenges and prospects. *AAPPS Bulletin*, 18(6):33–40, 2008.

[13] Igor Žutić, Jaroslav Fabian, and S Das Sarma. Spintronics: Fundamentals and applications. *Reviews of modern physics*, 76(2):323, 2004.

[14] Jacob Linder and Jason WA Robinson. Superconducting spintronics. *Nature Physics*, 11(4):307–315, 2015.

[15] Shashi K Upadhyay, Akilan Palanisami, Richard N Louie, and RA Buhrman. Probing ferromagnets with andreev reflection. *Physical review letters*, 81(15):3247, 1998.

[16] RJ Soulen, JM Byers, MS Osofsky, B Nadgorny, T Ambrose, SF Cheng, Pr R Broussard, CT Tanaka, J Nowak, JS Moodera, et al. Measuring the spin polarization of a metal with a superconducting point contact. *Science*, 282(5386):85–88, 1998.

[17] TY Chen, CL Chien, and C Petrovic. Enhanced curie temperature and spin polarization in mn4fege3. *Applied Physics Letters*, 91(14):142505–142505, 2007.

[18] SX Huang, TY Chen, and CL Chien. Spin polarization of amorphous cofeb determined by point-contact andreev reflection. *Applied Physics Letters*, 92(24):2509, 2008.

[19] B Nadgorny, II Mazin, M Osofsky, RJ Soulen Jr, P Broussard, RM Stroud, DJ Singh, VG Harris, A Arsenov, and Ya Mukovskii. Origin of high transport spin polarization in la 0.7 sr 0.3 mno 3: direct evidence for minority spin states. *Physical Review B*, 63(18):184433, 2001.

[20] Y Ji, CL Chien, Y Tomioka, and Y Tokura. Measurement of spin polarization of single crystals of la 0.7 sr 0.3 mno 3 and la 0.6 sr 0.4 mno 3. *Physical Review B*, 66(1):012410, 2002.

[21] L Wang, K Umemoto, RM Wentzcovitch, TY Chen, CL Chien, JG Checkelsky, JC Eckert, ED Dahlberg, and C Leighton. C o 1- x f e x s 2: A tunable source of highly spin-polarized electrons. *Physical review letters*, 94(5):056602, 2005.

[22] Y Ji, GJ Strijkers, FY Yang, CL Chien, JM Byers, A Anguelouch, Gang Xiao, and A Gupta. Determination of the spin polarization of half-metallic cro 2 by point contact andreev reflection. *Physical Review Letters*, 86(24):5585, 2001.

[23] JS Parker, SM Watts, PG Ivanov, and P Xiong. Spin polarization of cro 2 at and across an artificial barrier. *Physical review letters*, 88(19):196601, 2002.

[24] TW Chiang, YH Chiu, SY Huang, SF Lee, JJ Liang, H Jaffres, JM George, and A Lemaitre. Spectra broadening of point-contact andreev reflection measurement on gamnas. *Journal of Applied Physics*, 105(7), 2009.

[25] P Chalsani, SK Upadhyay, O Ozatay, and RA Buhrman. Andreev reflection measurements of spin polarization. *Physical Review B*, 75(9):094417, 2007.

[26] L Wang, TY Chen, C Leighton Chien, and C Leighton. Sulfur stoichiometry effects in highly spin polarized cos2 single crystals. *Applied physics letters*, 88(23):232509, 2006.

[27] TY Chen, SX Huang, and CL Chien. Pronounced effects of additional resistance in andreev reflection spectroscopy. *Physical Review B*, 81(21):214444, 2010.

[28] TY Chen, Z Tesanovic, RH Liu, XH Chen, and CL Chien. A bcs-like gap in the superconductor smfeaso0. 85f0. 15. *Nature*, 453(7199):1224–1227, 2008.

[29] Dario Daghero, Mauro Tortello, GA Ummarino, and RS Gonnelli. Directional point-contact andreev-reflection spectroscopy of fe-based superconductors: Fermi surface topology, gap symmetry, and electron–boson interaction. *Reports on Progress in Physics*, 74(12):124509, 2011.

[30] II Mazin, DJ Singh, and Claudia Ambrosch-Draxl. Transport, optical and electronic properties of the half metal cro2. *Journal of applied physics*, 85(8):6220–6222, 1999.

[31] Jose Maria De Teresa, Agnes Barthelemy, Albert Fert, Jean Pierre Contour, François Montaigne, and Pierre Seneor. Role of metal-oxide interface in determining the spin polarization of magnetic tunnel junctions. *Science*, 286(5439):507–509, 1999.

[32] RA De Groot, FM Mueller, PG Van Engen, and KHJ Buschow. New class of materials: half-metallic ferromagnets. *Physical Review Letters*, 50(25):2024, 1983.

[33] KEHM Hanssen and PE Mijnarends. Positron-annihilation study of the half-metallic ferromagnet nimnsb: theory. *Physical Review B*, 34(8):5009, 1986.

[34] KP Kämper, W Schmitt, G Güntherodt, RJ Gambino, and R Ruf. Cr o 2a new half-metallic ferromagnet? *Physical Review Letters*, 59(24):2788, 1987.

[35] H Van Leuken and RA De Groot. Half-metallic antiferromagnets. *Physical review letters*, 74(7):1171, 1995.

[36] Young-Woo Son, Marvin L Cohen, and Steven G Louie. Half-metallic graphene nanoribbons. *Nature*, 444(7117):347–349, 2006.

[37] MI Katsnelson, V Yu Irkhin, L Chioncel, AI Lichtenstein, and RA De Groot. Half-metallic ferromagnets: From band structure to many-body effects. *Reviews of Modern Physics*, 80(2):315, 2008.

[38] Sudipta Dutta, Arun K Manna, and Swapan K Pati. Intrinsic half-metallicity in modified graphene nanoribbons. *Physical review letters*, 102(9):096601, 2009.

[39] R Shan, H Sukegawa, WH Wang, M Kodzuka, T Furubayashi, T Ohkubo, S Mitani, K Inomata, and K Hono. Demonstration of half-metallicity in fermi-level-tuned heusler alloy co 2 feal 0.5 si 0.5 at room temperature. *Physical review letters*, 102(24):246601, 2009.

[40] Stuart Parkin. Spin-polarized current in spin valves and magnetic tunnel junctions. *MRS bulletin*, 31(05):389–394, 2006.

[41] Shinji Yuasa, Taro Nagahama, Akio Fukushima, Yoshishige Suzuki, and Koji Ando. Giant room-temperature magnetoresistance in single-crystal fe/mgo/fe magnetic tunnel junctions. *Nature materials*, 3(12):868–871, 2004.

[42] M. Tinkham. *Introduction to Superconductivity: Second Edition*. Dover Books on Physics. Dover Publications, 2004.

[43] Ivar Giaever. Energy gap in superconductors measured by electron tunneling. *Physical Review Letters*, 5(4):147, 1960.

[44] BT Matthias, TH Geballe, S Geller, and E Corenzwit. Superconductivity of nb 3 sn. *Physical Review*, 95(6):1435, 1954.

[45] AL Schawlow, GE Devlin, and JK Hulm. Intermediate state of hard superconductors. *Physical Review*, 116(3):626, 1959.

[46] Takeshi Kondo, AF Santander-Syro, O Copie, Chang Liu, ME Tillman, ED Mun, J Schmalian, SL Bud?Ko, MA Tanatar, PC Canfield, et al. Momentum dependence of the superconducting gap in ndfeaso 0.9 f 0.1 single crystals measured by angle resolved photoemission spectroscopy. *Physical review letters*, 101(14):147003, 2008.

[47] Andrea Damascelli, Zahid Hussain, and Zhi-Xun Shen. Angle-resolved photoemission studies of the cuprate superconductors. *Reviews of modern physics*, 75(2):473, 2003.

[48] JC Campuzano, MR Norman, and M Randeria. Photoemission in the high-t c superconductors. In *The Physics of Superconductors*, pages 167–273. Springer, 2004.

[49] HM Fretwell, A Kaminski, J Mesot, JC Campuzano, MR Norman, M Randeria, T Sato, R Gatt, T Takahashi, and K Kadowaki. Fermi surface of bi 2 sr 2 cacu 2 o 8. *Physical review letters*, 84(19):4449, 2000.

[50] J Mesot, M Randeria, MR Norman, A Kaminski, HM Fretwell, JC Campuzano, H Ding, T Takeuchi, T Sato, T Yokoya, et al. Determination of the fermi surface in high-t c superconductors by angle-resolved photoemission spectroscopy. *Physical Review B*, 63(22):224516, 2001.

[51] MR Norman, M Randeria, H Ding, and JC Campuzano. Phenomenology of the low-energy spectral function in high-t c superconductors. *Physical Review B*, 57(18):R11093, 1998.

[52] JC Campuzano, H Ding, MR Norman, M Randeira, AF Bellman, T Yokoya, T Takahashi, H Katayama-Yoshida, T Mochiku, and K Kadowaki. Direct observation of particle-hole mixing in the superconducting state by angle-resolved photoemission. *Physical review B*, 53(22):R14737, 1996.

[53] Fritz London and Heinz London. The electromagnetic equations of the supraconductor. In *Proceedings of the Royal Society of London A: Mathematical, Physical and Engineering Sciences*, volume 149, pages 71–88. The Royal Society, 1935.

[54] Walther Meissner and Robert Ochsenfeld. Ein neuer effekt bei eintritt der supraleitfähigkeit. *Naturwissenschaften*, 21(44):787–788, 1933.

[55] Lev Davidovich Landau and VL Ginzburg. On the theory of superconductivity. *Zh. Eksp. Teor. Fiz.*, 20:1064, 1950.

[56] John Bardeen, Leon N Cooper, and J Robert Schrieffer. Theory of superconductivity. *Physical Review*, 108(5):1175, 1957.

[57] John Bardeen, Leon N Cooper, and J Robert Schrieffer. Microscopic theory of superconductivity. *Physical Review*, 106(1):162, 1957.

[58] Leon N Cooper. Bound electron pairs in a degenerate fermi gas. *Physical Review*, 104(4):1189, 1956.

[59] NE Bickers, DJ Scalapino, and SR White. Conserving approximations for strongly correlated electron systems: Bethe-salpeter equation and dynamics for the two-dimensional hubbard model. *Physical review letters*, 62(8):961, 1989.

[60] Douglas J Scalapino. The case for d x2- y2 pairing in the cuprate superconductors. *Physics Reports*, 250(6):329–365, 1995.

[61] Tôru Moriya, Yoshinori Takahashi, and Kazuo Ueda. Antiferromagnetic spin fluctuations and superconductivity in high t c oxides. *Physica C: Superconductivity*, 185:114–119, 1991.

[62] Stuart SP Parkin, Christian Kaiser, Alex Panchula, Philip M Rice, Brian Hughes, Mahesh Samant, and See-Hun Yang. Giant tunnelling magnetoresistance at room temperature with mgo (100) tunnel barriers. *Nature materials*, 3(12):862–867, 2004.

[63] Charles Kittel. Physical theory of ferromagnetic domains. *Reviews of modern Physics*, 21(4):541, 1949.

[64] K Bussmann, GA Prinz, S-F Cheng, and D Wang. Switching of vertical giant magnetoresistance devices by current through the device. *Applied physics letters*, 75(16):2476–2478, 1999.

[65] Janice Nickel. *Magnetoresistance overview*. Hewlett-Packard Laboratories, Technical Publications Department Palo Alto, CA, USA, 1995.

[66] Robert E Camley and J Barnaś. Theory of giant magnetoresistance effects in magnetic layered structures with antiferromagnetic coupling. *Physical review letters*, 63(6):664, 1989.

[67] S Jin, Th H Tiefel, M McCormack, RA Fastnacht, R_ Ramesh, and LH Chen. Thousandfold change in resistivity in magnetoresistive la-ca-mn-o films. *Science*, 264(5157):413–415, 1994.

[68] PM Tedrow, R Meservey, and BB Schwartz. Experimental evidence for a first-order magnetic transition in thin superconducting aluminum films. *Physical Review Letters*, 24(18):1004, 1970.

[69] Michel Julliere. Tunneling between ferromagnetic films. *Physics letters A*, 54(3):225–226, 1975.

[70] Terunobu Miyazaki and N Tezuka. Giant magnetic tunneling effect in fe/al 2 o 3/fe junction. *Journal of Magnetism and Magnetic Materials*, 139(3):L231–L234, 1995.

[71] S Ikeda, J Hayakawa, Y Ashizawa, YM Lee, K Miura, H Hasegawa, M Tsunoda, F Matsukura, and H Ohno. Tunnel magnetoresistance of 604% at 300 k by suppression of ta diffusion in cofeb/mgo/cofeb pseudo-spin-valves annealed at high temperature. *Applied Physics Letters*, 93(8):2508, 2008.

[72] Claude Chappert, Albert Fert, and Frédéric Nguyen Van Dau. The emergence of spin electronics in data storage. *Nature materials*, 6(11):813–823, 2007.

[73] IK Yanson. Nonlinear effects in the electric conductivity of point junctions and electron-phonon interaction in normal metals. *Soviet Journal of Experimental and Theoretical Physics*, 39:506, 1974.

[74] Yu V Sharvin. Observation of dynamic intermediate state of superconductors with the aid of microcontacts. *JETP Lett.(USSR)(Engl. Transl.);(United States)*, 2, 1965.

[75] M Knudsen. The kinetic theory of gases, methuen & co. *Ltd., London*, 1934.

[76] IO Kulik, RI Shekhter, and AN Omelyanchouk. Electron-phonon coupling and phonon generation in normal-metal microbridges. *Solid State Communications*, 23(5):301–303, 1977.

[77] IO Kulik and IK Yanson. Microcontact phonon spectroscopy in the dirty limit. *Sov. J. Low Temp. Phys*, 4:596–602, 1978.

[78] James Clerk Maxwell. A treatise on electricity and magnetism, vol. i & ii, claredon, 1904.

[79] G Wexler. The size effect and the non-local boltzmann transport equation in orifice and disk geometry. *Proceedings of the Physical Society*, 89(4):927, 1966.

[80] MJM De Jong and CWJ Beenakker. Andreev reflection in ferromagnet-superconductor junctions. *Physical review letters*, 74(9):1657, 1995.

[81] GE Blonder, M Tinkham, and TM Klapwijk. Transition from metallic to tunneling regimes in superconducting microconstrictions: Excess current, charge imbalance, and supercurrent conversion. *Physical Review B*, 25(7):4515, 1982.

[82] JM Valles, Shih-Ying Hsu, RC Dynes, and JP Garno. Electron tunneling studies of ultrathin films near the superconductor-to-insulator transition. *Physica B: Condensed Matter*, 197(1):522–529, 1994.

[83] TY Chen, Z Tesanovic, and CL Chien. Unified formalism of andreev reflection at a ferromagnet/superconductor interface. *Physical review letters*, 109(14):146602, 2012.

[84] GT Woods, RJ Soulen Jr, I Mazin, B Nadgorny, MS Osofsky, J Sanders, H Srikanth, WF Egelhoff, and R Datla. Analysis of point-contact andreev reflection spectra in spin polarization measurements. *Physical Review B*, 70(5):054416, 2004.

[85] Yu V Sharvin. On the possible method for studying fermi surfaces. *Zh. Eksperim. i Teor. Fiz.*, 48, 1965.

[86] GJ Strijkers, Y Ji, FY Yang, CL Chien, and JM Byers. Andreev reflections at metal/superconductor point contacts: Measurement and analysis. *Physical Review B*, 63(10):104510, 2001.

[87] Igor Žutić and S Das Sarma. Spin-polarized transport and andreev reflection in semiconductor/superconductor hybrid structures. *Physical Review B*, 60(24):R16322, 1999.

[88] Igor Žutić and Oriol T Valls. Tunneling spectroscopy for ferromagnet/superconductor junctions. *Physical Review B*, 61(2):1555, 2000.

[89] Adam Daire. An improved method for differential conductance measurements. *Keithley Instruments*, 1(1):1–8, 2005.

[90] N.W. Ashcroft and N.D. Mermin. *Solid State Physics*. Saunders College, Philadelphia, 1976.

[91] Joseph John Thomson. Xxiv. on the structure of the atom: an investigation of the stability and periods of oscillation of a number of corpuscles arranged at equal intervals around the circumference of a circle; with application of the results to the theory of atomic structure. *The London, Edinburgh, and Dublin Philosophical Magazine and Journal of Science*, 7(39):237–265, 1904.

[92] JA Gifford, CN Snider, J Martinez, and TY Chen. Effect of three dimensional interface in determination of spin polarization using andreev reflection spectroscopy. *Journal of Applied Physics*, 113(17):17B105, 2013.

[93] AF Andreev. Thermal conductivity of the intermediate state of superconductors. *Zh. Eksperim. i Teor. Fiz.*, 46, 1964.

[94] II Mazin, AA Golubov, and B Nadgorny. Probing spin polarization with andreev reflection: A theoretical basis. *journal of applied physics*, 89(11):7576–7578, 2001.

[95] Martin Kupka. Current-voltage characteristic and differential conductance of a point contact and planar tunnel contact between an ordinary metal and superconductor in realistic three-dimensional geometry: comparison with a one-dimensional case. *Physica C: Superconductivity*, 281(1):91–106, 1997.

[96] Santanu Chaudhuri and Philip F Bagwell. Andreev resonances in the current-voltage characteristics of a normal-metal–superconductor junction. *Physical Review B*, 51(23):16936, 1995.

[97] H De Raedt, K Michielsen, and TM Klapwijk. Andreev reflection in nanoscale metal-superconductor devices. *Physical Review B*, 50(1):631, 1994.

[98] Niels Asger Mortensen, Karsten Flensberg, and Antti-Pekka Jauho. Angle dependence of andreev scattering at semiconductor–superconductor interfaces. *Physical Review B*, 59(15):10176, 1999.

[99] Satoshi Kashiwaya and Yukio Tanaka. Tunnelling effects on surface bound states in unconventional superconductors. *Reports on Progress in Physics*, 63(10):1641, 2000.

[100] Chr Bruder. Andreev scattering in anisotropic superconductors. *Physical Review B*, 41(7):4017, 1990.

[101] CH Kant, Oleg Kurnosikov, AT Filip, P LeClair, HJM Swagten, and WJM de Jonge. Origin of spin-polarization decay in point-contact andreev reflection. *Physical Review B*, 66(21):212403, 2002.

[102] Fr Heusler. Über magnetische manganlegierungen (in german). sl. *Verhandlungen der Deutschen Physikalischen Gesellschaft*, 5:219, 1903.

[103] SJ Youn and BI Min. Effects of the spin-orbit interaction in heusler compounds: Electronic structures and fermi surfaces of nimnsb and ptmnsb. *Physical Review B*, 51(16):10436, 1995.

[104] Delia Ristoiu, JP Nozieres, CN Borca, B Borca, and Peter A Dowben. Manganese surface segregation in nimnsb. *Applied Physics Letters*, 76(17):2349–2351, 2000.

[105] Delia Ristoiu, JP Nozieres, CN Borca, Takashi Komesu, H-K Jeong, and Peter A Dowben. The surface composition and spin polarization of nimnsb epitaxial thin films. *EPL (Europhysics Letters)*, 49(5):624, 2000.

[106] W Zhu, B Sinkovic, E Vescovo, C Tanaka, and JS Moodera. Spin-resolved density of states at the surface of nimnsb. *Physical Review B*, 64(6):060403, 2001.

[107] J Kübler, AR William, and CB Sommers. Formation and coupling of magnetic moments in heusler alloys. *Physical Review B*, 28(4):1745, 1983.

[108] Andreas Hütten, J Schmalhorst, Andy Thomas, S Kämmerer, Marc Sacher, Daniel Ebke, N-N Liu, X Kou, and Günter Reiss. Spin-electronic devices with half-metallic heusler alloys. *Journal of alloys and compounds*, 423(1):148–152, 2006.

[109] T Block, C Felser, G Jakob, J Ensling, B Mühling, P Gütlich, and RJ Cava. Large negative magnetoresistance effects in co 2 cr 0.6 fe 0.4 al. *Journal of Solid State Chemistry*, 176(2):646–651, 2003.

[110] Koichiro Inomata, Susumu Okamura, Ryota Goto, and Nobuki Tezuka. Large tunneling magnetoresistance at room temperature using a heusler alloy with the b2 structure. *Japanese journal of applied physics*, 42(4B):L419, 2003.

[111] R Kelekar and BM Clemens. Epitaxial growth of the heusler alloy co2cr1-xfexal. *Journal of applied physics*, 96:540–543, 2004.

[112] A Hirohata, S Ladak, NP Aley, and GB Hix. Si segregation in polycrystalline co2mnsi films with grain-size control. *Applied Physics Letters*, 95(25):252506, 2009.

[113] A Hirohata, H Kurebayashi, S Okamura, M Kikuchi, T Masaki, T Nozaki, N Tezuka, and K Inomata. Structural and magnetic properties of epitaxial l21-structured co2 (cr, fe) al films grown on gaas (001) substrates. *Journal of applied physics*, 97(10):3714, 2005.

[114] G Jakob, F Casper, V Beaumont, S Falk, N Auth, H-J Elmers, C Felser, and H Adrian. Thin epitaxial films of the heusler compound co2cr0. 6fe0. 4al. *Journal of magnetism and magnetic materials*, 290:1104–1107, 2005.

[115] M Takagishi, M Yoshikawa, T Funayama, H Iwasaki, M Sahashi, et al. The applicability of cpp-gmr heads for magnetic recording. *Magnetics, IEEE Transactions on*, 38(5):2277–2282, 2002.

[116] S Mizukami, F Wu, A Sakuma, J Walowski, D Watanabe, T Kubota, X Zhang, H Naganuma, M Oogane, Y Ando, et al. Long-lived ultrafast spin precession in manganese alloys films with a large perpendicular magnetic anisotropy. *Physical review letters*, 106(11):117201, 2011.

[117] M Oogane, T Kubota, Y Kota, S Mizukami, H Naganuma, A Sakuma, and Y Ando. Gilbert magnetic damping constant of epitaxially grown co-based heusler alloy thin films. *Applied Physics Letters*, 96(25):252501, 2010.

[118] Zhenchao Wen, Hiroaki Sukegawa, Shinya Kasai, Masamitsu Hayashi, Seiji Mitani, and Koichiro Inomata. Magnetic tunnel junctions with perpendicular anisotropy using a co2feal full-heusler alloy. *Applied Physics Express*, 5(6):063003, 2012.

[119] Warren E Pickett and Jagadeesh S Moodera. Half metallic magnets. *Physics Today*, 54(5):39–45, 2001.

[120] S Fujii, S Sugimura, S Asano, et al. Hyperfine fields and electronic structures of the heusler alloys co2mnx (x= al, ga, si, ge, sn). *Journal of Physics: Condensed Matter*, 2(43):8583, 1990.

[121] Shoji Ishida, Shinpei Fujii, Shoei Kashiwagi, and Setsuro Asano. Search for half-metallic compounds in co2mnz (z= iiib, ivb, vb element). *Journal of the Physical Society of Japan*, 64(6):2152–2157, 1995.

[122] Hem Chandra Kandpal, Gerhard H Fecher, Claudia Felser, and Gerd Schönhense. Correlation in the transition-metal-based heusler compounds co 2 mnsi and co 2 fesi. *Physical Review B*, 73(9):094422, 2006.

[123] Lance Ritchie, Gang Xiao, Yi Ji, TY Chen, CL Chien, Ming Zhang, Jinglan Chen, Zhuhong Liu, Guangheng Wu, and XX Zhang. Magnetic, structural, and transport properties of the heusler alloys co 2 mnsi and nimnsb. *Physical Review B*, 68(10):104430, 2003.

[124] BSD Ch S Varaprasad, A Rajanikanth, YK Takahashi, and K Hono. Enhanced spin polarization of co2mnge heusler alloy by substitution of ga for ge. *Applied physics express*, 3(2):023002, 2010.

[125] A Rajanikanth, YK Takahashi, and K Hono. The enhancement of the spin polarization of co2mnsn by fe doping. *Journal of Applied Physics*, 103(10):3904, 2008.

[126] T Furubayashi, K Kodama, H Sukegawa, YK Takahashi, K Inomata, and K Hono. Current-perpendicular-to-plane giant magnetoresistance in spin-valve structures using epitaxial co2feal0. 5si0. 5/ag/co2feal0. 5si0. 5 trilayers. *Applied Physics Letters*, 93(12):122507, 2008.

[127] Hiroaki Sukegawa, Shinya Kasai, Takao Furubayashi, Seiji Mitani, and Koichiro Inomata. Spin-transfer switching in an epitaxial spin-valve nanopillar with a full-heusler co2feal0. 5si0. 5 alloy. *Applied Physics Letters*, 96(4):2508, 2010.

[128] Wenhong Wang, Hiroaki Sukegawa, Rong Shan, and Koichiro Inomata. Large tunnel magnetoresistance in co2feal0. 5si0. 5/mgo/co2feal0. 5si0. 5 magnetic tunnel junctions prepared on thermally oxidized si substrates with mgo buffer. *Applied Physics Letters*, 93(18):2504, 2008.

[129] Wenhong Wang, Enke Liu, Masaya Kodzuka, Hiroaki Sukegawa, Marec Wojcik, Eva Jedryka, GH Wu, Koichiro Inomata, Seiji Mitani, and Kazuhiro Hono. Coherent tunneling and giant tunneling magnetoresistance in co 2 feal/mgo/cofe magnetic tunneling junctions. *Physical Review B*, 81(14):140402, 2010.

[130] WH Butler, X-G Zhang, TC Schulthess, and JM MacLaren. Spin-dependent tunneling conductance of fe— mgo— fe sandwiches. *Physical Review B*, 63(5):054416, 2001.

[131] M Vahidi, JA Gifford, SK Zhang, S Krishnamurthy, ZG Yu, L Yu, M Huang, C Youngbull, TY Chen, and N Newman. Fabrication of highly spin-polarized co2feal0. 5si0. 5 thin-films. *APL Materials*, 2(4):046108, 2014.

[132] The presence of metallic al after oxidation will not significantly affect the tunneling measurements with the superconducting pb electrodes. however, the al thickness should be reduced to eliminate unwanted spin-flip scattering in the excess al for spintronic devices.

[133] TM Nakatani, A Rajanikanth, Z Gercsi, YK Takahashi, K Inomata, and K Hono. Structure, magnetic property, and spin polarization of co2fealxsi1-x heusler alloys. *Journal of Applied Physics*, 102(3):3916, 2007.

[134] Wang Wenhong, Hiroaki Sukegawa, Shan Rong, Takao Furubayashi, and Koichiro Inomata. Preparation and characterization of highly l2 {sub 1}-ordered full-heusler alloy co {sub 2} feal {sub 0.5} si {sub 0.5} thin films for spintronics device applications. *Applied Physics Letters*, 92(22), 2008.

[135] N Tezuka, N Ikeda, A Miyazaki, S Sugimoto, M Kikuchi, and K Inomata. Tunnel magnetoresistance for junctions with epitaxial full-heusler co2feal0. 5si0. 5 electrodes with b2 and l21 structures. *Applied physics letters*, 89(11):2514, 2006.

[136] CL Chien, D Musser, EM Gyorgy, RC Sherwood, HS Chen, FE Luborsky, and JL Walter. Magnetic properties of amorphous fe x b 1 0 0- x (72¡˜ x¡˜ 8 6) and crystalline fe 3 b. *Physical Review B*, 20(1):283, 1979.

[137] N Lustig, JS Lannin, JM Carpenter, and R Hasegawa. Inelastic neutron scattering in amorphous fe 0.78 p 0.22 and crystalline fe 3 p systems. *Physical Review B*, 32(5):2778, 1985.

[138] M Maurer, JM Friedt, and JP Sanchez. Local structure of amorphous and crystalline fezrx (x= 2, 3) phases: Mossbauer spectroscopy and exafs investigations. *Journal of Physics F: Metal Physics*, 15(7):1449, 1985.

[139] Magnetic Glasses. K. moorjani and jmd coey, 1984.

[140] David D Djayaprawira, Koji Tsunekawa, Motonobu Nagai, Hiroki Maehara, Shinji Yamagata, Naoki Watanabe, Shinji Yuasa, Yoshishige Suzuki, and Koji Ando. 230% room-temperature magnetoresistance in cofeb/ mgo/ cofeb magnetic tunnel junctions. *Applied Physics Letters*, 86(9):092502, 2005.

[141] Chul-Min Choi, Jin-Oh Song, and Seong-Rae Lee. Thermal stability of magnetic tunnel junctions with new amorphous zral-alloy films as the under and capping layers. *Magnetics, IEEE Transactions on*, 41(10):2667–2669, 2005.

[142] Panagiotis T Korelis, Andreas Liebig, Matts Björck, Björgvin Hjörvarsson, Hans Lidbaum, Klaus Leifer, and AR Wildes. Highly amorphous fe 90 zr 10 thin films, and the influence of crystallites on the magnetism. *Thin Solid Films*, 519(1):404–409, 2010.

[143] Hossein Raanaei, Hugo Nguyen, Gabriella Andersson, Hans Lidbaum, Panagiotis Korelis, Klaus Leifer, and Björgvin Hjörvarsson. Imprinting layer specific magnetic anisotropies in amorphous multilayers. *Journal of Applied Physics*, 106(2):023918, 2009.

[144] G Suran, M Naili, H Niedoba, F Machizaud, O Acher, and D Pain. Magnetic and structural properties of co-rich cofezr amorphous thin films. *Journal of magnetism and magnetic materials*, 192(3):443–457, 1999.

[145] Jason SC Jang, CF Chang, YC Huang, JC Huang, WJ Chiang, and CT Liu. Viscous flow and microforming of a zr-base bulk metallic glass. *Intermetallics*, 17(4):200–204, 2009.

[146] CJ Gilbert, JM Lippmann, and RO Ritchie. Fatigue of a zr-ti-cu-ni-be bulk amorphous metal: Stress/life and crack-growth behavior. *Scripta Materialia*, 38(4):537–542, 1998.

[147] Akihisa Inoue, Baolong Shen, Hisato Koshiba, Hidemi Kato, and Alain R Yavari. Cobalt-based bulk glassy alloy with ultrahigh strength and soft magnetic properties. *Nature materials*, 2(10):661–663, 2003.

[148] Jason SC Jang, SR Jian, DJ Pan, YH Wu, JC Huang, and TG Nieh. Thermal and mechanical characterizations of a zr-based bulk metallic glass composite toughened by in-situ precipitated ta-rich particles. *Intermetallics*, 18(4):560–564, 2010.

[149] DH Lee and SH Lim. Increase of temperature due to joule heating during current-induced magnetization switching of an mgo-based magnetic tunnel junction. *Applied Physics Letters*, 92(23):233502, 2008.

[150] HX Wei, QH Qin, M Ma, R Sharif, and XF Han. 80% tunneling magnetoresistance at room temperature for thin al-o barrier magnetic tunnel junction with cofeb as free and reference layers. *Journal of applied physics*, 101(9), 2007.

[151] Yuan-Tsung Chen and SM Xie. Magnetic and electric properties of amorphous co 40 fe 40 b 20 thin films. *Journal of Nanomaterials*, 2012:29, 2012.

[152] Tatsuya Aoki, Yasuo Ando, Mikihiko Oogane, and Hiroshi Naganuma. Reproducible trajectory on subnanosecond spin-torque magnetization switching under a zero-bias field for mgo-based ferromagnetic tunnel junctions. *Applied Physics Letters*, 96(14):142502, 2010.

[153] Shinji Isogami, Masakiyo Tsunoda, Kojiro Komagaki, Kazuyuki Sunaga, Yuji Uehara, Masashige Sato, Toyoo Miyajima, and Migaku Takahashi. In situ heat treatment of ultrathin mgo layer for giant magnetoresistance ratio with low resistance area product in cofeb/mgo/cofeb magnetic tunnel junctions. *Applied Physics Letters*, 93(19):192109, 2008.

[154] Ya-Hong Xie. Spin injection device having semiconductor-ferromagnetic-semiconductor structure and spin transistor, January 17 2012. US Patent 8,098,515.

[155] Jonathan Hack. Spintonic devices and methods of making spintronic devices, January 26 2004. US Patent App. 10/765,671.

[156] G Marchal, Ph Mangin, M Peicuch, Chr Janot, and J Hubsch. Magnetic measurements on amorphous fesi alloys. *Journal of Physics F: Metal Physics*, 7(6):L165, 1977.

[157] M Velez, R Morales, JM Alameda, Fernando Briones Fernández-Pola, JI Martin, JL Vicent, et al. Coercive and anisotropy fields in patterned amorphous fesi submicrometric structures. *Journal of Applied Physics*, 87(9):5654–5656, 2000.

[158] Georg Schmidt. Concepts for spin injection into semiconductorsa review. *Journal of Physics D: Applied Physics*, 38(7):R107, 2005.

[159] R Jansen, Saroj Prasad Dash, S Sharma, and BC Min. Silicon spintronics with ferromagnetic tunnel devices. *Semiconductor Science and Technology*, 27(8):083001, 2012.

[160] Ian Appelbaum. Introduction to spin-polarized ballistic hot electron injection and detection in silicon. *Philosophical Transactions of the Royal Society of London A: Mathematical, Physical and Engineering Sciences*, 369(1951):3554–3574, 2011.

[161] Mark Johnson and Robert H Silsbee. Interfacial charge-spin coupling: Injection and detection of spin magnetization in metals. *Physical Review Letters*, 55(17):1790, 1985.

[162] Friso Jacobus Jedema, AT Filip, and BJ Van Wees. Electrical spin injection and accumulation at room temperature in an all-metal mesoscopic spin valve. *Nature*, 410(6826):345–348, 2001.

[163] G Schmidt, D Ferrand, LW Molenkamp, AT Filip, and BJ Van Wees. Fundamental obstacle for electrical spin injection from a ferromagnetic metal into a diffusive semiconductor. *Physical Review B*, 62(8):R4790, 2000.

[164] K Hamaya, K Ueda, Y Kishi, Y Ando, T Sadoh, and M Miyao. Epitaxial ferromagnetic fe _{3} si/si (111) structures with high-quality hetero-interfaces. *arXiv preprint arXiv:0810.2835*, 2008.

[165] J Karel, YN Zhang, C Bordel, KH Stone, TY Chen, CA Jenkins, David J Smith, J Hu, RQ Wu, SM Heald, et al. Using structural disorder to enhance the magnetism and spin-polarization in fe x si1- x thin films for spintronics. *Materials Research Express*, 1(2):026102, 2014.

[166] AX Gray, J Karel, J Minár, C Bordel, H Ebert, J Braun, S Ueda, Y Yamashita, L Ouyang, DJ Smith, et al. Hard x-ray photoemission study of near-heusler fe x si 1- x alloys. *Physical Review B*, 83(19):195112, 2011.

[167] Y Ando, K Hamaya, K Kasahara, Y Kishi, K Ueda, K Sawano, T Sadoh, and M Miyao. Electrical injection and detection of spin-polarized electrons in silicon through an fe_3si/si schottky tunnel barrier. *arXiv preprint arXiv:0904.2980*, 2009.

[168] Jonathan Martinez, Charles Snider, Jessica Gifford, and Tingyong Chen. Determination of spin polarization of fe65si5 using andreev reflection spectroscopy. In *APS Meeting Abstracts*, volume 1, page 18014, 2013.

[169] Ssu-Yen Huang, X Fan, D Qu, YP Chen, WG Wang, J Wu, TY Chen, JQ Xiao, and CL Chien. Transport magnetic proximity effects in platinum. *Physical review letters*, 109(10):107204, 2012.

[170] A Ionescu, CAF Vaz, T Trypiniotis, CM Gürtler, H García-Miquel, JAC Bland, ME Vickers, RM Dalgliesh, S Langridge, Y Bugoslavsky, et al. Structural, magnetic, electronic, and spin transport properties of epitaxial fe 3 si/ gaas (001). *Physical Review B*, 71(9):094401, 2005.

[171] EG Moroni, W Wolf, J Hafner, and R Podloucky. Cohesive, structural, and electronic properties of fe-si compounds. *Physical Review B*, 59(20):12860, 1999.

[172] Hideo Hosono, Keiichi Tanabe, Eiji Takayama-Muromachi, Hiroshi Kageyama, Shoji Yamanaka, Hiroaki Kumakura, Minoru Nohara, Hidenori Hiramatsu, and Satoru Fujitsu. Exploration of new superconductors and functional materials, and fabrication of superconducting tapes and wires of iron pnictides. *Science and Technology of Advanced Materials*, 16(3):033503, 2015.

[173] Yoichi Kamihara, Hidenori Hiramatsu, Masahiro Hirano, Ryuto Kawamura, Hiroshi Yanagi, Toshio Kamiya, and Hideo Hosono. Iron-based layered superconductor: Laofep. *Journal of the American Chemical Society*, 128(31):10012–10013, 2006.

[174] Siegfried Graser, Peter J Hirschfeld, Thilo Kopp, Ralph Gutser, Brian Møller Andersen, and Jochen Mannhart. How grain boundaries limit supercurrents in high-temperature superconductors. *Nature Physics*, 6(8):609–614, 2010.

[175] Special issue on satellite communications. *Proc.IEEE*, 78:1033–1312, 1990.

[176] Nathan Newman and W Gregory Lyons. High-temperature superconducting microwave devices: fundamental issues in materials, physics, and engineering. *Journal of Superconductivity*, 6(3):119–160, 1993.

[177] Yoichi Kamihara, Takumi Watanabe, Masahiro Hirano, and Hideo Hosono. Iron-based layered superconductor la [o1-x f x] feas (x= 0.05-0.12) with t c= 26 k. *Journal of the American Chemical Society*, 130(11):3296–3297, 2008.

[178] Hiroki Takahashi, Kazumi Igawa, Kazunobu Arii, Yoichi Kamihara, Masahiro Hirano, and Hideo Hosono. Superconductivity at 43 k in an iron-based layered compound lao1-xfxfeas. *Nature*, 453(7193):376–378, 2008.

[179] Iron based superconductors: Preprint of contribution to teh mcgraw-hill yearbook of science and technology 2010, 2010.

[180] Xi Dai, Zhong Fang, Yi Zhou, and Fu-Chun Zhang. Even parity, orbital singlet, and spin triplet pairing for superconducting lafeaso 1- x f x. *Physical review letters*, 101(5):057008, 2008.

[181] T Tzen Ong, P Coleman, and J Schmalian. Entangled orbital triplet pairs in iron-based superconductors. *arXiv preprint arXiv:1410.3554*, 2014.

[182] Jiangping Hu. Iron-based superconductors as odd-parity superconductors. *Physical Review X*, 3(3):031004, 2013.

[183] Jiangping Hu, Ningning Hao, and Xianxin Wu. Mechanism for odd parity superconductivity in iron-based superconductors. *arXiv preprint arXiv:1303.2624*, 2013.

[184] Ningning Hao and Jiangping Hu. Odd parity pairing and nodeless antiphase s±in iron-based superconductors. *Physical Review B*, 89(4):045144, 2014.

[185] Jessica Gifford, BB Chen, Ji Zhang, Gejian Zhao, Dongrin Kim, D Wu, and Tingyong Chen. Determination of spin polarization using fe-superconductor smo _{0.82} f _{0.18} feas. *Bulletin of the American Physical Society*, 59, 2014.

[186] Kenji Ishida, Yusuke Nakai, and Hideo Hosono. To what extent iron-pnictide new superconductors have been clarified: a progress report. *Journal of the Physical Society of Japan*, 78(6):062001, 2009.

[187] J Prakash, SJ Singh, SL Samal, S Patnaik, and AK Ganguli. Potassium fluoride doped laofeas multi-band superconductor: Evidence of extremely high upper critical field. *EPL (Europhysics Letters)*, 84(5):57003, 2008.

[188] Marta C Gonzalez, Cesar A Hidalgo, and Albert-Laszlo Barabasi. Understanding individual human mobility patterns. *Nature*, 453(7196):779–782, 2008.

[189] Parasharam M Shirage, Kiichi Miyazawa, Hijiri Kito, Hiroshi Eisaki, and Akira Iyo. Superconductivity at 43 k at ambient pressure in the iron-based layered compound la 1- x y x feaso y. *Physical Review B*, 78(17):172503, 2008.

[190] Zhi-An Ren, Jie Yang, Wei Lu, Wei Yi, Guang-Can Che, Xiao-Li Dong, Li-Ling Sun, and Zhong-Xian Zhao. Superconductivity at 52 k in iron based f doped layered quaternary compound pr [o1–xfx] feas. *Materials Research Innovations*, 12(3):105–106, 2008.

[191] Parasharam M Shirage, Kiichi Miyazawa, Kunihiro Kihou, Chul-Ho Lee, Hijiri Kito, Kazuyasu Tokiwa, Yasumoto Tanaka, Hiroshi Eisaki, and Akira Iyo. Synthesis of erfeaso-based superconductors by the hydrogen doping method. *EPL (Europhysics Letters)*, 92(5):57011, 2010.

[192] Parasharam M Shirage, Kunihiro Kihou, Chul-Ho Lee, Hijiri Kito, Hiroshi Eisaki, and Akira Iyo. Emergence of superconductivity in 32522 structure of (ca3al2o5–y)(fe2pn2)(pn= as and p). *Journal of the American Chemical Society*, 133(25):9630–9633, 2011.

[193] Parasharam M Shirage, Kunihiro Kihou, Chul-Ho Lee, Hijiri Kito, Hiroshi Eisaki, and Akira Iyo. Superconductivity at 28.3 and 17.1 k in (ca4al2o6-y)(fe2pn2)(pn= as and p). *arXiv preprint arXiv:1008.2586*, 2010.

[194] Jie Yang, Zheng-Cai Li, Wei Lu, Wei Yi, Xiao-Li Shen, Zhi-An Ren, Guang-Can Che, Xiao-Li Dong, Li-Ling Sun, Fang Zhou, et al. Superconductivity at 53.5 k in gdfeaso1- δ. *Superconductor Science and Technology*, 21(8):082001, 2008.

[195] Yi Yin, M Zech, TL Williams, XF Wang, G Wu, XH Chen, and JE Hoffman. Scanning tunneling spectroscopy and vortex imaging in the iron pnictide superconductor bafe 1.8 co 0.2 as 2. *Physical review letters*, 102(9):097002, 2009.

[196] J George Bednorz and K Alex Müller. Possible hight c superconductivity in the ba- la- cu- o system. *Zeitschrift für Physik B Condensed Matter*, 64(2):189–193, 1986.

[197] A Schilling, M Cantoni, JD Guo, and HR Ott. Superconductivity above 130 k in the hg-ba-ca-cu-o system. *Nature*, 363(6424):56–58, 1993.

[198] Donald M Ginsberg. *Physical properties of high temperature superconductors III*, volume 3. World Scientific, 1992.

[199] Kevin S Bedell, D Coffey, DE Meltzer, D Pines, and JR Schrieffer. High temperature superconductivity: Proceedings. Technical report, Los Alamos National Lab., NM (USA), 1990.

[200] B Batlogg. A critical review of selected experiments in high-t c superconductivity. *Physica B: Condensed Matter*, 169(1):7–16, 1991.

[201] Dan Shechtman, Ilan Blech, Denis Gratias, and John W Cahn. Metallic phase with long-range orientational order and no translational symmetry. *Physical Review Letters*, 53(20):1951, 1984.

[202] Dov Levine and Paul Joseph Steinhardt. Quasicrystals: a new class of ordered structures. *Physical Review Letters*, 53(26):2477, 1984.

[203] Li Guohong, He Haifeng, Wang Yunping, Lu Li, Li Shanlin, Jing Xiunian, and Zhang Dianlin. Tunneling spectroscopy in alnico decagonal quasicrystals. *Physical review letters*, 82(6):1229, 1999.

[204] Xiao-Liang Qi and Shou-Cheng Zhang. Topological insulators and superconductors. *Reviews of Modern Physics*, 83(4):1057, 2011.

[205] Andreas P Schnyder, Shinsei Ryu, Akira Furusaki, and Andreas WW Ludwig. Classification of topological insulators and superconductors in three spatial dimensions. *Physical Review B*, 78(19):195125, 2008.

[206] Masatoshi Sato. Topological odd-parity superconductors. *Physical Review B*, 81(22):220504, 2010.

[207] Liang Fu and Charles L Kane. Superconducting proximity effect and majorana fermions at the surface of a topological insulator. *Physical review letters*, 100(9):096407, 2008.

[208] Liang Fu and Erez Berg. Odd-parity topological superconductors: theory and application to cu x bi 2 se 3. *Physical review letters*, 105(9):097001, 2010.

[209] Satoshi Sasaki, M Kriener, Kouji Segawa, Keiji Yada, Yukio Tanaka, Masatoshi Sato, and Yoichi Ando. Topological superconductivity in cu x bi 2 se 3. *Physical review letters*, 107(21):217001, 2011.

[210] Frank Wilczek. Majorana returns. *Nature Physics*, 5(9):614–618, 2009.

[211] Marcel Franz. Viewpoint: Race for majorana fermions. *Physics*, 3:24, 2010.

[212] KT Law, Patrick A Lee, and TK Ng. Majorana fermion induced resonant andreev reflection. *Physical review letters*, 103(23):237001, 2009.

[213] Karsten Flensberg. Tunneling characteristics of a chain of majorana bound states. *Physical Review B*, 82(18):180516, 2010.

[214] Jay D Sau, Sumanta Tewari, Roman M Lutchyn, Tudor D Stanescu, and S Das Sarma. Non-abelian quantum order in spin-orbit-coupled semiconductors: Search for topological majorana particles in solid-state systems. *Physical Review B*, 82(21):214509, 2010.

[215] Vincent Mourik, Kun Zuo, SM Frolov, SR Plissard, EPAM Bakkers, and LP Kouwenhoven. Signatures of majorana fermions in hybrid superconductor-semiconductor nanowire devices. *Science*, 336(6084):1003–1007, 2012.

[216] Sebastien R Plissard, Dorris R Slapak, Marcel A Verheijen, Moïra Hocevar, George WG Immink, Ilse van Weperen, Stevan Nadj-Perge, Sergey M Frolov, Leo P Kouwenhoven, and Erik PAM Bakkers. From insb nanowires to nanocubes: looking for the sweet spot. *Nano letters*, 12(4):1794–1798, 2012.

[217] Thomas Walsh. Zero-bias anomalies in the current-voltage and conductance-voltage characteristics of high-critical-temperature superconductor junctions. *International Journal of Modern Physics B*, 6(02):125–170, 1992.

[218] DA Brawner, E Kaufmann, and HR Ott. Explanation of the zero-bias anomaly in the tunneling characteristics of single-crystal bi 2 sr 2 ca cu 2 o 8 with intrinsic josephson tunneling. *Physical Review B*, 53(21):14581, 1996.

[219] LYL Shen and JM Rowell. Zero-bias tunneling anomaliestemperature, voltage, and magnetic field dependence. *Physical Review*, 165(2):566, 1968.

[220] Praha International Conference on Semiconductor Physics. 1960. *Proceedings of the International Conference on Semiconductor Physics: Prague 1960,[Czechoslovakia, from August 29th to September 2nd 1960].* Publishing House of the Czechoslovak Academy of Sciences, 1961.

[221] JC Fisher and Ivar Giaever. Tunneling through thin insulating layers. *Journal of Applied Physics*, 32(2):172–177, 1961.

[222] AG Chynoweth, RA Logan, and DE Thomas. Phonon-assisted tunneling in silicon and germanium esaki junctions. *Physical Review*, 125(3):877, 1962.

[223] RA Logan, JM Rowell, and FA Trumbore. Phonon spectra of ge-si alloys. *Physical Review*, 136(6A):A1751, 1964.

[224] Robert Thomas Payne. Phonon energies in germanium from phonon-assisted tunneling. *Physical Review*, 139(2A):A570, 1965.

[225] Robert C Jaklevic and John Lambe. Molecular vibration spectra by electron tunneling. *Physical Review Letters*, 17(22):1139, 1966.

[226] JM Rowell, WL McMillan, and WL Feldmann. Phonon emission and self-energy effects in normal-metal tunneling. *Physical Review*, 180(3):658, 1969.

[227] RN Hall, JH Racette, and H Ehrenreich. Direct observation of polarons and phonons during tunneling in group 3-5 semiconductor junctions. *Physical Review Letters*, 4(9):456, 1960.

[228] AFG Wyatt. Anomalous densities of states in normal tantalum and niobium. *Physical Review Letters*, 13(13):401, 1964.

[229] DJ Kim. A theory of anomalous tunneling conductance. *Physics Letters*, 18(3):215–216, 1965.

[230] JM Rowell and LYL Shen. Zero-bias anomalies in normal metal tunnel junctions. *Physical Review Letters*, 17(1):15, 1966.

[231] Jun Kondo. Resistance minimum in dilute magnetic alloys. *Progress of theoretical physics*, 32(1):37–49, 1964.

[232] R Stratton, E Burstein, and S Lundqvist. Tunneling phenomena in solids, 1969.

[233] Joel A Appelbaum, JC Phillips, and G Tzouras. Microscopic theory of tunneling anomalies. *Physical Review*, 160(3):554, 1967.

[234] J Sólyom and A Zawadowski. Theory of zero bias anomalies due to paramagnetic impurities. *Physik der kondensierten Materie*, 7(5):325–341, 1968.

[235] HR Zeller and I Giaever. Tunneling, zero-bias anomalies, and small superconductors. *Physical Review*, 181(2):789, 1969.

[236] Jessica Gifford, Gejian Zhao, Bochoao Li, Ji Zhang, Dongrin Kim, and TY Chen. Zero bias anomaly in point contact andreev reflection spectroscopy. In *APS Meeting Abstracts*, volume 1, 2015.

[237] Roland Weiss, Roland Mattheis, and Günter Reiss. Advanced giant magnetoresistance technology for measurement applications. *Measurement Science and Technology*, 24(8):082001, 2013.

[238] Roland Weiss, Roland Mattheis, and Gnter Reiss. Advanced giant magnetoresistance technology for measurement applications. *Measurement Science and Technology*, 24(8):082001, 2013.

[239] J Pelegrí-Sebastiá and D Ramíỳrez-Muñoz. Safety device uses gmr sensor. *EDN*, 48(15):84–86, 2003.

[240] Càndid Reig, S Cardoso, and Subhas Chandra Mukhopadhyay. *Giant Magnetoresistance (GMR) Sensors*. Springer, 2013.

[241] CH Smith and RW Schneider. Low-field magnetic sensing with gmr sensors. nonvolatile electronics, inc.

[242] Paul Delooze, Larissa V Panina, Desmond J Mapps, Kasuhiko Ueno, and Hiroyuki Sano. Sub-nano tesla resolution differential magnetic field sensor utilizing asymmetrical magnetoimpedance in multilayer films. *Magnetics, IEEE Transactions on*, 40(4):2664–2666, 2004.

[243] Michael J Caruso, Tamara Bratland, Carl H Smith, and Robert Schneider. A new perspective on magnetic field sensing. *SENSORS-PETERBOROUGH-*, 15:34–47, 1998.

[244] Carl H Smith and Robert W Schneider. Low-field magnetic sensing with gmr sensors. In *Sensors EXPO*. Citeseer, 1999.

[245] Bob Kemp, Ad JMW Janssen, and Bob van der Kamp. Body position can be monitored in 3d using miniature accelerometers and earth-magnetic field sensors. *Electroencephalography and Clinical Neurophysiology/Electromyography and Motor Control*, 109(6):484–488, 1998.

[246] David R Baselt, Gil U Lee, Mohan Natesan, Steven W Metzger, Paul E Sheehan, and Richard J Colton. A biosensor based on magnetoresistance technology. *Biosensors and Bioelectronics*, 13(7):731–739, 1998.

BIOGRAPHICAL SKETCH

Jessica Gifford was born on November 2, 1988 in South Lake Tahoe, California. She spent most of her life in Oregon with her parents and twin sister Nicole. She joined the Physics Department at Oregon State University after graduating valedictorian from Roseburg High School in 2007. While attending Oregon State University she received many awards including the SMART grant (2007-2011), the Krane Physics Scholarship (2009-2011), Pi Mu Epsilon Honors Math Society 2011 and graduated magna cum laude with an honors B. S. in physics with a minor in math. In 2011, Jessica joined the Physics Department at Arizona State University in the PhD program. Since 2012 she has worked with Dr. Tingyong Chen in experimental condensed matter physics and had the honor of being his first graduate student. During her PhD study she has published seven referenced articles, four of which are first authorships.